UNIVERSITY OF SOUTHAMPTON

FACULTY OF PHYSICAL SCIENCE AND ENGINEERING

OPTOELECTRONICS RESEARCH CENTRE

NEXT GENERATION HEAVILY MULTIPLEXED INTERFEROMETRIC SENSOR ARRAYS

by

YI LIAO

Thesis for the degree of Doctor of Philosophy

(June 2013)

UNIVERSITY OF SOUTHAMPTON

ABSTRACT

FACULTY OF PHYSICAL SCIENCE AND ENGINEERING
OPTOELECTRONICS RESEARCH CENTRE

Doctor of Philosophy

By Yi Liao

Permanent reservoir monitoring (PRM) is an emerging market with significant potential in the oil and gas industrials, where data from several thousand pressure and acceleration sensors are used to monitor the condition of an underground hydrocarbon reservoir. Fibre-optic sensor arrays offer significant potential benefits, and highly efficient multiplexing and telemetry architectures can combine the several thousand sensors onto just a few fibres, the fewer the better. This study presents a novel, high performance interferometric fibre-optic sensor array using a distributed erbium doped fibre amplifier (EDFA) within a hybrid time and wavelength division multiplexed (TDM/DWDM) architecture, to reduce the multiplexing loss and to increase the number of sensors per fibre pair. The performance of the new heavily multiplexed sensor array is characterised, both theoretically and experimentally, which demonstrates its significant advantages in multiplexing level, insertion loss and interconnecting fibre count compared with the previous state of the art.

The amplification behaviour of a single stage EDFA is first modelled. The key properties of the doped fibre are validated by experimental comparison with simulations. This allows definition of general design guidelines for interferometric multiplexed sensor systems incorporating a distributed EDFA. The author also presents an analytical approach to accurately model the phase sensitivity in such systems. The model incorporates the various key noise contributions and also defines a novel term ‘Demod phase sensitivity’ to take into account the effects of noise aliasing in TDM based architectures. Furthermore, the author configures and characterizes sensor networks of increasing scale: 1) a 4-wavelength sensor network, 2) 16-wavelength sensor networks with 4 active, and 12 idle channels, 3) a 16-wavelength sensor network with real TDM groups, 4) 16 TDM×16 WDM and 64 TDM×16 WDM sensor networks, and finally a study of crosstalk effects is presented.

Both the simulation and experimental results show that, the network can address up to 64×16 sensors, along one single fibre pair, and can support up to 256×16 within an acceptable phase sensitivity for many applications. This work provides a novel, efficient and low-cost sensor array design to meet the significant demands of the current commercial PRM market.

Keywords: Large scale fibre-optic sensor array, hybrid TDM/DWDM, distributed EDFA, phase sensitivity, crosstalk, PRM.

Table of Contents

List of Figures

List of Tables

Declaration of Authorship

I, Yi Liao, declare that the thesis entitled

Next Generation Heavily Multiplexed Interferometric Sensor Arrays

and the work presented in it are my own and has been generated by me as the result of my own original research.

I confirm that:

- this work was done wholly or mainly while in candidature for a research degree at this University;
- where any part of this thesis has previously been submitted for a degree or any other qualification at this University or any other institution, this has been clearly stated;
- where I have consulted the published work of others, this is always clearly attributed;
- where I have quoted from the work of others, the source is always given. With the exception of such quotations, this thesis is entirely my own work;
- I have acknowledged all main sources of help;
- where the thesis is based on work done by myself jointly with others, I have made clear exactly what was done by others and what I have contributed myself;
- parts of this work have been published as: [See *List of Publications*].

Signed: ……

Date: ……

Acknowledgements

The research work presented in this thesis has been carried out under the valuable and expert guidance of Prof. David J. Richardson and Dr Ed Austin. I consider it a privilege to have been associated with them for carrying out the research work towards my Ph.D. degree. I have greatly benefited from their deep insight into the subject and constant support during numerous discussions. It is with a deep sense of affection and gratitude that I wish to express my sincere thanks to them.

The author would like to thank the Optoelectronics Research Centre (ORC) and the Stingray Geophysical (now with TGS) for the research funding and support on this project. My former supervisor Prof. Zhou Meng from the National University of Defence technology in China supports me to pursue my Ph.D. in ORC. I want to thank her for all her understanding and support. The author acknowledges her indebtness to the authorities of the university and the department for providing an opportunity to pursue the research work along with the normal departmental duties.

Most sincere thanks are due to all those who helped me to get to this stage. The author also expresses her thanks to respected Dr Shaif-ul Alam, Dr Radan Slav ĭk, Prof Michalis Zervas and Prof. Periklis Petropoulos whose suggestions helped me a lot on early stages of my research progress. The author is greatly appreciative of the help from those people who have helped on experiments and equipment, including Xin Yang, Ee Leong Lim, Francesca Parmigiani, Qian Zhang, Liam Jones, David Wu, Victor Rancano, Sheng Liu, Joseph Kakande, Peh Siong Teh, Dr Dejiao Lin, and the ORC technicians. I would like to thank those helped on my writing, including Dr. Stuart A. Kingsley, Dr Kevin O'shea and Dr John Wooler.

The author would also like to thank all those people who cooperated in one way or the other way to complete the research work in time, including Eve Smith, Miss Tanya Morrow, Dr Ping Hua, the ORC Secretaries etc...

The author is deeply indebted to her parents, her sister and brother for their motivation, support and encouragements and to Dr Siliang Niu who motivated her to speed up the research work, with patient understanding and cooperation.

List of Abbreviations

ADC	analogue to digital convertor
AOM	acousto-optic modulators
ASE	amplified spontaneous emission
CW	continuous-wave
DBR	distributed Bragg reflector
DC	direct current
DFB	distributed-Feedback
EDF	erbium doped fibre
EDFA	erbium doped fibre amplifier
ER	extinction ratio
FBG	fibre Bragg gratings
FC	fibre coupler
FDM	Frequency division multiplexed
FWHM	full-width half-maximum
FWM	four-wave mixing
GVD	group velocity dispersion
HUC	homogeneous upconversion
IL	insertion loss
ITU	international telecommunications union
MI	modulation instability
MZ	Mach-Zehnder
MZSA	Mach-Zehnder ladder sensor array
NLFL	narrow linewidth fibre laser
NA	numerical aperture
NF	noise figure

NRL	Naval Research Laboratory
OAM	optical add multiplexer
OADM	optical add drop multiplexer
OBC	ocean-bottom seismic cable
ODM	optical drop multiplexer
OSA	optical spectrum analyser
OSNR	optical signal noise ratio
OSU	optical sensor unit
PGC	phase generator carrier
PINFET:	p-intrinsic-n, field-effect transistor
PRM	permanent reservoir monitoring
PSD	power spectral density
PZT	piezoelectric transducer
RIN	relative intensity noise
SBS	stimulated Brillouin scattering
SPM	self-phase modulation
SRS	stimulated Raman scattering
SMF	single mode fibre
SNR	signal noise ratio
SPM	self-phase modulation
SSB	single sideband noise
SHB	spectral hole burning
TXAMP	transmitter amplifier
TDM	time division multiplexing
VPI	VPIphotonics
WDM	wavelength division multiplexer/ multiplexing
XPM	cross-phase modulation

List of Symbols

A	channel isolation	dB
A_{eff}	effective mode area	μm^2
$\alpha_{RS}(\upsilon_k)$	background loss caused by Rayleigh scattering	dB/km
$\alpha(\lambda)$	absorption spectrum per unit length	dB/m
b	erbium ion dopant radius	μm
B	detection bandwidth	Hz
B_a, B_{ak}	aliased bandwidth	Hz
B_e	electrical bandwidth at the receiver	Hz
B_O	optical bandwidth of the ASE	Hz
B_{OSNR}	optical bandwidth for the OSNR	Hz
B_S	optical linewidth of the fiber lasers	Hz
c	speed of light	m/s
C	back-scattering capture fraction	-
C_R	Rayleigh constant parameter	$dB\ km^{-1}\mu m^4$
C_{WDM}	Sensor crosstalk between wavelength	dB
C_{UP}	up-conversion efficient	m^3/s
D	optical duty cycle in the time domain	-
Δn	index difference	-
$\Delta\upsilon_k$	noise bandwidth	-
e	electron charge	coulombs
d	fibre length imbalance	m
$\delta\phi(t)$	phase deviation from the ASE field	rad
$\delta\varphi$	phase noise to the demodulation signal	rad
$\delta\phi$	phase noise of the laser	rad/√Hz
$\delta\nu$	frequency noise of the laser	Hz/√Hz
$\delta\upsilon$	ASE spectrum unit	Hz
$\delta\varphi_{shots}$	signal-shot noise induced phase noise amplitude	μrad/√Hz
$\delta\varphi_{shot-ASE}$	ASE-noise-shot noise induced phase noise amplitude	μrad/√Hz
$\delta\varphi_{S-ASE}$	signal to ASE beat noise induced phase noise amplitude	μrad/√Hz
$\delta\varphi_{SASE-ASE}$	ASE-ASE beat noise induced phase noise amplitude	μrad/√Hz
$\delta\varphi_{receiver}$	receiver noise induced phase noise amplitude	μrad/√Hz
$\delta\varphi_{laser-freq}$	laser frequency noise amplitude	μrad/√Hz
$\delta\varphi_{laser-RIN}$	laser intensity noise induced phase noise amplitude	μrad/√Hz
$\delta\varphi_{RF}$	oscillator noise induced phase noise amplitude	μrad/√Hz
$\delta\varphi_{ASE-XPM}$	ASE-XPM noise induced phase noise amplitude	μrad/√Hz
$\delta\varphi_{ASE-PHASE}$	ASE-PHASE noise induced phase noise amplitude	μrad/√Hz
$\delta\varphi_{Demod}$	Demod phase sensitivity amplitude	μrad/√Hz

ER	extinction ratio	dB
$E_{s1,s2}$	signal field's amplitudes of the two beat pulse	-
$E_{n1,n2}$	noise field's amplitudes of the two beat pulse	-
E_s^{out}	amplified signal field	-
E_1	in-phase component of the ASE	-
E_2	quadrature component of the ASE	-
$E_{ASE}(t)$	random, time varying amplitude of the ASE	-
f	optical frequency	-
f_B	effective aliased bandwidth	Hz
$f_{1,2}$	optical frequency of the intermediate pulses	Hz
f_e	effective starting frequency to be aliased	Hz
f_s	interrogation rate, system sapling rate	Hz
f_{rep}	pulse interrogation/repetition rate	Hz
f_m	frequency of the phase signal of interest	Hz
f_{LPF}	bandwidth of the low pass filter	Hz
f_1, f_2	optical frequency of the two beating pulses	Hz
Ψ	measured phase with noise	rad
$\varphi(t)$	measured time-dependent phase signal of interest	rad
ϕ_0	amplitude of the time-dependent phase signal of interest	
ϕ_e	environmental phase bias	-
ϕ_s	total phases of the signals from the signal arms	-
ϕ_r	total phases of the signals from the reference arms	-
ϕ_k	random phase of the individual ASE spectrum	-
$\phi_{ASE}(t)$	random, time varying phase of the ASE	-
g_B	Brillouin gain	m/W
g_R	Raman gain coefficient	m/W
$g^*(\lambda)$	emission spectrum per unit length	dB/m
G_i	gain at each EDF segment	dB
G	gain at the optical frequency	dB
h	Planck constant	m^2kg/s
$i_k(r,\phi)$	normalized optical intensity	-
$I_k(r,\phi,z)$	light intensity distribution of the kth beam	-
$\overline{i_{sh}^2}$	photon shot noise	-
$i_s(t)$	heterodyne photocurrent from the signal	-
I_{S-DC}	heterodyne photocurrent from the signal	-
I_I	in-phase components	-
I_Q	quadrature components	-
IL_x	insertion loss of the splice between EDF –to-(SMF)	dB
IL_e	background loss of the EDF	dB
IL_f	transmission loss of the SMF	dB
IL_m	insertion loss of the OA/DM (add/drop)	dB
IL_{ad}	insertion loss of the OA/DM(pass)	dB

IL_s	insertion loss of a single sensor	dB
IL_{OSU}	insertion loss of an OSU	dB
IL_{TDM}	insertion loss of a TDM group	dB
IL_{WDM}	insertion loss of a WDM	dB
k	free space optical wave wavenumber	-
k_B	Boltzmann's constant	J/K
K_R	Rayleigh constant parameter	dB/km
L	physical path length of the section fibre	m
ζ	saturation parameter	-
L_{eff}	effective interaction length	m
L_s	sensor fibre length	m
λ	operation wavelength of the optical signal	nm
λ_s	signal wavelength	nm
λ_p	pump wavelength	nm
λN	last wavelength	nm
$\mathcal{L}(f)$	single sideband noise (SSB) density	dBc/Hz
M	an integral for the ASE calculation	-
M	number of sensors in each TDM group/number of lasers in FDM	
m	crosstalk channel light intensity to another wavelength channel	
N	number of wavelength channels	-
NA	numerical aperture of the fibre	-
N_C	intensity noises in the in-phase parts	rad
N_s	intensity noises in the quadrature parts	rad
N_1	population of the ground state in EDF	-
N_2	population of the metastable state in EDF	-
N_3	population of the $^4I_{11/2}$ level	
N_{sp}	population inversion factor	-
n_φ	phase noise term	-
n_I	intensity noise term	-
n_2	nonlinearity refractive index	m/W
n_t	erbium ion concentration	ions/m^3
n_{eff}	fibre effective refractive index	-
ω_m	time-dependent phase signal of interest	Hz
ω_M	phase carrier frequencies	Hz
ω_{IF}	angular carrier (heterodyne intermediate) frequency	Hz
$P_B(L)$	initial spontaneous SBS noise power at the fibre output	W
P_{Bcr}	threshold SBS power	mW
P_{Rcr}	SRS threshold power	W
P_l	optical power when the pulse modulator is off	dBm
P_h	optical power when the pulse modulator is on	dBm
P_s	peak optical power/ incident signal power	dBm
P_{sin}	input signal	dBm

P_{se}	equivalent signal power ($P_s - IL_{TDM}$)	dBm
P_p^{th}	threshold input pump power	mW
P	mean laser power	mW
P_{0k}	spontaneous emission contribution	-
$P_{s1,s2}$	signal power of the two beat pulse	-
P_{in}	pump power of lauched into the amplifer stage	mW
P_{out}	exiting pump power from the amplifer stage	mW
P_{abs}	absorption of pump power by the amplifier's erbium ions	mW
P_p	pump power	mW
P_{sout}	output signal power	mW
q	contribution from the subtraction operation in the demodulation	
P_{ASE}	ASE noise power injected at the receiver	mW
r	distance from the fibre axis	-
σ_a	absorption cross-section	-
σ_e	emission cross-section	-
$RIN_{Inter}(f)$	expected RIN from an interferometer	dBc/Hz
R	photodiode responsivity	A/W
R_f	Receiver trans-impedance	kΩ
RIN(f)	relative intensity noise (RIN) of a laser	dBc/√Hz
$RIN_{Inter}(f)$	RIN after optical combined together	dBc/√Hz
S_{ASE}	ASE noise power	-
SSB	AOM driver signal imposes single sideband noise	dBc/√Hz
$S_{\delta P}(f)$	mean-square spectral density of the laser power fluctuation	mW/√Hz
$S_{\Delta\varphi}(f)$	spectral density of the phase fluctuation of a RF source	dBc/√Hz
$S_{\Delta\varphi}(f)_{beat}$	spectral density of the beat phase fluctuation	dBc/√Hz
τ	metastable lifetime parameter	s
$t_1 t_1$	pulse separation in normal system	ns
t_1'	pulse separation in derivative system	ns
t_p	pulse length	ns
t_r	pulse repetition time	ns
$\Gamma(\lambda)$	overlap integral function	-
V_{PINFET}	noise voltage in the receiver	mW
V	visibility of the interferometer	-
V_{nv}	voltage noise	mV
V_{ni}	current noise	mA
V_{th}	resistor thermal noise (Johnson or Nyquist noise)	mV/√Hz
ν, υ	optical frequency of the signal	Hz
ω_0	mode field radius	μm

Chapter 1
Introduction

In recent years, there is growing interest in acoustic sensing systems for subsea and sea-bottom permanent reservoir monitoring (PRM) applications. Over the past 20 years, acoustic measurement systems have been installed permanently on the seafloor and in-well for reservoir monitoring. Such sensors are being used to map reservoirs, understand how they develop and to monitor the processes used to separate oil, gas and water. However, most of these systems have been electrical, with fibre-optic systems only now starting to emerge.

Fibre-optic technology provides several advantages over electrical instrumentation for PRM applications in the oil and gas industry [1-3]. Fibre-optic sensors are highly reliable owing to their passive nature, eliminating failures caused by electronic components exposed to water. In permanent seabed reservoir monitoring systems, the small size and weight of fibre sensors are added benefits, enabling sensors to be located at otherwise inaccessible sites. In addition, the low loss and large bandwidth of optical fibres enables the transmission of huge amounts of data over tens of kilometres. In the case of subsea wells, the fibre can provide a connection to the topside facility thereby avoiding the need for any electronics beneath the surface.

In fibre-optic seismic PRM systems, the passive nature of the fibre-optic sensing system can be fully exploited. A fibre-optic seismic PRM system comprises thousands of sensors placed in grids on the seabed, as illustrated in Figure 1.1[4]. They are installed on the seafloor in a regular pattern. A strong acoustic wave is generated using a pneumatic airgun suspended at a few metres depth and propagated to the subsea floor. Each sensor measures the direct pressure wave from this airgun as well as the reflection of this wave from the rock formations underneath the sensor. In some systems, tri-axial accelerometers are also included, to measure acoustic waves propagating through the earth (the shear wave) generated by the incoming pressure impulse (p wave). Appropriate signal processing and interpretation from the multiple reflected airgun shots from different surface positions makes it possible to predict the location of oil and gas reservoirs kilometres under the sea bottom, even to monitor dynamically the effect of oil production on the reservoir over time. With thousands of sensors installed on the seafloor it is possible to cover a large area of the subsurface for global reservoir monitoring.

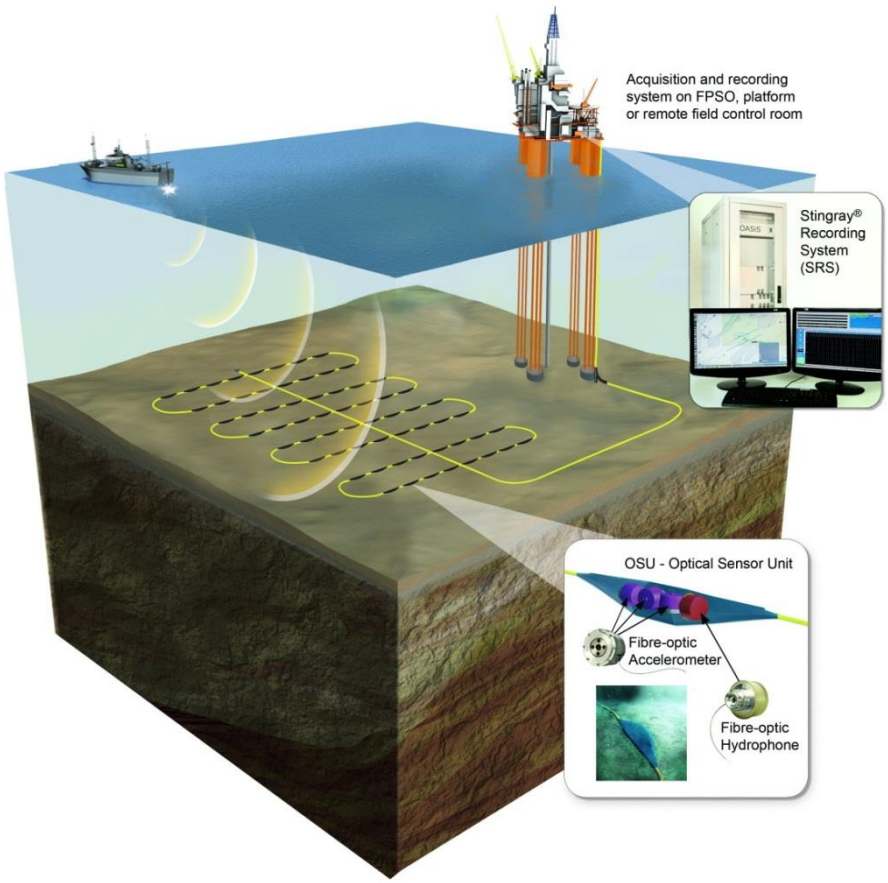

Figure 1.1: A fibre-optic ocean-bottom seismic reservoir monitoring system. Thousands of sensors are trenched in the seafloor and connected back to the topside facilities for monitoring (source: TGS).

In such large scale systems, the interrogator is mounted on a sea surface, and connected the sensor array via a riser, simply increasing the number of fibre pairs to carry source light and resulting modulation light to and from, all the sensors is impractical, expensive, and hard to operate. To commercially succeed with such large-scale systems, an efficient sensor array architecture to address a large number of sensors with as few fibres as possible is mandatory. Fortunately, fibre-optic sensors lend themselves to multiplexing, which allows the cost of the lasers and other expensive components to be divided between many channels. Many multiplexing schemes have been proposed and investigated based on techniques including time, frequency, coherence, and wavelength multiplexing, and combinations thereof [1, 5-8].

High multiplexing efficiency means a low fibre count in the riser and a small, efficient interrogator. More specifically, to keep the size of the array cable small and lower the system cost, it is desirable to multiplex a few hundreds of sensors on only one fibre pair, one fibre being used to send an optical signal to the sensors, and a second fibre to collect the signals returning

from the sensors. It is also useful to reduce the number of fibres within the cable which interconnects the array of sensors on the seafloor. To multiplex such a large number of sensors on one fibre pair, fibre splitters/couplers are used to distribute the light into and recombine the light from each sensor. The insertion loss from the fibre splitters/couplers increases with the level of multiplexing, and ultimately reduces the power of the return signal from each sensor below the detectable level. On the other hand, the launched optical power is limited by nonlinear effects. In PRM applications, sensor arrays are connected to the interrogating system on the platform using cables with lengths of up to 3 km (water depth). In some systems, to cover a large area of field, 20 km of transmission cable might be required for the furthest sensor array, and for remote measurements, light may be transmitted along over a very much greater distance (>50-100 km) [9]. Therefore, the peak optical power which can be launched into the sensor array is limited, because nonlinear effects, which degrade system performance, are more pronounced in systems using high-transmitted power on long transmission lengths. Consequently, in each instance, the splitting/recombination loss ultimately defines the scalability of the approach, with the number of fibres required for telemetry a further critical factor that significantly impacts the overall system cost and practicality.

This study proposes a novel, highly efficient fibre-optic network architecture for large-scale systems, which fully exploits the current mature dense wavelength division multiplexing (DWDM) technology and the wide bandwidth amplification nature of the erbium doped fibre amplifier (EDFA). As illustrated in Figure 1.2, this architecture uses only one pair of fibres (distribution bus and return bus) to interrogate all the multiplexed sensors. Sub-arrays are multiplexed by optical add/drop multiplexers (OA/DMs), which increase the total number of sensors by N times (with N wavelengths). M sensors in each sub-array are multiplexed by time domain multiplexing (TDM), constituting a TDM group. The proposed architecture reduces the array loss by using a distributed EDFA along the return fibre to compensate for the optical loss and splitting loss from multiplexing components, which leads to a WDM-loss-free network, therefore, the limitation from the inherent splitting loss in the WDM is successfully removed.

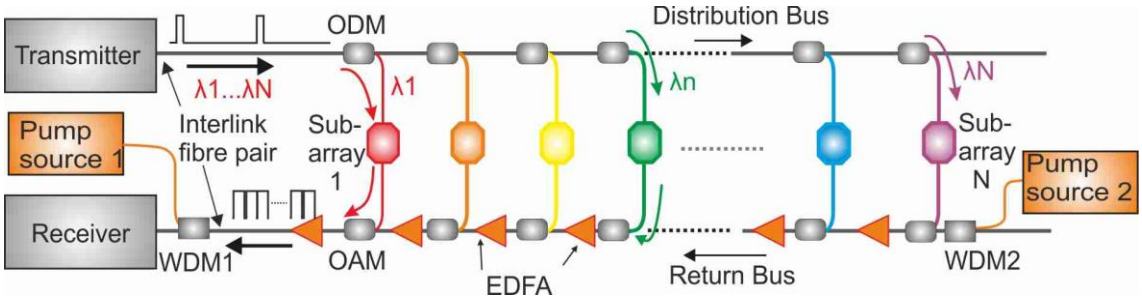

Figure 1.2: Distributed amplified hybrid TDM/WDM sensor array. OA/DM: optical add/drop multiplexers, WDM: wavelength division multiplexer.

The new architecture only uses one telemetry fibre pair to interrogate several hundreds of (N×M) sensors in a seismic fibre-optic sensor system, which is of great interest to PRM applications, both commercially and scientifically, as follows:

- The distributed EDFA reduces the insertion loss of the whole array, which leaves a higher power budget for the signal transmission along cables and connections between fibres, which enables remote interrogation with a longer transmission link.
- The lower insertion loss of the sensor array also allows for lower input signal power to the array, which lowers the signal power along the network and limits the chance of nonlinear effects.
- The lower splitting loss for each sub-array leaves a higher insertion loss budget for the TDM group in each sub-array, and allows more sensors to be addressed in it.
- The WDM-splitting-loss-free network enables us to increase the total number of sensors by simply adding more wavelength channels.
- This array architecture enables remote interrogation of sensor arrays from only one pair of multi wavelength telemetry fibres without sensor performance degradation, and can be expanded to thousands of sensors. (Previous architectures have required multi-stage wavelength splitting, requiring multiple multi-wavelength carrying telemetry fibres). The physical architecture is simple and light, and can be easily expanded.

The aim of this study is to investigate and characterize the viability, effectiveness, and the scalability of the new heavily multiplexed sensor array, both theoretically and experimentally emphasising its significant advantages in the level of multiplexing, insertion loss and interconnecting fibre count compared with the previous state of the art. The viability of the distributed amplifier in the new array is determined by an effective configuration of the distributed EDFA and commercial availabilities of the pump sources and multiplexing components. The performance of the new architecture, including the system sensitivity, the crosstalk, and the scalability, depends on the effect of the amplification on the optical signal, will also be investigated theoretically and experimentally in the work.

Thesis outline

The chapter that follows introduces the fundamentals of interferometric fibre-optic sensors and multiplexing technologies, and then summarizes current developments on large-scale fibre sensor arrays. The performance of the new amplified network is governed by the behaviour of the distributed EDFA, and therefore, Chapter 3 addresses the behaviour of EDFAs, and

determines key factors affecting the overall behaviour of EDFAs. On the basis of this knowledge, Chapter 4 demonstrates the distributed amplified sensor array architecture in more detail, including the design guidelines, and the performance of the designed architecture.

The fibre sensor system phase noise floor is strongly influenced by the array architecture and its demodulation technology. A full phase noise model for the interferometric heterodyne sensor system is developed and presented in Chapter 5. The effect of the amplification on the system performance is investigated. The trade-off between the number of sensors and the phase sensitivity in the new system is modelled analytically.

Experimental demonstration of the proposed sensor array and validations of the theoretical analysis are given in the following chapters. The emphasis is placed on the signal gain, optical signal noise ratio, pump power dissipation and system phase sensitivity. Chapter 6 demonstrates the experimental results in a network with four wavelengths, and Chapter 7 further increases the number of wavelengths to 16.

Crosstalk is a critical factor in multiplexed systems. Therefore, the crosstalk in sensor arrays is also investigated in Chapter 8. Chapter 9 then investigates the overall performances in sensor systems with 16×16 and 16×64 sensors, separately. Chapter 10 concludes the whole work in this project and discusses directions for further works.

Chapter 2
Background and literature review

Overview: This chapter reviews the fundamental science of fibre-optic interferometric sensors and multiplexing technologies, and presents a review of the present evolution of the optical fibre sensor networks, on the basis of existing literature data.

2.1 Background

Fibre-optic sensing is a varied subject with many different approaches, such as the use of interferometers, gratings, etc., for sensing a variety of parameters [9]. The subject of fibre-optic sonar, acoustic and seismic sensing is very diverse with multiple interferometric configurations and sensor multiplexing schemes being used in practical applications. Each interferometric configuration and optical multiplexing scheme has its own set of advantages and disadvantages that can be optimized for any particular application.

2.1.1 Fibre-optic acoustic sensors

The fibre-optic acoustic sensor is at the heart of seismic sensing array technology [1]. Practically all fibre-optic underwater sensor systems are based on the interferometric measurement of the strain induced in the optical fibre by the field to be measured. This functions by converting the tiny acoustic pressure/vibration variations into changes in length of the fibre, and producing phase changes of the light traveling in the optical fibre, which are then converted to amplitude modulation by an interferometer. The fibre-optic interferometric sensor simultaneously provides a high sensitivity and a high dynamic range (as been shown in [1]), it can detect a dynamic phase change of one ten-millionth of a radian, which corresponds to dynamic strains as small as ~10^{-15}, in the presence of static strains of over 1%.

Mach-Zehnder (MZ) and Michelson interferometers are the most common interferometer configurations used in deployed systems, and are shown schematically in Figure 2.1 (a) and (b), along with some of the terms applied to different parts of the interferometer. The source is amplitude-divided into two fibre arms through a 50:50 coupler, which can be thought of as representing a signal beam and a reference beam, the signal beam is exposed to the strain

change to be measured, whereas the reference beam is shielded from the acoustic field. In the Michelson configuration, the light passes through the arms twice (one each way), doubling the optical phase shift compared with that in a MZ interferometer with the same length of fibre arms. In applications where the transmissive properties of the MZ interferometer are not required, the Michelson configuration is usually favoured due to the scale factor improvement and lower cost (single coupler).

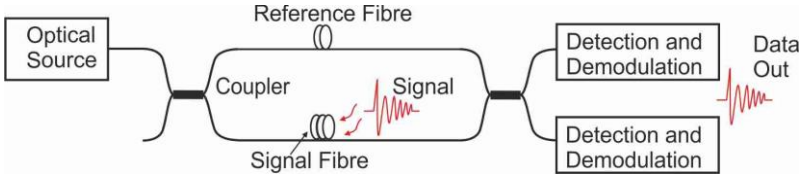

(a)

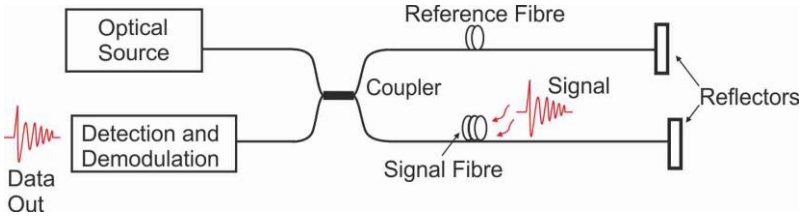

(b)

Figure 2.1: Fibre-optic interferometer configuration (a) Mach-Zehnder and (b) Michelson.

The total phase (in radians) of light travelling through a fibre is given by

$$\phi = n_{eff} kL = \frac{2\pi n_{eff} L}{\lambda} \tag{2.1}$$

where n_{eff} is the effective core refractive index, k is the optical wave number ($2\pi/\lambda$), λ is the operation wavelength, and L is the physical path length of the section fibre. Modulation of the index of refraction, wavenumber, or path length of the fibre results in a change in the total phase of the light. The differential phase shift due to a change in the physical path length L is given by:

$$\Delta\phi(L) = n_{eff} k\Delta L = \frac{2\pi n_{eff} \Delta L}{\lambda} \tag{2.2}$$

The most direct way to detect this phase change is to use an interferometer to compare it to light from the same source that is unperturbed. The two beams recombine at the coupler into the up-leads terminating in the photodetectors for detection and demodulation. The detector signal is given by

$$I = P_s R[1 + V\cos(\phi_e + \phi_0 \sin\omega_m t)] \tag{2.3}$$

where P_s is the returned optical power and $\phi_0 sin(\omega_m t)$ is the time-dependent phase signal of interest. ϕ_e is an environment phase shift, and *R* is the photodiode responsivity in A/W. V is the visibility of the interferometer determined by characteristics of the interferometer such as coupler-splitting ratios, optical loss, polarization effects, and the coherence of the optical source. As can be seen, the phase term is inside the cosine function in equation (2.3) and so the interferometer has a non-linear response. The nonlinear sensor process provides us with the huge dynamic range for underwater seismic sensing, but also results in the interferometric signal fading and frequency doubling, as shown in Figure 2.2, depending on the value of ϕ_e. To overcome interferometric signal fading, either the interferometer must be actively locked in quadrature or another means of obtaining quadrature signals must be used such as phase or frequency modulation. Interrogation schemes of phase generator carrier (PGC) and differential delay heterodyne technique are relatively mature, and under current developments [1, 10, 11]. The heterodyne technique is applied in this study, and it will be discussed later in Chapter 5.

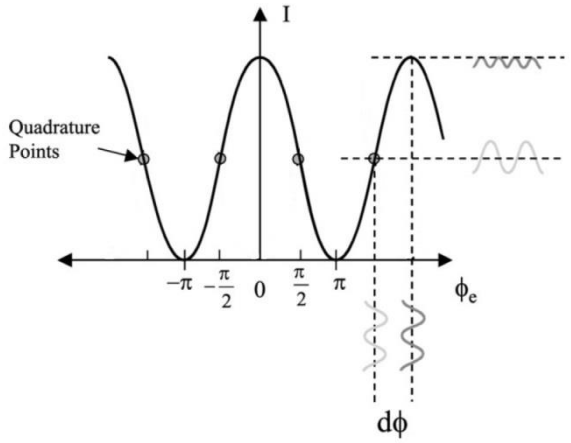

Figure 2.2: Interferometric output with environmental phase bias ϕ_e *and small-signal phase* $d\phi = \phi_0 \sin(\omega_m t)$, *shows the signal fading when the bias is near* $2n\pi$ *and* $(2n+1)\pi$ *radians, and linear operation near* $(2n+1)\pi/2$ *radians.*

The design of the sensors is beyond the scope of this work, but both pressure and vibration sensors operate in the same optical way, differing only in the mechanical packaging of the changing pressure, straining the fibre [12]. In a pressure sensor (hydrophone) the fibre coil is normally wound around a tube which deforms under the changing pressure, usually in the form of air-backed mandrel hydrophone. The typical dynamic frequency range for a hydrophone is 10Hz to 10 kHz with typical responsivity of -120 to -150 dB re rad/uPa. In a vibration sensor (geophone or accelerometer), the sensor is designed as a mass spring system (i.e., push-pull moving-mass accelerometers), where the fibre measures the strain in the spring. The typical dynamic frequency range is 10 Hz to 500 Hz, with typical responsivity of 55 dB re rad/g.

A typical mandrel hydrophone design [13, 14] is schematically shown in Figure 2.3. This comprises a central supporting structure, an air-backed mandrel, and a layer of fibre wound onto the mandrel, usually with a thin layer of encapsulant over the fibre. The presence of the air layer considerably increases the compliance of the overall structure and, therefore, the induced length change ΔL in the fibre.

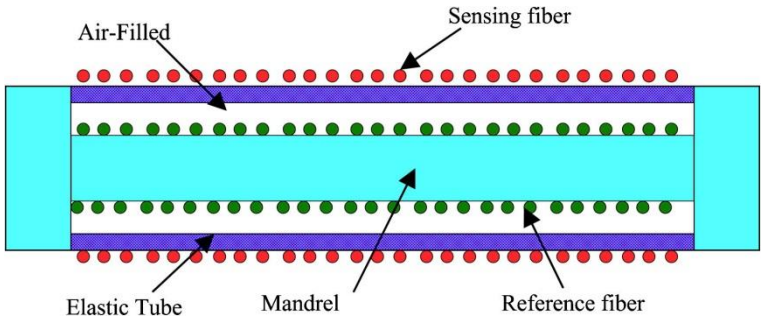

Figure 2.3: Air-backed fibre-optic mandrel hydrophone design.

2.1.2 Multiplexing

To realize the cost advantages of fibre-optic sensor systems, some form of sensor multiplexing must be performed to amortize the opto-electronics cost over multiple sensors. Fortunately, fibre optics lends itself to multiplexing and there are a large number of approaches to multiplexing fibre optic sensors [2, 3]. In practice, only a few of these approaches have seen widespread use in underwater systems and those will be the focus of this section.

Figure 2.4 shows an M×N frequency division multiplexed (FDM) sensor array utilizing M lasers to interrogate N sensors each. The outputs of the sensors are then recombined in such a way that each return fibre carries one output from each source [15]. If different phase carrier frequencies are used for each source, from ω_1 to ω_M, then each detector has M carrier frequencies and feeds M demodulators, one set to each carrier frequency. The multiplexing penalty with the FDM architecture is that the lasers cannot be at exactly the same optical frequency or they will interfere with each other. FDM is a high performance multiplexing approach with continuous interrogation allowing for wide bandwidth and high dynamic range because it is a continuous-wave (CW) approach.

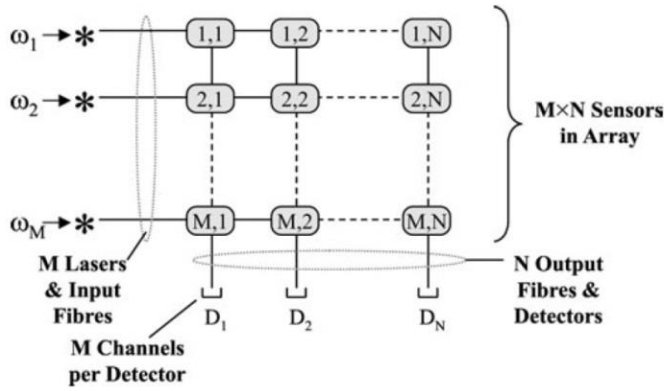

Figure 2.4: M×N frequency division multiplexed array.

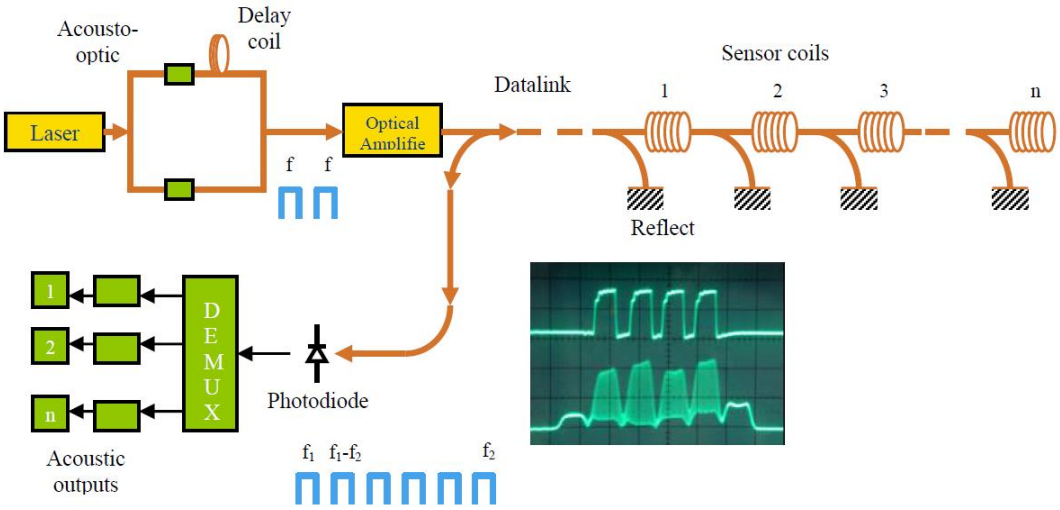

Figure 2.5: Inline Michelson TDM sensor array architecture.

Time division multiplexing (TDM) is typically achieved using a pulsed source to interrogate an array of interferometric sensors with different optical delays built into their respective paths. Sensors are sequentially addressed using the pulsed input signal such that the time of flight of optical pulses in the multiplexed array allows individual sensor signals to be distinguished. Many sensor networks based on TDM have been proposed. They generally differ in terms of the way in which optical pulses are delivered to, and returned, from the sensor. However, in general, the launched and received signals for these different networks are very similar. The choice of TDM network is usually determined by constraints on crosstalk levels, number of components, and cost. Figure 2.5 shows a basic TDM architecture (image from [12]). A series of sensor coils are spliced together, each coil separated by a directional coupler with a reflective mirror attached to one port. The other port of the coupler is index matched to ensure the suppression of multi-path reflections. The sensors are interrogated with two optical pulses which are frequently shifted relative to each other and separated in time by twice the transient time in the sensor fibre.

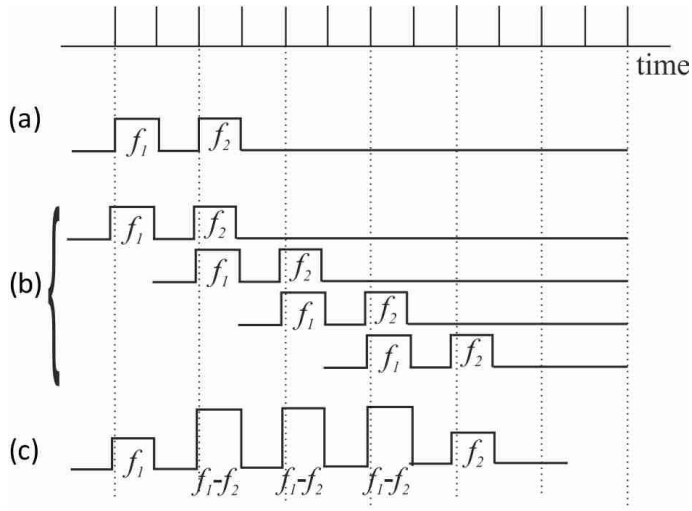

Figure 2.6: System time domain diagram for the pulses (a) to the sensors, (b) reflected pulse pairs from different reflectors, (c) beat at the photo-diode.

The timing diagram of the pulses in the system is shown in Figure 2.6. The return signal from the sensors consists of overlaps of two pulses: one being reflected form the first mirror forming the reference signal, and the other being reflected from the second mirror after passing through the sensor fibre. The overlapping pulses received at the photo-diode generate the heterodyne carrier signal that contains the phase modulation associated with the seismic signal received at the sensor coils. The couplers in the architecture figure can be replaced with partial reflectors or fibre Bragg gratings (FBGs). The multiplexing penalty with TDM is the optical splitting loss that goes as $1/n^2$ (n = the number of sensors) and aliased noise due to the inherent under-sampling of the optical return [16].

Hybrid approaches utilizing both wavelength division multiplexing (WDM) and TDM offer the highest channel counts per fibre [17, 18]. Figure 2.7 shows an example of the architecture of a hybrid TDM/WDM sensor array. With the proliferation of optical amplifiers, hybrid WDM/TDM sensor systems with channel counts of 200 to 1000 sensors per fibre and standoffs/array spans of several hundred kilometres are becoming practical. The limitation on the number of wavelengths that can be used in such a system is the minimum wavelength spacing on one hand and the available optical bandwidth on the other. The minimum wavelength spacing is limited by the availability of optical sources and wavelength multiplexing components. The optical loss of the WDM components also prohibits development. Table 2.1 presents some of the trade-off and performance issues associated with the multiplexing schemes presented above.

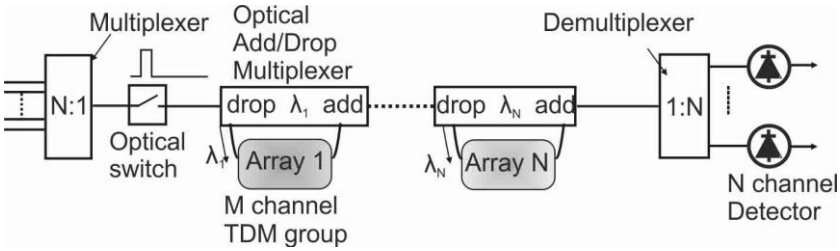

Figure 2.7: Hybrid TDM/WDM passive sensor array architecture. Each TDM group has M sensors multiplexed in the time domain. This array has M×N sensing elements.

Table 2-1: Trade-offs and performance between multiplexing technologies (with lumped EDFA).

Multiplexing	# of sensors	Sensors /fibre	Comments
FDM	(50~100)	(4~16)	Continuous interrogation, wide bandwidth, high dynamic range
TDM	10~100	10~64	Low cost, limited bandwidth
Hybrid TDM/WDM (FBG)	40~24000	80~100	Low cost, limited bandwidth
Hybrid TDM/WDM (coupler/multiplexers)	40~1600	~ 256	Low cost, limited bandwidth, high multiplexing level

2.2 Development and challenge

The development of fibre-optic acoustic sensors underwater has been ongoing for the last 30 years. As stated previously, because of the requirement of high dynamic range and sensitivity (often determined by the fact that they have to detect very small pressure changes in the presence of large hydrostatic pressures), interferometric techniques have shown themselves to be the only viable approach. The techniques used to multiplex the sensors have changed over time to simplify the array design and further lower system costs. Topologies and multiplexing schemes similar to local area networks have been explored, including ladder, serial, and star configurations, and also time, frequency, and wavelength domain multiplexing. A summary of reported experimental results on multiplexed fibre sensor arrays is illustrated in Table 2.2. (NRL: Naval Research Laboratory, DFB FL: Distributed feedback fibre laser sensor).

Table 2-2: Summary of experimental results published on fibre-optic sensor networks.

Year	Amp	Multiplex	Number of sensors	Net length	Sensor	Organization
1988 [19-22]	-	TDM serial	8	-	MZ	NRL(USA)
1989[23]	-	TDM ladder	10	-	MZ	NRL(USA)
1991[24]	-	TDM/WDM	10+4(48)	-	MZ	NRL(USA)
1995 [25-27]	-	WDM	2~4	-	FBG inter	NRL(USA)
1996 [28]	Lumped EDFA	TDM	64	50 km	MZ	NRL(USA)
1997 [29]	Lumped EDFA	TDM/WDM	64(128)	15(100) km	(MZ)	NRL(USA)
1998 [30]	Lumped EDFA	TDM	32	5 km	MZ	QinetiQ(UK)
2000 [31]	Lumped EDFA	TDM/WDM	12(96)	-	Michelson	QinetiQ(UK)
2002[5, 13, 32, 33]	Lumped EDFA	TDM/WDM	96	40 km	Michelson	NRL, QinetiQ(UK)
2005[34]	-	WDM	8	-	DFB FL	QinetiQ(UK)
2009 [17]	Lumped EDFA	TDM/WDM	256	-	Michelson	Stingray(UK), QinetiQ
2011[35]	Lumped EDFA	WDM/TDM	4(256)	500 km	Michelson	Stingray(UK), ORC(UK)
2008 [36]	Lumped EDFA	WDM	14×4	-	FBG inter-	Optoplan(Norway)
2010 [37]	Lumped EDFA	WDM	(1600)		FBG inter-	Optoplan(Norway)
1997 [2, 7, 38, 39]	Distributed EDFA	TDM	200(300)	-	MZ	Ginzton lab(USA)
2002 [40]	Distributed EDFA	TDM	16	0.1	Sagnac	Ginzton lab(USA)
1993 [41]	-	WDM	4(45)	0.6	-	Ciudad Universitaria (Spain)
2005 [42]	Raman	WDM	4	22	-	Univ. Publica de Navarra (Spain)
2005[43, 44]	Raman	WDM	8	35	-	
2009 [45]	Raman	WDM	4	50	-	
2003 [46]	Lumped EDFA	WDM	10	-	FBG	National Chiao-Tung University (Taiwan/China)
2004 [47]	Lumped EDFA	SDM	32	-	MZ	National University of Defense Technology (China)
2005 [48]	Raman	WDM	1	50	FBG	Korea Institute of Science and Technology (Korea)
2006 [49] 2009 [50]	-	WDM	16/4	800 m	DFB FL	Defence Science & Technology Organisation (Australia)

2.2.1 From FDM to lumped amplified TDM architecture

In the early 1990s at the USA Naval Research Laboratory (NRL), a considerable effort was expended developing fibre sensor arrays (towed array and fixed hydrophone arrays) based on MZ interferometers. In 1994, NRL deployed a 16-element vertical line acoustic array using FDM interrogation. This was a fixed 16-element vertical array interrogated over a 10 km cable [11]. For many systems, however, the number of fibres required in the FDM matrix approach is unattractive in terms of cost, especially for systems where there is a very long distance between the sources/receivers/electronics and the passive array, such that a cable with a large fibre count is very expensive.

For this type of system, pulsed TDM multiplexing becomes far more economical. A tapered serial array with eight-elements was demonstrated early in 1988 [21]. A small fraction of the optical power in this fibre is tapped off an output fibre bus at points between each sensor element, as illustrated in Figure 2.8. If the optical propagation delay in each sensor element is greater than the width of the input pulse, the output obtained from the array consists of a series of N+1 pulses which are separated in the time domain. Applying this output pulse train to a compensating interferometer coherently mixes pulses obtained from consecutive tap points.

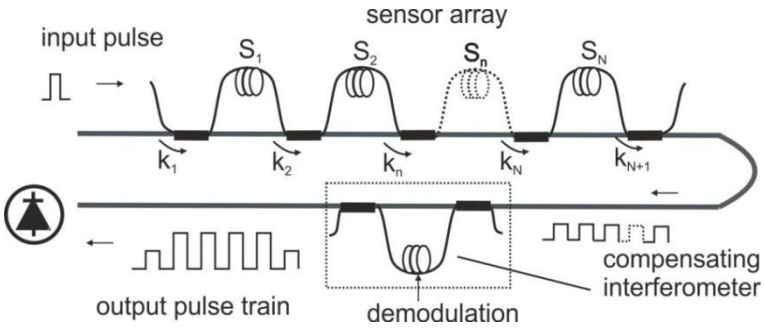

Figure 2.8: Eight sensor elements tapered serial array.

This type of configuration works well for small numbers of sensors (i.e. < 10) [23], but there are two issues in such TDM configurations, one of the issues has been the uniformity with which a sensor signal can be coupled to the array and transmitted to the receiver system. Larger arrays become problematic due to the very small coupling ratios required, and the tolerances within which the coupling ratios have to be set. A second issue commonly faced is the optical power budget: in a TDM array, the average received power per sensor falls linearly with the total number of sensors, with the splitting loss proportional to 1/(number of sensors)^2. The splitting and dissipative losses increase proportionally with the array size. For a 64-element array, the total optical loss approaches 50 dB. Such a big loss in large channel count system is prohibitive.

Lumped EDFAs are widely used in interferometric fibre sensing systems, frequently to compensate for splitting loss as well as inherent fibre transmission loss. Due to the long lifetime of the Er^{3+} transition [51], EDFAs operate on the average optical power in the amplifier and not the peak power, which makes them extremely well suited to amplifying low duty cycle (low average power) pulses in most TDM applications. Pre-amplifiers, post-amplifiers and in-line amplifiers are all often used [28]. NRL developed a system in which 64 sensors can be efficiently multiplexed in a TDM configuration with optical amplifiers for boosting the input power and telemetry over 100 km [28]. The architecture is based on a forward-coupled ladder array topology to improve uniformity between sensors, as illustrated in Figure 2.9.

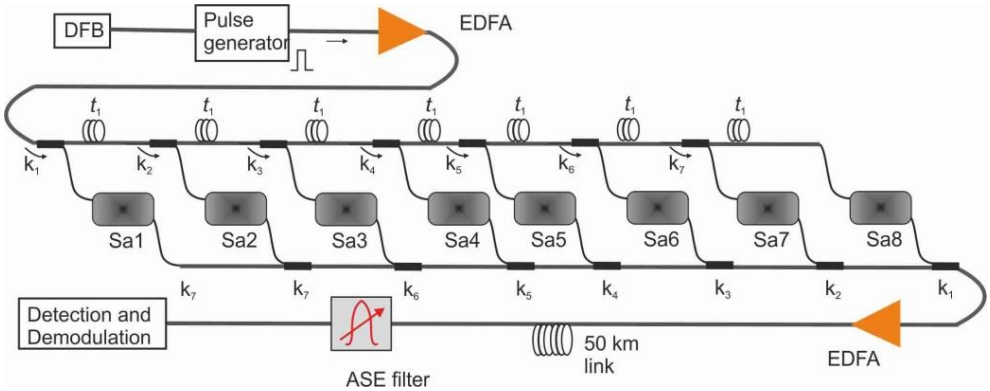

Figure 2.9: Forward-coupled array topology array with 64 sensors. Each sub array (Sa) comprises eight sensors multiplexed in time.

The use of lumped EDFA both before and after the array has enabled the TDM architecture to support 64 sensors in [29], however, increasing the number of sensors requires higher input signal powers, and nonlinear effects in the buses ultimately limit the number of sensors. A better solution from a noise standpoint is to use the in-array amplified TDM architecture. This is the subject of the work we will investigate further in the thesis.

2.2.2 In-array EDFA amplified TDM architecture

Another alternative means of improving the multiplexing level in TDM architectures is to use in-array distributed amplifiers. Researchers in the Ginzton lab of Stanford University have developed in-array distributed amplified TDM architectures, in which distributed amplifiers have been introduced along the buses in ladder architectures to compensate for the coupler losses and improve uniformity between sensors, increasing the number of sensors to ~300 in TDM architectures. Efforts have been made to improve the TDM Mach-Zehnder ladder sensor arrays (MZSA) since 1997 [7, 38, 52].

In the earlier MZSAs, sensors are TDM multiplexed onto a common fibre using splitters within a basic double bus topology. The passive array is shown in Figure 2.10. The number of sensors per fibre pair in the passive array can be maximized through careful selection of the couplers' coupling ratio, and it was also shown by Hodgson *et al* that, even after optimization, such passive multiplexing can only support 10 ~20 sensors per fibre pair [7]. This limitation is illustrated in Figure 2.11 (a), which plots the simulated noise figure (NF) of the signal returning from the last sensor versus the number of sensors in the TDM array. A passive array of 1000 sensors would therefore require ~100 bus fibres, which is unmanageable.

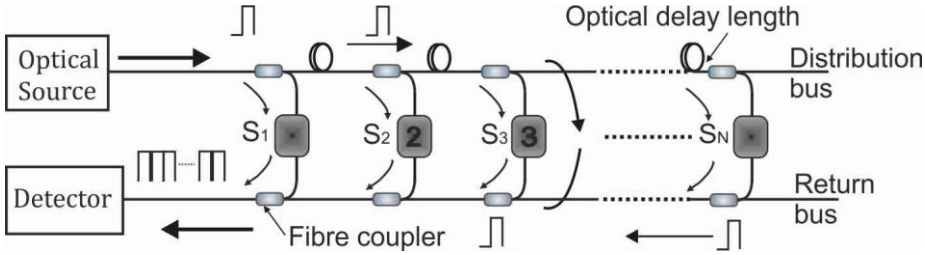

Figure 2.10: Passive MZSA TDM network in a standard ladder configuration with a distribution bus (top) and a return bus (bottom). This array has N sensors multiplexed in the time domain.

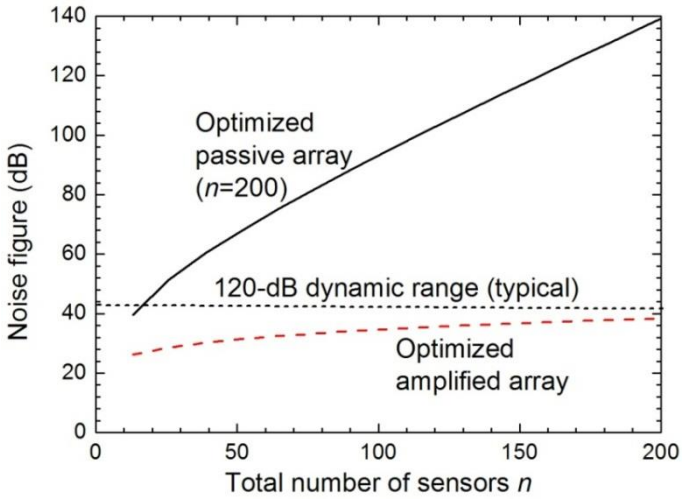

Figure 2.11: MZSA performances: calculated dependence of NF on the number of sensors for an optimized passive and amplified ladder MZSA.

Hodgson *et al* have developed a distributed amplified MZSA topology to increase the number of sensors that can be supported, by effectively compensating for the insertion loss at each coupler. In this topology, amplifiers are placed in front of each coupler on both buses as shown in Figure 2.12. The gain of each amplifier is set to exactly compensate for all the losses before the next amplifier. In this fashion all sensors return a large and equal amount of signal power to the

detector, and all the sensors have the same signal noise ratio (SNR) and sensitivity. The curve at the bottom in Figure 2.11 shows that all sensors have nearly the same SNR up to hundreds of sensors, benefiting from the distributed amplifiers. The improvement has been qualified through laboratory testing with 10 sub arrays and 20 amplifiers [6, 18, 38] .

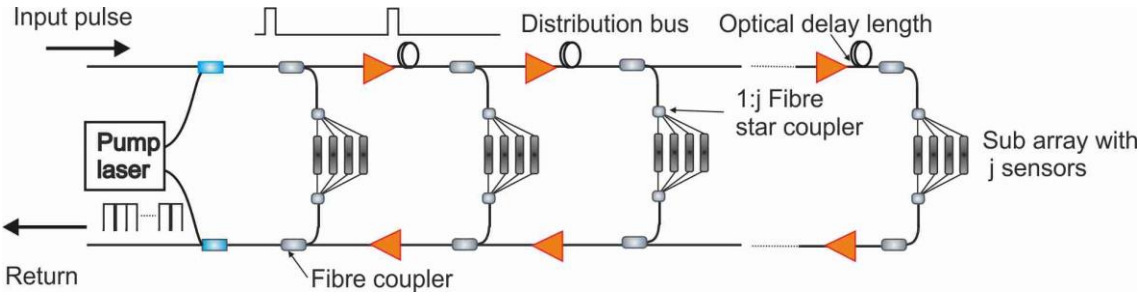

Figure 2.12: Distributed amplified MZSA TDM network with amplifiers on the distribution bus (top) and the return bus (bottom). Each sub array has j sensors multiplexed in the time domain. The pump power for the amplifier is launched from either or both ends of the buses. This array has m×j sensing elements.

However, the use of optical amplifiers adds a new source of noise to the system that quite often becomes the limiting noise in amplified TDM systems. The noise properties of optical amplifiers will be covered in more detail in Chapter 5.

2.2.3 Raman amplified WDM sensor networks

Throughout recent years, numerous groups tried other approaches for multiplexing and amplification, to extend the sensing range. Although initially optical amplification was mostly exclusively performed with EDFA, the last decade has witnessed an increase in the use of Raman amplification in fibre transmission systems.

Distributed amplification applied by EDFA and Raman effects have been investigated and compared in schemes of WDM bus topology for intensity sensors, by researchers from the University Public de Navarra in Spain [53-58], as shown in Figure 2.13. In these schemes, various intensity sensors are wavelength-division multiplexed by placing an FBG filter after each intensity sensor. In this method, only the optical power lying within the FBG filter bandwidth and modulated by the corresponding sensor will be reflected back to the receiver.

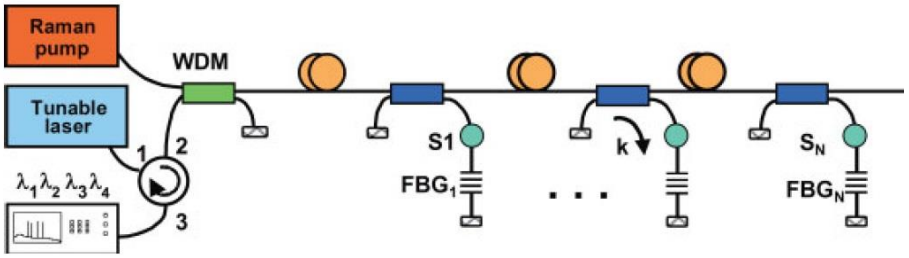

Figure 2.13: WDM multiplexing bus network

The inclusion of amplifiers has been proven to overcome the losses of the transmission fibre and the directional couplers, as well providing the capacity to equalize the received powers from all the channels. Different multiplexing topologies employing Raman amplification and distributed EDFA are studied theoretically and experimentally, with schemes shown in Figure 2.14 and Figure 2.15, separately.

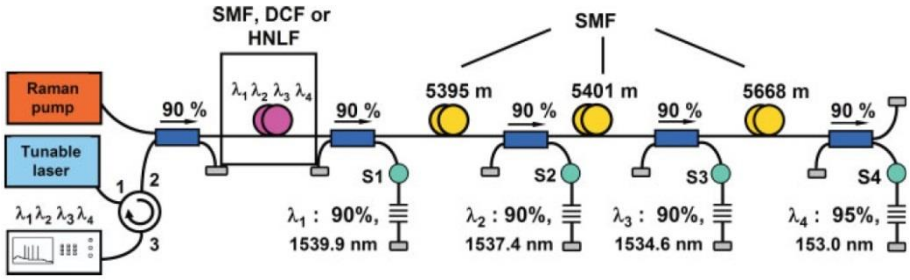

Figure 2.14: WDM multiplexing bus network with Raman amplification

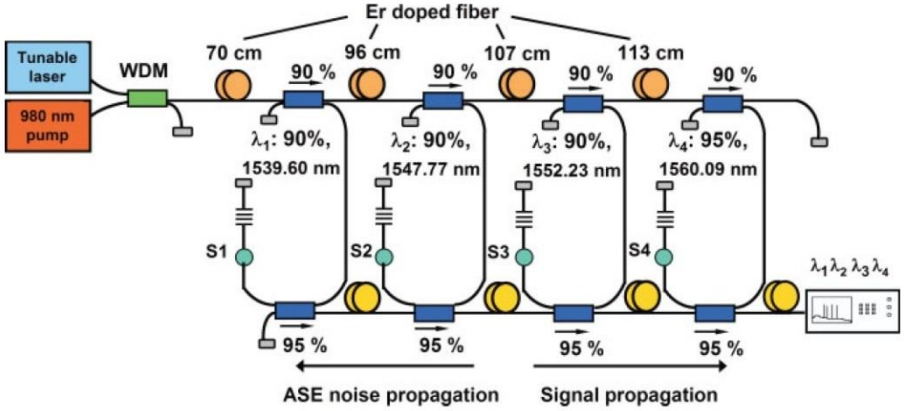

Figure 2.15: Improved WDM multiplexing double bus network with Er-doped distributed amplification.

Better optical signal noise ratio (OSNR) performance is obtained when using Raman amplification in single bus networks. However, the dominating amplified spontaneous emission (ASE) noise in the Er-doped distributed amplification based network can be reduced in an improved double bus network configuration, as shown Figure 2.15 [54]. This network removes

most of backward ASE from Er-doped fibres, providing SNR values limited only by the receiver's noise sources and not by the amount of amplification noise, allowing a higher number of sensors to be multiplexed together without degrading the SNRs achieved.

When comparing EDFA and Raman configurations, the type of optical fibre and the required pump power must be considered. For the EDFA configurations, a doped fibre is required, which increases the cost and complexity of the structure, but relatively small pump powers can be employed (less than 100 mW). On the other hand, Raman amplification is able to provide amplification over a wider wavelength range by correctly selecting the pump-power wavelengths [59]. This would allow for a greater number of sensors to be multiplexed in this kind of structure, which would ultimately be limited by the available amplification bandwidth. However, this requires longer fibres and greater pump powers (over 270 mW) and longer fibres Therefore, it makes the system complicated, and especially not viable in current TDM architectures, where the tens of metres of optical delay lengths available at each sensors are not sufficient for Raman amplification.

2.2.4 Hybrid TDM/WDM architecture

With the TDM architecture alone, the level of multiplexing that can be achieved is limited by a combination of sampling frequency and the optical power budget. To achieve the high degree of multiplexing required for a high channel count, the seismic array requires an additional multiplexing. The preferred combination of TDM and WDM allows the level of multiplexing to be increased significantly.

WDM has primarily been considered for use in communication systems. Two TDM systems operating at two separate wavelengths of 835 nm and 790 nm have been combined using this approach to allow the interrogation of a total of 14 sensor elements over a single input/output fibre pair in 1991 [24], this was the first demonstration of the hybrid TDM/WDM in NRL. In recent years, mainly due to the cheap reliable parts available from the telecommunications industry, WDM technology is fairly mature with multiple sources for lasers and multiplexing components. TDM multiplexing of sensors with the maximum output augmented with WDM multiplexing became extremely attractive. In 1996, NRL deployed a hybrid WDM/TDM array capable of interrogating 128 fibre-optic sensors over a single fibre. In the demonstration in Figure 2.16, two wavelengths were used to interrogate two half-populated (to reduce cost) TDM arrays for a total of 64 hydrophones [29]. This demonstration included an optical amplifier telemetry module to increase the standoff distance to shore.

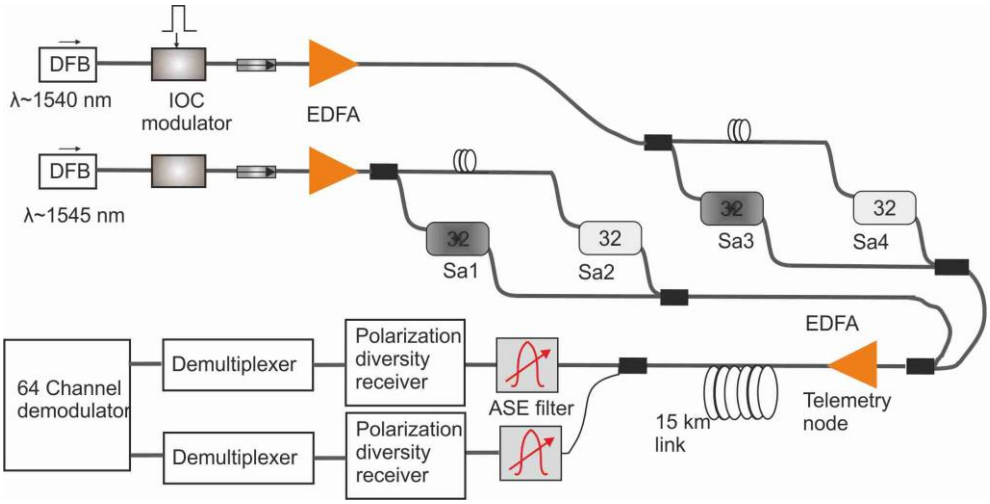

Figure 2.16: *All-optical deployable system array diagram with two multiplexed wavelengths to interrogate the half-populated 64 sensors.*

The techniques used to multiplex sensors in each TDM sub-array have also been improved over time to simplify the array design and lower the system cost [31, 60]. Previous analysis has shown that the Michelson interferometer requires less couplers and their associated splices with doubled phase shift, and is therefore preferred to Mach-Zehnder interferometers, where transmissive properties are not required. The top architecture in Figure 2.17 shows a ladder Michelson TDM array. In this case, each sensor requires three couplers, resulting in a significant amount of manual labour being needed to splice the components together and package the couplers and splice protectors when building these arrays.

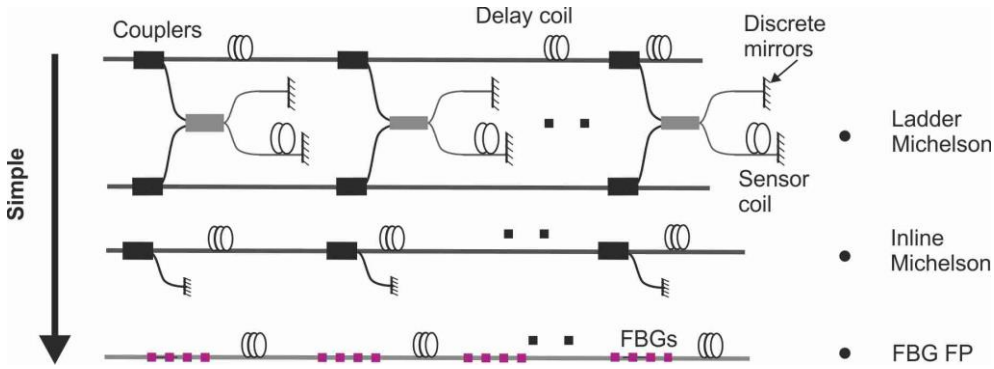

Figure 2.17: Fibre optic sensor TDM sub array.

To reduce the cost of the array, multiplexing architectures have been developed to reduce the component count and simplify the array manufacture. The inline-Michelson TDM architecture, as shown in the middle, has only one coupler per sensor. The sensors are time multiplexed on a single line, and are separated by reflectors which are constructed by silvering one port of a fibre x-coupler. With this architecture the couplers can also be purchased with the sensor fibre so that

only one splice is required per sensor. This TDM architecture was adopted in arrays from the late 1990s in NRL.

The architecture can be further simplified by incorporating low reflectivity FBGs between sensor elements. In this case the FBGs are simply acting as mirrors and should be completely decoupled from any signal-induced strain [61, 62]. This architecture eliminates the need for couplers and splices. To eliminate all the splices, the gratings must be written into a continuous piece of optical fibre which can be accomplished by writing on the draw tower while the fibre is being pulled. Now the array can be built with a continuous piece of optical fibre with no couplers or splices required, greatly simplifying the array fabrication and is adopted by the Optoplan to develop the ocean-bottom seismic cable (OBC) system.

2.2.5 Optoplan OBC system

Recently there have been significant interests in a rather different approach utilizing FBG to form Fabry-Perot (FP) sensors for TDM sub-arrays. Optoplan/Weatherford in Norway has qualified fibre ocean-bottom seismic cable (OBC) systems, based on this technology, through extensive laboratory testing with 14 stations [36, 37, 63], and has recently been awarded the world's first commercial contract for a fibre-optic OBC system for permanent reservoir monitoring which includes 24 000 FBGs and more than 3 500 km of optical fibres [64]. The seismic sensor network, as illustrated in Figure 2.18, is based on combined wavelength- and time-multiplexing of FBG based reflective Fabry-Perot type interferometric sensors, interrogated through one fibre pair connected to the sensor fibre using an optical circulator. Each sensor station consists of an inline array of five to six FBG reflectors driven by the same wavelength, equally spaced by five sensor fibre coils, i.e., five sensors in each TDM sub array.

FBGs are a very efficient way of producing an optical reflector [36], but they are intrinsically bi-directional mirrors, and their use introduces multipath-reflection based optical crosstalk, which has to be minimized in the processing [65, 66]. These crosstalk issues generally limit the number of sensor channels which can be time-multiplexed using FBGs to five. The number of sensor stations along one single fibre pair is increased by wavelength multiplexing of n sensor stations (n is typically 16 to 20) in the full C-band, ending up to 80 (100 including references) sensors to be multiplexed on a single fibre pair [36]. Polarization induced signal fading in interferometers is another issue in such systems. Therefore, we need to manipulate the input polarization state [67-69] and carry out complicated algorithms during processing. This increases the complexity in the interrogation system and limits further expansion of sensors on each single fibre pair.

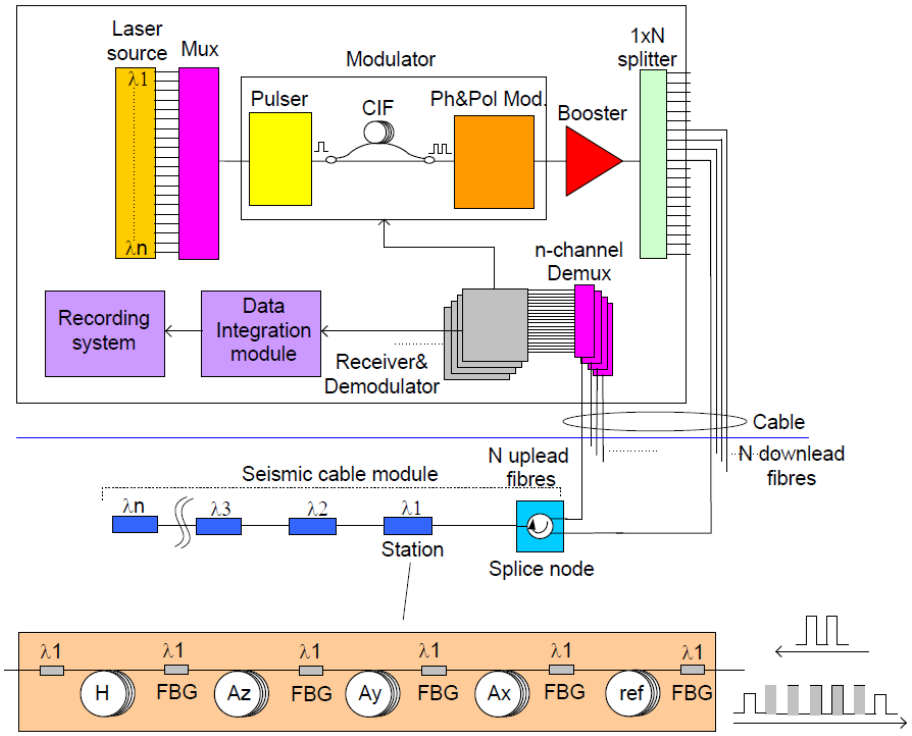

Figure 2.18: Fibre-optic OBC system configuration of Optoplan.

2.2.6 Stingray FosarDeep system

This work is partly supported by the Stingray Geophysical (now with TGS). Stingray Geophysical offers excellent fibre optic seismic systems, and was aiming to reduce the cost and improve the reliability of permanent seabed seismic monitoring, thereby making seismic PRM systems practical. It has developed various remote large scale sensor arrays for PRM applications since 2006. The current FosarDeep system is based on a 256 (allows up to 480 [12]) interferometric fibre optic sensors array, as illustrated in Figure 2.19, which involves 16 WDM and 16 levels of TDM [17]. Light from up to 16 sources is multiplexed into a single fibre and down lead to each array, where they are wavelength division de-multiplexed and each wavelength fed into a TDM sensor group, each group containing 16 fibre sensors. These sensors time multiplexed in an inline Michelson configuration, which will be discussed in detail in Chapter 4. The light is then again multiplexed back into a signal fibre and fed back via an up-lead fibre to the detection optics.

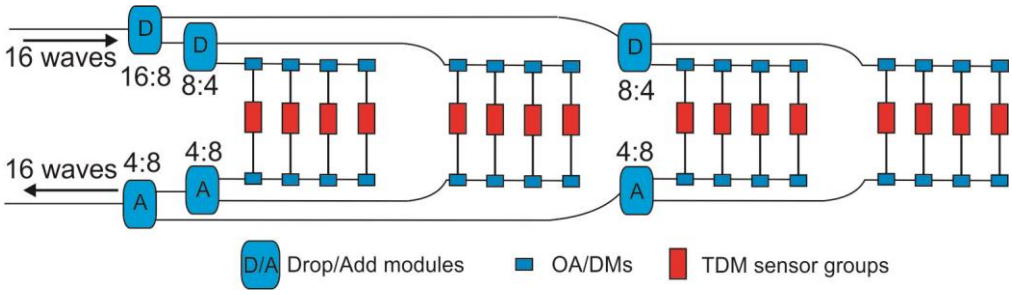

Figure 2.19: Sensor array in the Stingray Fosar optical architecture [70].16:8 and 8:4 are the wavelengths splitters.

The FosarDeep system cannot meet the requirements of current PRM developments. In order to meet the power budget, the multiplexing architecture is based on a multi-stage wavelength splitting using 16:8 and 8:4 splitters, which requires multiple multi-wavelength carrying telemetry fibres. Therefore, the array requires three pairs of fibres to interrogate 256 sensors. In a full-scale PRM system, an area of hundreds of square kilometers needs to be covered by tens of thousands of sensors. Simply increasing the number of fibre pairs to achieve this number is impractical, expensive, and hard to operate. Therefore, we need to develop an active optical architecture for the array, which can be easily expanded, to interrogate the large number of sensors required to meet this goal.

2.3 Discussion and conclusion

Practically all fibre-optic seismic sensor systems undersea are based on interferometric measurements, due to the coexisting high sensitivity and high dynamic range. The choice of the interferometric configuration is based on the complexity and cost to multiplex sensors in TDM architectures. Inline Michelson TDM architectures are preferred and have become a mature technology in the research field of the fibre-optic acoustic and seismic sensor array.

The maximum number of sensors per fibre pair in a passive TDM array is limited to 10~20 due to the coupler losses in TDM arrays. Compensation for splitting loss as well as fibre loss has been achieved by incorporating fibre amplifiers in the array. This overcomes the high optical loss in large TDM arrays, enabling TDM technology to increase the number of sensors to 64, and also allows for spans of several hundred kilometres, dramatically increasing the capabilities. However, nonlinear effects in the bus limit the maximum input power to the TDM architectures, and ultimately limit the number of sensors in lumped amplified TDM architectures to be further increased.

In-array amplification technology was alternative developed to increase the number of sensors in TDM arrays, which allows 200∼300 sensors to be addressed by only one fibre pair. However, the TDM addressing results in a lower *duty cycle* (defined as the ratio between the pulse duration and the period of a rectangular waveform) of every sensor in large scale architectures, which reduces the bandwidth available for signal interrogation and puts a premium on the detected SNR.

Raman amplification was also adopted in multiplexed sensor arrays and turned out to be impractical in TDM based architectures, where limited fibre delay length are not sufficient for the amplification.

Compared to the TDM architecture, the combination of DWDM with several TDM schemes is significantly more efficient, both in terms of the number of sensors per fibre and the number of sensors per laser [17, 18]. DWDM allows many TDM sensors at different wavelengths to be combined on a single fibre simultaneously, such that the multiplexing factor is now given by the product of the number of TDM sensors (typically >10) and the number of wavelengths. Recent advances in DWDM further impact fibre-optic sensor architectures and capabilities. Twenty years ago, WDM was not practical due to the lack of availability of sources and multiplexing components. Today, mainly due to the telecommunication industry, WDM technology is fairly mature with multiple sources for lasers and multiplexing components. The limitation on the number of wavelengths that can be used in such a system is the minimum wavelength spacing on one hand and the available optical bandwidth on the other hand. The minimum wavelength spacing is limited by the availability of optical sources and wavelength multiplexing components. Currently, 50 GHz (∼0.4 nm in the 1550 nm band) WDM components are readily available. The trend in telecommunications is for closer and closer spacing; so 25 GHz and even some 12.5 GHz spaced components are available. The optical bandwidth is limited by the optical amplifier technology, which similarly continues to evolve. The erbium band, which is known as the *C* band in telecommunications, provides 40 nm of usable bandwidth, from 1525 to 1565 nm; amplifier technology for the L band from 1568 to 1610 nm has also been developed, which provides nearly 100 nm of usable optical bandwidth. Using the C + L erbium band and the 50 GHz WDM components, up to 200 wavelengths can be multiplexed on a single fibre.

However, although WDM technology exists to support the multiplexing of this many wavelengths, the optical loss of the WDM components prohibits WDM arrays of large size (i.e., the Fosar Deep system), unless additional amplification is used. The new architecture proposed in this work adopts a distributed EDFA in the hybrid TDM/DWDM architecture, making full use of the well-developed DWDM and amplification technologies. This architecture uses

distributed amplifications among the wavelength multiplexed TDM sub-arrays, to compensate for the optical loss from WDM components, lowers the input optical signal power in the buses, and avoids nonlinear effects on the system phase noise.

To conclude, our recommended distributed amplified architecture to interrogate hundreds of hybrid multiplexed sensors from only one pair of fibres will be great potential commercial value to the fibre seismic sensing and PRM industry.

Chapter 3

Erbium doped fibre amplification and modeling

Overview: The performance of new proposed amplified network is largely governed by the amplification behaviour of the doped fibre and qualifying the key properties that define it sufficiently allow reliable numerical performance prediction of the amplifier network. This chapter addresses issues affecting the simulation performance of EDFAs and the principal factors that affect the overall behaviour of EDFAs, and will allow us to predict the performance of the new proposed architecture. Comparison between theory and experimental measurements on the properties of a single stage EDFA is presented, with good agreement achieved thereby validating our numerical modeling approach.

3.1 Light amplification in EDFA

EDFAs are optical amplifiers that use a doped optical fibre as a gain medium to amplify an optical signal. The signal to be amplified and a pump laser are multiplexed into the doped fibre, and the signal is amplified through interaction with the doping ions. EDFA, as shown in Figure 3.1, where the core of a silica fibre is doped with trivalent erbium ions and can be efficiently pumped with a laser at a wavelength of 980 nm or 1480 nm, and exhibits gain in the 1550 nm region. Segments of erbium doped fibres (EDFs) are distributed along the sensor array in the new proposed hybrid TDM/WDM sensor array. The amplification properties dominate the sensor array performance; therefore, it is necessary to investigate the EDFA behaviour, which will allow us to predict the sensor array performance.

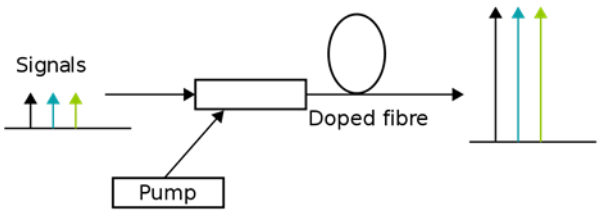

Figure 3.1: Schematic diagram of a single EDFA.

3.1.1 Atomic rate equations and propagation equations

We start the EDFA modeling by considering the amplification spectrum in an erbium-doped fibre. Erbium is a rare-earth metal with particularly useful energy dynamics for making telecom wavelength optical sources. Erbium ions, Er^{3+}, have a series of excited states which mean that it can absorb at one wavelength and emit at another. The absorption and emission spectrum of the Er^{3+} ion, as shown in Figure 3.2 (a), are signatures of the energy states of its 4f inner electrons [71-75]. Erbium is modelled as a three-level system; with a signal band from about 1520 to 1570 nm. Er^{3+} ions can be pumped at several wavelengths including 510, 532, 665, 810, 980, and 1480 nm, though pumping at 980 nm and 1 480 nm is favoured as it avoids excited state absorption (ESA) of the pump energy, where the Er^{3+} ions may be further excited by additional pump power absorption, as shown in Figure 3.2 (b) [76]. ESA briefly prevents these ions from providing useful gain and so is detrimental to efficient output.

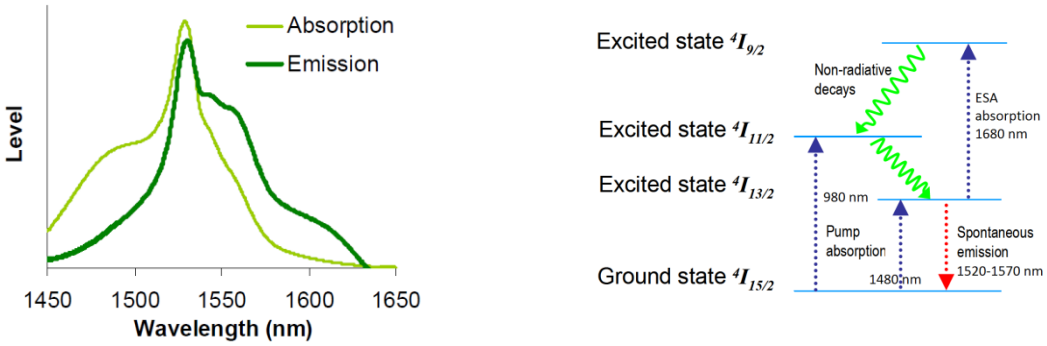

(a) (b)

Figure 3.2: (a) Absorption and emission spectra of an erbium doped fibre (b) Energy transition diagram of an erbium doped fibre.

At 1480 nm, pumping directly excites the upper sublevels of the $^4I_{13/2}$ metastable manifold (the excited state is broadened into closely spaced sublevels due to Stark splitting), with ground to excited state transition $^4I_{15/2} \rightarrow {}^4I_{13/2}$, corresponding to both a 1520 to1570 nm signal band and 1460 to1500 nm pump band [75]. When pumped in the 980 nm absorption band, Er^{3+} ions are moved from the ground state to the $^4I_{11/2}$ excited state. In silica, this state has a short lifetime (~5 to 10 μs) and the ions undergo non-radiative decay to the metastable level. The population density N_3 of the $^4I_{11/2}$ level is negligible with regard to its effect on average gain [77]. Therefore, the energy transition can be simplified to a two-level system.

For a simplified two-level system with k optical beams, the rate equations describing the effects of absorption, stimulated emission, and spontaneous emission on the populations of the ground (N_1) and the metastable (N_2) state, are given by

$$\begin{aligned} -\frac{dN_1}{dt} &= \frac{dN_2}{dt} \\ &= \sum_k \frac{\sigma_a(\upsilon_k)}{h\upsilon_k} \cdot i_k(r,\phi) \cdot P_k(z) \cdot N_1(r,\phi,z) \\ &\quad -\sum_k \frac{\sigma_e(\upsilon_k)}{h\upsilon_k} \cdot i_k(r,\phi) \cdot P_k(z) \cdot N_2(r,\phi,z) - \frac{1}{\tau} \cdot N_2(r,\phi,z) \end{aligned} \tag{3.1}$$

$$N_1(r,\phi,z) + N_2(r,\phi,z) = N_t(r,\phi,z) \tag{3.2}$$

where h is the Planck constant, τ is the metastable lifetime parameter, which indicates the decay from the metastable state to ground state and has a life time of around 10 ms. υ_k is the frequency, and P_k is the power of the kth beam. The absorption and emission cross-section of the kth beam are $\sigma_a(\upsilon_k)$ and $\sigma_e(\upsilon_k)$ respectively, and N_t is the local erbium ion density. The normalized optical intensity $i_k(r,\phi)$ is defined as $i_k(r,\phi) = I_k(r,\phi,z)/P_k(z)$, where $I_k(r,\phi,z)$ is the light intensity distribution of the kth beam.

The propagation equations that describe the propagation of the beam through the doped fibre are given by:

$$\begin{aligned} \frac{dP_k}{dt} &= \underbrace{u_k \cdot \sigma_e(\upsilon_k) \cdot (P_k(z) + P_{0k}) \cdot \int_0^{2\pi}\int_0^{\infty} N_2(r,\phi,z)\, i_k(r,\phi) \cdot r \cdot dr \cdot d\phi}_{\text{Amplification of the signal and spontaneous noise from the upper level}} \\ &\quad \underbrace{-u_k \cdot \sigma_a(\upsilon_k) \cdot P_k(z) \cdot \int_0^{2\pi}\int_0^{\infty} N_1(r,\phi,z)\, i_k(r,\phi) \cdot r \cdot dr \cdot d\phi}_{\text{Absorption from the lower level}} \end{aligned} \tag{3.3}$$

where each beam propagates in the forward ($u_k = 1$) or backward direction ($u_k = -1$), and $P_{0k} = mh\upsilon_k\Delta\upsilon_k$ is the spontaneous emission contribution from the local metastable population N_2, where the normalized number of modes (m) is normally 2, and $\Delta\upsilon_k$ is the noise bandwidth. Once the boundary conditions are specified at $z = 0$ and L, equation (3.1), (3.2) and (3.3) are integrated over space z, optical frequency f and time t. By setting the time derivative in equation (3.1) equal to zero, the problem is reduced to the steady-state case.

3.1.2 Giles parameters

Giles and Desurvire in [75] rewrote the propagation equation and the steady-state solution of the rate equation in terms of Giles parameters. The Giles parameters given after C.R. Giles are $\alpha(\lambda)$ the absorption spectrum per unit length, and $g^*(\lambda)$ the emission spectrum per unit length. The Giles parameters allow full characterization of the EDFA, and can be obtained by conventional fibre measurement techniques [75]. The Giles parameters are expressed in terms of erbium ion concentration n_t, overlap integral function $\Gamma(\lambda)$, and the absorption and emission cross sections $\sigma_a(\lambda)$ and $\sigma_e(\lambda)$:

$$\alpha(\lambda)=\Gamma(\lambda)\cdot\overline{N_t}\cdot\sigma_a(\lambda) \tag{3.4}$$

$$g^*(\lambda)=\Gamma(\lambda)\cdot\overline{N_t}\cdot\sigma_e(\lambda) \tag{3.5}$$

The overlap integral function Γ_k denotes the overlap of the optical mode and the erbium ion distribution. Only the portion of the optical mode which overlaps with the erbium ion distribution will stimulate absorption or emission from the Er^{3+} transitions. For a step-index fibre the lowest order mode can be approximated by a Gaussian curve [78], and the transverse overlap of the mode and ion distribution becomes:

$$\Gamma=1-e^{-\frac{2b^2}{\omega_0^2}} \tag{3.6}$$

where b is the erbium ion dopant radius, and ω_0 is the mode field radius. Also needed for the modelling is the saturation parameter,

$$\zeta=\pi b^2\cdot\overline{N_t}/\tau \tag{3.7}$$

The saturation parameter can be obtained from a measurement of the fibre saturation power as $\zeta=P_k^{sat}(\alpha_k+g_k^*)/h\nu_k$, which is measured by reducing the pump power to the value where the fluorescence from a short fibre sample is half its maximum value (value at saturation) [79]. This power is the saturation power. The saturation power determines the amount of input power of an amplifier required for achieving most of the possible output power.

The equations of the spatially integrated model become

$$\frac{\overline{N_2}}{\overline{N_t}}(z)=\frac{\sum_k\frac{P_k(z)\alpha_k}{h\upsilon_k\zeta}}{1+\sum_k\frac{P_k(z)(\alpha_k+g_k)}{h\upsilon_k\zeta}} \tag{3.8}$$

$$\frac{dP_k(z)}{dt} = u_k \cdot (\alpha_k(\upsilon_k) + \underbrace{g_k(\upsilon_k)) \cdot \frac{\overline{N_2}}{\overline{N_t}} P_k(z)}_{\text{Amplification of the signal}} + \underbrace{u_k g_k(\upsilon_k) \cdot \frac{\overline{N_2}}{\overline{N_t}} P_{0k}}_{\text{Amplification of the spontaneous noise}} - u_k(\alpha_k(\upsilon_k) + \underbrace{l_k}_{\text{Background loss}})P_k(z) \quad (3.9)$$

where l_k is the background loss.

3.1.3 Rayleigh scattering

In EDFAs, the *quantum conversion efficiency*, defined as the number of photons output at the signal wavelength divided by the number of input pump photons, may be reduced by many physical effects, which need to be considered when we model the pump dissipation and investigate the pump requirement for the distributed EDFA in our new architecture.

The internal Rayleigh back scattering is one of the major effects. Rayleigh scattering is the scattering of light on the local density fluctuations in the fibre. A small part of light is always back scattered due to this effect. The Rayleigh back scattering will not only produce excess background loss to the signal, but also has an additional impact on the performance of the EDFA [80, 81]. Part of the scattered light is recaptured by the fibre and propagates in the opposite direction to the incident wave (internal Rayleigh back scattering), as well as, in the same direction. The back scattered light can be amplified during the propagation in the fibre and can lead to the degradation of system performance. Double Rayleigh scattering occurs when a portion of the back scattered signal is reflected again and is re-coupled to the forward direction. The power of the back-scattered and forward-scattered light $dP_{RS}(z)$ caused by continuous incident power at a point z, is given by [81]

$$\frac{dP_{RS}(z)}{dz} = \alpha_{RS}(\upsilon_k) C P_k(z) \quad (3.10)$$

where $\alpha_{RS}(\upsilon_k)$ is the background loss caused by Rayleigh scattering, which is the main intrinsic loss mechanism outside absorption, and C is the back-scattering capture fraction increased with $(NA)^2$, which is given by $C = (NA/n_{eff})^2/m_n$ [82]. Here m_n is 4.55 for a single mode fibre, and NA is the numerical aperture. The Rayleigh back-scattering loss α_{RS} varies as λ^{-4} and is dominant at short wavelengths. This intrinsic loss level (in dB/km) [83] is estimated to be

$$\alpha_{RS} = C_R / \lambda^4 \quad (3.11)$$

where the constant C_R is in the range from 0.7 to 0.9 dB $\text{km}^{-1}\mu\text{m}^4$ depending on the constituents of the fire core. However, in Erbium doped fibres, we usually define a Rayleigh

constant parameter of K_R, which varies with the dopants, and the Rayleigh back-scattering loss α_{RS} in a doped fibre is given by [80]

$$\alpha_{RS} = (0.63 + K_R \Delta n) / (\lambda / \mu m)^4 \tag{3.12}$$

The first term 0.63 dB/km is the intrinsic scattering loss for pure silica at 1 μm, and the second term accounts for the material and geometrical dependence. Δn is the refractive index difference. The Rayleigh constant parameter K_R is generally equal to approximately 70 dB/km for a Gernanium co-doped fibre, and approximately 150 dB/km for an Aluminum co-doped fibre[80].

3.1.4 Up-conversion process

Other various physical effects may lead to reduced quantum conversion efficiency in EDFAs. At large erbium concentrations, additional pump power loss can occur by energy transfer between two excited erbium ions, resulting in a homogeneous upconversion (HUC) process [84, 85], which will add a term $-C_{up}(N_2)^2$ to the right side of equation (3.1) with C_{up} the up-conversion efficient. Moreover, Er^{3+} ions can form pairs and larger clusters, in which a rapid energy transfer will lead to fast decay and inhomogeneous upconversion. For pair clusters, this effect is often called pair-induced quenching (PIQ). Depending on the details of the fabrication process, clusters may be present even at low concentrations of erbium, when homogeneous upconversion is negligible. Another upconversion mechanism, the excited-state absorption (ESA) from the metastable level, will also affect the amplifier performance. By comparing measured and calculated characteristics for a series of suitably designed steady state and dynamic experiments, researchers discovered that PIQ and HUC are the dominant mechanisms, while ESA is negligible when pumped at 1480 nm [84].

3.2 Numerical modelling of EDFA in VPIphotonics

Accurate prediction and design of the new array strongly depends upon knowledge of behaviour of the distributed EDFA. The overall behaviour of an EDFA is determined by three sets of physical properties [86], including:

1) The physical properties of the erbium ions, such as Giles parameters, excited state lifetimes and the gain and absorption cross sections. These properties, along with many of the fundamental physical processes, governing the gain behaviour of the amplifier, are generally dependent upon the composition of the host material.

2) The geometry of the fibre waveguide, in particular the overlap of the propagating optical fields (pump and signals) with the active ions within the core or cladding glass. The transverse field profile is itself determined by the refractive index profile of the fibre, which may be similar or different in form to the distribution of the dopant ions.
3) The ambient conditions, such as the temperature at which the amplifier is operated, which will be lower in the sea environment.

In most general case, the complexity of the pump, signal and ASE rate and propagation equations derived in the previous section obviously requires numerical solving. Only in some particular cases (unsaturated gain and low gain regime) these equations can be solved exactly, with analytical expression for the signal and pump. Numerical solution of equation (3.8) and (3.9) involves three basic degree of difficulty: evaluation of boundary conditions; interrogation in the transverse plane to obtain the absorption and gain coefficients for pump and signal; interrogation over the fibre length. Essentially there are numerical approaches (shooting method, the relaxation method etc.) to solve such problems with computer programs. All theoretical models are based on several assumptions, and owning to its complicated configurations in our applications, the home made computer programs are not recommended.

There are several commercially photonic/optical communication design and simulation software, such as VPIphotonics, Optisystem etc., which includes modules for numerical modelling of EDFA. The simulation performance of EDFA from VPIphotonics was compared with that from Optisystem, and they provided us with similar performance predictions. Therefore, I only take VPIphotonics as an example, and use it for our later array performance prediction.

In VPIphotonics, there are three options of energy system to simulate the EDFA performance: the two-level, three-level and the Er/Yb co-doped laser system. The choice between them depends on the dopant ions, the type of glass used to make the fibre to host the dopant ions and the pumping scheme. As previously shown in Section 3.1.1, the two-level system with the states $^4I_{15/2}$ and $^4I_{13/2}$ is the best choice for silica glass hosts with erbium doping, in which the $^4I_{11/2}$ erbium energy level is comparatively short-lived and can be neglected compared to the decay time from the metastable level.

In VPIphotonics, the gain and absorption characteristics of the doped fibre can be specified using cross-sections or Giles parameters. Emission and absorption cross-sections are the more fundamental representation of the properties of the doped fibre; however the Giles parameters, which represent the gain and absorption of the fibre per unit length, are generally easier to obtain experimentally and are often provided by manufacturers. Once the gain and absorption

properties are described using Giles parameters, very few additional parameters are required. This is because the measured gain and absorption per unit length in an actual fibre already includes the effect of parameters such as the excited state lifetimes, and the details of how the optical field overlaps and interacts with the dopant ions. In addition to the Giles parameters themselves, the only additional parameter required to complete the description of the gain and absorption characteristics of the doped fibre is the saturation factor ζ, specified in equation (3.7). Therefore, a description of the amplifier properties using Giles parameters is quite simple.

The disadvantage of using the Giles parameters is that they are unable to account for many physical processes that may occur within the doped fibre. In particular, the effect of position- and power-dependent variations in the overlap between the optical field and the excited ions cannot be determined based on measurements of the unsaturated net gain and absorption per unit length. Only by using the cross-sections description along with other known properties of the fibre can such effects be fully described. When cross-sections parameters are used, a number of additional parameters are required to specify further properties of the dopant ions. These properties are: the lifetimes of the relevant excited states, the concentration of ions and the Overlap Factor. In order to take into account the effect of Concentration Quenching characteristics (such as Er Upconversion and Er Pair induced Quenching) or of position- and power-dependent variations of the overlap between the optical field and the excited ions while using the Giles parameters, an automatic conversion of the Giles parameters to cross-sections can be performed. In this case, the specified Giles parameters are used by the doped fibre module to calculate the corresponding cross-sections, which are then used for simulation. In order to convert the Giles parameters to cross-sections, the following additional parameters are required and must be specified: Overlap Factor, and Concentration Profile (or Erbium concentration).

The underlying fibre properties of background loss and fibre end losses, Rayleigh backscattering and fibre end reflection also need to be specified when applying the Doped Fibre module in VPIphotonics. Furthermore, Excited State Absorption (ESA), Self-Phase Modulation via the Kerr nonlinearity, Spectral Hole Burning (SHB), can also be accounted for in the simulation. These effects lead to an increase in pump power dissipation in the EDF, which is essential for our application and will be discussed in the following section.

3.3 Experimental verification of EDFA modelling

Accurate prediction of experimental data strongly depends upon knowledge of experimental parameters, such as mode envelopes, cross sections, doping concentrations. The basic physical parameters of the two doped fibres (I4 and Er1550C) prepared for our applications are illustrated in Table 3-1, and comparisons between accurate theoretical modelling and experiment data are discussed in this section.

Table 3-1: Basic physical parameters used in the EDFA modelling.

Parameters		I4 (Fibercore)	Er1550C (Corning)	Data source
EDF length (m)		12.3	11.95	Measured
Pump wavelength (nm)		1466	1466	Measured
Absorption and gain coefficients				Manufacturer
Erbium Lifetime (ms)		10	10	[75]
Overlap Factor	980 nm	0.64	0.64	[86]
	1480 nm	0.43	0.43	
	C and L band	0.4	0.4	
Erbium concentration ($ions/m^3$)		5.35×10^{24}	4.72×10^{24}	Manufacturer
Erbium core radius (μm)		1.6	1.6	Manufacturer
Background loss (dB/km)@1200 nm		5	5	Manufacturer
Fibre end loss per splice (dB)		0.16	0.16	Measured
Fibre end Reflectance Parameter (dB)		−60	−60	[86]
Temperature (K)		296	296	

3.3.1 Experimental setup for simulation verification

An experimental setup for a single stage EDFA was built to allow for a full verification of the performance of the EDFA simulation using VPIphotonics, as illustrated in Figure 3.3. A tunable laser source ranges from 1520 nm to 1580 nm and a 1466 nm pump laser source (1480 nm pump power sources are required but the supplier provided us with pumps of such wavelengths instead, and they are fine enough for our application) coupled by a 1480/1550 nm Wavelength-Division Multiplexer (WDM) co-propagate through a low doped erbium-doped fibre (EDF). The input and output optical spectra are recorded by an Optical-Spectrum Analyzer (OSA) to calculate the gain in the EDFA. The residual pump power is routed out through an additional 1480/1550 nm WDM located at the remaining end of the EDF and monitored by an optical power meter to calculate the absorbed pump power in the EDF.

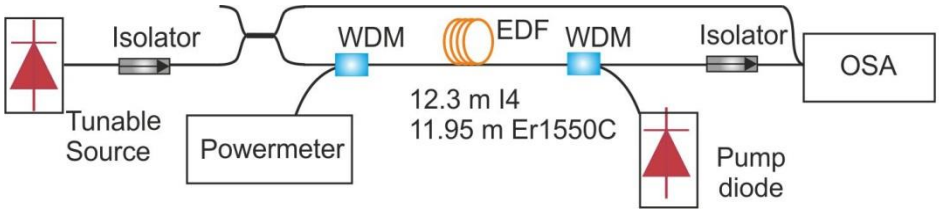

Figure 3.3: Experiment setup of the single stage EDFA, OSA: Optical spectrum analyzer, EDF: erbium-doped fibre, WDM: 1480/1550 nm wavelength division multiplexer.

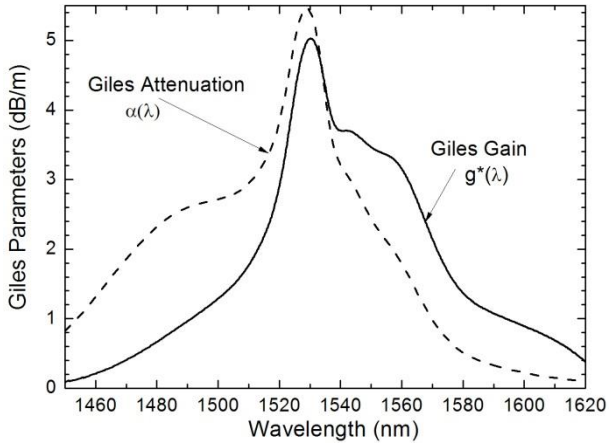

Figure 3.4: Giles parameters (from the supplier) of the Er-doped fibre I4 used in the experimental setup.

Both the gain and absorbed pump power are calibrated as a function of the signal wavelength for different pump powers of 250 mW, 100 mW, 32 mW, 20 mW and 10 mW separately, for simulation verification. Two types of low doped EDF are characterized for the EDFA: a) A 12.3 m of fibre I4 from Fibrecore Ltd and b): An 11.95 m of Er1550C from Corning Inc., both have a nominal absorption peak of 5.6 dB/m at 1530 nm. Figure 3.4 illustrates the Giles parameters of the I4 EDF from Fibercore Ltd.

3.3.2 Comparison with simulation results using given parameters

We first simulate the gain and absorbed pump power in both of the EDFAs with respect to the operation wavelength using the Giles parameters provided by the manufacturer and other basic physical parameters, as illustrated in Table 3-1. Figure 3.5 displays the comparisons of the gain in (a) and the absorbed pump power in (b) between the experimental results and simulations for the I4 fibre, with an input signal power of –20 dBm, for different pump powers at 100 mW, 32 mW and 10 mW. Coloured points in both figures illustrate the measured value and coloured curves denote the simulations.

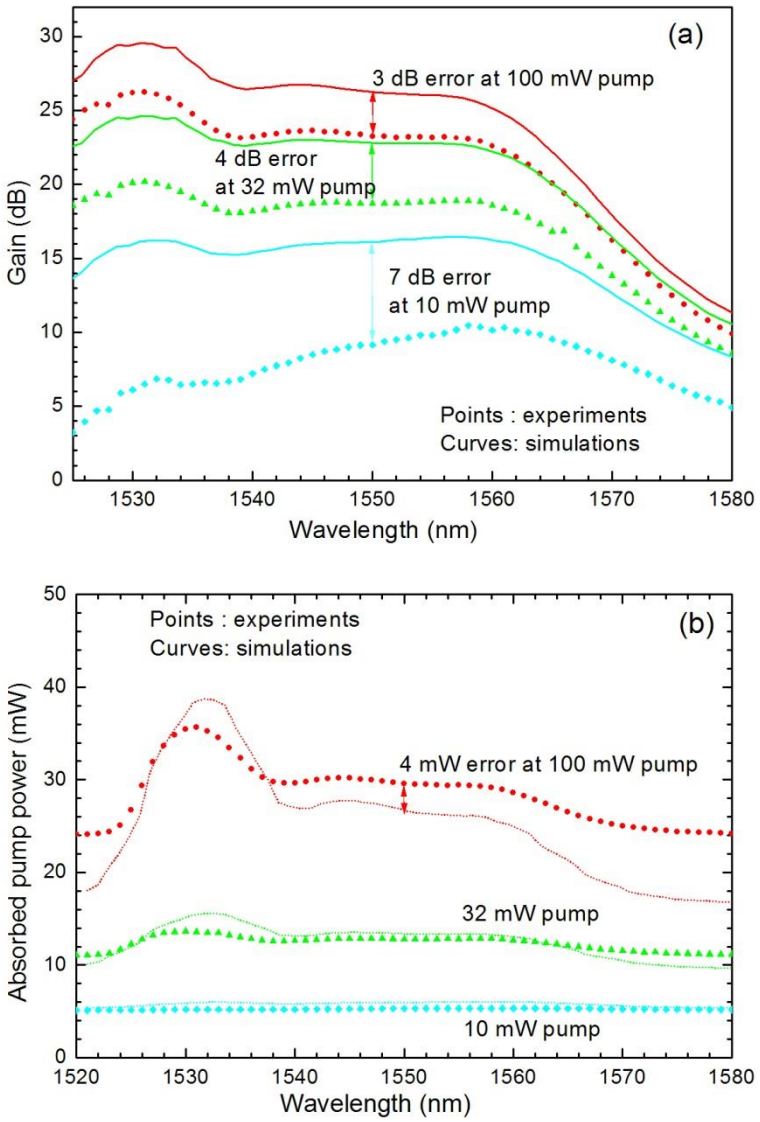

Figure 3.5: (a) Gain spectrum and (b) absorbed pump power as a function of wavelength in the EDFA setup with fibre I4 for different counter pump powers. Coloured points are experimental results. Coloured lines are simulations with given parameters.

In Figure 3.5 (a), the simulation error in gain at 1550 nm is as large as 7 dB. The tests show a lower gain, especially with lower pump powers, which indicates an overestimated-gain emission or underestimated-pump-power consumption in the simulations. In Figure 3.5 (b), the pump power absorption in the EDF is in agreement with the experiments and simulations for a pump powers of below 100 mW, while for the pump power at 100 mW, the predicted absorbed pump power at 1550 nm is 4 mW lower than the tests, which shows a lower pump absorption in the simulation.

The most essential thing for our application of the co-pumped cascaded EDF chain in the new array architecture is to ensure enough pump power for the last EDF segment. The

underestimated-pump absorption is unacceptable because it will predict pump power requirement in an amplifier network lower than needed in realities. The gain flatness in the spectrum is another essential performance. The effects of gain flatness on output flatness will be discussed in Section 4.5, which determine the EDF length arrangement.

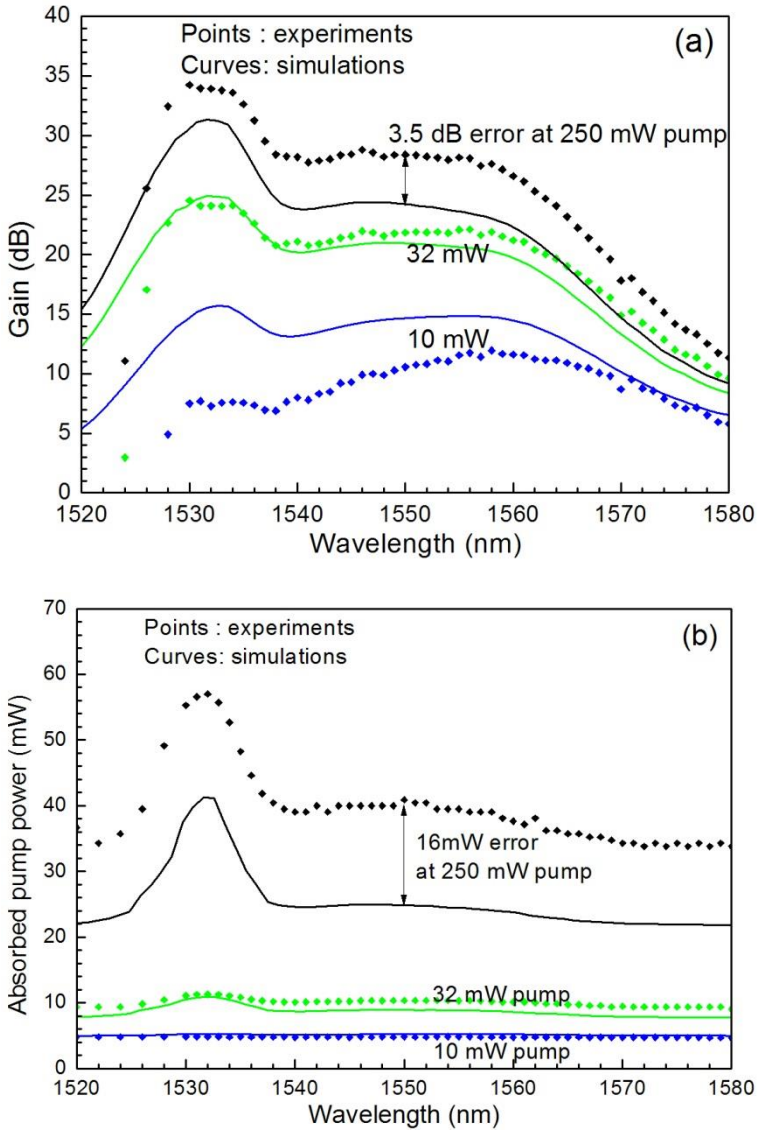

Figure 3.6: (a) Gain spectrum and (b) absorbed pump power as a function of wavelength in the EDFA setup with fibre Er1550C for different counter pump powers. Coloured points are experimental results. Coloured lines are simulations with parameters given by manufacturer.

There are also disagreements in the comparison of gain and absorbed pump power for the fibre Er1550C. Figure 3.6 shows the comparison between the experimental results and simulations for the fibre Er1550C with an input signal power of –20 dBm and different pump powers at

250 mW, 32 mW and 10 mW, respectively. Coloured points in both figures illustrate the measured value and curves denote the simulations. Unlike the comparison for fibre I4, the simulation predicts a higher gain spectrum for a pump power at 10 mW, while a lower gain spectra for pump powers larger than 32 mW in Figure 3.6 (a). The simulation error in gain also varies between different pump powers. For the pump power absorption spectra in Figure 3.6 (b), similar to the I4 fibre, the simulations predicted less pump power absorption in the EDF, especially with higher pump powers.

3.3.3 Parameter tuning for EDFA modeling

The disagreement between the experimental results and simulations, existing in the gain and pump power absorption, cannot be ignored, and reveals the requirement for fibre parameter verification to obtain effective performance predictions for the new distributed amplified network. The verification of EDF properties including Giles parameters and other extended parameters was carried by cross referencing from various sources and comparison with experimental results. Let's take the Er1550C fibre as an example.

In VPIphotonics, the two-level Er system model is the best choice for the 1466 nm pumped erbium-doped fibre, as discussed in the previous section. Both simulation modes 'Giles parameters' and 'Giles parameters to cross-sections' have been used and compared for the Gain and pump absorption characterization of the EDFA. Simulations show that they predict similar performances with parameters from Table 3.1, in the absence of considering the effect of Concentration Quenching characteristics (such as Er Upconversion and Er Pair induced quenching), ESA and Spectrum Hole Burnings (SHB). The gain and absorption characteristic shape depends on the host glass composition including: alumina Al_2O_3, Germania GeO_2 and phosphorous oxide P_2O_5 [51], which is provided by the manufacturer, but their peak values vary within 10% to 30% depending on the measurement methods [51]. So we tune the simulation by sweeping both emission and absorption parameters with a multiplication factor from 0.8 to 1.5, and discover the best adjusted parameters ($1.25g_k^*$, $0.9\alpha_k$ for Er1550C), based on the comparison between the measured and simulated gain spectra, with the pump powers of 250 mW and 100 mW, as shown in Figure 3.7. Different colors indicate different pump power levels. Coloured points illustrate the measured values and Coloured curves denote the simulations.

As can been seen from Figure 3.7, the error in the top curve of the gain spectrum with 250 mW of pump power is minimized, but big differences still exist in the gain spectra with lower pump power of 32 mW and 10 mW. Besides this, a gain reduction around 1531 nm (the peak-pump-

absorption area) was observed in the measured gain spectra, especially with lower pump powers, which indicates that there exists additional pump power dissipation when the pump is not over saturated. Upconversion including HUC and PIQ, ESA, Rayleigh scatterings and Spectral Hole Burnings may all lead to this reduced pump efficiency. In order to take into account these effects, we choose the mode 'Giles parameters to cross-sections' for the Gain and absorption characteristics of the fibre in the following simulations.

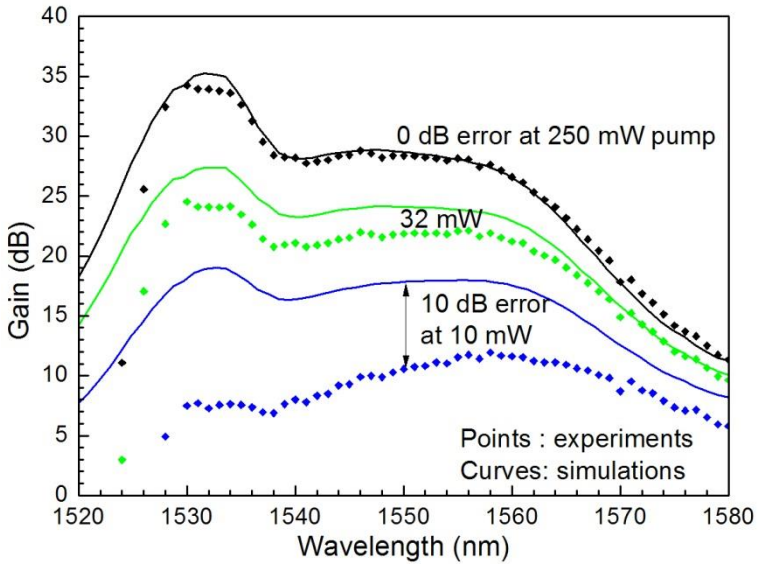

Figure 3.7: Gain spectrum as a function of wavelength in the EDFA setup with fibre Er1550C for different counter pump powers. Coloured points are experimental results; coloured solid lines are simulations with adjusted Giles emission and absorption parameters.

In the 'Giles parameters to cross-sections' mode, effects from HUC, Rayleigh effects, and PIQ can be added to the simulation. Simulations were first carried out with combinations of different UPC and PIQ coefficients. They show similar gain degradation at lower pump powers, therefore I only take the UPC parameter to represent the overall up conversion effect for reasons of simplicity. From the manufacturer, the EDF has a Rayleigh constant of 150 dB/km for the Aluminum co-doped fibre, which is equivalent to a Rayleigh back-scattering loss of 0.000125/m from equation(3.12). Simulations show that it leads to gain reductions, especially around 1530 nm in the gain spectrum. References [84] have concluded that the ESA is negligible compared to HUC and PIQ when pumped at 1480 nm, and our simulations with different ESA parameters show that they reduce the gain by 2 to 3 dB only at wavelengths longer than 1570 nm. Spectral Hole Burning [87] happens only when there is a saturated signal co-propagating in the fibre, and it leads to a reduction of gain around 1530 nm. Therefore these two effects are ignored in our upgraded simulations.

Table 3.2 summarized the optimized results of parameters for both the fibre I4 and Er1550C from the parameter tuning process. Both emission and absorption coefficients are adjusted according to the measured gain and pump absorption spectra. The upconversion effects are introduced to represent the gain degradation at low pump powers. This effect is more notable for the fibre Er1550C. Both of the fibres are Aluminum co-doped with the same Rayleigh backscattering coefficient of 0.000125/m.

Table 3-2: Adjusted fibre parameters for the fibre I4 and Er1550C.

Parameters	Effects	I4	Er1550C
Emission coefficient	Gain	$0.88 \times g_k^*$	$1.25 \times g_k^*$
Absorption coefficient	Pump absorption	$0.9 \times \alpha_k$	$0.9 \times \alpha_k$
UPC parameters [84, 85] (m^3/s)	Gain degradation at low pump	1.5×10^{-23}	2.5×10^{-23}
Rayleigh backscattering coefficient (/m)	Maximum gain at peak pump absorption	0.000125	0.000125
PIQ [88]	Gain degradation	off	off
ESA	Gain degradation in longer wavelength	off	off
Spectrum Hole Burning[87]	Spectrum around 1530 nm	off	off
Kerr Nonlinearity		off	off

3.3.4 Accurate modelling with optimized parameters

Using these adjusted and extended parameters from Table 3.2 for EDFA simulations in VPIphotonics, we achieve better agreement with experimental results for both fibres. Figure 3.8 demonstrates the simulated gain spectrum and absorbed pump power with optimized parameters for the Er1550C fibre, together with the measured values in coloured points. Curves in these figures denote upgraded simulations with adjusted Giles parameters and extended parameters including Up-conversion and Rayleigh backscattering as illustrated in Table 3.2. They exhibit better agreement with the experimental results (coloured points) in both gain and pump absorption spectra.

Figure 3.9 demonstrates the simulated gain spectra and absorbed pump power with optimized parameters for the I4 fibre. Curves denote improved simulations with adjusted Giles parameters and extended parameters including Up-conversion and Rayleigh backscattering as illustrated in

Table 3.2 for the parameter tuning process. They also exhibit better agreement with experimental results (coloured points) in both gain and pump absorption spectra.

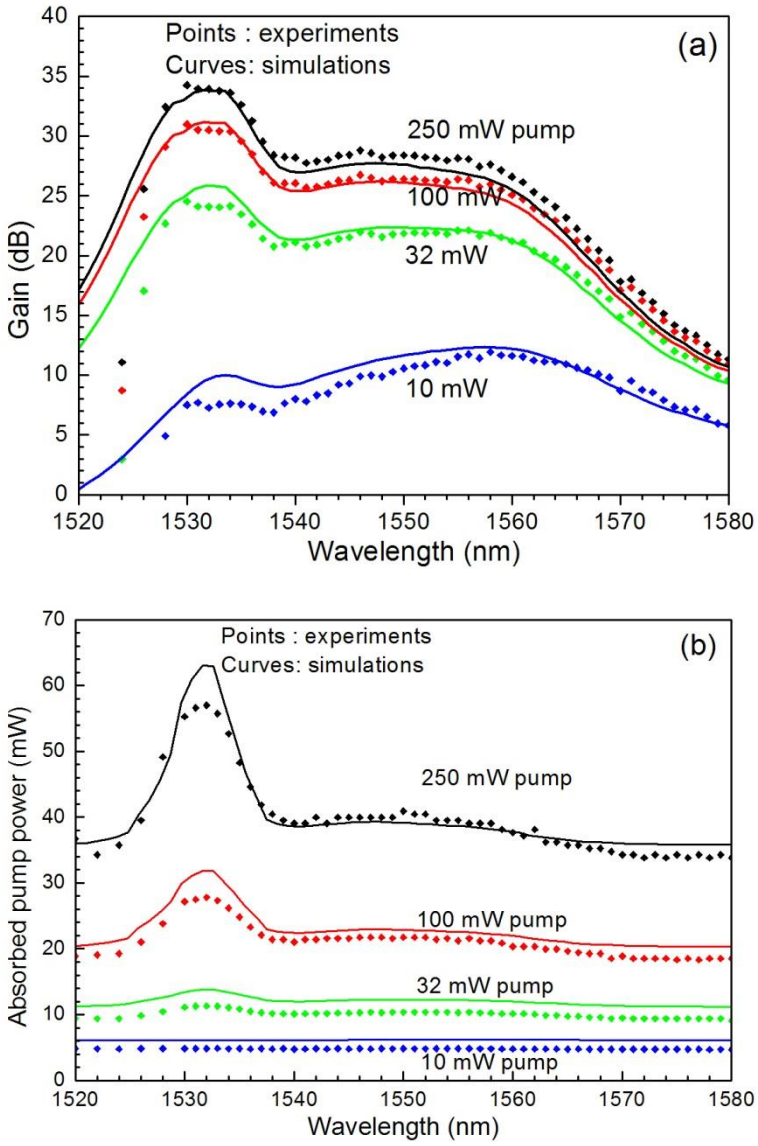

Figure 3.8: (a) Gain spectrum and (b) absorbed pump power as a function of wavelength in the EDFA setup with fibre Er1550C for different counter pump powers. Coloured points are experimental results; coloured lines are simulations with verified coefficients.

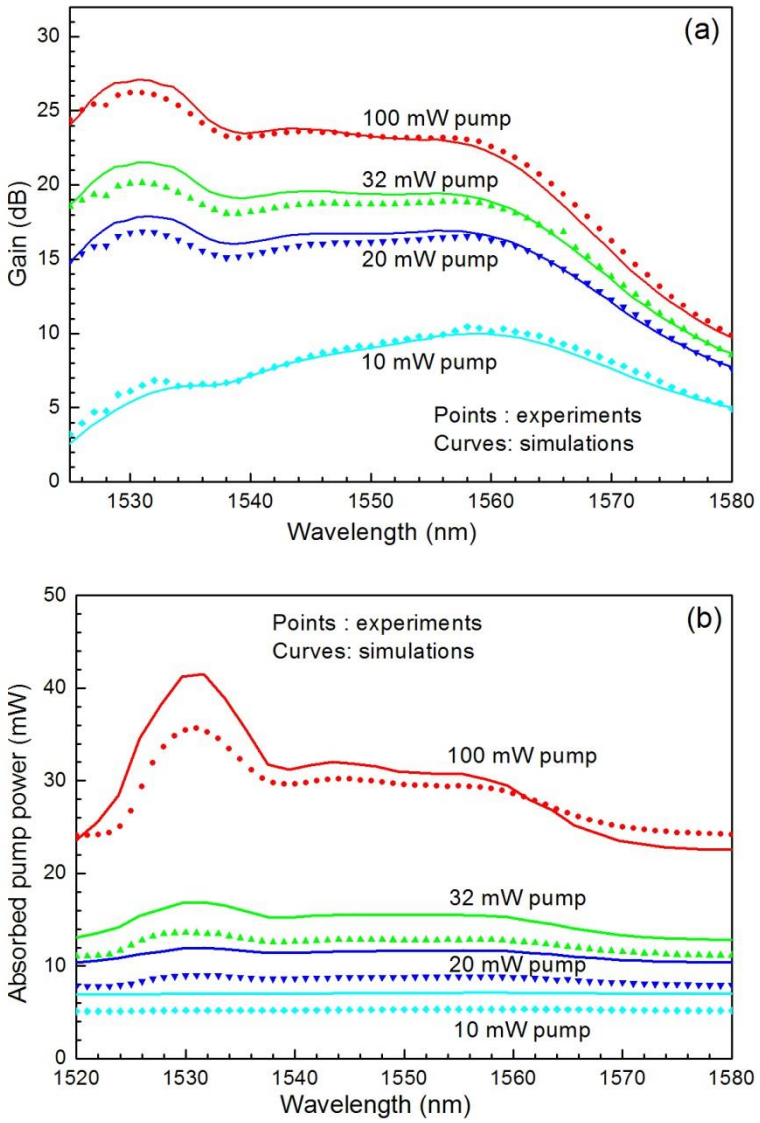

Figure 3.9: (a) Gain spectrum and (b) absorbed pump power as a function of wavelength in the EDFA setup with fibre I4 for different counter pump powers. Coloured points are experimental results; coloured lines are simulations with verified parameters.

The simulations with adjusted fibre properties are in good agreement with experimental results, in terms of EDFA gain spectrum and absorbed pump power spectrum with different pump powers ranges from 10 mW to 100 mW, for both the fibre Er1550C and I4. For the Er1550C fibre, the differences in gain spectra are less than 2 dB. There is also a good agreement in the absorbed pump power spectra except for wavelengths around 1530 nm, which is out of the wavelength range of interest for our sensor application. For the I4 fibre, the differences in gain spectrum are less than 1 dB. The difference in the absorbed pump power spectra is less than 1 dB when the pump power is larger than 20 mW, and it increases to 2 dB when pumped at 10 mW, but the absolute difference is still less than 2 mW.

The simulation with adjusted parameters shows significant improvements. Both with a –20 dBm input signal at 1550 nm and the pump power at 100 mW, for the I4 fibre, the adjusted simulations decrease the difference in the absorbed pump power from 4 mW to 1 mW, and remove the absorption peak back to 1531 nm from 1532 nm, it also reduces the gain error from 3 dB to 0 dB for the signal; while for the Er1550C fibre, the adjusted simulation minimizes the error in pump absorption from 7 mW to 1 mW, and the gain difference from 3 dB to 0 dB.

Accurate prediction of experimental data and array performance strongly depends upon knowledge of experimental parameters. In the experimental procedure to determine the EDF basic parameters by the suppliers, the fibre length is usually very short, e.g., L < 2 m. The measurement accuracy depends on the filtering of the signal cladding modes [51]; also the environmental temperature is an issue to affect the measurement results. The disagreements in the comparisons between the theoretical modeling (using given parameters) and experiment data show the necessity to tune the EDF parameters. Therefore, we have adjusted the EDF basic parameters and have achieved accurate prediction of experimental data. This will ensure the architecture design (where EDF segments are distributed along the new array) and performance prediction in the follow Chapter 4.

3.4 Conclusions

We make use of short lengths of EDF segment to compensate for the splitting losses in an array. Each EDFA segment is required to provide an exact amount of gain, the amplification behaviour of the EDFA and the reliable numerical performance prediction of the distributed EDFA are of significant importance. The overall behaviour of an EDFA is determined by sets of physical properties. The numerical simulation of EDFAs has been carried out using VPIphotonics, based on the solutions of the rate and propagation equations. Significant disagreements existed between simulations using manufacturer parameters and the tests, therefore, we adjusted the Giles parameters provided by the manufacturer, and extended the fibre parameters to fit the experimental results in EDFAs, using two types of low doped fibres. The adjusted simulation reduces the gain errors at 1550 nm from 3 dB to 0 dB with 100 mW pump power, as well as absorbed pump power error from 7 mW to 1 mW. Results show that correct values of EDF basic parameters are key properties for accurate prediction of experimental data. The following chapter will carry on the architecture design and performance predication based on these adjusted EDF parameters.

Chapter 4
Architecture design and performance

Overview: This chapter addresses design rules for basic parts of the previously recommended interferometric sensor system which affect the overall performance, including the architecture design, the laser source, the optical power handling capacity, the pump power dissipation and the length of the EDF segments, based on the validated EDF parameters from Chapter 3. Then, the array performances are demonstrated, including the output power flatness between sensors, the transient response and the OSNR. The sensitivity of simulation results to EDF parameters is also investigated. Finally, this chapter compares the NF with previous reported architectures, and estimates the maximum number of sensors that can be supported.

4.1 Distributed amplified TDM/DWDM array

The system performance of a sensor array is governed by the architecture design. Chapter 1 have briefly introduced a new array architecture using a distributed EDFA among wavelength multiplexers in hybrid TDM/DWDM arrays. The new design utilizes the benefits of EDFA technology to compensate for the splitting/recombination loss of the array and to increase the total number of sensors per fibre pair. The performance of an EDFA was experimentally investigated and accurately modelled in Chapter 3. Therefore, the details of the distributed amplified architecture design will be discussed in this chapter, and the results from the recommended architecture will be presented.

4.1.1 Array configuration

The recommended architecture is demonstrated in Figure 4.1. The array is composed of two fibre buses, the distribution bus (top) and the return bus (bottom). The optical pulses from the transmitter are coupled into the distribution bus. At the first optical drop multiplexer (ODM), the signal at wavelength $\lambda 1$ is coupled into the first TDM group, where all sensors are multiplexed in the time domain and driven by one wavelength (its design will be discussed later), passes from the sensors inside it, and then is coupled onto the return bus through an optical add multiplexer (OAM), which takes it back to the return detector. The remaining wavelengths of the input interrogation signal continue along the distribution bus to the

subsequent ODMs, successively feeding into each TDM group. This architecture performs the 'add' and 'drop' functions by separate devices, and thus provides the advantage that if the telemetry fibre is severed within the array, then only the signals from the TDM groups corresponding to ODM/OAMs positioned after the break are lost.

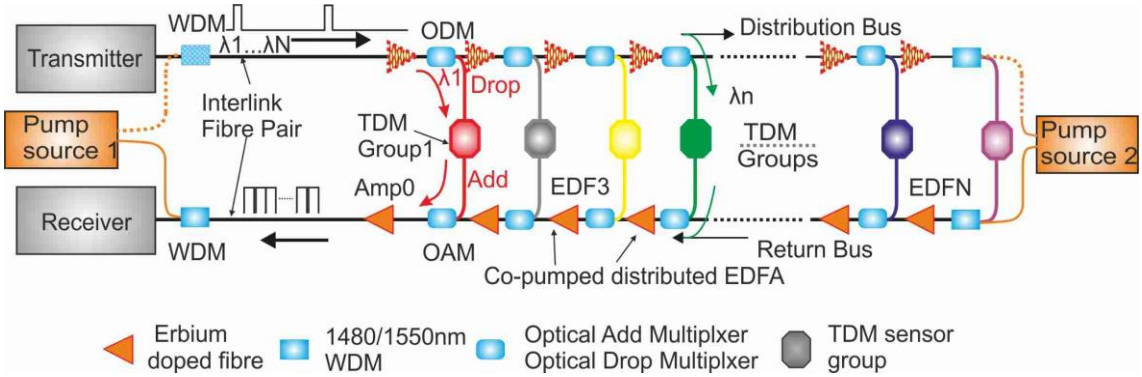

Figure 4.1: A new hybrid TDM/WDM sensor array architecture using a distributed EDFA with N amplifier segments which can be applied either on the distribution bus (top) and/or on the return bus (bottom). The pump power for the amplifier is launched from either or both ends of the buses. Each TDM group has M sensors multiplexed in the time domain. This array has M×N sensing elements.

To reduce the splitting losses due to the optical add/drop multiplexer (OA/DM) pairs and to balance the powers among different wavelengths, EDFA segments are distributed along the buses to compensate for the insertion loss of the OA/DMs, therefore the optical signals from all the TDM groups now experience approximately the same net optical gain. As shown in Figure 4.1, there exist three options to employ the amplification: (i) amplifiers on the distribution bus, (ii) amplifiers on the return bus and (iii) amplifiers on both of the buses. With a practical input peak optical power over one hundred mW per wavelength, the travelling optical power on the distribution bus is far beyond the EDFA's small-signal regime, i.e. where the gain is independent of the input signal power, and it will be hard to balance the power at each wavelength. Therefore, in our array, amplifier segments are applied only on the return bus.

The gain of each amplifying section on the return bus is set to exactly compensate for the subsequent losses for each sensor group (Amp0 provides a gain of 20 ~25 dB for the loss from the TDM group, the remaining EDFs just gain to offset the loss from each OA/DM pair). The amplifiers are all co-pumped remotely through the existing return bus fibre by pump lasers located at the front and/or back ends of the array. Since each amplifier must compensate for only a small insertion loss (except for Amp_0), they provide a low gain and require only a small pump power. Given that the insertion losses from the multiplexers are exactly compensated for

at each stage, on the return bus, the gain of each amplifier is twice the value of the OAM insertion loss on each of the buses. Accumulated ASE power will also experiences a gain twice the OAM loss at each stage, which leads to a worse SNR at the new array output than in a non-amplified array. This issue will be discussed later.

This novel architecture is considered to be the best approach to support high sensitivity, high sensor count interferometric sensor arrays through only one pair of telemetry fibres. It provides dramatic advantages over other designs for large scale arrays. The insertion loss of the array is compensated for by the co-pumped distributed amplifier, which leaves a higher power budget for the remote transmission of the signal along the cable, and limits the chance of nonlinear effects within the fibre bus. These benefits are of prime importance in many applications. The topology uses a hybrid TDM/amplified-DWDM architecture for the first time, such that the number of multiplexed sensors is now given by the product of the number of TDM sensors and the available number of wavelengths, which is increased by several times compared to the number multiplexed in amplified TDM arrays with the same interrogation repetition rate [6]. The array allows the interrogation of thousands of multiplexed sensors utilizing only one single telemetry fibre pair, which significantly decreases the array complexity, cost, weight, and also provides for ready expansion.

4.1.2 Advantages of OA/DMs

Wavelength multiplexers for the new array should be designed to have low transmission loss at the pump wavelength so that the pump never couples out of the buses, therefore the amplifier absorbs only a small fraction of the pump power, and a large remaining power is transmitted to the downstream amplifiers, which can also operate in a pump saturation regime. It is thus possible to pump tens of widely distributed low-gain amplifiers with a modest pump power. The thin film OA/DMs chosen for the wavelength multiplexing are perfect for the new architecture. They do not only provide low insertion loss on the pump wavelength range, but also show great advantages in the reduction of accumulated ASE power along the return bus. OA/DMs have limited channel bandwidth on their transmission spectrum, which is shown in Figure 4.2. The figure shows a stop (pass) bandwidth of 0.4 nm on the pass (drop) channel, with a channel isolation of 20 (45) dB, respectively. The insertion loss of the OA/DM is defined as IL_m at its common channel and IL_{ad} at the add/drop channel.

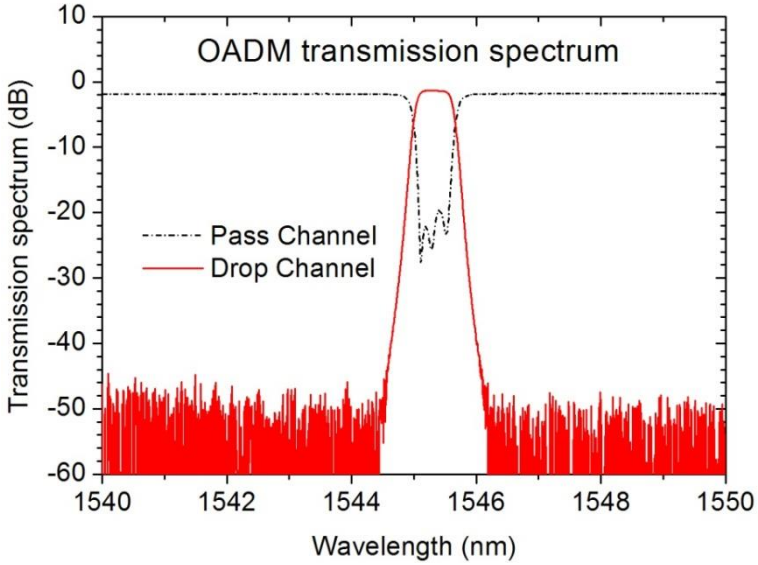

Figure 4.2: Optical transmission spectra at the pass channel and drop channel of the OADMs used in the experiment setup.

Figure 4.3 shows a simulated output optical spectrum at the output of an amplified array with 16 wavelengths using VPIphotonics. Since only wavelengths out of the add channel bandwidth (~0.4 nm) are passed through the pass channel of the OAMs on the return bus, there exists a measured stop band attenuation of ~20 dB on it. The OA/DMs also provide a partial rejection effect on the accumulated in-band ASE power, named as the 'band pass filter' effect and shown as 'hollow' shapes around the multiplexer's centre wavelength in the ASE spectrum.

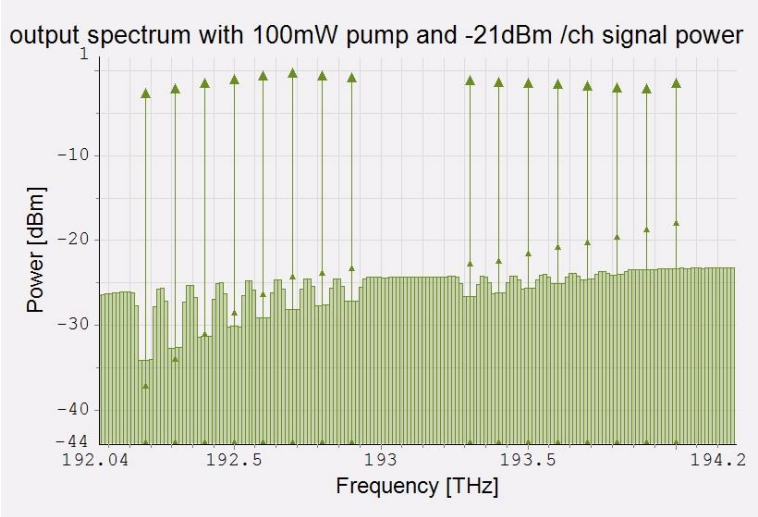

Figure 4.3: Demonstration of the 'band pass filter' effect on the accumulated ASE power from the OA/DM-EDF segment in the optical spectrum at the array output (from simulation).

4.1.3 TDM group

The TDM group (all sensors driven by one wavelength) in the recommended array is developed based on the inline-Michelson TDM architecture, to reduce the component count and simplify the array manufacture. The inline-Michelson TDM architecture has only one coupler per sensor. The sensors are time multiplexed in a single line, and are separated by reflectors which are constructed by connecting one port of a fibre x-coupler with a Faraday mirror, as shown in Figure 4.4.

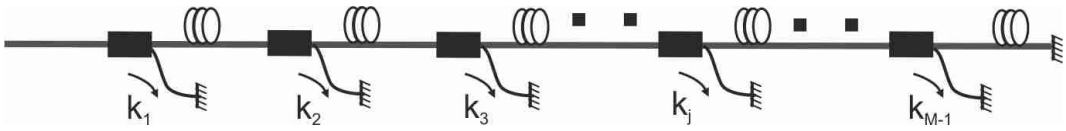

Figure 4.4: Schematic representation of an inline-Michelson TDM group with M reflectors.

In order to couple an equal power level to and from each sensor the coupler splitting ratios have to be set to a certain predetermined value. These coupling values are trivial to determine for a system in the absence of excess loss. Along the line, M arms are formed from M reflectors, to equal the power among these arms, each arm returns a power portion of $1/M^2$. Therefore, the coupling ratio of the first coupler is given by 1/M, and the relationship between adjacent coupler ratios is given by $k_j^2 = (1-k_j)^2 k_{j+1}^2$. The last coupling ratio is given by 1/2 to equalise the power levels from the last two arms. We then get $k_1 = 1/M$, $k_2 = k_1/(1-k_1) = 1/(M-1)$, $k_3 = 1/(M-2)$, ... , $k_{M-1} = 1/2$, and the coupling ratios for k_j are given by (for the j-th coupler in a series of M reflectors):

$$k_j = \frac{1}{(M+1-j)} \tag{4.1}$$

Additional losses due to splices and couplers lead to the need to skew the distribution in coupling ratios along the group to compensate for these effects. This type of compensation works well for small numbers of sensors (i.e. < 10), larger arrays become problematic due to the very small coupling ratios required, and the tolerances within which the coupling ratios have to be set. To overcome this, we have developed an optical sensor unit (OSU), each with four sensors inside, packaged with a cluster of three orthogonally mounted accelerometers and a hydrophone. Each sensor has an insertion loss IL_s of 5 dB. The four sensors in each OSU are time multiplexed on a single line, in the form of an inline-Michelson TDM architecture, with the coupling ratios of 15.8%, 21.1%, 30.2% and 48.7%, to each sequential Faraday mirror, consecutively. We then implement each TDM group with a number of OSUs, arranged in a tree

configuration, on branch couplers, as shown in Figure 4.5. These OSUs are effectively parallel, with optical delays between each other, and therefore can be physically arranged to form a single continuous sensor train.

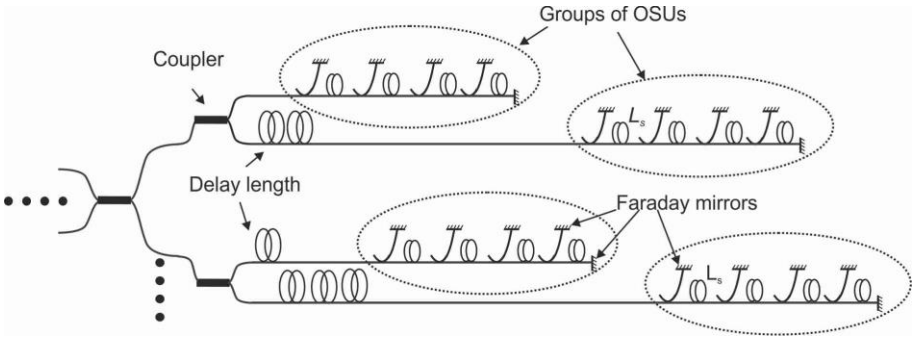

Figure 4.5: Optical configuration of the TDM group.

The number of sensors *M* that can be multiplexed into a TDM group can be multiples of four, and is limited by the required interrogation rate for each sensor and the optical power. The maximum interrogation rate f_{rep} can be deduced from the transit time of the optical pulse through the TDM group, and the maximum interrogation rate in Figure 4.5 can be expressed in terms of the return sensor coil fibre length $2L_s$ and the fibre effective refractive index n_{eff}

$$f_{rep} = \frac{c}{2n_{eff}L_s(M+1)} \tag{4.2}$$

where c is the speed of light in vacuum. The optical duty cycle D is $1/(\mathrm{M}+1)$. The timing arrangement for the heterodyne demodulation of a single OSU is shown in Appendix A in detail.

4.2 Laser source and optical power handling capacity

When designing a sensor system, one must determine the source, the power handling capacity, and the excess loss along the array. In the new array with a distributed EDFA, we must also determine the pump power budget and the EDF length distribution at each stage.

4.2.1 Laser sources

One of the key components in a fibre-optic interferometric system is the laser source used. Obviously the laser needs to be frequency stable and single polarization. For seismic sensor applications, the phase noise of the laser source in the low frequency range is of critical importance since the seismic signal is usually collected between 1 Hz and 500 Hz [89]. The performance of the sensors is largely dependent on the phase noise level of the light source (will

be shown in Chapter 5), as well as the source's sensitivity to environmental vibrations, particularly at low frequencies.

In general, the laser phase noise in semiconductor and solid-state lasers is dominated by 1/f or $1/\sqrt{f}$ noise at low frequencies (<100 kHz) [90]. At higher frequencies, it is the spontaneous emission (or white) noise that dominates, scaling inversely with emitted power. The phase noise level of telecom grade semiconductor lasers is too high and as a result they have not been considered as a potential source. Today only solid-state lasers and fibre lasers have phase noise levels low enough to be used with seismic systems, with typical phase noise spectra as shown in Figure 4.6. Single mode, single frequency, low noise fibre lasers have significant advantages over semiconductor DFB laser sources in the phase noise level, e.g., the Rock module (a NP photonics FBG laser), the Koheras Basik OEM module (a NKT Photonics Distributed-Feedback laser), and the Sensilaser. However, even though the phase noise levels are very low, they are highly susceptible to environmental perturbations (vibration, noise, temperature), showing vibration sensitivities ranges from –30 to –80 dB rad/g, which have the detrimental effect of increasing measurable phase noise levels. Among these lasers, the Sensilaser source gave the best overall performances, providing a very low phase noise level of 3 µrad/√Hz/m at 100 Hz and a low vibration sensitivity around –80 dB rad/g [91]. Therefore, the optimum laser source has low phase noise (< 10 µrad/√Hz/m at 100 Hz) and vibration insensitivity, is compact, has high output power (e.g., 30 mW), and low cost.

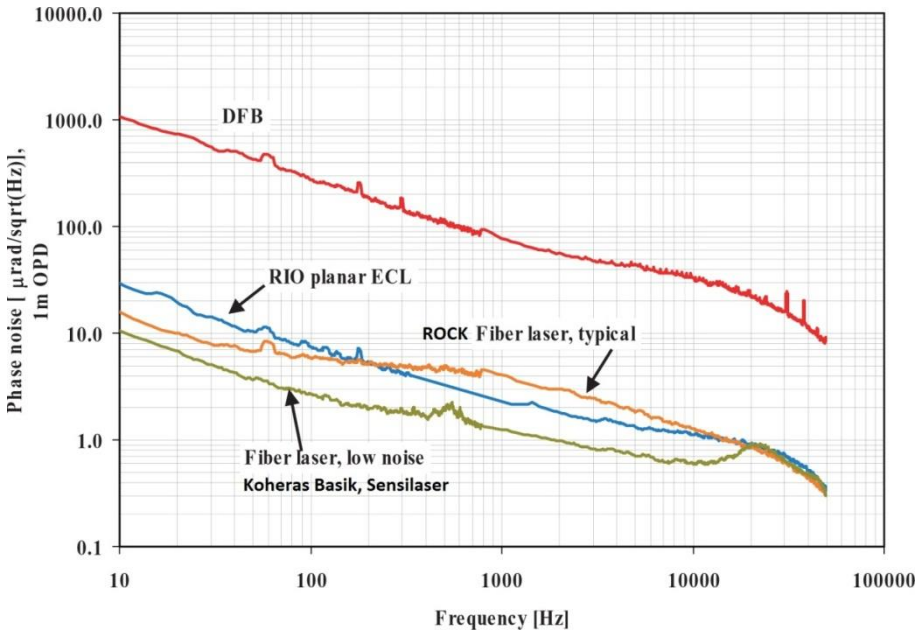

Figure 4.6: Phase noise comparison between the various lasers.

4.2.2 Optical power handling

As we illustrated previously in Chapter 1, the transmitted optical power to the array is limited by nonlinear effects. This is the reason why we put distributed amplifiers in the array. In this study, the value of the critical peak optical power into the array will be determined assuming a fibre transmission length of 50 km, therefore, the conclusions in this work suit all the sensor systems with signal transmission length ranging from 0 to 50 km.

The nonlinear effects pronounced in systems with high-transmitted power includes: Stimulated Brillouin Scattering (SBS), Stimulated Raman Scattering (SRS), Self-Phase Modulation (SPM), Cross-Phase Modulation (XPM) and the Four-Wave Mixing (FWM). Those nonlinear effects will not only result in a severe attenuation of the forward travelling, but also lead to an information-carrying signal. Due to the transfer of energy to the stimulated wave, the stimulated wave will lead to channel crosstalk into the sensing system. Other nonlinear effects give rise to various effects, e.g., phase noise, wavelength conversion. Therefore, it is important to keep the signal power under a certain threshold.

4.2.2.1 SBS

Brillouin scattering is one of the most prominent optical effects. In SBS, the original signal produces density variations through electrostriction, resulting in an index grating which generates a Stokes wave through Bragg diffraction. In a spontaneous process, a photon from an incident light wave is transformed into a scattered photon and a phonon. The Stokes wave grows from noise provided by spontaneous Brillouin scattering occurring throughout the fibre. The initial noise power at the fibre output $P_B(L)$ is equivalent to injecting a fictitious photon per mode at a distance where the gain exactly equals the fibre loss. When input pump power exceeds a threshold level, the process becomes stimulated, i.e., strongly dependent on the pump power [83]. The Brillouin stokes power is found to grow exponentially in the backward direction as

$$P_B(0) = P_B(L)\exp(g_B P_s L_{eff} / A_{eff} - \alpha L) \tag{4.3}$$

where P_s is the incident signal power at Z = 0, A_{eff} is the effective mode area, α is the fibre attenuation loss, g_B is the Brillouin gain, L is the actual fibre length, and L_{eff} is the effective fibre length of interaction, defined by $L_{eff} \approx (1-e^{-\alpha L})/\alpha$. Typically, α = 0.2 dB/km at 1.55 μm wavelength, and for long links where $L >> 1/\alpha$, we have $L_{eff} \approx 20$ km.

The threshold SBS is defined as the input pump power at which the Brillouin scattering becomes a stimulated process such that [92]

$$P_{Bcr} \approx \frac{21A_{eff}}{L_{eff}\, g_B} \tag{4.4}$$

The peak value of the Brillouin gain g_B is in the range of $3 \sim 5 \times 10^{-11}$ m/W for typical silica fibres. The mode field diameter is 10.4 μm at 1550 nm for standard single-mode corning SMF-28e, provides us with an effective mode area A_{eff} of 85 μm^2. Equation (4.4) leads to $P_{Bcr} \approx 10$ mW for a continues wave (CW) signal with $L_{eff} \approx 20$ km.

In the pulsed regime the SBS threshold is expected to depend on the width of the optical pulse rather than the whole transmission fibre length. In the sensor array architecture, the fibre interaction section is relatively short; say the width of one pulse pair in each period. The threshold value can be increased, and the value can be approximated by [92]

$$P_{Bcr'} \approx \frac{21A_{eff}}{L_{eff}\, g_B}\left(\frac{1}{D}\right) \tag{4.5}$$

The threshold increases to 500 mW in a transmission fibre of less than 1 km with a pulse width of 100 ns and a period of 5 μs. Figure 4.7 shows the measured backward propagating spectra from a fibre transmission over 50 km, as the peak input optical power increases from 60 mW to 250 mW [1]. The spectra show the Rayleigh backscattering peak at 1545.3 nm and the corresponding SBS peak at 1545.38 nm, approximately 11 GHz away from the main peak as expected from a germane silicate fibre. It can be seen from the figure that the SBS peak starts to grow rapidly as the peak optical power of the pulse exceeds ~100 mW (in red). Approximately half of the forward propagating power appears in the backward direction when the input peak optical power was increased to 250 mW (~10 mW average power).

[1] The experimental data in section 4.2.2 was conducted together with Mr Charles Zhang for the TSB project to reveal the nonlinear effects in long transmission link of 50 km.

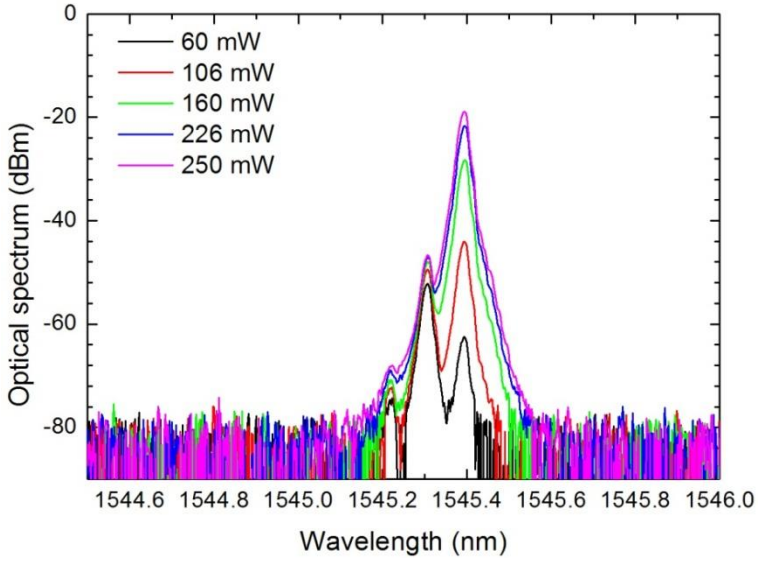

Figure 4.7: Measured (1%) backward travelling spectra of a 50 km long SMF-28e fibre for different input peak optical powers highlighting the effect of SBS.

4.2.2.2 SRS

Unlike SBS, SRS is the scattering of light from vibrating silica molecules, and it can occur in both directions, i.e., forward and backward. The threshold power level for SRS is quite large compared to that of SBS, and is given by [93]

$$P_{Rcr} \approx \frac{16A_{eff}}{L_{eff}\, g_R} \tag{4.6}$$

The Raman gain coefficient g_R is around 0.6×10^{-13} m/W, and leads to a threshold power $P_{Rcr} = 1$W, which is too large to be of concern. The Raman gain spectrum extends over 40 THz and its maximum is located approximately 13 THz away, which is far beyond our interests of channels.

4.2.2.3 MI

Modulation instability (MI) [94] in fibre-optics is a phenomenon, whereby a small perturbation in an optical pulse leads to the destabilization of the pulse itself, due to the interplay between group velocity dispersion (GVD) and SPM. This MI can be induced by SPM and XPM in the transmission fibre. As a consequence, new spectral sidebands are created and the original pulse is broken into a train of sub-pulses. In the context of optical fibres, MI requires anomalous dispersion to sustain its growth. The gain becomes a maximum at two frequencies given by $\Omega_{max} = \pm(2\gamma P/|\beta_2|)1/2$, where γ is the nonlinear parameter, P is the optical peak power of the

pulse and β_2 is the group velocity dispersion. Figure 4.8 shows the forward propagating spectra at various input powers in a 50 km long SMF-28e fibre (anomalous dispersion at 1.55 μm).

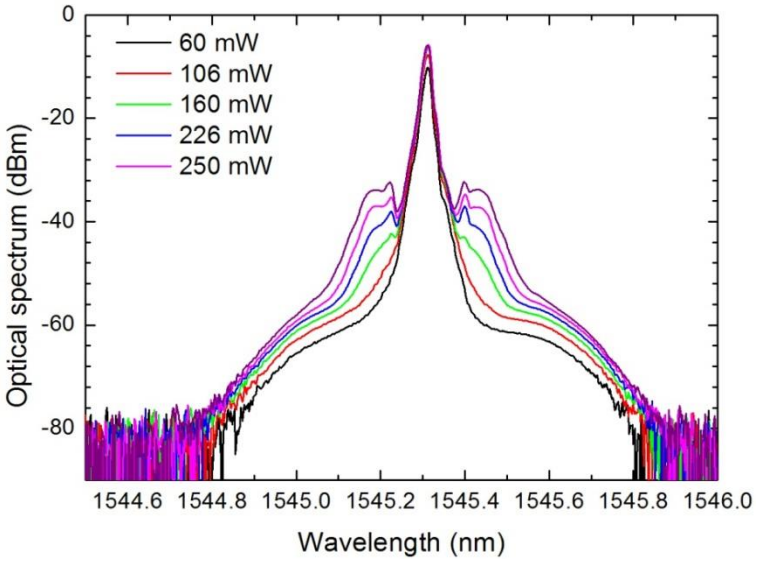

Figure 4.8: Measured output spectra of a 50 km long SMF-28e fibre with different input peak optical powers highlighting the effect of MI.

One can see from Figure 4.8 that spectral broadening starts to take place at peak optical powers of ~100 mW and sidebands start to appear when the peak optical power is raised to ~160 mW (in green). The sidebands become more pronounced and move away from the signal peak with an increase in input peak optical power of the pulse. This is due to MI induced instability suffered by the optical pulses as they propagate down the transmission fibre. To avoid MI induced noise in the sensor system, it is recommended that the input peak optical power along the transmission fibre is less than ~160 mW over a SMF-28e fibre transmission of 50 km, and this will get reduced with an increasing in the transmission length of the link fibre.

4.2.2.4 FWM

FWM occurs [95] when photons from one or more waves are annihilated and new photons are created at different frequencies such that the net energy and momentum are conserved during the process.

Since commercial optical amplifiers involves long lengths of active/passive fibres to ensure flat top gain profiles across the C-band, rapid build-up of FWM components was even noticed within the optical amplifier and needs to be addressed, as illustrated in Figure 4.9. It can be seen from the figure that multi FWM peaks are observed at the output spectrum of the transmitter amplifier. Therefore, it is essential to avoid this FWM process inside the transmitter.

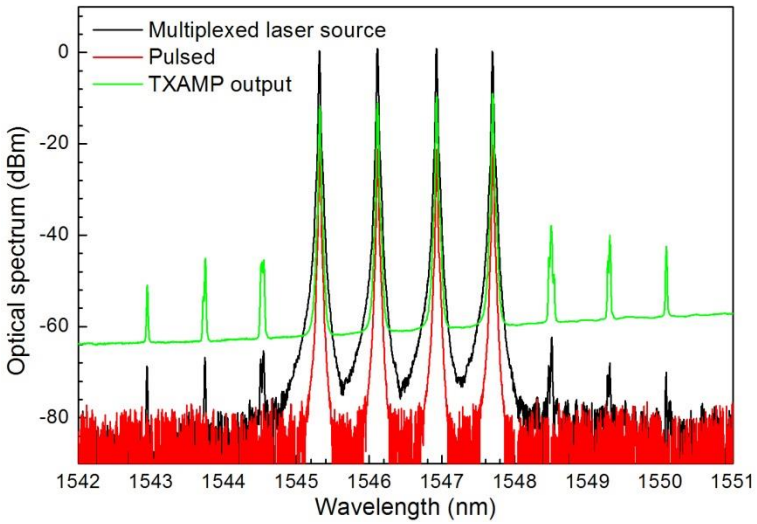

Figure 4.9: Measured output spectra from the transmitter (includes a multiplexed source, a pulse generator, and a transmitter optical amplifier (TXAMP)).

The FWM process can be reduced by rearranging the optical components, since the strength of the FWM process depends on the separation of the WDM channels and was found to be decreasing with an increase in channel separation. Furthermore, the deleterious effect of FWM can even be avoided completely by sequencing the optical pulses in such a way so that they don't overlap in time. Figure 4.10 clearly shows the merit of the staggered pulse sequencing (pulses at different wavelengths are produced at different time) to eliminate the FWM process after amplification, especially after the fibre transmission over 50 km.

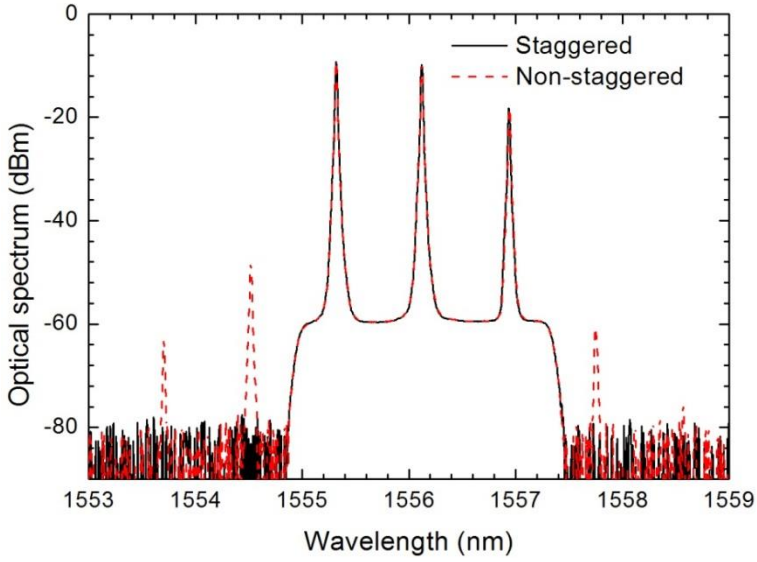

Figure 4.10: Measured output spectra after fibre transmission over 50 km with staggered and non-staggered pulse sequences.

In conclusion, the optical power handling capacity is determined by nonlinear effects at the transmission fibre. In the pulse regime, the thresholds of the SBS with a 50 km of transmission link are increased to 250 mW. The SRS threshold is much larger than the SBS threshold. And the critical threshold in the sensor system is limited by the SPM and XPM induced MI, which is ~160 mW with 50 km of transmission fibre (SMF 28e). FWM will also introduce phase noise and crosstalk into the system and needs to be avoided at all costs. The most direct route to eliminate FWM among the neighbouring wavelength division multiplexed channels is to separate the optical pulses in the time domain (staggered pulse sequencing).

To summarize, nonlinear effects introduce light attenuation, crosstalk and phase noise into the sensor system, and they are more pronounced in systems with higher optical powers. MI is one of the very strong nonlinear processes, and to avoid the occurrence of the MI effect in 50 km of transmission fibre (SMF 28e), it is necessary to keep the peak optical power under 160 mW. The achieved critical peak signal power of 22 dBm will be used for later network design and array capacity prediction. Therefore, the conclusions in this work suit all the sensor systems with signal transmission length ranges from 0 to 50 km. However, the long distance transmission of pump radiation will not be covered in this work, as the pump lasers can be physically packaged in one of the hubs which are located closer to the sensor arrays.

4.3 Pump diode and pump power budget

4.3.1 Pump wavelength

EDFAs can be pumped at either 980 nm or 1480 nm. In PRM applications, the down-lead cables for the pump are typically 1 m to 10 km long, and typically have a transmission loss of 0.3 dB/km at 1480 nm and 1.5 dB/km at 980 nm. Therefore it is critical to use 1480 nm pump sources for in-array amplifier pumping, so that a significant amount of the pump power actually reaches the amplifiers.

4.3.2 Pump power consumption in a single amplifier segment

To determine the pump power budget for an entire amplified array, we must first consider the power consumption of a single amplifier stage. Figure 4.11 shows one stage of a typical amplifier segment (OA/DM-EDF) on the bus, comprising one segment of EDF and one OAM. Let us assume IL_x is the insertion loss of the splice between one EDF and the single mode fibre (SMF), IL_e the background loss of the EDF, IL_f the transmission loss of the SMF, and IL_m the insertion loss of the OAM, all these parameters being characterized at 1480 nm.

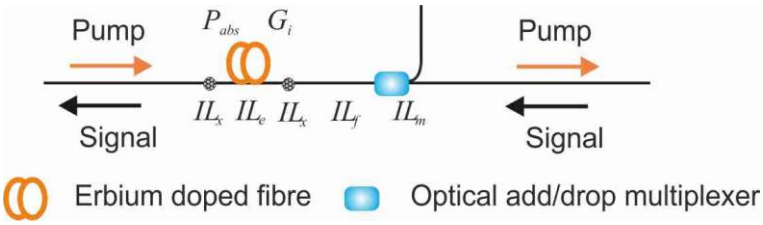

Figure 4.11: Details of single amplifier segment from the new amplified network. All of the loss mechanisms for the pump power are included.

Now that we can define the accurate pump power budget for a single amplifier stage, the pump loss mechanisms, includes absorption of pump power (P_{abs}) by the amplifier's erbium ions, the insertion loss of the two splices, the insertion loss of the multiplexers at 1480 nm, and the transmission loss of the EDF and bus fibre. In the strongly pump saturated regime, with a pump power of P_{in} lauched into the amplifer stage, the exiting pump power P_{out} is given by

$$P_{out} = [P_{in} \cdot IL_x \cdot IL_e - P_{abs}] \cdot IL_x \cdot IL_m \cdot IL_f \tag{4.7}$$

This output pump power is considered to be the input pump power for the subsequent amplifier segments. When calculating the signal power in linear equations from (4.7) to (4.28), one should take care to use the linear value transferred from the value in decibels (i.e., $IL = 10\wedge(-IL_{dB}/10)$ and $G = 10\wedge(G/10)$).

The absorbed pump power P_{abs} in a single segment of EDFA can be simplified by $P_{abs} = (\lambda_s/\lambda_p)(G_i - 1)P_s$, with λ_s the signal wavelength, λ_p the pump wavelength, P_s the input signal power, and G_i the gain at each EDF segment. As stated above, the length of each EDF is set to provide a gain of G_i that exactly compensates for the subsequent signal losses before the next amplifier. This pump to signal conversion is independent of the input pump power, provided that the input pump power is much larger than both the *threshold input pump power* P_p^{th} (defined later) and P_s. Each amplifier also produces ASE and amplifies ASE originating in other amplifier stages. An individual amplifier adds 2 ~3 μW of new ASE power to the incident ASE in both directions and amplifies the total ASE.

The largest dissipative loss for the pump power is the OA/DM multiplexer insertion loss IL_m (typically less than 1 dB). The small multiplexer loss dominates the large EDF absorption because P_{abs} is independent of the pump power P_p when P_p is very large, while the dissipated power due to IL_m is proportional to P_p.

The second largest dissipative pump loss arises from the two splices between the EDF and the bus fibre. Such splices tend to have a larger insertion loss than SMF-to-SMF splices because of

the mode field diameter mismatch between the EDF and the SMF. The bus fibre is a standard SMF with low numerical aperture (NA) (typically 0.12) and a large mode area. On the other hand, for the EDF a higher NA (typically greater than 0.20) is preferable to lower the amplifier pump power requirement. Presently, our lab EDF-to-SMF splices have a typical value of $IL_x = 0.16\ dB$ per splice at 1550 nm, compared to 0.01 dB for SMF-to-SMF splices.

The third pump power loss mechanism is fibre transmission loss. The background loss per km tends to be larger for an EDF than for a standard SMF. The I4 EDF fibre from Fibercore Ltd has typically a background loss under 3 dB/km at 1550 nm (specified <10 dB/km at 1200 nm with a low NA = 0.23). The transmission loss IL_f over tens of meters of SMF (< 0.2 dB/km) between adjacent OA/DMs is sufficiently small to be ignored.

4.3.3 Pump power consumption in the distributed amplified array

Now that we have developed a pump power budget for a single amplifier, we can construct a budget for a large array of amplifier segments, all pumped from a single source at the front end. The array topology is shown in Figure 4.12, based on the recommended architecture design.

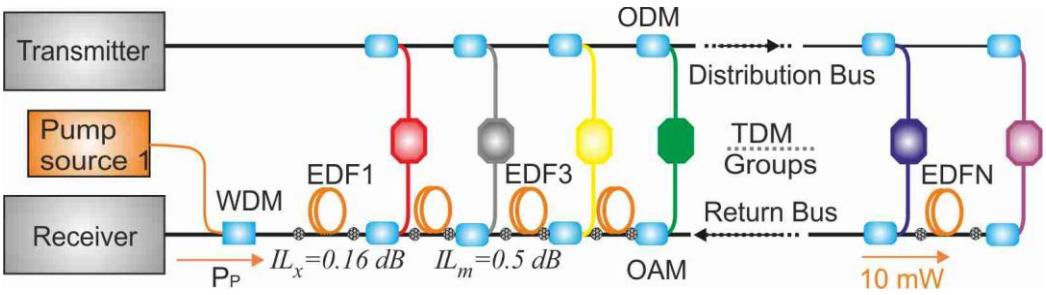

Figure 4.12: Pump power transmission in the distributed amplified array.

Let us now define more accurately the pump power budget. From (4.7), the pump power P_k incident on the *k*th amplifier is related to the pump power P_{k-1} transmitted by the previous ((*k*–1)th) amplifier by

$$P_k = [P_{k-1} \cdot IL_x \cdot IL_e - P_{abs}] \cdot IL_x \cdot IL_m \cdot IL_f \tag{4.8}$$

Remember that P_{abs} is a function of the signal power incident on the *k*th amplifier. In the pump power budget, typically less than a few mW of pump power are converted to ASE power in the entire array and is thus negligible. The input pump power P_1 must be large enough so that the pump power P_n that reaches the last amplifier is greater than some minimum value. The latter is set to ensure that the last amplifier provides enough gain, i.e., it is much larger than both P_p^{th} and P_s. As P_1 is increased, all of the amplifiers receive more pump power and the gain across all of

the amplifiers is more uniform, and therefore the returned signal powers are more uniform across the array. Therefore, P_n is set to keep the variation in gain among all of the amplifiers below some desired level, and consequently, this determines the pump power that must be supplied to the first amplifier. In this analysis, we set P_n to be 10 mW, which is many times larger than both the amplifier threshold pump power and the average signal power.

Figure 4.13 shows the evolution of the pump power incident on each amplifier along an array with 16 amplifier stages and 16 sensors per TDM group, using (4.8) and the loss budget given in detail previously. The insertion loss is 5 dB per sensor in the TDM group. The curve is dominated by the multiplexer insertion loss. The launched peak optical power is set at 22 dBm per wavelength. The power level is limited by the MI effects over 50 km of transmission fibre as previously discussed. I choose this value for performance investigations, thus the investigated sensor array would be versatile for sensor systems with interlink fibre length less than 50 km. Providing that D = −14 dB, IL_m = 0.5 dB, IL_x = 0.16 dB, $\lambda_p = 1480$ nm, the required input pump power for this application is 220 mW.

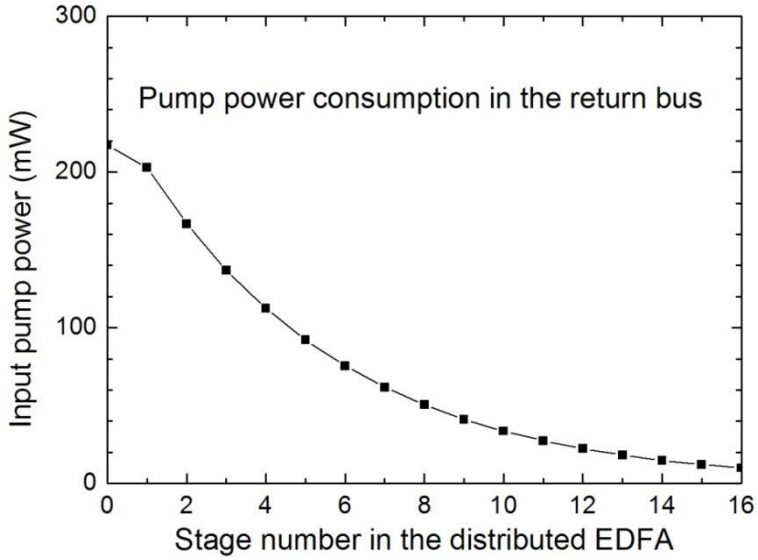

Figure 4.13: Pump power incident at each amplifier stage in return bus, respectively, for an array with 16 amplifier stages. Parameters are peak optical power P_s = 22 dBm per wavelength, D = −14 dB, IL_x = 0.16 dB, IL_m = 0.5 dB, λ_p=1480 nm. Input pump power is selected such that 10 mW is incident on the last amplifier on the return bus.

This insertion losses from the OA/DMs (IL_m) and the EDF-to-SMF splicing (IL_x) are proportional to the input pump power and typically dominates. Therefore, I have simulated the required pump power on the return bus with different values of IL_m and IL_x, separately.

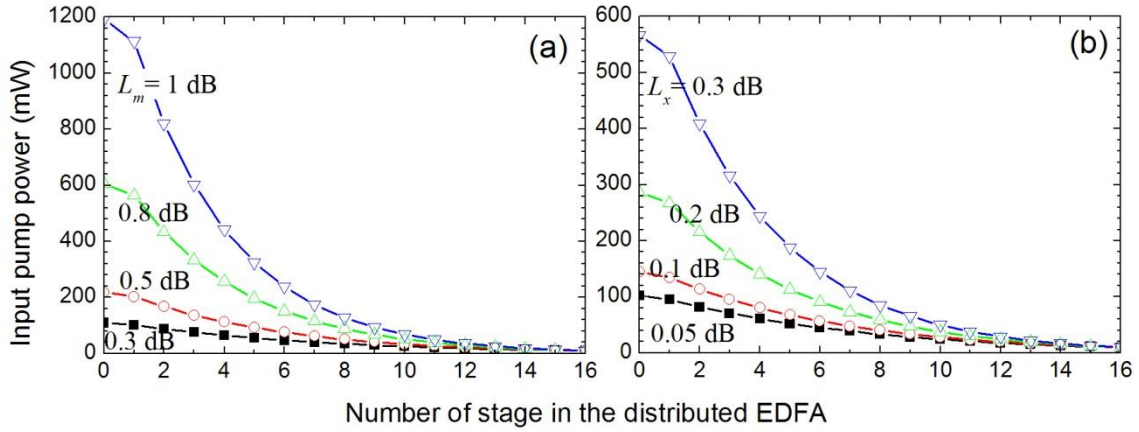

Figure 4.14: Pump power incident at each amplifier stages with (a) different IL_m of 0.3 dB, 0.5 dB, 0.8 dB and 1 dB and (b) different IL_x of 0.05 dB, 0.1 dB, 0.2 dB and 0.3 dB, with 16 amplifier stages and 16 sensors per TDM group. Parameters: peak optical power P_s = 22 dBm per wavelength, IL_x = 0.16 dB for (a) and IL_m = 0.5 dB for (b). Input pump power is selected such that 10 mW is incident on the last amplifier.

Figure 4.14 (a) shows the power dissipation with different IL_m of 0.3 dB, 0.5 dB, 0.8 dB and 1 dB, separately. The required pump power increases from 110 mw to 1200 mW as the insertion loss of the OAM increases from 0.2 dB to 1 dB. Commercial OAMs have typical insertion losses of 0.4 dB (from the Bookham), 0.5 dB (from the Fiberer) and 0.8 dB (from the Laser 2000). It would be a challenge to significantly reduce IL_m further, which is one of the reasons why we need a distributed amplifier to compensate for this loss in large multiplexed arrays. The insertion loss from the two splices in each OA/DM-EDF segment has similar effects to the loss due to the optical multiplexer on the return bus, therefore an increase in the insertion loss from an EDF-to-SMF splice dissipates the pump power twice as fast as it does from the multiplexers alone. Figure 4.14 (b) shows the required pump power to the 16 wavelengths system with different EDF-to-SMF splicing losses of 0.05 dB, 0.1 dB, 0.2 dB, 0.3 dB. The required pump powers are 102 mW, 144 mW, 286 mW, and 567 mW respectively. Good commercial fusion machine splicers produce EDF-to-SMF splices with typical insertion losses ranging from 0.08 dB to 0.2 dB at 1550 nm. Improper operation may increase this value to larger than 0.5 dB. Limited by the commercial availability of higher power pump sources, the combined insertion loss of ($IL_m + 2IL_x$) should be less than 0.8 dB, for the distributed amplifier with only one single pump source. The array is segmented and connected. Connectors add loss to the pump power budget in the same way as multiplexers. A good connector may have an insertion loss as low as 0.25 dB.

4.3.4 Number of wavelengths

The maximum number of wavelengths in the array is limited by the insertion loss on the return bus at the pump wavelength and the available maximum output power of the pump sources. The transmission loss of the pump power is dominated by the insertion loss of the OAMs (IL_m) and the EDF-to-SMF splicing loss (IL_x). The pump power decreases rapidly along the return bus. So far, I have developed a pump budget and signal performance evaluation for an array with one pump source located at the front end of the new array. However, the number of wavelength channels in the array can be increased by constructing a dual-pump source configuration, as presented in Figure 4.15.

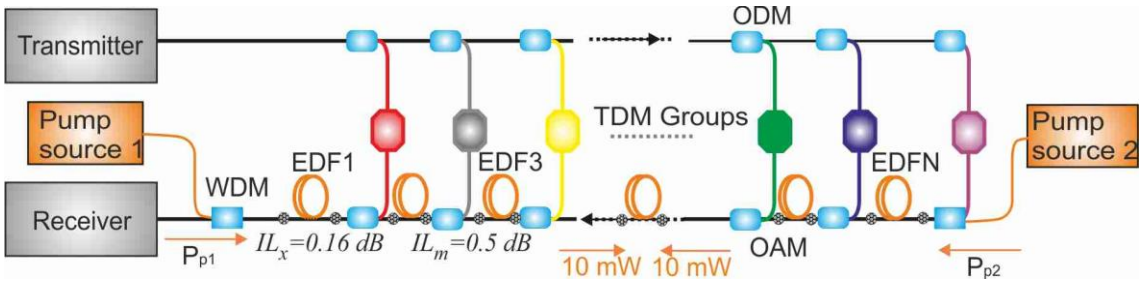

Figure 4.15: Pump power transmission in the distributed amplified array with dual pumps.

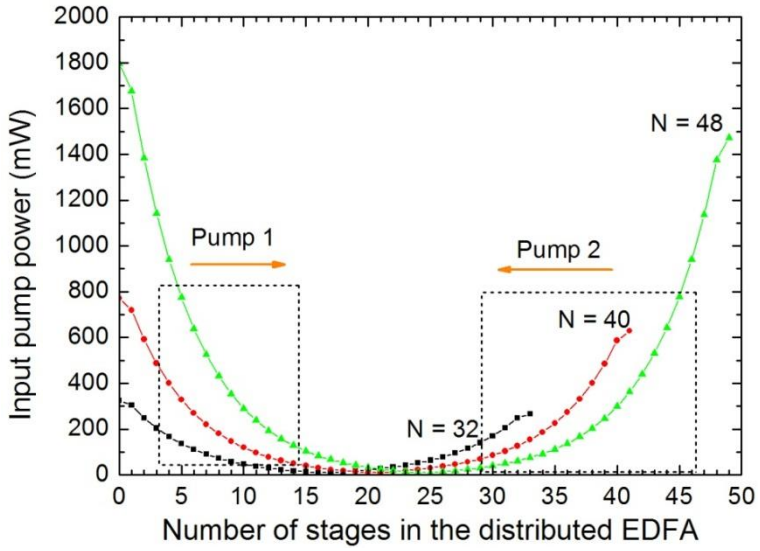

Figure 4.16: Pump power incident at each amplifier stage for an array with 32, 40, and 48 amplifier stages in the return bus with dual-pump sources (512, 640, 768 total sensors). Parameter values are, signal peak optical power P_s = 22 dBm per wavelength, IL_x = 0.15 dB, IL_m = 0.5 dB. Input pump power is selected such that 10 mW is incident on the middle amplifier.

The required pump power increases with an increase in the number of wavelengths. Figure 4.16 shows the required pump power for an array with 32, 40, and 48 amplifier stages (equivalent to the number of wavelengths) along the return bus with a pump source at both ends. The required forward and backward pump pairs for 32, 40 and 48 wavelengths are 325/267 mW, 771/630 mW, and 1 800/1 473 mW, respectively. The recommended network can support at least 32 wavelength channels, based on the dual-pump configuration, with two pump sources of 400 mW (commercially available from FITEL) at 1480 nm.

4.4 Distributed EDFA

4.4.1 Fibre length for EDF 2 to EDF 16

Since each segment of EDF 2 to EDF 16 in the distributed EDFA, shown in Figure 4.12, is to compensate for only the insertion losses added by each pair of OA/DMs, we use short, low-gain erbium doped fibres. The optical power at each wavelength from the distributed EDFA varies with the optical frequency and its position in the array, because of the intrinsic wavelength dependent gain in erbium doped fibres. The spectral power discrepancy (i.e., difference between maximum and minimum optical power values at different wavelengths) is as large as 9.3 dB if constant lengths of doped fibre are applied for all the stages. Figure 4.17 (a) shows the simulated output spectrum from the distributed amplified network, with an equal EDF segment length of 1 m. All the following simulations are made using VPIphotonics, with EDF parameters of I4 characterized and validated in Chapter 3.

Larger pump power could be used to decrease the power discrepancy between wavelengths, but this is not a practical solution. Simulations show a gain flatness of 0.1 dB from each single EDF stage, which indicates the possibility of a lower accumulated power discrepancy between wavelengths from the 16-wavelength network. Figure 4.17 (b) demonstrates the lowest wavelength discrepancy that can be achieved from the distributed EDFA, with an equal EDF segment length arrangement. Comparison of the simulations between Figure 4.17 (a) and (b) indicates that it is necessary to optimize the EDF length arrangement in the array, to decrease the power discrepancy between wavelengths.

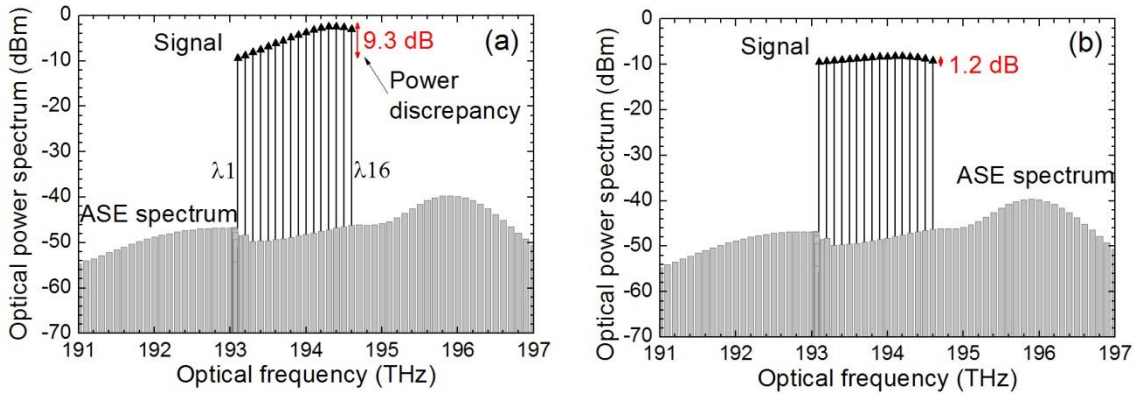

Figure 4.17: Output power discrepancy between wavelengths (a) with equal EDF lengths of 1 m and (b) with optimized EDF lengths of 0.7 m. Parameter values are, signal peak optical power P_s = 22 dBm per wavelength, IL_x = 0.15 dB, IL_m = 0.5 dB. IL of the TDM group = 29 dB. Input pump power P_p = 250 mW. Output power spectral discrepancies are 9.3 dB and 1.2 dB, respectively, in the system with EDF 2 to EDF 15.

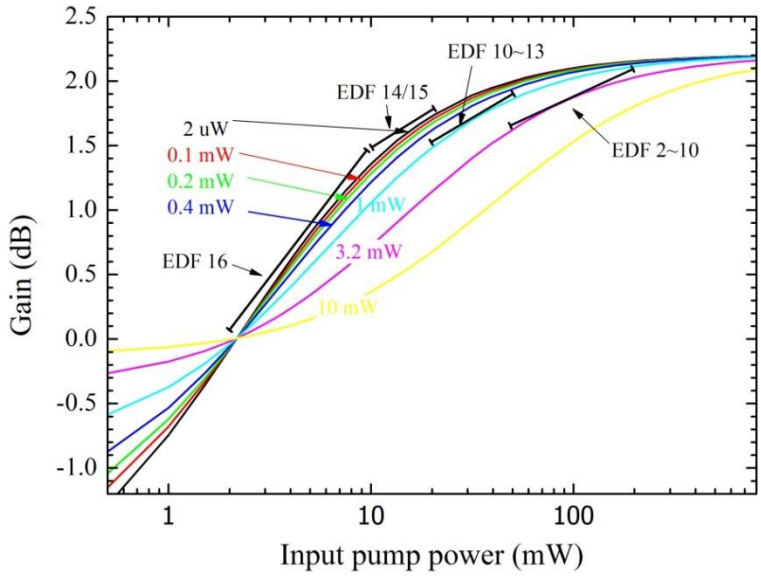

Figure 4.18: Gain as a function of input pump power in a 1 m-length EDFA of I4 with a range of different input signal powers.

The gain in each amplifier stage also depends on the level of pump power and signal power. The dependence of the gain on the pump power, with different signal powers, is shown in Figure 4.18. These curves were obtained in a 1 m single stage EDFA, without considering the insertion loss of the EDF-to-SMF splices, for exact characterization of the EDF net gain performance. A pump wavelength of 1466 nm (in view of lab availability) counter-propagates with a signal of 1550 nm. The EDF shows a threshold input pump power of P_p^{th} = 2 mW and it provides a maximum small signal gain of 2.1 dB with an increasing input pump power. It can be seen from

Figure 4.18 that low input signals have higher gain; however, for signal powers less than 0.4 mW, the gain difference is small. As the signal power increases, the gain difference increases. Fortunately, this difference also decreases with an increase in the pump power. Meanwhile, the gain per unit length increases with an increase in the input pump power as well.

In a practical array, the amplifier segments at the front of the array are operating in strong pump saturation, and the amplifier segments at the back of the array are not fully pump saturated and therefore have slightly lower gain per unit length. On the other hand, the number of signal wavelengths injected to each EDF stage depends on the EDF position on the return bus; this determines the input signal power into each EDF stage. Therefore, for simplicity, I have distributed EDF 2 to EDF 16 into four groups, according to the pump power level and signal power at each segment. The number of four was chosen because the EDFs in each group are under similar amplification conditions and provide similar unit gain per metre, as can be seen from Figure 4.18 and were summarized in Table 4-1. Table 4-1 indicates the nominal pump range and signal level as a function of L_m and L_x in an array with residual pump power P_n = 10 mW, signal peak optical power P_s = 22 dBm per wavelength, N = 16, and TDM group insertion loss of 29 dB. The unit gain for the EDF in each group is also labelled in Figure 4.18, varies from 1.2 to 2 dB/m, with the values shown in Table 4-1. The last column of the table recommends the EDF length for each group. The lengths (L) of the EDFs are chosen by L × unit Gain = 2($IL_m + IL_x$), such that the gain of each EDF segment compensate for the insertion loss from each OA/DM-EDF section. Amplifier segments at the back of the array have lower unit gain, thus need longer fibre lengths to compensate for the same insertion loss from OAM and EDF-to-SMF splices.

Table 4-1: Lengths of EDF segments on fibre I4.

EDF	*Pp (mW)*	*Ps (mW)*	*Gain (dB/m)*	*EDF length (m)*
2 ~10	> 50	0.2 ~3	1.7 ~2	$(IL_m + IL_x)/0.95$
11 ~13	20 ~50	0.02 ~0.4	1.6 ~1.75	$(IL_m + IL_x)/0.85$
14 ~15	< 20	0.005 ~0.15	1.2 ~1.6	$(IL_m + IL_x)/0.7$
16	~10	< 0.01	0 ~1.2	$(IL_m + IL_x)/0.6$

4.4.2 Pre Amplifier segment and length optimization

The signal power into the array is usually lower than the critical power of 22 dBm per wavelength, and the signal power on the return bus can be lower than −30 dBm per wavelength which is not adequate for signal detection, therefore we use a co-pumped pre-amplifier stage (Amp0) to compensate for part of the insertion loss of the TDM group, as illustrated in Figure 4.19. The pump power for Amp0 is mainly from the pump source 1 in configurations either with a single pump or with dual pumps. Considering the dominant loss from the optical multiplexers and the absorption in the pre-amp segment, the pump power budget can be given by

$$P_{in} = [P_n \cdot IL_m^{N-1} \cdot IL_x^{2(N-1)} \cdot IL_x + P_s \cdot N \cdot (G_0 - 1)] \cdot IL_x \cdot IL_{WDM} \tag{4.9}$$

with G_0 the gain in the pre-amplifier stage EDF1(Amp0).

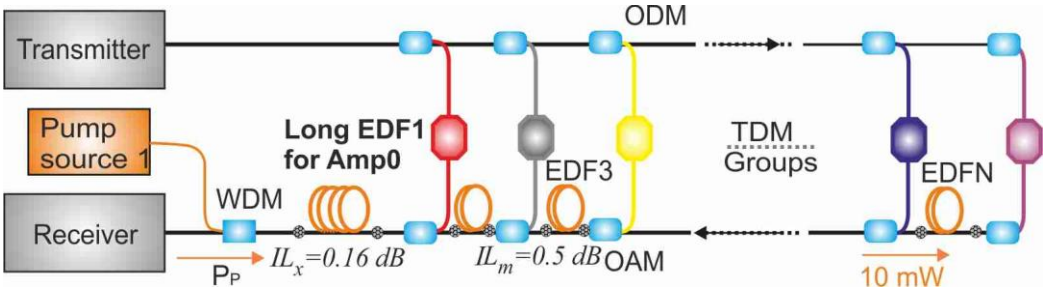

Figure 4.19: Pump transmission in the distributed amplified array with a pre-amplifier segment.

Basically, the more loss Amp0 compensates for, the better, but in EDFA chains where no optical isolators are used, the effect of Rayleigh back-scattering limits the maximum gain in each amplifier stage, which has been discussed in Chapter 3. This can be seen from Figure 4.20, which shows the simulated gains in a single stage EDFA as a function of EDF length for different input pump power of 400 mW and 250 mW. The dotted lines are taken with a Rayleigh scattering coefficient of 0.000125/m (i.e., Rayleigh constant parameter of 150 dB/km for the Aluminum co-doped EDF, and their relationship can be found in equation(3.12)), while curves are with a negligible value of 0.000035/m. The input signal power is set at −7 dBm, which is the nominal signal power at each wavelength into Amp0, providing an input signal peak optical power of 22 dBm per wavelength and TDM group IL of 29 dB. The two dotted lines show that EDFA gain experiences a reduction when it increases over 17 dB and its maximum value is limited to 28 dB, even with an increased pump power of 400 mW, because the light is scattered or double scattered in the fibre.

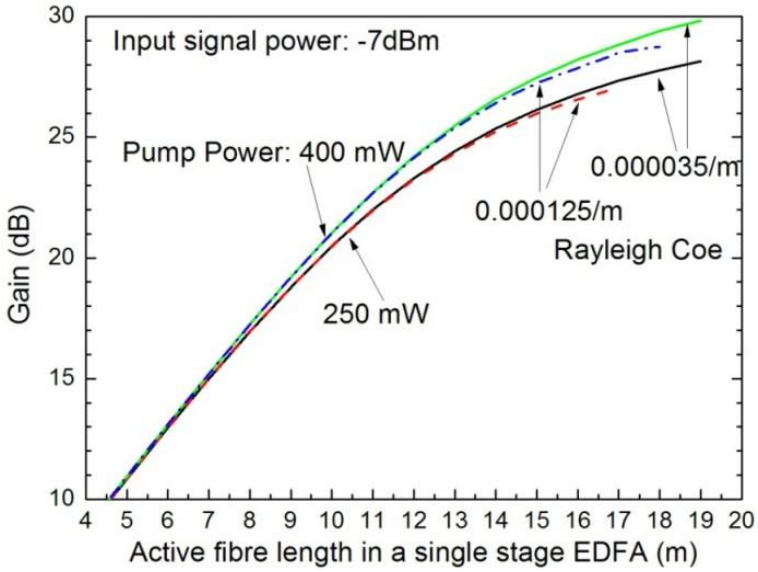

Figure 4.20: Gain as a function of EDF length for two different Rayleigh scattering coefficients with pump power of 400 mW and 250 mW respectively, in a single stage EDFA.

I use 11.65 m I4 fibre for the pre-amplifier segment. The gain and pump dissipation in a single stage pre-amplifier segment with this fibre as a function of signal power for various pump powers are shown in Figure 4.21 (a) and (b) separately, obtained using VPI.

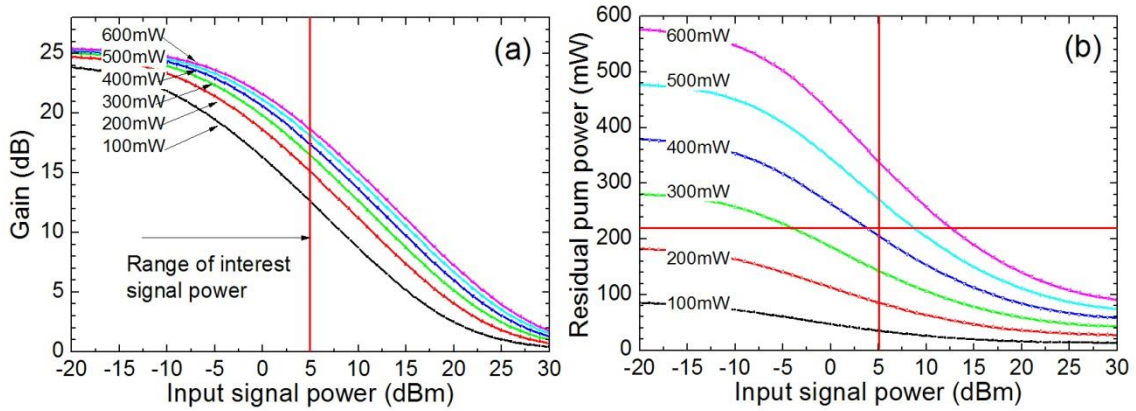

Figure 4.21: (a) Gain and (b) residual pump power in the single-stage 11.65 m EDFA of I4 with input pump power from 100 to 600 mW. These are taken without considering the insertion loss from the 1480/1550 nm multiplexer and the EDF-to-SMF splicer.

It can be seen from Figure 4.21 (a) that this amplifier segment provides a maximum gain of 25 dB in a small signal gain region, when the input signal power is smaller than −5 dBm. This gain decreases with an increase in the input signal power, and it ranges from 12 to 18 dB depending on the input pump at a signal power of 5 dBm. Figure 4.21 (b) shows the residual pump power after the EDFA, which will be conducted to the remaining amplifier segments. In order to support an array with IL_m+2IL_x = 0.8 dB, a pump power of 220 mW is required for

EDF 2 to EDF 16, thus a pump power of larger than 400 mW is required at the input of Amp0, regardless of the insertion loss of the 1480/1550 nm multiplexer and the EDF-to-SMF in the Amp0.

Let's now reconsider the power discrepancy in an array with a pre-amplifier segment. Although we have an approximate empirical length arrangement for the EDF segments in Table 4-1, we can further reduce the power discrepancy between wavelengths by tuning the fibre length of each amplifier segment, using VPI. As stated previously in Table 4-1, the lengths of amplifier segments are distributed into four groups. Sweep simulations on the length of each group in the architecture around the nominated length from the table can be performed to discover the best length distributions. The power discrepancy between wavelengths can be reduced from 3.5 dB to 1.38 dB for a 16-wavelength network with the pre-amp0, as shown in Figure 4.22, with the optimized length arrangements shown below. The power discrepancy between wavelengths can be reduced to less than 1.5 dB by length arrangement optimization in an array with specified excess loss on the bus.

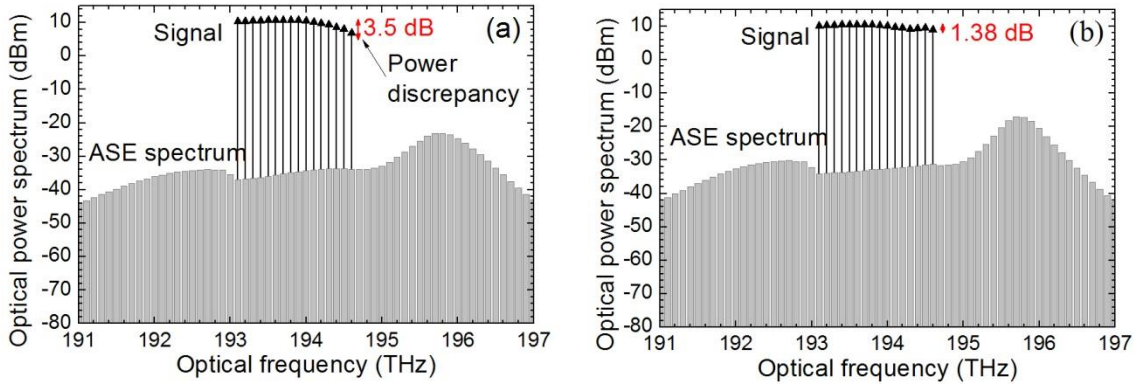

Figure 4.22: Output power discrepancy between wavelengths (a) with equal EDF lengths of 0.7 m and (b) with optimized EDF lengths (EDF 1 = 11.65 m for Amp0, EDF 2 to 11 = 0.7 m, EDF 12 to 13 = 1 m, EDF 14 = 2 m, EDF 15 to 16 = 3 m). Output power discrepancies between wavelengths are 3.5 dB and 1.38 dB, respectively. IL_x = 0.158 dB, IL_m = 0.5 dB, IL_{ad} = 1.2 dB. Signal peak optical power P_s = 22 dBm per wavelength and input pump power is set at 600 mW.

To summarize, it is important to optimize the EDF length arrangement in the new array, decreasing the optical power discrepancy between wavelengths. There are steps to flow: Firstly, we choose short, low-doped fibres. The gain flatness of the doped fibre is also important to achieve a flat output spectrum. Once the fibre is determined, we then characterize the gain performance of the fibre, and figure out the range of the input signal power and pump power into each amplifier segment along the array. When the required gain and the gain per unit length

are identified for separate EDF segments, we can achieve an EDF length arrangement of $2\times(IL_m + IL_x)$/(unit Gain). In addition, we can future optimize this length arrangement using simulation. Longer doped fibre can be placed at the front end, sharing the same pump and working as a preamplifier to compensate for part of the IL of the TDM group. An EDF fibre length of over 10 m provides us with a gain ranging from 15 to 25 dB.

4.5 Array performance

4.5.1 Output power discrepancy and output channel power

To summarize, the output performance from the designed array with 16 wavelengths, with the configuration shown in Figure 4.19, as a function of the pump power and signal power was characterized, due to the realities that pump powers and signal powers which can be launched into the array are limited by the commercial availability and interlink connection loss. The output power discrepancy between wavelengths and mean power per wavelength (i.e., mean value of the output signal power at each wavelength) as a function of the pump power, with the optimized lengths arrangement, is shown in Figure 4.23.

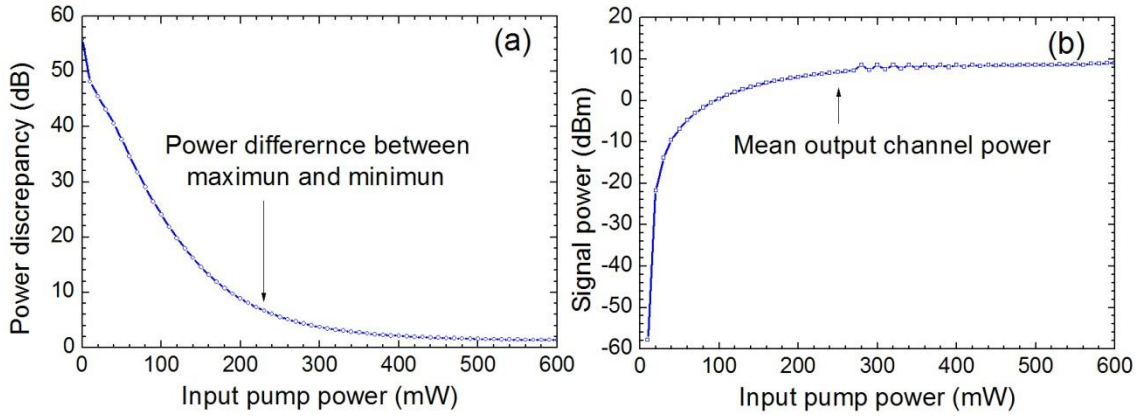

Figure 4.23: System output signal performance: (a) power discrepancy between wavelengths and (b) mean output signal power as a function of the input pump power for an array with 16 amplifiers in the return bus and 16 sensors per TDM group. Parameters are EDF 1 = 11.65 m, EDF 2 to11 = 0.7 m, EDF 12 to 13 = 1 m, EDF14 = 2 m, EDF 15 to 16 = 3 m, input signal peak optical power P_s = 22 dBm per wavelength, IL_x = 0.158 dB, IL_m = 0.5 dB, IL_{ad} = 1.2 dB.

It can be seen from Figure 4.23 that the optimized fibre lengths arrangement results in a discrepancy of less than 2 dB and a mean output channel power of 8 ~10 dBm, when the input pump power is larger than 400 mW. When pump power is smaller than 400 mW, the power

discrepancy between wavelengths deteriorates and the mean output power decreases with a decrease in the pump power.

We define a systematic parameter of *equivalent signal power* $P_{se} = P_s - IL_{TDM}$, the input signal power minus the insertion loss of the TDM group, indicating the signal power into the distributed EDFA. This parameter summarizes both of the changes in the launched signal power and the number of sensors in the TDM group. The output performance as a function of the equivalent signal power P_{se} is shown in Figure 4.24. Previous length optimization in VPI has shown that the optical performance can be improved by increasing the EDF lengths at the back of the array. Therefore Curve A and Curve B in Figure 4.24 show results with EDF length arrangements for IL_m of 0.3 dB and 0.5 dB, which are obtained from Table 4-1 (on Page 65), while curve C shows the results with the optimized length arrangement for IL_m of 0.5 dB. Parameters used in the simulation are shown in Table 4-2.

Table 4-2: Parameters in the array with a pre-amplifier segment

Curve	*IL_m (dB)*	*P_p (mW)*	*EDF 1 (m)*	*EDF 2 to 10 (m)*	*EDF 11 to 13 (m)*	*EDF14 (m)*	*EDF15 (m)*	*EDF16 (m)*
A	0.3	500	11.65	0.47	0.53	0.64	0.64	0.75
B	0.5	620	11.65	0.68	0.76	0.93	0.93	1.08
C	0.5	620	11.65	0.7	1	2	3	3

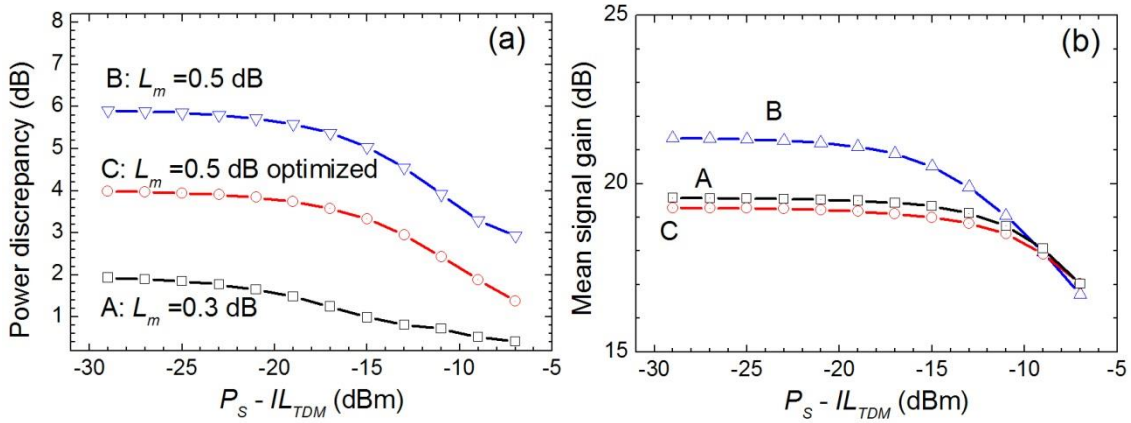

Figure 4.24: System output signal performance: (a) power discrepancy between wavelengths and (b) mean channel gain as a function of the equivalent signal power (P_s –IL_{TDM}) for an array with 16 amplifier stages on the return bus and 16 sensors per TDM group. Common parameters are input signal peak optical power P_s = 22 dBm per wavelength, IL_x = 0.15 dB, IL_{ad} = 1.2 dB.

It can be seen from curve A in the Figure 4.24 that the fibre length arrangement from Table 4-1 results in a power discrepancy between wavelengths of less than 2 dB and a mean output signal

gain of 19 dB, in the small signal region for IL_m of 0.3 dB, with a proper input pump power of 500 mW. The gain decreases as P_{es} increases. Curve B shows the performance for an IL_m of 0.5 dB, the optical power at back of the array drops, thus, resulting in a large discrepancy up to 6 dB. Because the backwards ASE from the pre-amplifier gets amplified on the return bus and arrives its maximum at the back of the array, longer EDF segments are needed at the back to provide efficient gain under limited pump power. Curve C shows the results with increased EDF lengths for EDF 11 to EDF 16. The optimized length arrangement provides us with uniform channel gain, and provides us with smaller discrepancy ranges from 1.4 dB to 4 dB.

4.5.2 Sensitivity of simulation results to EDF parameters

The accurate prediction of system performances (e.g., gain versus pump power and signal power, residual pump power) strongly depends upon knowledge of experimental parameters. I have adjusted the basic parameters of I4 in Chapter 3 by experimental validation. However, the validation was based on a sing stage EDFA with doped fibre lengths longer than 10 m, and the performance may vary in a distributed configuration with short lengths of doped fibre and excess pump power dissipation.

Therefore, the sensitivity of the system performances to variations in key parameters describing the system, which includes the EDF emission coefficient, absorption coefficient, up conversion coefficient and IL_m in the new amplified network with 16 stages, is investigated. The network configuration with parameters used for the simulation is illustrated in Figure 4.25. Previous adjusted parameters of the EDF fibre I4 in Table 3-2 are used for the simulation. The input signals are CW in the simulation, and I will show later in Chapter 6 that the amplification performances in the spectrum domain with CW light are the same as those with pulsed light. System performance metrics, including mean output power per wavelength, power discrepancy between wavelengths, residual pump power and OSNR (noise bandwidth of 0.1 nm) at the last channel with regards to these parameters when they are varied are shown in Table 4-3

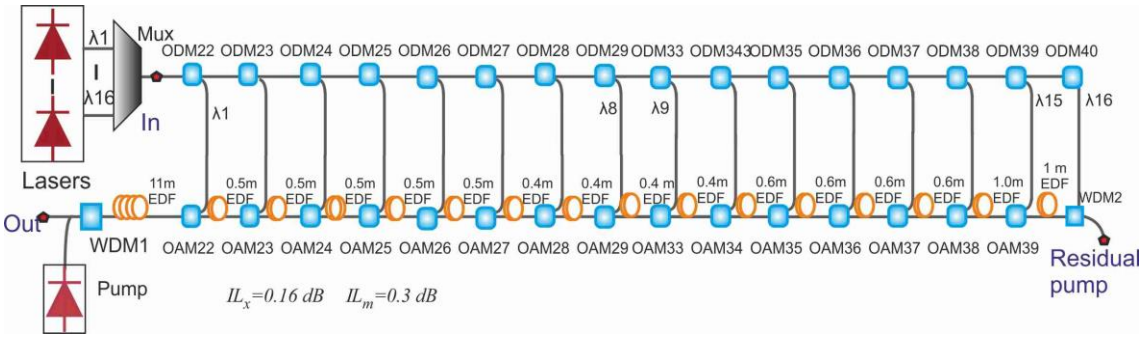

Figure 4.25: Array architecture to investigate the sensitivity of simulation results to system parameters. Pump power at 150 mW and input signal peak optical power of 22 dBm per wavelength.

Table 4-3: System sensitivity to EDF parameters

Parameters	*Changes*	*Output power (dBm)*	*Power discrepancy (dB)*	*Residual pump (mW)*	*OSNR (dB)*
Optimized values		1.92	1.17	13.34	27.73
Up conversion coefficient	ignored	2.2	1.57	13.8	27.86
	-10%	2.02	1.31	13.49	27.77
	+10%	1.82	1.03	13.17	27.67
Absorption coefficient	-10%	1.55	1.28	14.3	27.91
	+10%	2.19	1.07	12.59	27.56
Emission coefficient	-10%	0.82	1.31	15.35	28.18
	+10%	**3.08**	1.25	**10.63**	27.18
IL_m	+0.2 dB	-0.08	**5.39**	7.31	22.8
	+0.5 dB	-4.14	**15.81**	2.62	13.81

It can be seen from Table 4-3 that the system is less sensitive to the upconversion parameters and absorption parameters, 10% variation of them will not affect the pump and signal performances greatly; but the output power is sensitive to both the emission coefficient and insertion loss of the multiplexers, and 0.2 dB variance in IL_m (so as the IL_x)increases the power discrepancy between wavelengths significantly in this system, which shows that we need to choose the doped fibre lengths carefully according to the given multiplexer insertion loss and the achievable EDF-to-SMF splicing loss, and this was investigated in detail in the previous section of the distributed EDFA design.

4.5.3 Transient response of multiple amplification

4.5.3.1 Amplification in the pulsed region

In pulsed interferometric sensor systems, amplifiers operate in the pulse region. The transient effects related to the gain dynamics during the pulse duration may introduce gain variation and need to be considered. VPIphotonics can simulate the dynamic amplification process in EDFAs with input signal pulsed. Figure 4.26 illustrates the simulated output pulse pair in the time domain after multiple amplifications. It can be seen from the pulse shape that there is no power spike or over shoot observed at the leading and falling edges of the output signal pulse, with a pulse width of 100 ns. From reference [51], in EDFAs, transient effects of gain saturation and recovery typically occur on a 100 μs to 1 ms time scale, any periodic signal perturbation of frequency $B \gg 1/T_{sat}$ is of no effect on the medium inversion. Therefore, no transient effects of gain saturation and recovery occur in the pulsed interferometric sensor systems with pulse width of hundreds of nanoseconds. This will be verified by experimental measurement before and after the amplifier in Chapter 8.

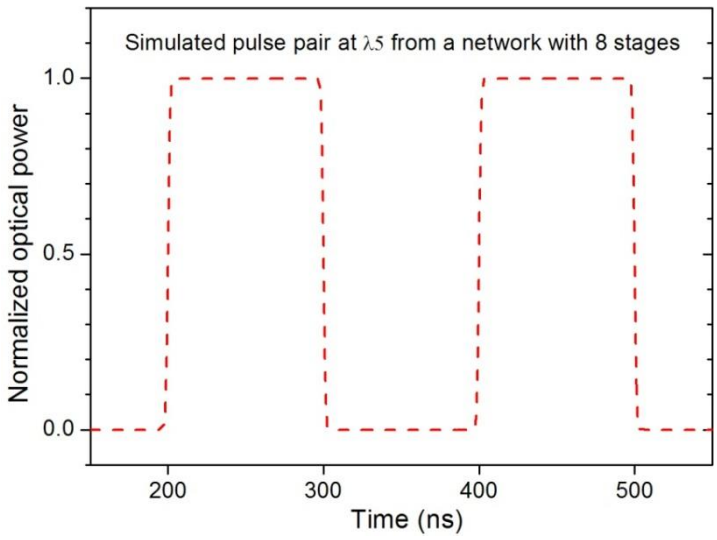

Figure 4.26: Simulated gain transient during the 100 ns pulse after multiple amplifications. The transient gain is small enough to be neglected.

4.5.3.2 Amplification performance when channel drops

In multichannel amplifier systems, in the event of either a wavelength channel being added or dropped (i.e., failure of any channel), the number of WDM signals traversing the amplifiers would change, and the power of surviving wavelengths would change and could give rise to surviving signal errors. This may be a practical problem where TDM groups are partially populated on some wavelengths.

In our application, when the pump power is sufficient enough to excite the ions, the input pulse duration is short and the average signal power is low, the signal will experience a steady small-signal gain during the pulse even when there is channel dropping. Therefore, I simulated the gain variance in a single stage EDFA with CW input signal power ranges from – 30 dBm to – 10 dBm, with two different pump powers of 200 mW and 400 mW. The simulated gain as a function of input signal power is demonstrated in Figure 4.27. With an increase in the total number of wavelengths in the network, the average signal power increases, and the EDFA gain is more sensitive to the number of wavelengths dropping and adding. However, it can be seen from the figure that the gain variance is less than 1 dB when the input signal is halved or doubled at 7 dBm. Therefore, the gain variance is sufficiently small to be ignored and this was experimentally demonstrated and measured. The results will be shown in Chapter 7.

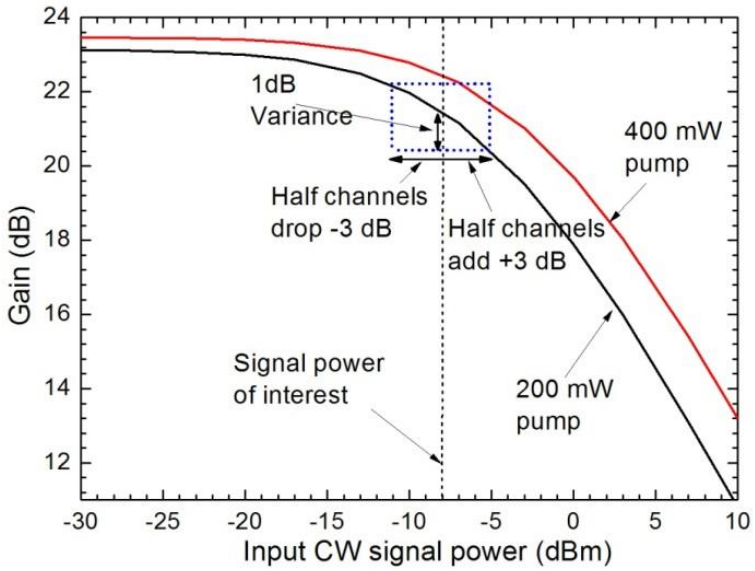

Figure 4.27: Gain as a function of input signal power for pump power of 200 mW and 400 mW in 12 metres of single stage EDFA.

To summarize, the system performance in the presence of system parameter variation in the new array with 16 wavelengths was investigated. Results show that knowledge of EDF emission parameters and proper EDF length arrangement are important to make accurate performance prediction and provide good system performance. Furthermore, simulation shows that providing sufficient pump power, low input signal power and short pulse duration, the transient responses during the pulse and gain variance in the presence of channel failing/adding is small enough to be ignored.

4.5.4 Optical signal noise ratio

Because of the presence of optical amplifiers, which add ASE power to the signal, the optical signal noise ratio (OSNR) with ASE power in the 0.1 nm bandwidth at the output of an amplified array deteriorates, compared to that in a non-amplified-network. OSNR, which can be observed from an OSA, provides us with a direct way to monitor the optical performance of the signal at the array output, without specifying particular optical powers, optical filter bandwidths, receiver bandwidths and receiver noise. The OSNR is given by

$$OSNR = \frac{P_s}{P_{ASE}} \tag{4.10}$$

For an input signal of P_{sin} to an amplifier with a gain of *G*, the amplifier output is

$$P_{sout} = P_{sin}G + P_{ASE} \tag{4.11}$$

Here, $P_{ASE} = 2n_{sp}hv(G-1)B_O$ and B_O is the optical bandwidth. $h = 6.63 \times 10^{-34} J.s$ is the Planck constant. The gain G here is the gain in each segment of SMF-EDF-SMF, which takes into account the two splicing losses of the EDF-to-SMF.

In the proposed array, as illustrated in Figure 4.28, the output signal power at each wavelength is given by

$$P_{sout} = P_{\sin}(IL_m)^{n-1}(L_{ad})(IL_s / M^2)IL_{ad}(G_i IL_m)^{n-1} \tag{4.12}$$

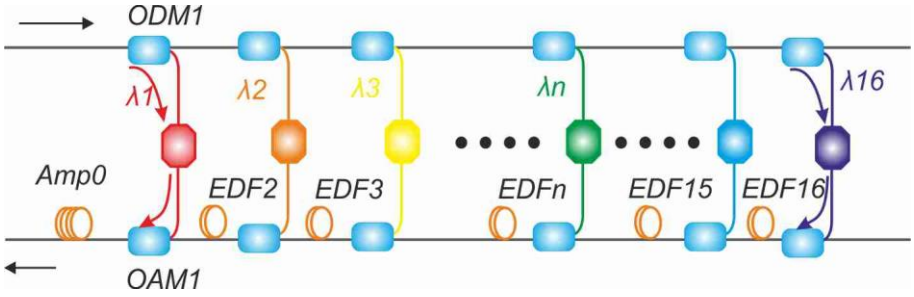

Figure 4.28: Illustration of ASE accumulation in the distributed amplified array

If the gain from the amplifier stages exactly compensate for the insertion loss from each OA/DM pair, we can get G_i= constant= G, and the signal experiences no net gain or loss as it propagates through the returning bus and only experiences a net gain at the pre-amplifier. But the ASE calculation is different. The ASE power produced at each amplifier segment in each optical bandwidth is

$$P_{ASEi} = 2n_{sp}hv\left(G_i - 1\right)B_O \tag{4.13}$$

Co-propagating with the signal, the forward ASE coupled into the next amplifier stage *m* is given by

$$P_{ASE_m} = P_{ASE_{m-1}}(IL\ G_i) + P_{ASEi} \tag{4.14}$$

In which IL_m is the insertion loss when the signal travels through the OAMs.

The *m*th OAM along the return bus provides advantages to remove the ASE power centred at its operating wavelength, which are produced and accumulated from back amplifier stages (*m*+1 to N). Figure 4.29 demonstrates the transmission and accumulation along the return bus (the 'band pass filter' effect and the simulated output optical spectrum can be found in Section 4.1: advantage of OA/DMs). It can be seen from the figure that the ASE power at the front wavelengths λ1 in the array is smaller than those at the back (far end) of the array, because the ASE power accumulated from amplifier segments at the back (EDF(n+1),… ,EDF N) are filtered out at the *n*th OAM, therefore, the signal at the last wavelength (λN) has the worst OSNR.

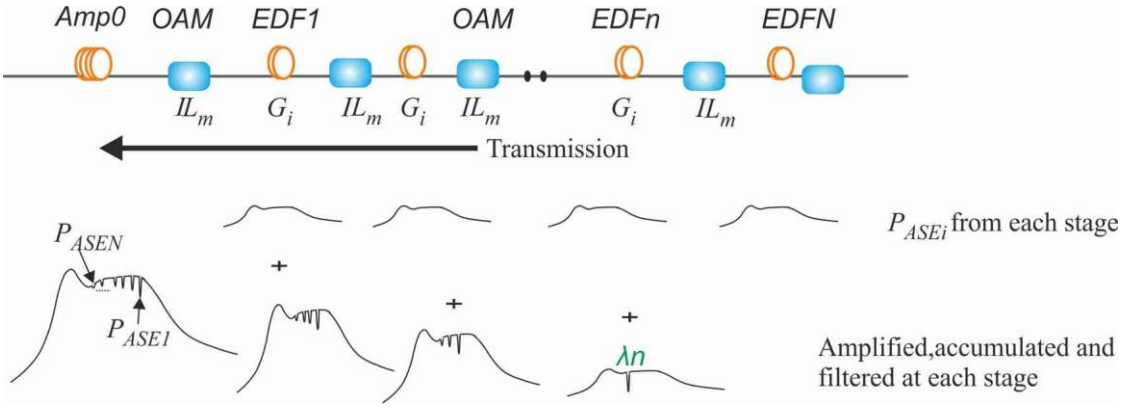

Figure 4.29: Transmission of the ASE power along the return bus.

With G_i= constant, the output ASE power centred at wavelength channel n > 2 is thus given by

$$\begin{aligned} P_{ASEn} &= P_{ASEi}[1 + (IL_m G_i) + \ldots + (IL_m G_i)^{n-2}]IL_m \\ &= P_{ASEi}\frac{[1-(IL_m G_i)^{n-1}]IL_m}{1-IL_m G_i} \end{aligned} \tag{4.15}$$

When there is a pre-amplifier segment along the bus, the amount of the signal power and ASE power at the output of the pre-amplifier centred at wavelength channel *n* becomes

$$P_{sout} = P_{\sin}(IL_m)^{n-1}(L_{ad})(IL_s / M^2)IL_{ad}(G_i IL_m)^{n-1}G_0 \tag{4.16}$$

$$P_{ASEn} = P_{ASEi}\frac{[1-(IL_m G_i)^{n-1}]IL_m}{1-(IL_m G_i)}G_0 + P_{ASE0} \tag{4.17}$$

Substitute the signal power and ASE power from equation (4.16) and (4.17) into equation(4.10), we obtain the $OSNR_n$ of the output signal from the pre-amplifier with B_o=0.1 nm.

$$OSNR_n = \frac{P_{\sin}(IL_m)^{n-1}(IL_{ad})(IL_s/M^2)IL_{ad}(G_iIL_m)^{n-1}G_0}{2n_{sp}hv(G_i-1)B_O\frac{[1-(IL_mG_i)^{n-1}]IL_m}{1-IL_mG_i}G_0+2n_{sp}hv(G_0-1)B_O} \xrightarrow{G_0-1\to G_0} \frac{P_{sin}IL_m^{2n-3}IL_{ad}^2(IL_s/M^2)G_i^{n-1}}{2n_{sp}hvB_O[(G_i-1)\frac{[1-(IL_mG_i)^{n-1}]}{1-IL_mG_i}+1]} \quad (4.18)$$

The expression shows that the channel OSNR increases with the input signal power level P_{sin}, and decreases with the number of sensors in each TDM group *M*, i.e., OSNR decreases with the *equivalent signal power* of $P_{se} = P_{sin}(IL_s/M^2)$. Figure 4.30 (a) illustrates the OSNR at the worst channel as a function of the *equivalent signal power* in the network with 16 amplifier stages, with given insertion loss value for each of the OA/DM pairs. Figure 4.30 (b) demonstrates the OSNR as a function of the number of sensors in each TDM group.

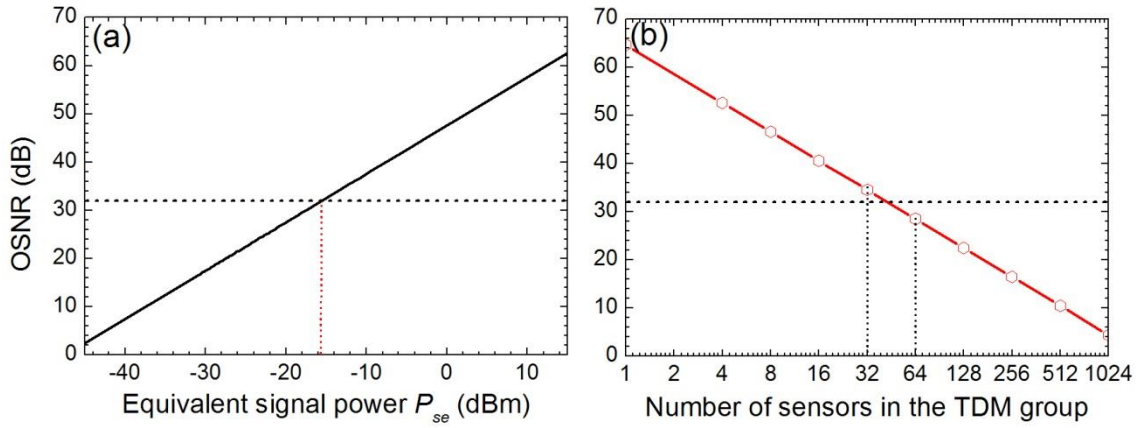

Figure 4.30: OSNR at the worst wavelength channel as a function of (a) the equivalent signal power of P_{se}=P_{sin} (IL_s/M^2) and (b) the number of sensors in each TDM group for an array with 16 amplifier stages on the return bus. Parameter values are, signal peak optical power P_{sin} = 22 dBm per wavelength, IL_s= 5 dB, n_{sp} = 1, IL_{ad} = 0.8 dB, IL_m = 0.25 dB, G_i = 0.9 dB. Input pump power selected such that enough power is incident on the last amplifier.

The OSNR decreases in proportion to an increase in M^2. For an allowed OSNR of 30 dB, 64 sensors can be addressed by each wavelength, resulting in a total number of 16×64 sensors integrated by one fibre pair. As stated previously, due to the long lifetime of the Er^{3+} transition, EDFAs operate on the average optical power in the distributed amplifier and not the peak optical power. When the array is fully occupied in the time domain (i.e., $D = 1/(M+1)$ as

discussed in the TDM group design part), the light on the return bus is approximately CW, thus the average signal power is equivalent to the peak optical power. The calculated OSNR as a function of array parameters in equation (4.18) can be used to predict the ASE-noise-limited phase sensitivity in a sensor system (will be discussed in Chapter 5).

4.5.5 System noise figure comparison with other configuration

In this section, without specifying particular optical powers, interrogation times, pulse widths, repetition rates, and the optical filtering needed to determine an absolute output signal to noise ratio (SNR), we use a *system noise figure* (NF) as defined in [2] for configuration comparison. The optical noise figure is the input source SNR divided by the output SNR for the worst sensor in the array. Assuming a shot noise limited input pulse, the input SNR is given by

$$SNR_{in} = \frac{|S_0|^2}{\sqrt{|S_0|^2}} = S_0 \tag{4.19}$$

where S_0 is the input photon count in the electronic integration time. Even with a post amplifier after the source, when the OSNR of the input signal is normally larger than 40 dB, the signal can still be considered as shot noise limited. While the signal output from an amplified array is no longer shot noise limited as from a non-amplified-network, but is signal-ASE beat noise limited.

The system noise figure is defined as

$$NF_{system} = \frac{SNR_{in}}{SNR_{out\ worst\ sensor}} = \frac{S_0}{SNR_{out\ worst\ sensor}} \tag{4.20}$$

This definition can be used to describe the whole system as an amplification-loss transmission. Let us now compare the NF in the presented configuration with previously reported configurations.

4.5.5.1 Passive-coupler TDM array

The SNR of the input and output signal in a passive coupler TDM array, as illustrated in Figure 2.10 (see page 17), are both shot noise limited. With the IL_x the excess loss due to splices and coupler insertion ,the system NF in an optimized passive array with n sensors is given by [2]

$$NF_{passsive-TDM} = \frac{(n-1)^{2n-2}}{IL_s IL_x^{2n-2}(n-2)^{2n-4}} \tag{4.21}$$

4.5.5.2 Amplifier-coupler TDM array

The optimized NF in an amplified TDM architecture, as illustrated in Figure 2.12(see page 18), is given by [2]

$$NF_{amplified-TDM} = \frac{j^2(1-C_r)(1-C_d)}{C_r C_d IL_s} + j[1-(1-C_d)L_x]i(i+1)n_{sp} + \frac{2j^2 IL_x i(1-C_d)[1-(1-C_r)IL_x]n_{sp}}{C_r C_d IL_s} \quad (4.22)$$

In which j is the number of sensors per subarray, and i denotes the number of subarrays, C_d is the coupling ratio for the distribution bus, and C_r is the coupling ratio for the return bus.

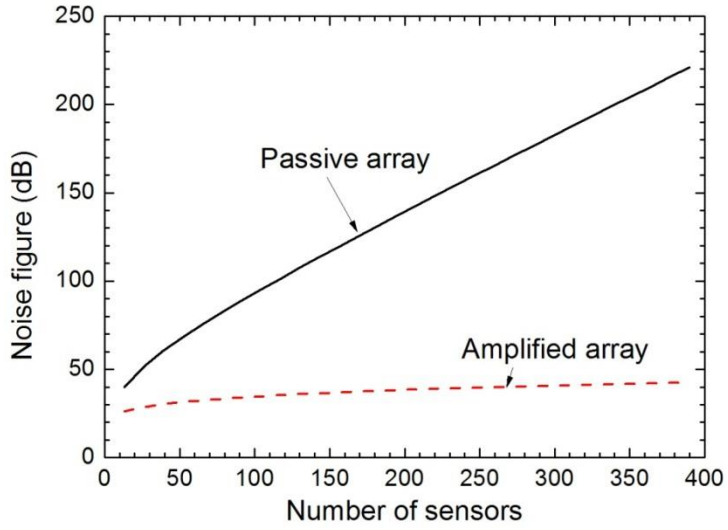

Figure 4.31: Noise figure versus total number of sensors for a passive array (solid curve) and an amplified array (dashed curve) in a system with architecture of the TDM ladder array.

Figure 4.31 demonstrates the comparisons between system NFs in the TDM array as a function of the number of sensors. The black curve indicates the NF in passive arrays, while the red dotted line denotes the system NF in amplified arrays. The figure illustrates the dramatic effect of sensor loss on the passive array and its negligible effect on the amplified arrays. The NF in an amplified array does not increase with an increase in the number of sensors up to 400 sensors, however, it becomes increasingly difficult to support more sensors beyond a total number of 300 approximately, limited by signal power level and channel power discrepancy [7].

4.5.5.3 Passive hybrid TDM/WDM array

In a passive TDM/WDM, as illustrated in Figure 2.7 (page 13), with N wavelengths and M sensors at each wavelength, the output signal at the last wavelength is

$$P_{sout} = \frac{P_{\sin} IL_m^{2(N-1)} IL_{ad}^2 IL_s}{M^2} \tag{4.23}$$

Both input and output SNR in a passive TDM/WDM are shot noise limited, thus we can write the system NF in a non-amplified TDM/WDM architecture as

$$NF_{passive\_TDM/WDM} = \frac{M^2}{IL_m^{2(N-1)} IL_{ad}^2 IL_s} \tag{4.24}$$

4.5.5.4 TDM/WDM array with a distributed amplifier

The output signal from the proposed array with a distributed amplifier is no longer shot noise limited, but signal to ASE beat noise limited, and the output SNR is given by

$$SNR = \frac{P_s^2}{\sqrt{P_s}^2 + 2P_s S_{ASE}} \tag{4.25}$$

in which $S_{ASE} = n_{sp} hv(G-1)$ is the ASE power per Hz in a single polarization state. The output signal from the array is

$$P_{sout} = P_{sin} IL_m{}^{N-1} IL_{ad} (IL_s / M^2) IL_{ad} G_i^{N-1} IL_m{}^{N-1} \tag{4.26}$$

Substitute the ASE power per Hz from equation (4.15) and (4.17) into equation(4.25), we can write the system NF as

$$NF = \frac{M^2}{IL_{ad}^2 IL_s} + \frac{2n_{sp} hv\left(1+IL_m\right)(1-IL_m{}^{N-1})M^2}{IL_{ad}^2 IL_s IL_m^N} \tag{4.27}$$

and for the array with a pre amplifier

$$NF' = \frac{M^2}{IL_{ad}^2 IL_s G_0} + \frac{2n_{sp} \mathrm{h}v\left(1+IL_m\right)(1-IL_m{}^{N-1})M^2}{IL_{ad}^2 IL_s IL_m^{N-1}} + \frac{2n_{sp} \mathrm{h}vM^2}{IL_{ad}^2 IL_s} \tag{4.28}$$

The excess loss from the sensors affects the system noise figure as the number of sensors increases. Figure 4.32 demonstrates the comparisons between the system NFs in the hybrid TDM/WDM array as a function of the total number of sensors. Black curves in these figures are NF in a non-amplified-TDM/WDM network, while the red dotted lines denote the system NF in amplified configurations. Figure (a), (b), and (c) illustrates the comparison with 16, 32 and 48 wavelengths, respectively. The right-Y axes show the SNR of the output signal.

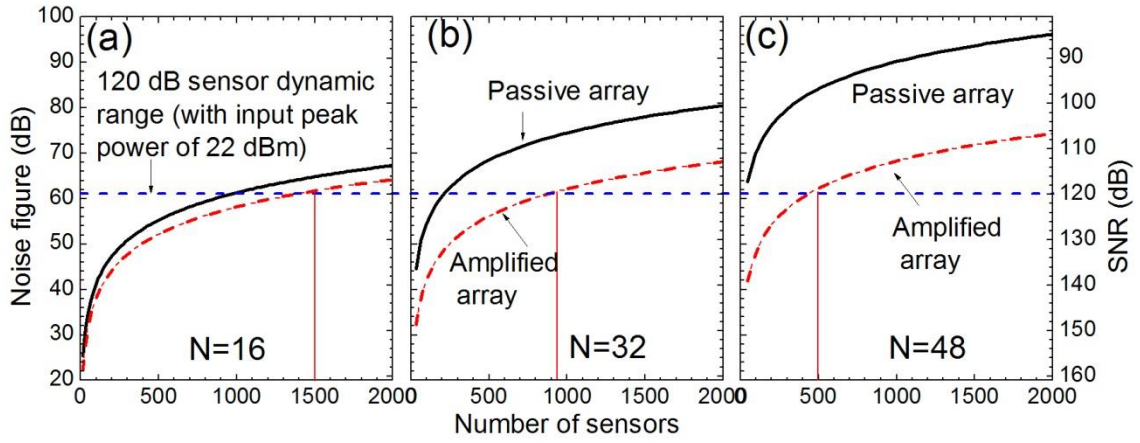

Figure 4.32: Noise figure versus the total number of sensors for passive array (solid curve) and amplified array (dashed curve) in system with architecture of the hybrid WDM/TDM array with (a) 16 wavelengths (b) 32 wavelengths and (c) 48 wavelengths.

These figures show that the system NF in a non-amplified array increases rapidly when the number of sensors increases, especially with larger N. The NF in an amplified array has a weaker dependence on the number of sensors, but also increases with an increase in N. Although the comparison between the three figures indicates that SNR improves as N is reduced from 48 to 32 and 16, for any number of sensors between 0 and 2000, one needs to be aware that these SNR values are achieved without considering the 'aliasing noise' from the TDM multiplexing, which will be discussed in detail in the following chapter. The increase in M introduces additional effects (aliasing noise) in TDM multiplexed systems. For the same total number of sensors, accompanied by a decrease in N, the TDM aliasing noise will increase linearly with an increase in the number of TDM sensors (M). On the other hand, as we have discussed in Chapter 2, the maximum number of sensors in a passive TDM group (M) is limited to 64. Therefore, simply reducing the number of wavelengths for a large array is not practical.

We can conclude from figure (a) and (b) with the right-Y axes that an amplified WDM/TDM array can support up to 1500 (close to $16 \times 64 = 1024, 32 \times 32 = 1024$) interferometric sensors in a distributed amplified network with 16/32 wavelengths, providing all sensors with an excellent SNR superior to 120 dB/√Hz, and the sensitivity of all sensors would be superior to 1 μrad/√Hz, with an input signal peak optical power of 22 dBm, which is better than any other existing arrays.

To conclude, the calculation and comparison between NF gave us a rough evaluation of the number of sensors and wavelengths that can be supported in the recommended network and shows significant improvements over other architectures.

4.6 Conclusions

This chapter summarized the principle required for the design of a distributed-amplified sensor array architecture. Quiet fibre laser sources with improved stability to temperature and external vibration are preferred in sensor systems. The optical power handling capacity is determined by nonlinear effects at the transmission length of the link fibre. MI is a very strong nonlinear process that limits the maximum peak optical power to ~160 mW along 50 km SMF 28e fibre, and the power will be reduced with an increasing of the fibre length. Wavelengths are preferred to be staggered in the time domain to avoid the deleterious effect of FWM. Pump diodes around 1480 nm are preferred, due to their low transmission loss. Pump power dissipation along the buses was discussed, which showed that pump power is commercially available for our application. Passive components with low insertion loss and a good fusion machine to produce good EDF-to-SMF splicing are recommended and are available to support the array. Design of the distributed amplifier requires optimization on the basis of the operating signal wavelength, input pump power, handling signal power and especially the gain coefficient of the active fibre and the insertion loss of the OA/DMs.

Signal performances of the designed architecture were characterized. Optimized length arrangements of the erbium doped fibre provided us with a power discrepancy from 1.4 dB to 4 dB between wavelengths, varies with the *equivalent signal power* of $P_{se} = P_s - IL_{TDM}$. The OSNR is found to be linear with the square value of the number of sensors in each TDM group, and it is better than 30 dB when the number of sensors is less than 64, which indicates that the recommended amplified architecture can support 64×16 sensors, with a sensor sensitivity not grossly affected by the ASE noise.

Comparison between the NF showed the advantages of the distributed amplified array over other architectures, and that the benefit increases as the number of wavelengths increases. With a total number of 1024 sensors in the architecture, the system noise figure remains less than 60 dB, and the sensitivity of all the sensors remains superior to 120 dB/√Hz (1 μrad/√Hz).

Chapter 5
Phase noise model for interferometric sensor systems

Overview: The interferometric phase sensitivity is the most important performance metric for a sensor system. This chapter presents an analytical approach to accurately model the phase sensitivity, and provide simple analytical formulae, useful in the design, comparison and optimization of interferometric fibre-optic sensor systems. The phase sensitivity model incorporates the various key noise contributions including receiver noise, ASE induced noise, active sources noise and other phase noise terms. We define and present a novel term '*Demod phase sensitivity*' to take into account the effects from noise aliasing in systems based on time division multiplexed (TDM) architectures. Experimental results from a derivative-approach based multiplexed amplified interferometric fibre sensor system confirm the appropriateness and accuracy of the phase sensitivity model. The approach is widely applicable but particularly appropriate for fibre-optic sensor systems using amplifiers and TDM. Furthermore, the system phase sensitivity and the maximum number in the new array are discussed based on the predictions from the phase sensitivity model. Results show that the recommended network can address up to 32×32 sensors with a system phase sensitivity of −90 dB re rad/√Hz, limited only by shot noise and receiver noise.

5.1 Phase signal demodulation

I start by considering the operational principle and the phase demodulation of pulsed interferometric sensor systems. A typical configuration is illustrated in Figure 5.1. The input light is pulsed, frequency-shifted and split into two fibres through a 50:50 fibre coupler. The two beams are reflected back into the same coupler by Faraday mirrors (FRM) where they are combined and interfere. The resulting beam in the up-lead fibre is then fed into the demodulator system where the measurand induced phase modulation on the signal arm is detected and demodulated.

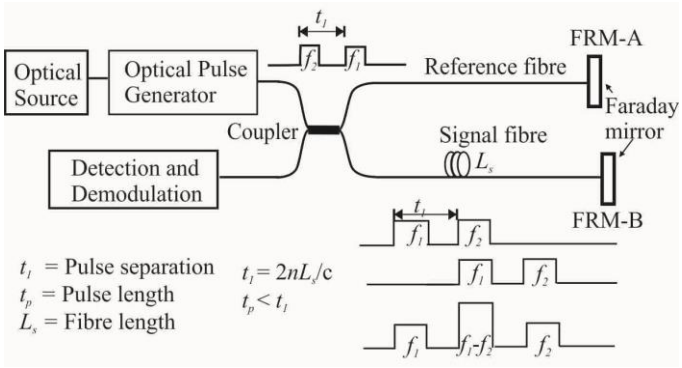

Figure 5.1: Pulsed fibre-optic Michelson interferometric sensor system configuration with time domain diagram.

The timing diagram of the pulses in the system is also shown in Figure 5.1. The interferometer sensor is interrogated with two optical pulses with frequencies of f_1 and f_2 separated in time by a period $t_1 = 2n_{eff}L_s/c$. Because the optical pulse separation is arranged to be twice the transit time of light through the sensor, the reflection of the first optical pulse from FRM-B arrives at the receiver at the same time as the reflection of the second optical pulse from FRM-A. The two reflections will therefore overlap at the receiver to produce a single pulse with a frequency equal to the frequency difference between the two pulses (at the carrier frequency $\omega_{IF} = 2\pi(f_1 - f_2)$), as shown in Figure 5.1. This pulse carries all the phase change information from the signal arm imposed as a phase modulation of the carrier frequency (because the first pulse has been through the coil twice and has been exposed to the seismic signal-induced phase change, whilst the second pulse has not).

The optical pulse train returned from the interferometric sensors will be converted into electrical pulses at the receiver. The photodiode signal for each equal launched optical pulse is

$$I = P_s R[1 + V\cos(\omega_{IF}t + \varphi(t))] \tag{5.1}$$

where V=1 is the visibility of the interferometer. R is the photodiode responsivity in A/W. P_s is the returned optical power and $\varphi(t)$ is the time-dependent phase signal of the interest.

The photodiode signal is sampled by an analogue to digital convertor (ADC), and then routed to a phase demodulation process based on the arctangent algorithm, which splits the digitized carrier signal into two streams; one is multiplied by $2\sin\omega_{IF}t$ and the other by $2\cos\omega_{IF}t$, to give the in-phase (I_I) and quadrature (I_Q) components:

$$\begin{aligned} I_I &= P_s R[\cos\varphi(t) + \cos(2\omega_{IF}t + \varphi(t))] \\ I_Q &= P_s R[\sin\varphi(t) + \sin(2\omega_{IF}t + \varphi(t))] \end{aligned} \tag{5.2}$$

The results of the mixing is low-pass filtered to provide the in-phase (I_I) signal proportional to $\cos\varphi(t)$ and the quadrature signal (I_Q) proportional to $\sin\varphi(t)$. The bandwidth of the low pass filter (LPF) is usually smaller than the intermediate frequency with $f_{LPF} < \omega_{IF}/2\pi$.

The measured phase $\varphi(t)$ is recovered from the arctangent of the ratio of the quadrature to the in-phase components where it is then unwrapped.

$$\tan\varphi(t) = \frac{\sin\varphi(t)}{\cos\varphi(t)} \tag{5.3}$$

Figure 5.2 shows a schematic of this process which is usually implemented digitally.

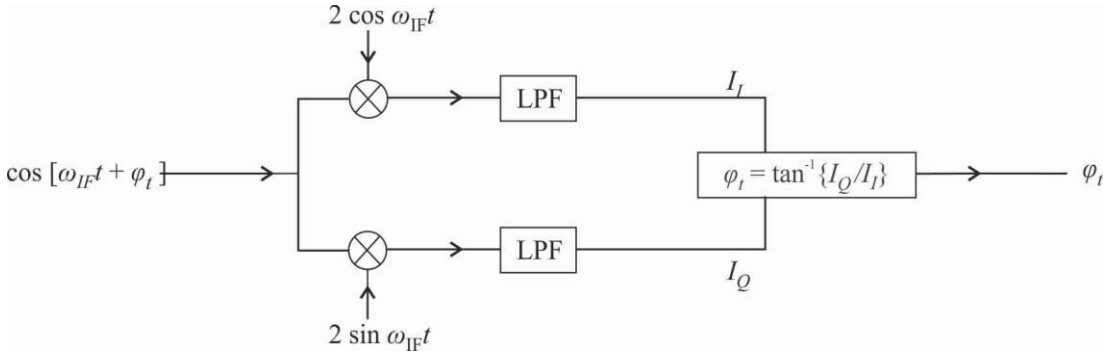

Figure 5.2: Schematic of the arctangent demodulation process for the pulsed heterodyne technique. LPF: low-pass filter.

5.2 Sensitivity of a single sensor

5.2.1 Demodulation of the phase signal with noise

To calculate the minimum detectable phase change, we note that the received signal from the pulsed heterodyne system with noise can be rewritten as

$$I = P_s R[1+\cos(\omega_{IF}t + \varphi(t) + n_\varphi(t))] + n_I(t) \tag{5.4}$$

Where $n_\varphi(t)$ is a phase noise term and $n_I(t)$ is the intensity noise contributions, in the arctangent demodulation process, the carrier signal is multiplied with $2\sin\omega_{IF}t$ and the other by $2\cos\omega_{IF}t$ (assumed noise free) to provide the in-phase and quadrature components:

$$\begin{aligned} I_I &= P_s R[\cos(\varphi(t)+n_\varphi(t)) + \cos(2\omega_{IF}t + \varphi(t) + n_\varphi(t))] + 2n_I\cos\omega_{IF}t \\ I_Q &= P_s R[\sin(\varphi(t)+n_\varphi(t)) + \sin(2\omega_{IF}t + \varphi(t) + n_\varphi(t))] + 2n_I\sin\omega_{IF}t \end{aligned} \tag{5.5}$$

After the LPF, the measured phase ψ with noise is given by

$$\tan\psi = \frac{\sin(\varphi(t)+n_{\varphi}(t))+N_s}{\cos(\varphi(t)+n_{\varphi}(t))+N_c} \tag{5.6}$$

where N_c and N_s are the intensity noises in the in-phase and quadrature parts with shifted noise spectrum centred at ω_{IF}.

$$\begin{aligned} N_s &= \sum \frac{n_I}{P_s R}\sin(\omega_n - \omega_{IF})t \\ N_c &= \sum \frac{n_I}{P_s R}\cos(\omega_n - \omega_{IF})t \end{aligned} \tag{5.7}$$

The total demodulated phase information $\psi = \varphi + \delta\varphi$, is given by

$$\psi = \tan^{-1}\left[\frac{\sin(\varphi(t)+n_{\varphi}(t))+N_s}{\cos(\varphi(t)+n_{\varphi}(t))+N_c}\right] \tag{5.8}$$

Let us now consider the phase noise and intensity noise, separately

1) When there is no intensity noise, (5.8) reduces to

$$\psi = \tan^{-1}\left[\frac{\sin(\varphi(t)+n_{\varphi}(t))}{\cos(\varphi(t)+n_{\varphi}(t))}\right] = \varphi(t)+n_{\varphi}(t) \tag{5.9}$$

This equation results in $\delta\varphi = n_{\varphi}(t)$, which shows the linear contribution from the phase noise to the demodulation signal.

2) When there is no phase noise, (5.8) reduces to

$$\tan\psi = \frac{\sin\varphi(t)+N_s}{\cos\varphi(t)+N_c} \tag{5.10}$$

For a sinusoidal modulating function $\varphi(t)$ equal to $\phi_0\cos\omega_m t$, using the Bessel functions and small angle approximations $\phi_0 \ll 1$, we obtain $J_0(\phi_0) \cong 1$ and $J_1(\phi_0) \cong \phi_0/2$, equation (5.10) can be re-expressed as,

$$\begin{aligned} \tan\psi &= \frac{\sin[\phi_0\cos\omega_m t]+N_s}{\cos[\phi_0\cos\omega_m t]+N_c} \\ &= \frac{-2\sum_{n=1}^{\infty}(-1)^n J_{2n-1}(\phi_0)\cos[(2n-1)\omega_m t]+N_s}{\{J_0(\phi_0)+2\sum_{n=1}^{\infty}(-1)^n J_{2n}(\phi_0)\cos(2n\omega_m t)\}+N_c} \\ &\approx \frac{\phi_0\cos\omega_m t+N_s}{1+N_c} \xrightarrow{N_c \ll 1} \phi_0\cos\omega_m t+N_s \end{aligned} \tag{5.11}$$

Consider the deduction of the phase information from equation (5.11) without N_s to be $\psi = \tan^{-1}(\varphi(t))$, we can achieve the differential of the demodulated phase ψ with respect to phase signal of interest φ as

$$\frac{\delta\psi}{\delta\varphi} = \frac{1}{1+\varphi^2} \tag{5.12}$$

Considering N_s to be the differential of φ, $N_s = \delta\varphi$, we then get

$$\delta\psi = \frac{1}{1+\varphi^2(t)} N_s \tag{5.13}$$

Use the previous approximations $\phi_0 \ll 1$, and substitute(5.7), the intensity noise is subsequently transformed into phase noise determined by the signal to noise ratio at the receiver

$$\delta\varphi(t) = N_s = \sum \frac{n_I \sin(\omega_n - \omega_{IF})t}{P_s R} \tag{5.14}$$

Therefore, the response between the optical phase modulation in the heterodyne signal and the intensity out of the interferometer is linearized by the demodulation operation. And the phase amplitude $\delta\varphi$ introduced by the intensity noises equals to the noise to carrier ratio [96]. The phase introduced by the intensity noise and phase noise, in μrad/$\sqrt{\text{Hz}}$ is given by

$$\delta\phi = \sqrt{\left[\frac{\langle n_I^2(t)\rangle}{(P_S R)^2} + \langle n_\varphi^2(t)\rangle\right]} \tag{5.15}$$

In which $\langle n_I^2 \rangle$ and $\langle n_\varphi^2 \rangle$ are the uncorrelated intensity noise power at the receiver and phase noise in 1 Hz bandwidth, and the total peak phase $\delta\phi_{peak}$ in dB re rad/$\sqrt{\text{Hz}}$ is given by

$$\delta\phi_{peak} = 20\lg\sqrt{2\left[\frac{\langle n_I^2(t)\rangle}{(P_S R)^2} + \langle n_\varphi^2(t)\rangle\right]} \tag{5.16}$$

5.2.2 Sources of noise in an interferometric fibre-optic sensor system

The noise power at the optical receiver is fundamentally limited by the signal shot noise (i.e., a quantum noise effect, related to the discreteness of photons and electrons). However, in practice, receiver trans-impedance introduces the resistor thermal noise; laser sources produce the intensity noise and frequency noise, and the RF generator employed to drive the acousto-optic modulator (i.e., pulse generator) produces the frequency noise.

5.2.2.1 Intensity noise at the receiver

We assume the signal power to the receiver is P_s, therefore the photon shot noise generated at the receiver is given by

$$\overline{i_{sh}^2} = 2e\overline{i(t)}B = 2eRP_sB \tag{5.17}$$

where B is the detection bandwidth, $e = 1.6 \times 10^{-19}$ coulombs is the electron charge.

Even when there is no optical signal at the receiver, there are several intrinsic forms of noise in the receiver, including contributions from the voltage noise V_{nv}, current noise V_{ni} and the resistor thermal noise V_{th} (also called as Johnson or Nyquist noise), the total noise at the optical receiver in the effective bandwidth can be computed from

$$V_{PINFET} = \sqrt{V_{nv}{}^2 + V_{ni}{}^2 + V_{th}{}^2} \tag{5.18}$$

in which $V_{th}^2 = 4\mathrm{k_B}TB_eR_f$ and $k_B = 1.38 \times 10^{-23}$ J/K is the Boltzmann's constant, T is an effective (absolute) temperature. According to the specification of a p-intrinsic-n, field-effect transistor (PINFET) optical receiver used in my experiments, the receiver trans-impedance $R_f = 40$ kΩ, and the total output noise voltage is 0.63 mV in the whole electrical bandwidth of $B_e = 120$ MHz, therefore the equivalent input current noise in bandwidth B can be expressed by

$$\sigma_{PINFET}^2 = \frac{V_{PINFET}^2 B}{R_f^2 B_e} \tag{5.19}$$

5.2.2.2 Frequency noise from fibre lasers

In an interferometric fibre sensor, the laser frequency noise is converted to phase noise by the interferometer and is proportional to the path imbalance in the interferometer. For a Mach-Zehnder interferometer, the phase difference between the two output arms of the interferometer is given by

$$\Delta\varphi = n_{eff}kd \tag{5.20}$$

where k is the free space wavenumber ($k = 2\pi/\lambda = 2\pi\nu/c$) and d is the fibre path-imbalance. Differentiating of φ with respect to the optical frequency υ yields

$$\delta\varphi = \frac{2\pi n_{eff}d}{c}\delta\nu \tag{5.21}$$

where $\delta\varphi$ and $\delta\nu$ are the phase and frequency noise, respectively. The laser frequency noise is expressed in unit of Hz/√Hz and μrad/√Hz (i.e., the phase noise produced in an interferometer with an imbalance of *d*).

In a sensor system, the laser frequency noise can be included by assuming that the interferometer time imbalance is the input pulse period. The phase noise amplitude, due to the laser frequency noise can be given by $\delta\varphi_{laser-freq}(f)$. In a practical system, the imbalance *d* is minimized by a path compensating unit or a referencing unit (see in Figure 2.8 and Figure A.1).

5.2.2.3 RIN from fibre lasers

The relative intensity noise (RIN) of a laser is defined as

$$\mathrm{RIN}(f)=\frac{S_{\delta P}(f)}{P^2} \tag{5.22}$$

where $S_{\delta P}(f)$ is the mean-square spectral density of the laser power fluctuation and *P* is the mean laser power. The relative intensity noise from a laser is equivalent to the amplitude modulation of the optical signal, causing the RIN spectrum to appear as amplitude modulation sidebands around the carrier. When two optical sources are optically combined together at the output of an interferometer, the expected RIN of the combined source can be given by

$$RIN_{Inter}(f)=\frac{S_{\delta P}(f)+S_{\delta P}(f)}{(P+P)^2}=\frac{S_{\delta P}}{2P^2} \tag{5.23}$$

Therefore the RIN will be reduced by 3 dB in an interferometer, and the equivalent noise contribution due to the RIN is thus,

$$\delta\varphi_{RIN}(f)=\sqrt{\frac{RIN(f)}{2}} \tag{5.24}$$

5.2.2.4 Noise from the RF generator

The RF generator introduces phase fluctuation when applying frequency modulation to the signal pulses. When the modulation sidebands are very small due to noise, i.e., if the phase deviation is much smaller than 1 rad, the spectral density of the phase fluctuation (phase noise) in $\mathrm{rad}^2/\mathrm{Hz}$ can be given by the approximation of $S_{\Delta\varphi}(f)=2\mathcal{L}(f)$, where $\mathcal{L}(f)$ is the single sideband noise (SSB) density (from Wikipedia). The spectral density of the resulting phase fluctuation from two locked oscillators is twice that associated with one oscillator, and can be

given by $S_{\Delta\varphi}(f)_{beat} = 2S_{\Delta\varphi}(f)$. Therefore the equivalent noise contribution due to the RF generator, in rad/√Hz, is given by,

$$\delta\varphi_{RF}(f) = \sqrt{4\mathcal{L}(f)} \tag{5.25}$$

5.2.3 Noises from optical amplifiers

EDFAs are incorporated in present interferometric sensors systems. In order to investigate the induced noise from optical amplifiers, firstly, I built a schematic of the beating process of the signal with ASE in an interferometer.

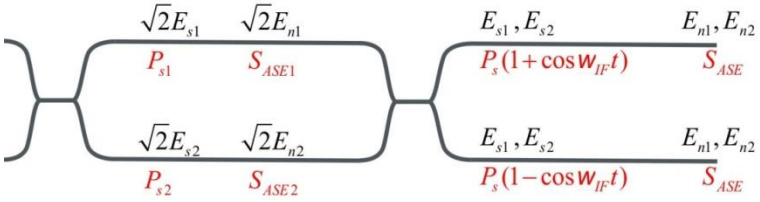

Figure 5.3: Schematic of the optical interference in an interferometer with amplifiers located before.

Figure 5.3 shows the schematic of the process, together with the defined expressions for the electrical field and optical power in each stage, for the signal and ASE, separately. The relationship between them can be expressed by

$$\begin{aligned} P_{s1} &= \frac{\left|\sqrt{2}E_{s1}(t)\right|^2}{2} = E_{s1}^2 \quad & S_{ASE1} &= \frac{\left|\sqrt{2}E_{n1}(t)\right|^2}{2} \\ P_{s2} &= \frac{\left|\sqrt{2}E_{s2}(t)\right|^2}{2} = E_{s2}^2 \quad & s_{ASE2} &= \frac{\left|\sqrt{2}E_{n2}(t)\right|^2}{2} \\ P_s &= \frac{E_{s1}^2 + E_{s2}^2}{2} & s_{ASE} &= \frac{E_{n1}^2 + E_{n2}^2}{2} \end{aligned} \tag{5.26}$$

In the above equations and schematic, $E_{s1,s2}$, $E_{n1,n2}$ are the electric field amplitudes of the signal and the ASE for optical pulses with frequencies f_1 and f_2, in two arms of the interferometer, and P_s is the mean optical power of the beating pulse at the interferometer output. $S_{ASE} = n_{sp}(G-1)hv$ is the ASE power in one polarization mode per bandwidth of $\delta v = 1$ Hz before the interferometer ,with G the gain at the optical frequency, h the Planck's constant, v the optical frequency, and N_{sp} the population inversion factor. For an ideal amplifier, N_{sp} is equal to 1, corresponding to complete inversion. However, in the usual case, the population inversion is partial and $n_{sp} > 1$. With coupling of 50:50 in the interferometer and equal launched powers, we can obtain $P_{s1} = P_{s2} = P_s$, and $S_{ASE1} = S_{ASE2} = S_{ASE}$.

5.2.3.1 ASE beat noise

In systems incorporating multiple amplifiers, the signal (S) to ASE beat noise, the ASE to ASE beat noise and the ASE shot noise at the receiver will contribute to the noise floor. The signal and noise field's amplitudes $E_{s1,s2}$, $E_{n1,n2}$ of the pulses with frequencies f_1 and f_2 incident on the detector from two arms of a compensating interferometer (see in Figure 2.8 and Figure A.1) before the receiver are first expressed as follows:

$$E_{s1,s2}(t)=E_{s1,s2}\cos(2\pi f_{1,2}t) \tag{5.27}$$

$$E_{n1,n2}(t)=\sum_{k=-M}^{M}E_{n1,n2}\cos[2\pi(f_{1,2}+j\delta\upsilon)t+\phi_k] \tag{5.28}$$

in which $M = B_O/2\delta\upsilon$ is an integral, and B_O is the optical bandwidth of the ASE. The total ASE field is assumed to be composed of superimposition of 2M independent radiation modes at optical frequencies $f_{1,2} + k\delta\upsilon$, with a random phase ϕ_k. Both fields are assumed to be in the same optical polarization. When the optical powers from the two arms are equal, we obtain $E_{s1} = E_{s2} = \sqrt{P_S}$ and $E_{n1} = E_{n2} = \sqrt{S_{ASE}}$. The instantaneous photocurrent $i(t)$ at the receiver is given by the relation:

$$i(t)=R[E_{s1}(t)+E_{s2}(t+t_1')+E_{n1}(t)+E_{n2}(t+t_1')]^2 \tag{5.29}$$

Substituting equation (5.27) and (5.28) into (5.29) yields:

$$\begin{aligned}
i(t)&=R\{E_{s1}\cos(2\pi f_1t)+E_{s2}\cos(2\pi f_2t+t_1')\\
&\quad+\sum_{i=-M}^{M}E_{n1}\cos[2\pi(f_1+i\delta\upsilon)t+\phi_i]+\sum_{j=-M}^{M}E_{n2}\cos[2\pi(f_2+j\delta\upsilon)(t+t_1')+\phi_j]\}^2\\
&=R[E_{s1}\cos(2\pi f_1t)+E_{s2}\cos\omega_2(t+t_1')]^2+2R[E_{s1}\cos(2\pi f_1t)+E_{s2}\cos(2\pi f_2(t+t_1'))]\\
&\bullet\{\sum_{i=-M}^{M}E_{n1}\cos[2\pi(f_1+i\delta\upsilon)t+\phi_i]+\sum_{j=-M}^{M}E_{n2}\cos[2\pi(f_2+j\delta\upsilon)(t+t_1')+\phi_j]\}\\
&\quad+R\{\sum_{i=-M}^{M}E_{n1}\cos[2\pi(f_1+i\delta\upsilon)t+\phi_i]+\sum_{j=-M}^{M}E_{n2}\cos[2\pi(f_2+j\delta\upsilon)(t+t_1')+\phi_j]\}^2
\end{aligned} \tag{5.30}$$

The first term in the above equation $i_s(t)$, corresponds to the heterodyne photocurrent from the signal. And the photocurrent of the heterodyne signal without ASE beat noise as

$$I=RP_s(1+\cos\omega_{IF}t) \tag{5.31}$$

in which $\omega_{IF} = 2\pi(f_1 - f_2)$. $I_{S\_DC} = R(E_{s1}^2 + E_{s2}^2)/2 = RP_s$.

The second and third terms correspond to the S-ASE beat noise and ASE-ASE beat noise, respectively, as illustrated in Figure 5.4.

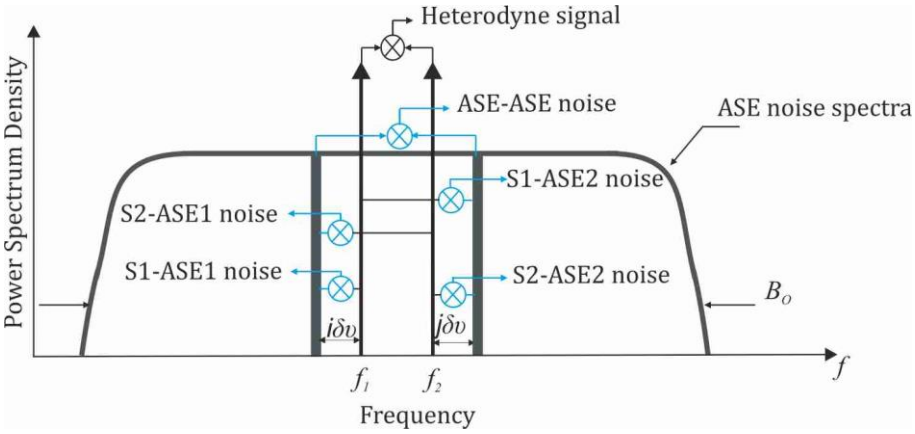

Figure 5.4: ASE to ASE beat noise and signal to ASE beat noise from mixing of the various spectral components at the receiver.

A detailed analysis of the different components is given in the Appendix B. It shows that the mean-square development $\langle i^2(t)\rangle$ of equation (5.30) yields S-ASE and ASE-ASE power spectral densities with the following expressions (Appendix B):

$$\sigma^2_{S-ASE}(f) = 8R^2 P_S S_{ASE} \tag{5.32}$$

$$\sigma^2_{ASE-ASE}(f) = 2R^2 S^2_{ASE} B_O \left(1+\frac{f}{B_O}\right)\left(1+\frac{\cos 2\pi f t_1'}{2}\right) \tag{5.33}$$

The S-ASE beat noise is uniform over the frequency interval $(0, B_o/2)$, while the ASE-ASE beat noise linearly decays with frequency to become zero at $f = B_o$.

When there is no polarizer used between the amplifier and the detector, there exist two ASE modes. The total ASE noise power injected at the receiver $P_{ASE} = 2S_{ASE}B_o$. The power spectral density due to the ASE noise at the receiver can be given by equation (5.34)

$$\sigma^2(f) = \sigma^2_{S-ASE}(f) + 2\sigma^2_{ASE-ASE}(f) \tag{5.34}$$

Within the electrical bandwidth of $B_e \ll B_O$, the power spectrum of the ASE to ASE noise can be approximated to be constant. Therefore, the total beat noise powers falling into the electronic bandwidth with ℵ polarization ASE modes are given by (Appendix B):

$$\sigma^2_{S-ASE} = 8R^2 P_S S_{ASE} B_e \tag{5.35}$$

$$\sigma^2_{ASE-ASE} = 2\aleph R^2 S^2_{ASE} B_e B_o \tag{5.36}$$

5.2.3.2 ASE shot noise

The mean photocurrent at the receiver is thus given by:

$$I_d = R(P_s + 2S_{ASE}B_o) \tag{5.37}$$

The shot noise at the receiver in the electrical bandwidth B_e is given by

$$\sigma_{shot}^2 = 2e(I_d + I_{dark})B_e \tag{5.38}$$

I_{dark} is only 0.5 nA for the Indium Galium Arsenide PIN photodiode, which can be ignored compared to the input optical signal range of -40 dBm to -15 dBm [97]. Therefore the signal and ASE shot noise are given by

$$\sigma_{shot}^2 = 2eR(P_s + \mathbb{N}S_{ASE}B_o)B_e \tag{5.39}$$

5.2.3.3 ASE induced phase noise

At the output of each amplifier, an ASE $E_{ASE}(t)\exp[i\phi_{ASE}(t)]$ with random, time varying amplitude $E_{ASE}(t)$ and phase $\phi_{ASE}(t)$ is added (coherent superposed) to the amplified signal field E_s^{out}. Classical treatment of this noise field as additive and Gaussian distribution is appropriate, since the energy per pulse greatly exceeds that of one photon. From the Phasor model in [51], as illustrated in Figure 5.5, the quadrature component E_2 produces an immediate phase shift, while the in-phase component of the ASE field E_1 alters the amplitude of the signal. Both these changes persist throughout the rest of the signal transmission; the amplitude change results in an additional nonlinear phase shift by the time the signal reaches the receiver, resulting from Kerr nonlinearity. Assuming that a number of signal photons are detected during the time of a single spontaneous photon emission event, with a random phase angle $-\pi < \phi < \pi$, the generated quadrature component E_2 produced signal phase deviation $\delta\phi(t)$ is given by

$$\tan(\delta\phi(t)) \approx \delta\phi(t) = \frac{E_{ASE}\sin(\phi_{ASE}(t))}{E_s^{out}} \tag{5.40}$$

Averaging over a large number of events, we obtain the standard phase deviation:

$$\delta\varphi_{ASE-PHASE} = \sqrt{\langle \delta\phi^2 \rangle} = \frac{1}{\sqrt{2}}\frac{E_{ASE}}{E_s^{out}} \tag{5.41}$$

in which $E_{ASE} = n_{sp}hv(G-1)B_s$ is the ASE power within the optical linewidth of the signal source, and B_s is the optical linewidth of the signal source. This noise only produces a phase deviation to the phase signal.

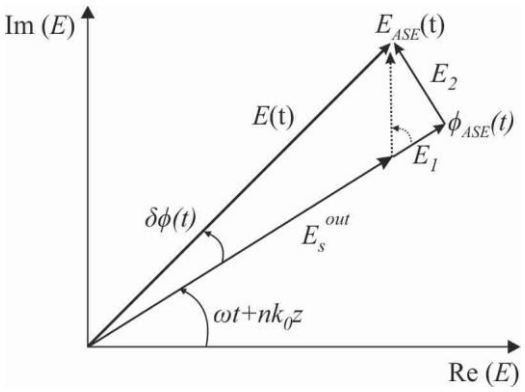

Figure 5.5: Phasor diagram for the ASE-induced phase noise.

5.2.3.4 Gorden-Mollenauer noise

Since the fibre's refractive index is dependent on the optical power through the Kerr effect, fluctuations in optical power, created by the ASE, give rise to phase fluctuations at the receiver. This phase noise, which increases with an increasing signal power, adds to the usual phase noise that the system would have if it were linear.

The intensity dependence of the refractive index leads to self-phase modulation (SPM) and cross-phase modulation (XPM) [51, 98], the variance of the phase fluctuations at the receiver produced by the amplitude fluctuations from the in-phase component E_1, along the line, which is called Gorden-Mollenauer noise can be given by

$$\delta\varphi_{G-M} = 2\times\frac{5}{6}\times\frac{2\pi n_2 L_{eff}}{\lambda A_{eff}}\delta P \tag{5.42}$$

in which n_2 is the nonlinearity refractive index, and usually ranges from 2.2 to 3.9×10^{-20} m^2/W for silica fibre. L_{eff} is the effective interaction length and A_{eff} is the effective area. Note that the Gorden-Mollenauer noise is always referred to as a nonlinear phase shift along the fibre.

5.2.4 Sensitivity of the sensor

The overall phase sensitivity of the sensor is given by the square root of the sum of the squares of each noise source as discussed above, assuming the noise sources are statically uncorrelated. Then the phase noise in a sensor system can be calculated in two categories: 1) the intensity noise induced phase noise and 2) the noise in the phase domain. From the analysis above and allowing for the existence of two ASE modes with single-mode EDFAs if no polarizer is used between the EDFA and the detector, we can express the total phase sensitivity from equation (5.15) as

$$\delta\varphi = \sqrt{\frac{\sigma_{shot}^2 + \sigma_{S-ASE}^2 + \sigma_{ASE-ASE}^2 + \sigma_{PINFET}^2}{(P_S R)^2} + \delta^2\varphi_{laser-freq} + \delta^2\varphi_{laser-RIN} + \delta^2\varphi_{RF} + \delta^2\varphi_{ASE-PHASE} + \delta^2\varphi_{G-M}} \quad (5.43)$$

Since the OSNR can be achieved by measuring the amplified optical spectrum of the returning optical signals to the receiver, I have deduced the ASE power related phase noise contributions as a function of the OSNR of the optical signal entering the receiver. Table 5-1 demonstrates the amplitude of contributions from different sources of noise to the phase sensitivity in a typical system (characterization of the laser and RF generator will be shown later). The third column simplified the expressions to functions of the OSNR in dB and P_s in dBm, with common values of: $B_{OSNR} = 0.1$ nm, $B_O = 0.4$ nm, $B_e = 120$ MHz, $R_f = 40$ kΩ, $L_{eff} = 1$ km, $B_s = 5$ kHz, $V_{PINFET} = 0.63$ mV, $R = 0.95$ A/W. The last column gives typical noise values when OSNR = 32 dB and $P_s = -20$ dBm into the receiver.

Table 5-1: Contributions of different sources of noise to the sensitivity of the sensor.

Noise contributions	*Expression*	*Expression in dBrad/√Hz*	*Noise at 1kHz μrad/√Hz*
$\boldsymbol{\delta\varphi_{shot-s}}$	$\sqrt{2eB/(P_S R)}$	$-154.7 - P_s$	0.18
$\boldsymbol{\delta\varphi_{shot-ASE}}$	$\sqrt{2e2S_{ASE}B_o/(RP_s^2)}$	$-148.7 - P_s - OSNR$	0.009
$\boldsymbol{\delta\varphi_{S-ASE}}$	$\sqrt{8S_{ASE}/P_S}$	$-95 - OSNR$	0.45
$\boldsymbol{\delta\varphi_{ASE-ASE}}$	$\sqrt{4S_{ASE}^2 B_o/P_s^2}$	$-95 - 2OSNR$	0.01
$\boldsymbol{\delta\varphi_{receiver}}$	$\sqrt{V_{PINFET}^2/(P_s^2 R^2 R_f^2 B_e)}$	$-176.4 - 2P_s$	0.15
$\boldsymbol{\delta\varphi_{laser-freq}}$	$\delta\varphi_{laser-freq}(f) n_{eff} d$	-80 with d = 40 m	95(< 2)
$\boldsymbol{\delta\varphi_{laser-RIN}}$	$\sqrt{RIN(f)/2}$	-129	0.35
$\boldsymbol{\delta\varphi_{RF}}$	$\sqrt{4\mathcal{L}(f)}$	−114 at 1 kHz	2
$\boldsymbol{\delta\varphi_{G-M}}$	$\sqrt{P_{ASE}B_s/(2P_s)}$	$-70 - OSNR$	0
$\boldsymbol{\delta\varphi_{ASE-XPM}}$	$\sqrt{7.2L_{eff}^2 S_{ASE}^2}$	$-233 + 2P_s - 2OSNR$	0
Total			95(<2) for n_{eff}d= 60(1) m

The comparison between different sources of noise indicates that laser frequency noise, due to the tens of metres of path imbalance of the interferometer, dominates the sensitivity of the sensors. There are methods to reduce this disadvantage. One common method is to use a path balance unit at the laser output when the light is pulsed and frequency shifted [99]. In such a unit, the output of one of the OAMs is delayed relative to the other by a time equal to twice the

transmit time of the sensor fibre, and driving them with a sinewave of the appropriate frequency, the two optical pulses are generated. This method has the advantage of reducing the effective path imbalance in each of the sensor interferometers to below 1 m. That reduces the impact of laser frequency noise on the overall system noise, since the two pulses are generated from the same segment of light. Another method to remove certain elements of the system noise (including the laser frequency noise and interrogator pickup) makes use of a reference sensor. This is usually a seismically insensitive fibre coil, located within the array, which is interrogated in the same way as other sensor coils in the system. However, because of the way the reference sensor coil is mechanically packaged, it will not pick up any seismic signal, but will pick up system generated noise. If the demodulated output from the reference sensor is then subtracted from the sensor output, the system noise is effectively subtracted also.

When the effective path imbalance in each of the sensor interferometers is reduced to below 1 m, the contribution from the laser frequency noise is mainly eliminated, and the sensitivity of the sensor is dominated by the relative intensity noise from the laser and the RF generator to below 2 μrad/√Hz, as illustrated in the last column in Table 5-1. I also investigated the dependence of the phase sensitivity on the signal power and the OSNR, as illustrated in Figure 5.6. It can be seen from the figures that both curves are flat when the OSNR is larger than 40 dB in figure (a) and when the signal power is larger than −25 dBm in figure (b). After these two critical values, the signal to ASE beat noise and the shot noise at the receiver start to dominate and deteriorate the phase sensitivity.

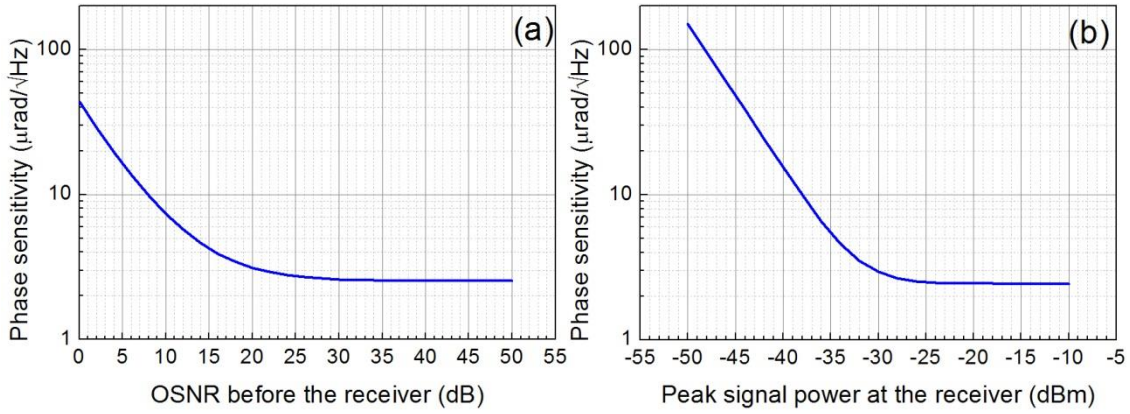

Figure 5.6: Predicted phase sensitivity of a single sensor as a function of (a) the OSNR and (b) the signal power, both with laser frequency noise reduced.

To conclude, the phase sensitivity of a single sensor is dominated by the laser frequency noise, due to the tens of metres of path imbalance in the interferometer, and the intensity noise from the laser and the RF generator follows. The laser frequency noise can be reduced using a

balance or referencing unit, and it is important to keep the OSNR better than 40 dB to avoid the deterioration from the S-ASE beat noise.

5.3 Demod phase sensitivity from TDM based sensor systems

Now that I have demonstrated the 'pure' sensitivity of a single sensor within an interferometric system incorporating optical amplifiers, I then investigate the phase sensitivity in multiplexed sensor systems. Part of the analysis is from the published paper [100].

5.3.1 Noise aliasing in TDM-based systems

Noise aliasing of high frequency components is one of the common issues associated with all TDM architectures [16, 101]. Let us start with the noise aliasing effect in TDM-based sensor systems. TDM architectures inherently sample each sensor at the interrogation repetition rate that depends on the number of TDM sensors and the length of fibre per sensor. This has several consequences, the first of which is an inherent bandwidth limitation for the sensor signal to occupy. In the receiver, it is important to retain the shape of the returned TDM pulse stream. The pulses will broaden and produce crosstalk with one another if there is excessive filtering in the electronics. The bandwidth requirement to maintain the pulse shapes is roughly equal to the reciprocal of the optical interrogation pulse width. Therefore anti-aliasing filters cannot be used prior to digitization to eliminate the high frequency phase noise. As a result, the high frequency phase noise components can be aliased to produce excess noise in the baseband spectrum which can limit the sensor sensitivity [16, 101].

The demodulation system samples the signal at the pulse repetition rate with $f_s = f_{rep}$. If the high frequency noise is up to the electrical bandwidth of the receiver $B_e \gg f_s/2$, the Nyquist sampling condition is not satisfied, adjacent copies overlap, and any frequency component above $f_s/2$ is indistinguishable from a lower-frequency component, called an alias, associated with one of the copies, as illustrated in Figure 5.7.

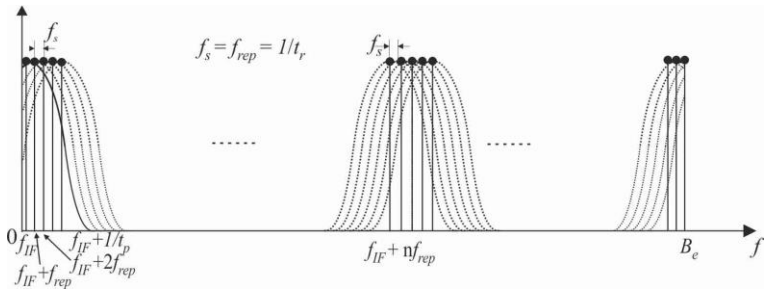

Figure 5.7: Noise aliasing in a TDM system.

The aliased noise determines the system's final performance. When the high frequency noise is white, the aliased high frequency components are directly related to the number of sampling times in the electrical bandwidth, and we can easily define an *effective aliasing parameter* in the demodulation process as

$$B_a = \frac{2B_e}{f_{rep}} \tag{5.44}$$

However, many of the noise sources, such as the laser frequency noise and intensity noise, along with the RF generator noise, are frequency dependent. The aliasing parameter B_a for these sources cannot be treated simply as a constant. Therefore, we introduce the '*Demod phase sensitivity*' for TDM-based systems to identify the noise aliasing from various noise sources.

5.3.2 Demod phase sensitivity in TDM-based systems

The effect of noise aliasing can be assessed by accumulating the noise at frequencies centred at harmonics of f_s from the specified noise spectrum $\delta\varphi_{\mathrm{k}}(f)$. To account for the noise aliasing effect in TDM multiplexed architectures, we introduce the '*Demod phase sensitivity*' to characterize the phase sensitivity after demodulation in a sensor system. For a given electrical detection bandwidth of B_e and a pulse repetition rate of f_s, the effect of noise aliasing at a signal frequency of f_m is given by

$$\delta\varphi_{\mathrm{Demod}} = q\sqrt{\sum_k \left[2 \sum_{p=0}^{(B_e - f_e - f_m)/F_s} \delta\varphi_k^2(f_e + f_m + pf_s) \right]} \tag{5.45}$$

in which q represents the contribution from the subtraction operation in the demodulation, q = 1 for normal signals of which no subtraction process is involved in the demodulation, and q = √2 for normal referenced signals and derivative signals (see Appendix A). k stands for the subscript of different noise sources, including shot, receiver, S-ASE, ASE-ASE, RIN, RF, laser frequency noise and ASE-XPM. f_e denotes the effective starting frequency to be aliased at various signals for different sources of noise. It is determined by the interrogation configuration. Most of the sources exhibit white noise properties except for the frequency noises from the laser and the RF generator [15], therefore, the 'Demod phase sensitivity' can be simplified to

$$\delta\varphi_{\mathrm{Demod}} = \frac{2B_e\mu}{F_s}\sqrt{\sum_k \delta\varphi_k^2(f_m)}. \tag{5.46}$$

The term 'Demod phase sensitivity' provides an effective way of comparing the performance of various interferometric fibre-optic based sensor systems, combining the noise contributions from both the array architecture and the interrogation technology employed.

5.4 Validation of the phase noise model

Now that we have developed a phase noise model for TDM multiplexed interferometric sensor systems incorporating optical amplifiers, based on the following parameters:

1) Heterodyne signal power P_s,
2) Accumulated ASE power spectral density S_{ASE} in one polarization mode per unit bandwidth,
3) Power spectral density of the frequency noise of the laser,
4) Power spectral density of the relative intensity noise of the laser,
5) RF generator SSB noise,
6) Receiver noise,
7) System sampling rate f_s,
8) Receiver electrical bandwidth of the receiver B_e.

I can go further to show the utilization of the developed model to predict the phase sensitivity in a specific derivative-approach based interferometric experimental sensor system.

5.4.1 Characteristics in the Derivative-approach based experimental system

Some applications require very a large dynamic range (i.e. >> ~120 dB) at low frequencies. These generate signals that induce phase modulations that exceed the bandwidth of the interferometric phase measurement method. To overcome this, a technique is implemented that measures the rate of change of the phase, thus greatly reducing the bandwidth at low frequencies required for the induced phase modulation. This operates by tracking the phase changes between successive optical samples. We developed the TDM group (4C sensor package) based on a derivative-approach based system, with its optical operation and interrogation timing arrangement as shown in Appendix A. There are three kinds of phases after signal demodulation in the derivative-approach based system:

1) Normal signals, i.e., Ch2, Ch4, Ch6, which represents all the noise contributions in the system.

2) Normal referenced signals, i.e., (Ch2 − Ch8), (Ch4 − Ch8), and (Ch6 − Ch8), in which certain systematic noise are reduced because the last coil only picks up system generated noise, which can be considered as a reference sensor coil.
3) Derivative signals, i.e., (Ch3 − Ch1), (Ch5 − Ch3), and (Ch7 − Ch5), in which certain systematic noises are reduced by subtraction. The amplitude of the phase change is frequency dependent.

The frequency noise spectrum of one of the Rock Single Frequency Narrow Linewidth Fibre Laser Modules (from NP Photonics) used in our systems was measured using a 26 meters imbalanced interferometer with homodyne detection (same frequency) [102]. The result is plotted in Figure 5.8, together with the phase noise normalized to 1 metre of optical path imbalance from a Mach-Zehnder interferometer.

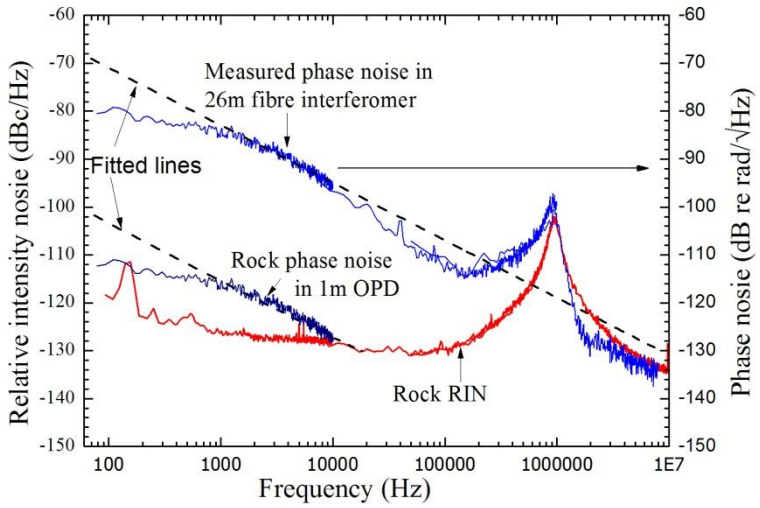

Figure 5.8: Measured frequency noise and relative intensity noise of the Rock laser used in the experiment.

There exists a peak around 1 MHz in the noise spectrum, which comes from the relative intensity noise of the laser. Previous work has shown that the frequency noise of a distributed Bragg reflector (DBR) Rock laser was found to exhibit a linear relationship for frequencies up 1 MHz, and the power spectrum of the frequency noise $\delta\nu(f)$ for fibre lasers has two components, a frequency independent component C due to spontaneous emission and a component K due to $1/f$ noise [103].

$$\delta\varphi_{laser-freq}(f)=\frac{K}{f^{n}}+\frac{C}{P} \tag{5.47}$$

Therefore, I plotted linear lines to fit the measured and normalized frequency noise of the laser, as shown in Figure 5.8. The phase noise amplitude, in rad/$\sqrt{\text{Hz}}$, due to the laser frequency noise thus can be expressed as,

$$\delta\varphi_{laser-freq} = (115\times10^{-6} f^{-0.6} + 5\times10^{-11})\times n_{eff} d \tag{5.48}$$

The measured RIN of the laser is also shown in Figure 5.8, and is −126.3 dBc/Hz around 1 kHz. The measured laser RIN shows a relaxation frequency around 1 MHz and is shot-noise limited elsewhere. The property of low phase noise and low RIN level makes the Rock laser an ideal laser source for our application.

The RF generator characterized in the study is the 400 MHz programmable signal source from Novatech (Model 440A). With the given phase noise at specified offset, I have fitted its single sideband noise density spectrum, as shown in Figure 5.9. The spectrum indicates a phase noise of −120 dBc/Hz around 1kHz.

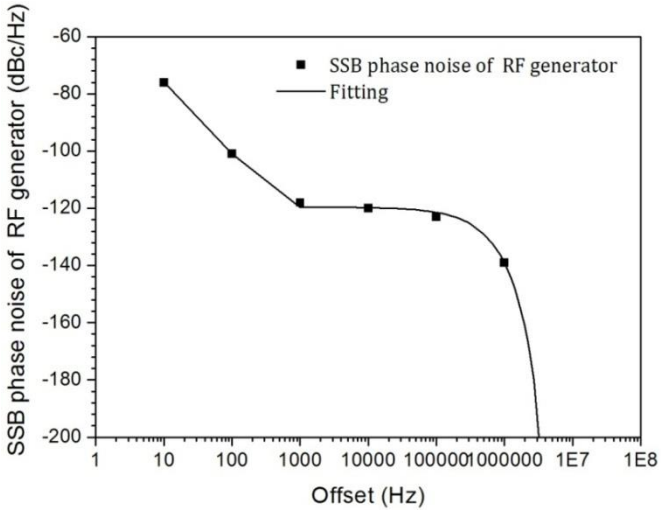

Figure 5.9: Fitted SSB phase noise spectrum of the RF generator.

Figure 5.10 summarizes all the potential noise sources in this system, and illustrates their noise components from 10 Hz to 100 MHz. The ASE related noise are taken from (5.32) and (5.33), with an OSNR of 30 dB, and a received signal power of −20 dBm.

The measured laser frequency noise was characterized in an interferometer with a delay length of 40 m, the same as the sensor imbalance length, and dominates over all other noise sources, ultimately limiting the phase sensitivity in such systems. However, there are methods to reduce this disadvantage (was discussed in Section 5.2.4). The measured laser RIN dominates the receiver noise, shot noise and signal to ASE beat noise. The ASE-ASE intensity noise exhibits an oscillating structure with a period determined by the delay length of the compensating

interferometer. The ASE phase noise is only a phase shift so can be ignored, along with the ASE-XPM noise, when the transmission distance is less than 1 km.

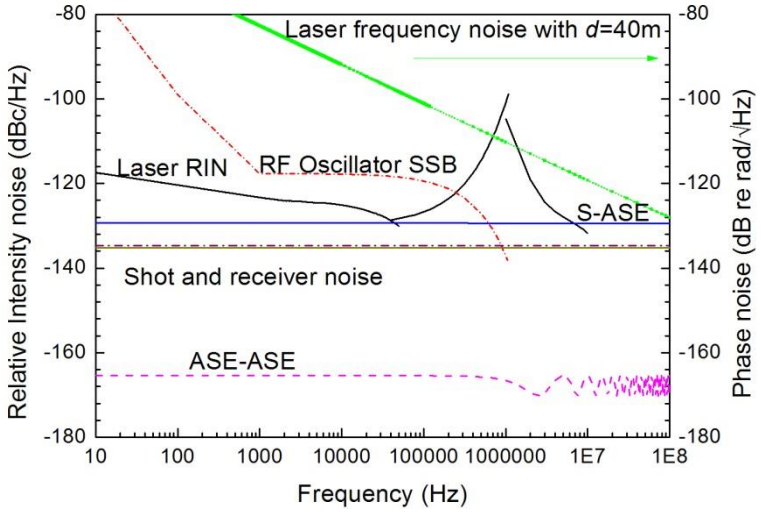

Figure 5.10: Fitted noise spectrum of various sources for phase noise prediction.

5.4.2 Calculation of the Demod phase sensitivity in the derivative system

The *Demod phase sensitivity* for the normal signal, the normal referenced signal and the derivative signal can be derived from equation(5.45). In equation (5.45), the noise aliasing from the various noise sources that need to be incorporated to calculate the *Demod phase sensitivity* varies according to the characteristics of their noise spectra. These are determined by detailed numerical calculations of the accumulated noise for each sampling period within their effective electrical bandwidths, supplemented with detailed measurements that allow us to determine the noise properties of these individual sources, as illustrated in Figure 5.10.

The contribution from various noise sources to the *Demod phase sensitivity* also depends on the demodulation of the phase signal. There are two differences in which the *Demod phase sensitivity* for the normal signal, normal referenced signal and derivative signal are calculated from equation (13). Firstly, the subtraction process used to obtain the normal referenced signal and the derivative signal introduces q =√2, which doubles the total noise. However, secondly, although the subtraction process doubles the white noise sources it also eliminates the 1/f noise sources. The laser frequency noise in the Rock laser is dominated by 1/f noise components up to 100 kHz to 1 MHz, while the measured phase noise at high frequency is usually dominated by laser RIN. Therefore, the subtraction process significantly reduces the produced dominant laser frequency noise, by increasing the starting frequency f_e from DC to 1 MHz for the laser frequency noise source, as shown in Table 5.2, such that, most of the aliasing noise components

from the laser frequency noise are eliminated for the normal referenced signal and the derivative signal.

Table 5-2: Starting frequency to be aliased.

f_e	*Normal signal*	*Normal referenced signal*	*Derivative signal*
$\boldsymbol{\delta\varphi_{laser-RIN}, \delta\varphi_{S-ASE}, \delta\varphi_{ASE-ASE}, \delta\varphi_{shot-s,} \delta\varphi_{receiver}}$	0	0	0
$\boldsymbol{\delta\varphi_{laser-freq,} \delta\varphi_{RF}}$	0	f_e	f_e

To facilitate the calculation of the *Demod phase sensitivity*, I reorganize the aliasing parameter from equation (5.44) by normalizing the aliased components to its 'basic' contribution at the signal frequency f_m. This versatile expression for the aliasing parameter is given by

$$B_{\mathrm{ak}} = \frac{\sqrt{2\sum_{p=0}^{(B_e - f_e - f_m)/F_s} \delta\varphi_k^2(f_e + f_m + pf_s)}}{\delta\varphi_k(f_m)} \tag{5.49}$$

Now that we have achieved the noise spectra for all the sources, and it is ready to calculate the B_{ak} and the *Demod phase sensitivity* for different signals in the derivative-approach based system. The parameter terms used for the prediction are illustrated in Table 5-3, and the peak Demod phase sensitivities around 1 kHz in the unit of dB re rad/√Hz at different channels are predicted in Table 5.4, 5.5 and 5.6, together with the amplitude from each source in μrad/√Hz, and their effective aliased bandwidths.

Table 5-3: Definition of terms in the derivative-approach based system.

Symbol	*Value*	*Unit*	*Description*
B_e	120	MHz	Electrical bandwidth at the receiver
R	0.95	A/W	Photodiode responsivity
f_s	200	kHz	Sampling ratio of the pulse
t_1'	200	ns	Pulse separation in the derivative approach
B_O	0.4	nm	Optical bandwidth of the ASE
B_{OSNR}	0.1	nm	Optical bandwidth for the OSNR calculation
B_S	5	kHz	Optical linewidth of the fibre lasers
P_S	−20	dBm	Peak optical power for the signal to the receiver
OSNR	40	dB	Peak OSNR for the signal to the receiver
V_{PINFET}	0.63	mV	Noise voltage in the receiver
R_f	40	kΩ	Receiver trans-impedance
$\delta\phi_{laser-freq}$	1.6	μrad	Laser frequency noise at 1 kHz in 1-m OPD
d	40	m	Fibre length imbalance in the interferometer
$\delta\phi_{laser-RIN}$	−126	dBc/$\sqrt{\text{Hz}}$	Laser RIN at 1 kHz
$\delta\phi_{RF}$	−120	dBc/$\sqrt{\text{Hz}}$	RF generator SSB at 1 kHz
f_e		Hz	1 kHz for $\boldsymbol{\delta\varphi_{RF}}$,1 MHz for $\boldsymbol{\delta\varphi_{laser-freq}}$

Table 5-4: Demod phase sensitivity for normal signal Ch2, Ch4, Ch6, Ch8.

Noise contribution	*Noise*	B_{ak}	*r*	**Demod phase sensitivity**
$\boldsymbol{\delta\varphi_{shot-s}}$	0.18	1200	1	6.4
$\boldsymbol{\delta\varphi_{S-ASE}}$	0.45	1200	1	6.2
$\boldsymbol{\delta\varphi_{receiver}}$	0.15	1200	1	5.2
$\boldsymbol{\delta\varphi_{laser-RIN}}$	0.35	970	1	11
$\boldsymbol{\delta\varphi_{shot-ASE}}$	0.01	1200	1	0.1
$\boldsymbol{\delta\varphi_{ASE-ASE}}$	0.01	1200	1	0.1
$\boldsymbol{\delta\varphi_{laser-freq}}$	95.1	2.1	1	138
$\boldsymbol{\delta\varphi_{RF}}$	2	7.7	1	5.5
Total	95.1			138
Peak in dB re rad/$\sqrt{\text{Hz}}$	−77.4			**−74.2**

Table 5-5: Demod phase sensitivity for normal referenced signal (Ch2/4/6−Ch8).

Noise contribution	*Noise*	B_{ak}	*r*	**Demod phase sensitivity**
$\boldsymbol{\delta\varphi_{shot-s}}$	0.18	1200	√2	9
$\boldsymbol{\delta\varphi_{S-ASE}}$	0.45	1200	√2	8.8
$\boldsymbol{\delta\varphi_{receiver}}$	0.15	1200	√2	7.4
$\boldsymbol{\delta\varphi_{laser-RIN}}$	0.35	970	√2	15.6
$\boldsymbol{\delta\varphi_{shot-ASE}}$	0.01	1200	√2	0.2
$\boldsymbol{\delta\varphi_{SASE-ASE}}$	0.01	1200	√2	0.1
$\boldsymbol{\delta\varphi_{laser-freq}}$	<1	0.09	√2	0.09
$\boldsymbol{\delta\varphi_{RF}}$	2	3.5	√2	5.3
Total				21.4
Peak in dB re rad/√Hz				**–90.4**

Table 5-6: Demod phase sensitivity for derivative signal (Ch3−Ch1), (Ch5−Ch3), (Ch7−Ch5).

Noise contribution	*Noise*	B_{ak}	*r*	**Demod phase sensitivity**
$\boldsymbol{\delta\varphi_{shot-s}}$	0.18	1200	√2	9
$\boldsymbol{\delta\varphi_{S-ASE}}$	0.45	1200	√2	8.8
$\boldsymbol{\delta\varphi_{receiver}}$	0.15	1200	√2	7.4
$\boldsymbol{\delta\varphi_{laser-RIN}}$	0.35	970	√2	15.6
$\boldsymbol{\delta\varphi_{shot-ASE}}$	0.01	1200	√2	0.2
$\boldsymbol{\delta\varphi_{SASE-ASE}}$	0.01	1200	√2	0.1
$\boldsymbol{\delta\varphi_{laser-freq}}$	<1	0.09	√2	0.09
$\boldsymbol{\delta\varphi_{RF}}$	2	3.5	√2	5.3
Total				21.4
Peak in dB re rad/√Hz				**–90.4**

The predicted peak *Demod phase sensitivity* in the interferometric sensor system are −74.2, −90.4 and−90.4 dB re rad/√Hz for the normal signal, normal referenced signal and derivative signal, respectively. It can be seen from Table 5-4 that the phase noise for the normal signals are dominated by the aliased laser frequency noise, while in the normal referenced channels, 1/f components in laser frequency noise among low frequency range are referenced out in Table 5-5 and Table 5-6. The reference sensor coil based approach shows significant improvement in reducing systematic noise. This leads to a phase noise floor of −90.4 dB re rad/√Hz, only limited by the intensity noises produced at the receiver (receiver noise, shot noise and laser RIN). The *Demod phase sensitivity* is given with an ideal OSNR of 40 dB, and an ideal input signal power to the receiver of −20 dBm.

Subtractions between different points within the system are used to obtain derivative signals, so that system noise components including optical power variations and vibrational pickup along the cable are mitigated. The derivative signals therefore give a much more 'lab friendly' method for measuring and comparing the system noise, because they are essentially insensitive to audio frequency acoustic pickup. In our application and experimental setups, I will use the *Demod phase sensitivity* of the derivative signal to characterize the noise floor and system sensitivity; In the crosstalk investigation, I will use the signal from the normal channels, for the applied signal will be much more distinguishable.

In systems incorporating amplifiers, the *Demod phase sensitivity* is limited by the ASE beat noise, which can be illustrated by the dependence of the phase sensitivity on the system OSNR. To further investigate the phase sensitivity in a sensor system based on the distributed amplified system, I investigated the dependence of the *Demod phase sensitivity* on the OSNR and the signal power, for the derivative signal, as illustrated in Figure 5.11.

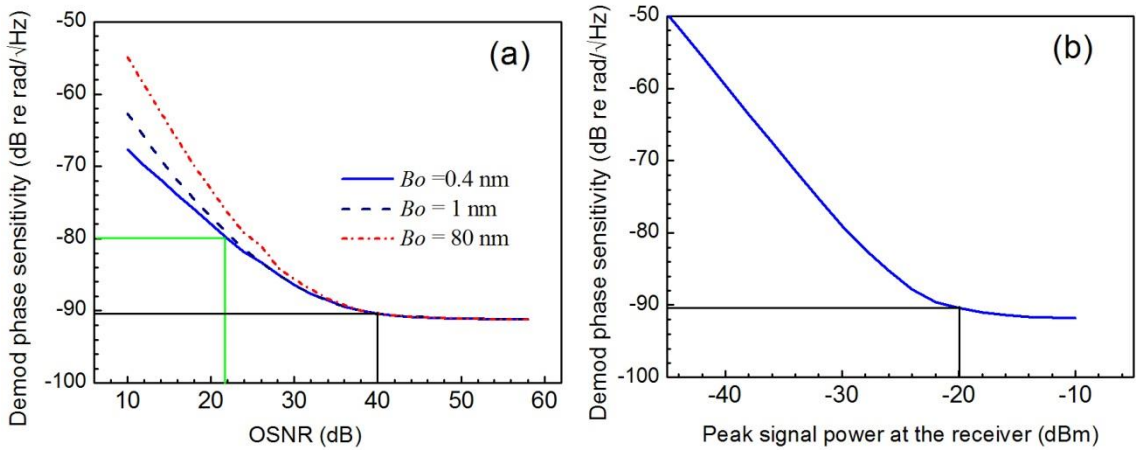

Figure 5.11: Predicted Demod phase sensitivity of derivative signal from TDM sensor arrays as a function of (a) the OSNR and (b) the signal power.

Figure 5.11 (a) shows the *Demod phase sensitivity* as a function of the OSNR when the received optical bandwidth of the ASE spectrum is 0.4 nm, 1 nm and 80 nm, separately. The *Demod phase sensitivity* is dominated by the shot noise and the receiver noise, when the peak OSNR of the signal is better than 40 dB. As the OSNR decreases, S to ASE beat noise starts to dominate, thus the sensitivity deteriorates. The OSNR should never drop below 21 dB to obtain an acceptable phase noise floor of −80 dB re rad/√Hz.

A proper optical filter to reduce the ASE bandwidth is important to mitigate the dominant ASE beat noise. When the ASE is small, i.e. with OSNR larger than 30 dB, the ASE to ASE beat noise is small enough to be ignored, and there is no improvement observed from the optical

filter. However, when the OSNR is smaller than 30 dB, without an optical filter, the ASE power within the whole optical bandwidth will be launched into the receiver, and an effective ASE bandwidth of 80 nm can be assumed, by normalizing the whole ASE bandwidth of the erbium ions gain spectrum to the ASE gain at 1550 nm, then the phase sensitivity deteriorates fast and significantly with a decrease in the OSNR. However, the difference between the sensitivities with ASE bandwidths of 0.4 nm and 1 nm is small.

The *Demod phase sensitivity* as a function of the signal power is shown in Figure 5.11 (b), which indicates that an injected signal power of larger than −20 dBm is required to avoid the domination of the signal-shot noise over the receiver noise.

5.4.3 Comparison with experimental results

To validate the phase sensitivity model, I have also compared the predicted *Demod phase sensitivities* for the normal signal and derivative signal with measured results. The test results are achieved from experimental setups based on the new array configured in Figure 6.1 and Figure 7.4 in the following chapters. The experimental data is obtained by averaging the measured phase noise values over the frequency range of 300 Hz to 1 kHz for the derivative signal and 2 to 4 kHz for the normal signal, since it is deteriorated by environmental noise at low frequencies. The system *Demod phase sensitivity* as a function of the signal OSNR to the receiver is shown in Figure 5.12. The points show the test results and the curve indicates the calculated results from equation(5.45), for both of the normal signal and the derivative signal. The measured values are in good agreement with the theoretical prediction.

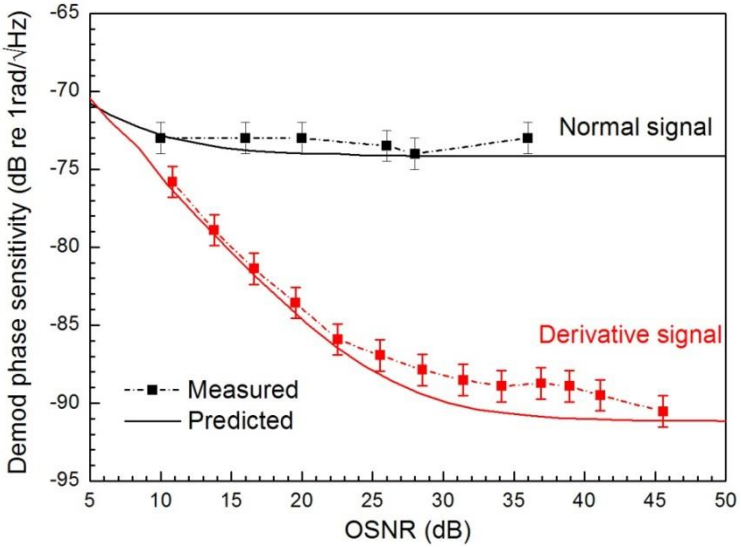

Figure 5.12: Comparison between the measured and predicted Demod peak phase sensitivity as a function of the average OSNR (D=–6.6 dB).

It can also be seen from the figure that the phase sensitivity in the normal channel is dominated by the laser frequency noise, thus, it remains independent of the OSNR when the average OSNR is larger than 15 dB (as is often the case). For the derivative signal, when the OSNR is better than 40 dB, the ASE beat noise can be ignored compared to the laser RIN. A system noise floor of −91 dB re rad/√Hz was measured. The system noise is dominated by laser RIN and shot noise and thus is very sensitive to the injected optical power level at the receiver, so the measured value ranges from −88 to −91 dB re rad/√Hz, which is 1 to 3 dB higher than the predicted ideal values.

5.5 Maximum number of sensors in the proposed network

I have now modelled the sensor sensitivity in the interferometric sensor systems incorporating amplifiers, and have also investigated the *Demod phase sensitivity* in amplified TDM sensor systems. In Chapter 4, I have analysed the optical performance from the presented distributed amplified sensor network, and have also predicted the OSNR as a function of the number of sensors. It is now possible to predict the system phase sensitivity in such systems and declare the maximum number of sensors it can support.

The total number of sensors in the designed new array can be increased by increasing the number of sensors in each TDM group and the number of wavelength channels. However, the number of sensors in each TDM group cannot be increased indefinitely, for two reasons. Firstly, because of the amplifier stages employed in the array, the S to ASE beat noise contributes to the system noise floor. In a small-signal regime, due to the high population inversion, a low noise figure is obtained and the generated ASE noise can be ignored. However, as the insertion loss (IL) of the TDM group is increased, a higher gain is required and a lower input signal is injected at the EDFA input. Consequently, ASE builds up rapidly and starts to saturate the EDFA, giving rise to signal-ASE beat noise which ultimately becomes the dominant noise source, increasing the system noise floor as the number of sensors per wavelength is increased.

The first five columns in Table 5-7 demonstrated the relationship between the number of sensors in each TDM group, the IL, the deduced OSNR and the sensitivity of each sensor in the distributed amplified network. The IL of one sensor IL_s was assumed to be 5 dB, increasing by 6 dB for every doubling of the number of sensors in the TDM group, as is consistent with current sensor technology. The value of 6 dB accounts for the insertion loss of the return of light across an additional 50:50 coupler. Assuming the returned optical signal from the TDM group is fully occupied in the time domain by interleaving the pulse returns from different sensors in the

group, i.e., the number of the sensors is the reciprocal of the duty cycle of the input pulse, and then the returned average optical power equals the pulse peak optical power. When a peak optical power of 22 dBm per wavelength is launched into a fully-loaded system in which a TDM group is included between each ODM/OAM pair, the optical power to the distributed amplifier can be found. With a given power to the amplifier, we can deduce the OSNR at the amplifier output, from Figure 4.30. Therefore, we can further predict the phase sensitivity of a single sensor from Figure 5.11. These columns show that the sensor sensitivity remains at the same level when the number of sensors increases from one to 64, with the phase sensitivity less than 2 μrad/√Hz, only limited by the shot noise and the receiver noise, similar to the performance of a non-amplified network. They also show that the system can support up to 256 sensors per wavelength with the phase sensitivity less than 10 μrad/√Hz, which is far superior to the reported phase sensitivity of ~100 μrad/√Hz in a passive TDM/DWDM array with 384 sensors [27].

Table 5-7: Sensitivity of sensors in the amplified sensor array.

Number of sensors M	*IL (dB)*	*Ps (dBm)*	*OSNR (dB)*	*Sensitivity (μrad/√Hz)*	*Pulse width (ns)*	*Repetition period $1/f_{rep}$(us)*	B_{ak}	*Demod phase sensitivity*
1	5	17	64	0.6				−125
4	17	5	52	0.6	100	5	1200	−94
16	29	−7	40	0.7	100	5	1200	−93
32	35	−13	34	0.9	50	5	1200	**−90**
64	41	−19	28	***1.5***	25	5	1200	−86
128	47	−25	22	3	25	10	2400	−77
256	53	−31	16	4	25	20	4800	−71
512	59	−37	10	7.3	25	40	9600	−63

Secondly, in TDM architectures, for a given pulse-width, the phase noise observed on each sensor increases with an increasing number of sensors in each TDM group, because the bandwidth available for each sensor decreases. As discussed previously, 1/f frequency noise from the laser and the RF generator can be reduced on the derivative signal, and the remaining noise sources are white, except for the RIN noise. The effective aliasing parameter for the remaining noise components can be approximated by (refer to equation(4.2))

$$B_{ak} = \frac{2B_e}{f_{rep}} \propto B_e L_s (M+1) \tag{5.50}$$

The *Demod phase noise* increases with the number of sensors in each TDM group. The predicted *Demod phase sensitivity* in Table 5-7 covers both contributions from the increasing ASE noise induced phase noise and the aliased high frequency noise components. In the last four columns, I provide a feasible combination of the pulse width and the sampling period to interrogate all the sensors in the TDM groups, together with the effective aliasing parameter B_{ak} for white noise sources, and predict the *Demod phase sensitivity* in dB re rad/√Hz in a sensor interrogation system based on the derivative-approach. The electrical bandwidth of the receiver is 120 MHz. The sensitivity remains at the same level when the number of sensors increases from 1 to 32, with a *Demod phase sensitivity* around −90 dB re rad/√Hz. It can be seen from the table that the phase noise floor is increased to −77 dB re rad/√Hz when the number of sensors is increased to 128 per wavelength, and this is still in the system acceptance range for many applications.

From previous analysis, with dual pump sources of 2×400 mW, the new array can support at least 32 channels of wavelengths. Therefore, the design can address up to 32×32 sensors with a phase sensitivity limited only by the noise from the lasers. The maximum number of sensors can be increase to 128×32 with a perfectly acceptable phase sensitivity for many applications of −77 dB re rad/√Hz, even with a decreased sampling rate. It is to be appreciated that increasing the number of sensors per wavelength means decreasing the duty cycle in the time domain. Bandwidth limitations and added aliased high frequency noise in the TDM architecture ultimately limit the highest level of multiplexing possible, even with a suitably adjusted sampling rate.

5.6 Conclusion

In conclusion, we have developed an analytical method to accurately predict the phase sensitivity of interferometric fibre-optic based sensor systems. The model covers all the potential phase noise sources and requires knowledge of the OSNR, laser frequency noise, laser intensity noise, intrinsic noise in the receiver and RF generator noise. This model also introduces the term '*Demod phase sensitivity*' to quantify the effect of noise aliasing from high frequency noise components. The aliasing effect is found to be determined by the interrogation repetition rate and it varies according to the noise source spectra. The most interesting result of the modelling is that the best *Demod phase sensitivity* can be achieved in our interrogation system with the new array is −91 dB re rad/√Hz, only limited by the laser RIN, the shot noise

and the receiver noise, and it deteriorates with an increase in the ASE noise. The phase noise model was validated by experimental results.

The *Demod phase sensitivity* as a function of the number of TDM multiplexed sensors was also discussed. The recommended architecture design can address up to 32×32 sensors with a perfect *Demod phase sensitivity* of −90 dB re rad/√Hz, limited only by the shot noise and the receiver noise. The number of sensors can be further increased to 128×32 by using dual pumps, providing an acceptable phase sensitivity for many applications of −77 dB re rad/√Hz, even with a decreased sampling rate.

To the best of our knowledge, this is the first time of a full analytical description of the phase sensitivity in interferometric sensor systems, combining both the effects from all the potential noise sources and the effect of the high frequency phase noise. The approach is widely applicable, and particular appropriate for fibre-optic sensor systems using amplifiers and TDM, providing us with a parallel comparison with other systems.

Chapter 6
Four-wavelength sensor network demonstration

Overview: In this chapter, I describe the construction of a four-wavelength distributed amplified network to interrogate the interferometric sensors. The optical performance from the distributed amplified network and the phase noise floor of the sensor system are characterized. The experimental results show good agreement with previous simulations using VPIphotonics and predictions from the phase noise model developed in Chapter 5.

6.1 Experimental arrangement and power budget

Commercial components were purchased to build wavelength-multiplexed distributed-amplified networks for interrogation of the pulsed interferometric fibre sensors. The first experiment was configured with only four wavelengths, due to lab limitations. The aim of this test was to

1) Evaluate the feasibility of the recommended architecture with commercially available fibre components and pump sources.
2) Validate the architecture simulation using VPI, and therefore predict the optical performance from the network, including network gain, OSNR and pump power dissipation etc..
3) Access the actual phase noise floor from the interferometric sensor system, and validate the Demod phase sensitivity model we developed in Chapter 5.

6.1.1 Experimental arrangement

The experimental arrangement was constructed as shown in Figure 6.1. The sensor system consists of three principal components: a transmitter, the multiplexed sensor array and a receiver section.

The transmitter consists of four narrow linewidth fibre lasers as interrogation sources. They were multiplexed in a 4 channel DWDM Mux, pulsed and frequently-shifted in an Acoustic-Optic Modulator (AOM) that operates as both a switch and a frequency shifter with f_1=200 MHz and f_2=200.05 MHz, and amplified in a TXAMP, then launched into the sensor array. The

maximum launched peak optical power into the sensor array was 22 dBm per wavelength, limited by nonlinear effects.

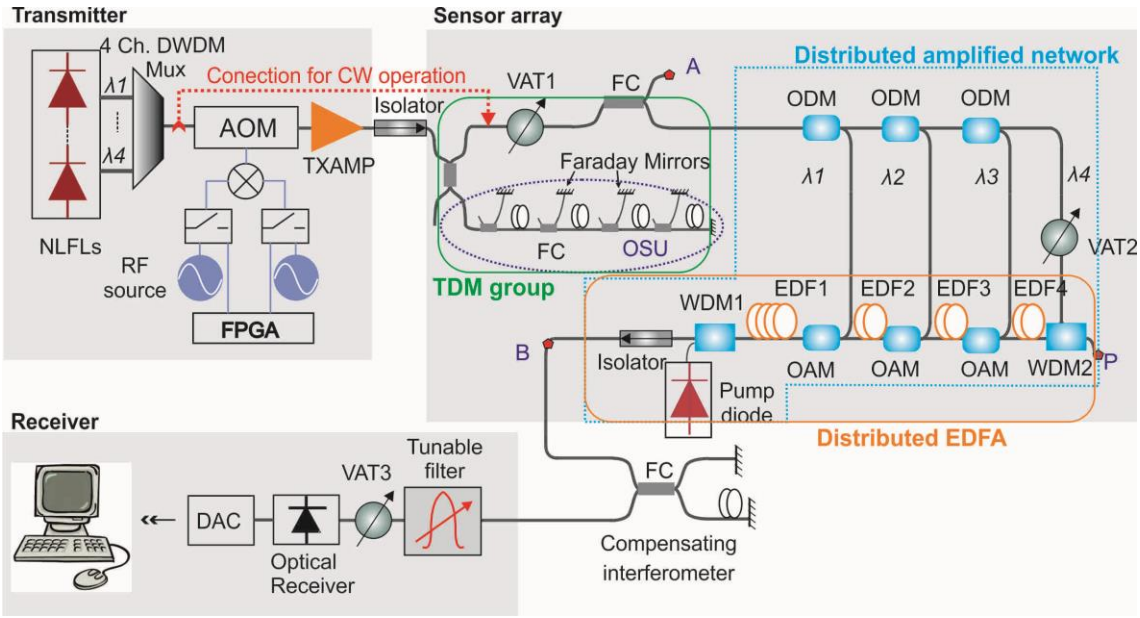

Figure 6.1: Experimental arrangement of the amplified four-wavelength sensor system. NLFLs: Narrow linewidth fibre lasers. CW: continues wave, DWDM Mux: Dense Wavelength Division Multiplexing Multiplexer, TXAMP: transmitter amplifier, AOM: Acoustic-Optic Modulator, FC: Fibre coupler, ODM: Optical drop multiplexer, OAM: Optical add multiplexer, OSU: Optical sensor unit, DAC: Digital to analogy converter, VAT: Variable attenuators.

Table 6-1: Characteristics of lasers used in the experiment.

Wavelength (nm)	*Full width @ 20 dB (kHz)*	*Lorentzian FWHM (kHz)*	*RIN peak @ 1MHz (dB/Hz)*
1545.3	71	3.5	−108.8
1546.12	77	3.9	−111.9
1546.92	101	5	−110.5
1547.22	91	4.5	−110.7

The fibre laser sources used are the Rock Laser Modules from NP Photonics, which are based on two Fibre Bragg gratings (FBGs) fusion spliced to a short piece of active material. A spectrally narrow grating (NB-FBG) selects the single longitudinal mode of the laser cavity and acts as the output coupler for the laser signal. The laser wavelengths align to the International Telecommunications Union (ITU) grid, of 1545.3 nm, 1546.1 nm, 1546.9 nm, and 1547.22 nm. The phase noise and the RIN of the Rock laser were characterized in Chapter 5 for phase noise

prediction. The heterodyne linewidth of this laser has been measured using 25 km of delay fibre with a carrier frequency of 100 MHz by the manufacturer, with the RIN of each laser also shown in Table 6-1. The RF sources used to generate the RF signals to the AOM have a SSB phase noise of −120 dBc/Hz at 1 kHz, which is also characterized in Chapter 5. The sensors are interrogated by two optical pulses separated in time by a period of 200 ns, which is the same as the transit time in the 40 metres of sensor fibre. The width of the pulse is 100 ns each, with a repetition rate of 200 kHz.

The sensor array is composed of a distributed amplified network with four wavelengths and one "TDM group" placed before the network. The network is composed of four segments of EDF-OA/DM combinations. The doped fibre is the I4 fibre from Fibercore Ltd, with its parameters validated and its optical performances verified in Chapter 3. The fibre length for EDF1 is 11.65 m, and other EDFs have a uniform length of 0.54 m, for simplicity. The pump source for the distributed EDFA is the FITEL 14 ×× nm (1466 nm in reality) series pump source FOL1435R40-317 with a maximum pump power up to 400 mW. There is an attenuator at the last wavelength to simulate the missing OA/DM pair, with its insertion loss set at 1.9 dB. The three OA/DM pairs are from Fiberer (China), with their specifications shown in Table 6-2. Their transmission spectra were characterized in Chapter 4 for network design.

Table 6-2: Characteristics of OADMs used in the experiment.

Parameters	*Specified value (dB)*	*Measured (dB)*
IL at pass channel	0.17~0.37	0.3
IL at reflective channel	0.6~0.9	0.8
IL at 1466 nm		0.3
Adjacent isolation	>25	20
Non-adjacent isolation	>35	
Return loss	>50	
Pass channel bandwidth @20 dB		0.4
Stop channel bandwidth @20 dB		1

The experimental setup was constructed with only one "TDM group" placed before the network representing all the multiplexed sensors in an array. This should provide similar optical performance in terms of loss to a fully loaded system, in which a TDM group is included at each wavelength between each ODM/OAM pair. The "TDM group" itself comprised an OSU along with a tunable attenuator to simulate a prescribed number of additional "missing sensors" as described below. The OSU is composed of a cluster of three orthogonally mounted accelerometers and a hydrophone, based on an in-line Michelson configuration. The return

transmit time in each sensor coil is 400 ns. The phase noise floor of the sensors in this OSU was measured to characterize the system phase sensitivity.

The returned signals from the TDM group which contains five pairs of pulses reflected from five mirrors in the group are then amplified by the distributed amplified network. The different wavelengths travel through different optical paths, and are amplified by different numbers of EDFA segments. The output of the amplified architecture is then launched into a compensating interferometer. This Michelson interferometer splits the light into two separate fibres and one of the pulse trains is delayed relative to the other by passing it through a delay coil (200 ns in delay time) and recombined with the other pulse onto a single fibre. The optical operation is described in detail in Appendix A. The tunable optical filter was used to discriminate between the wavelengths. The output of the filter was then attenuated before the receiver to achieve a peak optical power of −20 dBm per wavelength at the receiver as required to obtain the desired shot noise limited performance. The signal was then detected on a PINFET receiver and the TDM signal was electronically time gated and demodulated to extract the acoustic signals.

6.1.2 Power budget

The power budget determines the signal power entering the distributed EDFA and is calculated considering the insertion loss (IL) and gain of each component in the system. The power budget for the experimental arrangement in Figure 6.1 is provided in Table 6-3.

Table 6-3: Power budget.

Component		***Gain (dB)/Peak power(dBm)***
Laser source per wavelength		−10 dBm
AOM insertion		−6
Pulse unit		−14.6
TXAMP		+23
TDM group	Lab OSU	−29.5
	VAT1	−4 ~−30
OA/DM add/drop		−0.8
OA/DM pass		−0.3
Gain in EDF 2 to 15		1.5 ~ 2
Gain in EDF 1		20
Compensating interferometer		−9
Tunable filter		−5.5
VAT3		−1 ~ −30
Received signal power per wavelength		−27 dBm

Each fibre laser supplies 10 dBm optical power, which is reduced by a factor of 20.6 dB due to the IL of the AOM and the pulse carving loss (the duty cycle is D = −14.6 dB). The input signals to the amplified architecture were monitored by VAT1 to characterize the amplification performance of the network. The IL of the TDM group is defined by a lab OSU plus a tunable attenuator VAT1. The measured average insertion loss of the lab OSU is 22.5 dB, due to additional couplers at its input/output port. The number of pulses in the output pulse train is increased by five times, because each pulse has been reflected from the five Faraday mirrors in the OSU, and results in a duty cycle of D = −6.6 dB. The measured average power of the heterodyne signals to the optical receiver is thus set at −27 dBm by tuning VAT3.

6.2 Results and discussion

I first investigated the optical performances of the four-wavelength distributed amplified network, including the network gain, channel discrepancy, OSNR and pump power dissipation, which were also simulated using VPI. Experimental results are compared with simulations, to validate the simulation design using VPI. The system phase noise floor is the ultimate characteristic of concern in a sensor system. Therefore, the phase noise floor of the sensor in the system was also measured, to investigate its dependence on the system parameters.

6.2.1 Optical performances

The optical signal launched into the amplified network was monitored at point A by applying a 50:50 fibre coupler (FC) at the network input. Due to the insertion loss from the TDM group, the measured average signal power launched into the network was −22.85 dBm per wavelength. The optical spectrum is characterized and illustrated in Figure 6.2, together with the output optical spectrum measured at point B, which was taken with an input pump power of 40 mW. The spectrum comparison shows that the distributed EDFA effectively amplified the input optical signal. The amplified network provides us with a network gain of 20 dB at each wavelength, with the power discrepancy between wavelengths less than 1 dB. The output OSNR (noise in 0.1 nm) decreases from 50 dB to 30 dB, due to the accumulated ASE from the distributed EDFA. Further investigation and simulation comparisons on the gain, OSNR and pump power dissipation of the network will be discussed.

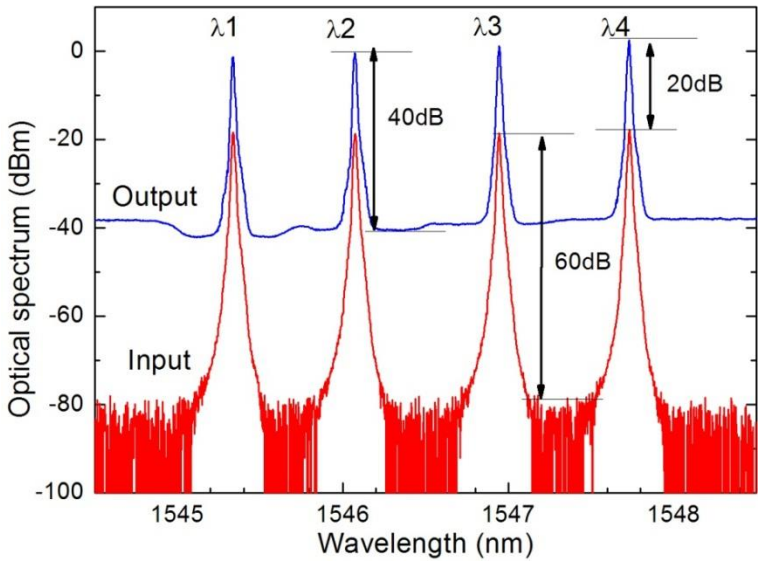

Figure 6.2: Measured optical spectrum at the network input and output. OSA resolution is 0.01 nm.

In the following tests, the multiplexed continuous-wave from the four channel Mux was also feed directly into the distributed amplified network by removing the AOM and TDM group, as illustrated in Figure 6.1, to measure the amplification performance of the network under the continuous-wave operation, for two reasons: firstly, for a small signal and a pulse period of 5 μs, the optical performance of the pulsed signal and continuous-wave signal can be considered as similar. Secondly, the simulation of continuous-wave in VPIphotonics is much faster than that with pulsed signals, especially for larger systems with the number of wavelengths over 16. Therefore, the comparison between experiments and simulations, on optical amplification performances under the continuous-wave operation, is reasonable.

6.2.1.1 Network gain

In order to facilitate the comparison, I define the *network gain* as the output signal power (at point B) minus the input signal power (at point A) at each wavelength under the continuous-wave operation. The measured network gain from the experimental setup and simulations using VPI are compared in Figure 6.3. Figure (a) shows the results with continuous-wave inputs as a function of the input pump power at different wavelengths. To validate the assumption that the continuous-wave signal and pulsed signal have similar optical amplification performances in the distributed amplified network, I also measured the network gain with the launched signal pulsed. The pulsed signal after the OSU has five pairs of pulses in each 5 μs separation, and the pulse width is 100 ns each. Figure (b) illustrates the measured network gain from the pulsed system as a function of launched average signal power per wavelength, with a pump power of 200 mW.

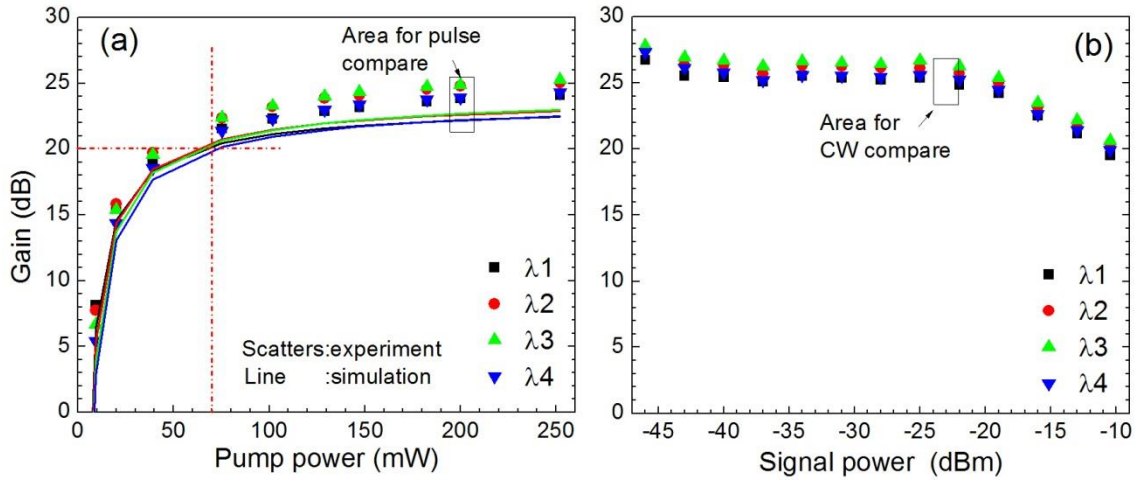

Figure 6.3: (a) Comparison between the experiments and simulations on network gain at different wavelengths as a function of input pump power with the input continuous-wave signal of −22.85 dBm per wavelength. (b) Measured network gain as a function of the average signal power per wavelength, when the launched signal is pulsed, with the pump power of 200 mW. Measured values at λ1 (in black) and λ4 (in blue) overlap.

It can be seen from figure (a) that the network gain is larger than 20 dB with launched pump powers larger than 70 mW. The gain differences between wavelengths are less than 1dB. The measured gain at different wavelengths is in quite good agreement with simulations, for different pump powers up to 260 mW. The maximum gain difference is less than 2 dB. Figure (b) demonstrates a power discrepancy between wavelengths less than 1.5 dB. In the small signal regime with average signal power smaller than −20 dBm, the measured gain of the pulsed system ranges from 25 to 27 dB, which are close to the measured results under the continuous-wave operation in Figure (a).

In conclusion, the four wavelengths amplified network provides us with a network gain of larger than 20 dB, providing that the launched pump power is larger than 60 mW and the input average signal power is less than –11 dBm per wavelength to the distributed EDFA. The gain can be further increased by increasing the pump power and decreasing the signal power. The power discrepancy between wavelengths is less than 1.5 dB, which is due to the gain flatness of the doped fibre and the non-uniform insertion losses from the OA/DM pairs. On the other hand, the experiments from the continuous-wave system and the pulsed system have similar gain performances. It also shows that the experiment and simulations are in good agreement, which validates the feasibility of using VPIphotonics for the design and performance characterization of larger systems with more wavelengths.

6.2.1.2 System OSNR

In order to clarify, the *system OSNR* is defined as the OSNR measured with an optical spectrum analyser (OSA) at point B for each wavelength, with the noise bandwidth of 0.1 nm. The input OSNR to the sensor array is usually larger than 45 dB, as can be found in the previous Figure 6.2, thus it is good enough to enable us to ignore the effects from the ASE noise in our later experiments. In practical applications, for a fully loaded sensor system, the time domain of the return signal from the TDM groups is usually fully occupied to maximize the number of sensors in each TDM group, thus, the average OSNR is equivalent to the peak OSNR for the return signal. While for interrogation systems in which the return signal from the TDM group is not fully occupied, this measured system OSNR should be compensated by subtracting the duty cycle D to produce a peak OSNR at each pulse, for phase sensitivity prediction from the phase noise model developed in Chapter 5.

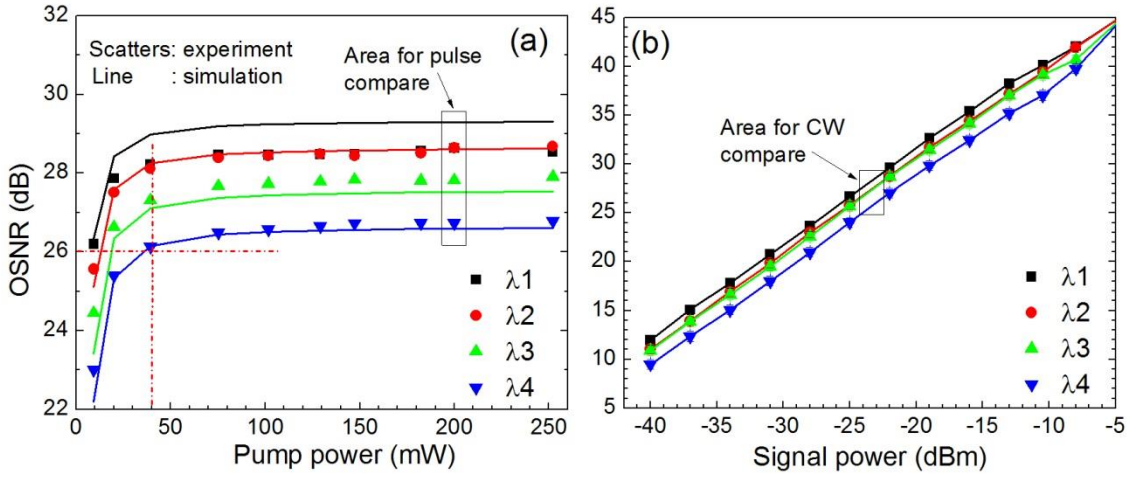

Figure 6.4: (a) Comparison of the experiments with simulations on system OSNR at different wavelengths as a function of the input pump power, under the continuous-wave operation. (b) Measured system OSNR vs. the average input signal power per wavelength, when the launched signal is pulsed, with the pump power of 200 mW in the four-wavelength network.

In the same way as above, firstly, I compared the experiments and simulations in a continuous-wave system. The experimental OSNR and simulated OSNR are compared in Figure 6.4 (a) as a function of the input pump power. There was a measurement error of ±1 dB when calculating the OSNR from the captured optical spectrum data. The measured OSNR is superior to 26 dB with pump powers larger than 40 mW. The best OSNR of 28.5 dB is achieved at λ1, followed by λ2, λ3 and λ4, all benefiting from the 'band pass filter' effect of the OAMs along the return bus. The experimental OSNR are superior to simulations by 0 to 1 dB, except at wavelength one

(in black) with 2 dB differences, which may be due to the larger experimental calculation error for higher OSNRs. The measured OSNR differences between wavelengths are less than that in the simulations, because the simulation has over calculated the OAM's band stop filter effect on the ASE power, when the light passes through its pass channel. The isolation for adjacent channels is specified as 25 dB, but the real stop band isolation is smaller.

Then, I characterized the system OSNR in a pulsed system as a function of the average signal power per wavelength, as shown in Figure (b). When the launched input signal power is around −23 dBm, the system OSNR are the same as results from the continuous-wave system. It is clear that the OSNR increases with an increase in the launched signal power, which was predicted in Chapter 4 theoretically. The linear dependence of the OSNR on the average input signal power will be very important for us to predict the system phase noise floor from the system noise model developed previously. As discussed previously, the duty cycle of the pulsed signal trains is D = −6.6 dB, so the peak OSNR in each pulse is 6.6 dB higher than the measured value.

To conclude, the four wavelengths amplified network provides us with a system OSNR of larger than 26 dB, providing that the launched pump power is larger than 60mW and the input signal power is larger than –23 dBm per wavelength on average into the distributed amplifier. This is equal to a peak OSNR of 33.6 dB and a peak equivalent signal power of −29.6 dBm per wavelength into the sensor array. The OSNR can be further improved by increasing the signal power launched into the distributed EDFA. The experiments from the continuous-wave system and the pulsed system show very similar performances. The experiment and simulations are in good agreement, which validates the feasibility of using VPIphotonics for the design and performance characterization of larger systems with more wavelengths.

6.2.1.3 Residual pump power

The residual pump power is of primary importance in a distributed amplified sensor array. The residual pump power from the system is monitored at point P in the experimental setup. The experiments and simulations as a function of the input pump power from the network are plotted in Figure 6.5. More than 40% of the input pump power remains at the network end. Experimental results and simulations are in good agreement.

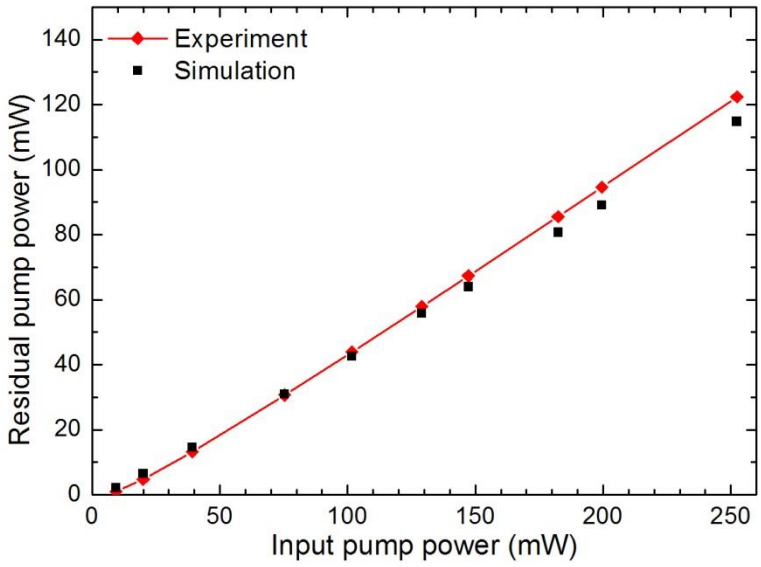

Figure 6.5: Comparison of the measured and simulated residual pump power as a function of the input pump power in the four-wavelength amplifier network.

In conclusion, the four-wavelength distributed amplified network works well with the low doped fibre from Fibercore and low loss multiplexers from Fiberer. Provided that pump power is higher than 70 mW and the input signal power is higher than −23 dBm, the distributed amplified network provides us with a network gain larger than 20 dB per wavelength, system OSNR larger than 26 dB (peak of 33.6 dB) and the power discrepancy between wavelengths less than 1 dB. More than 40% of the input pump power remains at the end of the network. The OSNR can be increased by increasing the launched power to the distributed amplifier. Furthermore, simulations and experimental results are in good agreement. Measured gains are 1.5 dB higher than simulations. OSNR differences between experimental results and simulations are less than 1 dB, which is also lower than the measurement error of ±1 dB. Residual pump power numbers also show good agreement. These comparisons fully validate our simulation model on the amplifier network.

6.2.2 System phase noise floor

The phase noise floor from the four-wavelength system was measured and is illustrated in Figure 6.6. The noise spectrum was measured at wavelength four, with a launched power to the network of −20.5 dBm. The demodulated phase shows a flat spectrum at frequencies above 300 Hz, showing a peak phase noise of −88 dB re rad/√Hz. The peaks in the spectrum below 300 Hz are from captured environment noise. The measured system OSNR to the receiver in this instance is 26.5 dB, which is equivalent to a peak OSNR of 33 dB. The predicted phase

noise value from the phase noise model at this OSNR is −88 dB re rad/√Hz. The measured value is in quite good agreement with the theoretical value from the noise model.

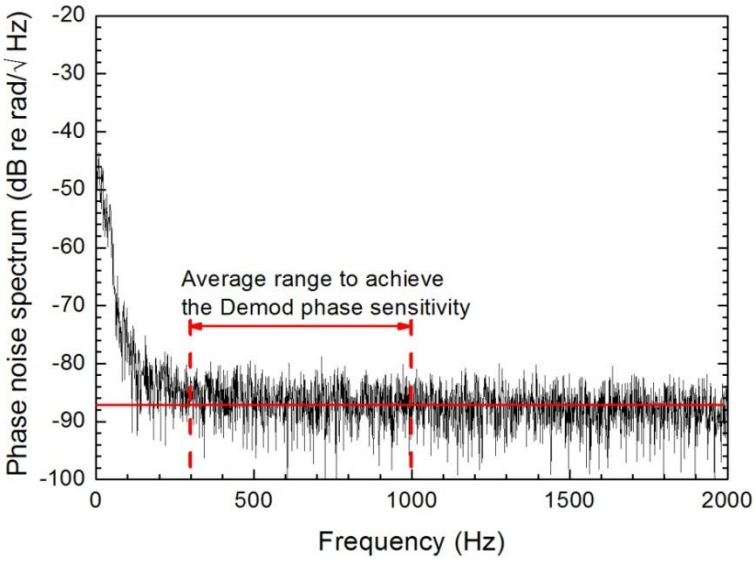

Figure 6.6: Measured phase noise spectrum from the four-wavelength system.

6.2.3 Discussion on the phase noise floor

For consistency and to facilitate comparison with the phase noise model, it is fair to define the Demod phase sensitivity and the phase noise floor as the mean value of the demodulated system phase noise over the frequency range from 300 Hz to 1 kHz, in the unit of dB re rad/√Hz, as illustrated in Figure 6.6.

6.2.3.1 Dependence on the signal power

The predicted Demod phase sensitivity of the system has shown its dependence on the signal to ASE power when the OSNR is below 30 dB. On the other hand, the OSNR from the four-wavelength network was measured to be dependent on the launched power at point A. Therefore I have measured the Demod phase sensitivity as a function of the launched power to the array, by tuning the IL of VAT1, giving the results shown in Figure 6.7. To demonstrate the phase deterioration from the ASE power, I have also removed the optical filter before the receiver, allowing the wideband ASE power to beat with the signal, which is also shown in Figure 6.7. The squares in in Figure 6.7 denote the phase noise floor with an ASE optical bandwidth of 0.3 nm, and the circles show the value measured when the optical filter is removed, which results in an equivalent optical bandwidth of 77 nm, with the ASE spectrum normalized to the ASE gain at 1550 nm. The dependence of the phase noise on the launched signal power is also demonstrated in Figure 6.7. It can be seen that the difference, in the phase noise values between

different optical bandwidths, increases when the signal power decreases below −22 dBm. The system OSNR at this instance is 25 dB (peak OSNR of 31.6 dB). When the system OSNR is better than 30 dB, shot noise dominates. However, with a decrease in the launched signal power, the OSNR decrease, and the ASE beat noise starts to dominate, thus the phase noise floor increases faster. These data reveal the importance of a proper optical filter to reduce the effect of the ASE-ASE beat noise to the phase noise, particularly in systems with significant ASE. A DWDM demultiplexer to route the wavelength would also help. Separate phase noise traces with different colours are taken at different wavelengths, they are with slightly different OSNRs at the same input signal power, and therefore are with different phase noise values when the signal power decreases below −22 dBm.

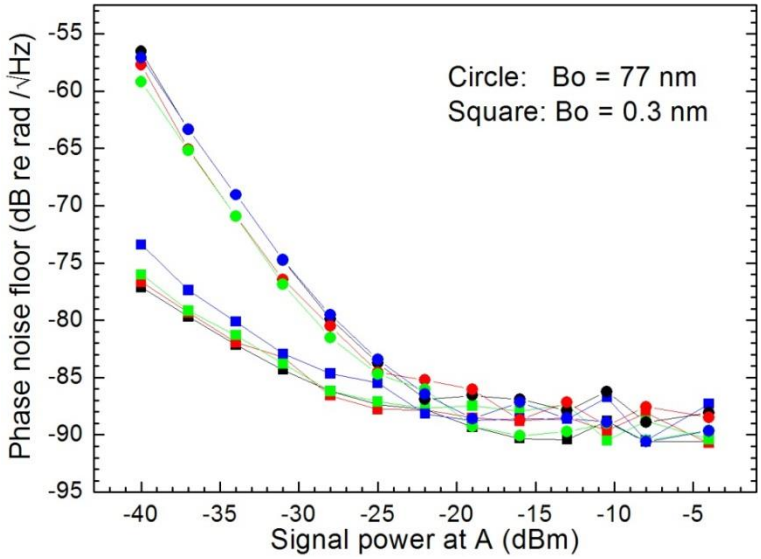

Figure 6.7: Measured phase noise floor in the four-wavelength sensor system as a function of the average signal power per wavelength to the distributed amplifier with input counter pump power of 200 mW.

6.2.3.2 Effect of the FWM

In a WDM system when the optical signals are not effectively staggered in the time domain, the WDM induced noise will deteriorate the phase noise floor. Due to lab limitations, my first experiment was carried out with input signals non-staggered in the time domain. Therefore, it is important to investigate the effect of the FWM.

I first measured the optical power spectrum before the optical receiver for individual wavelengths separately, all demonstrated in Figure 6.8. It is clear that there are FWM peaks located around λ1 and λ2. The FWM peaks are significant and as big as –17 dB. To assess the effect from these FWM peaks, I measured the Demod phase sensitivity at λ1 in the system with

only one wavelength on, and compared it with four wavelengths on, to investigate the phase noise degradation from the FWM effect. The results are compared in Figure 6.9. Circles are measured with only one wavelength on and stars are measured with four wavelengths on. There was an ideal optical filter before the receiver to suppress the ASE-ASE beat noise in both of the measurements.

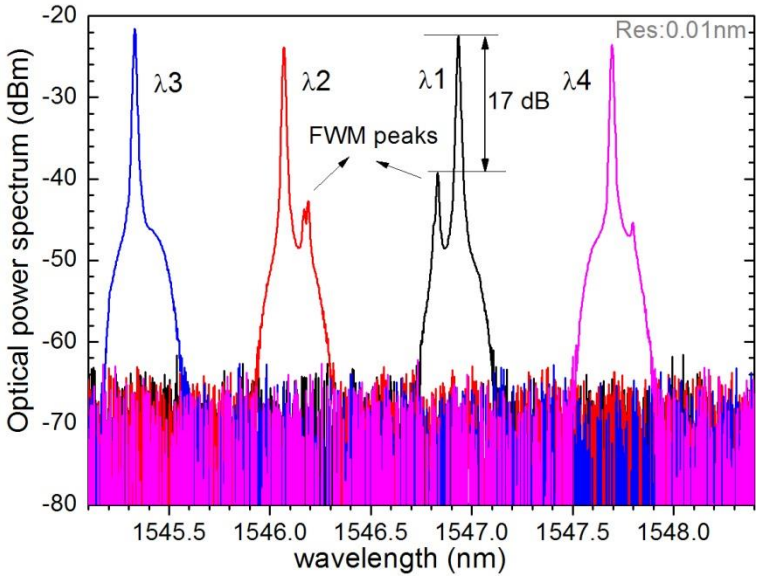

Figure 6.8: Measured optical spectra before the receiver with FWM peaks.

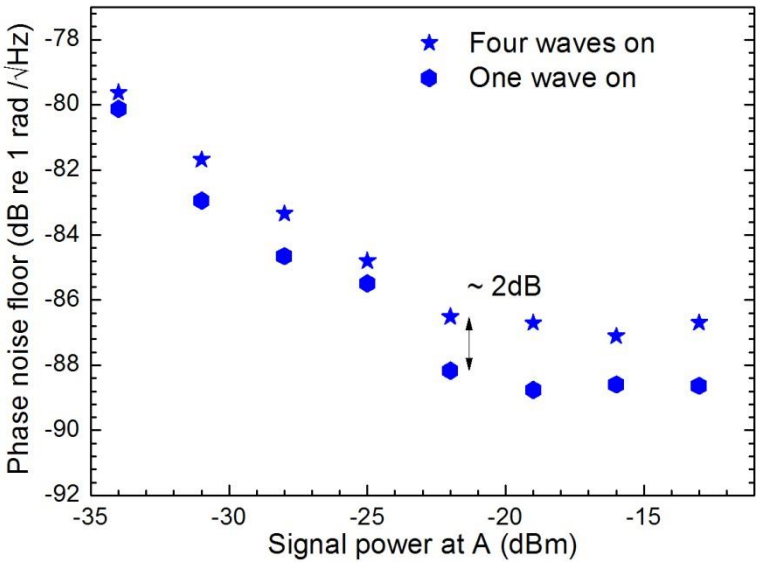

Figure 6.9: Measured phase noise floor in the four-wavelength sensor system as a function of the average signal power per wavelength to the distributed amplifier with input counter pump power of 200 mW.

It can be seen from Figure 6.9 that the effects from FWM are less than 2 dB which can be ignored. This can be explained by two reasons: firstly, the frequency grid between the four

wavelengths are not exactly 100 GHz, so their FWM peaks do not exactly overlap with the centre wavelength of the signals, as shown in Figure 6.8, therefore a narrow bandwidth optical filter can effectively eliminate most of the FWMs power. Secondly, these FWM also act as interrogation signals, only the intensity noise of these FWM peaks introduces intensity noise induced phase noise. The intensity fluctuation of these FWM peaks is quite small compared to the FWM peaks.

6.2.3.3 Comparison with the phase noise model

To be systematic, I also compared the measured system phase noise floor as a function of the measured OSNR, with the theoretical analysis from the phase noise model. The comparison results are shown in Figure 6.10. Comparison results show good agreement.

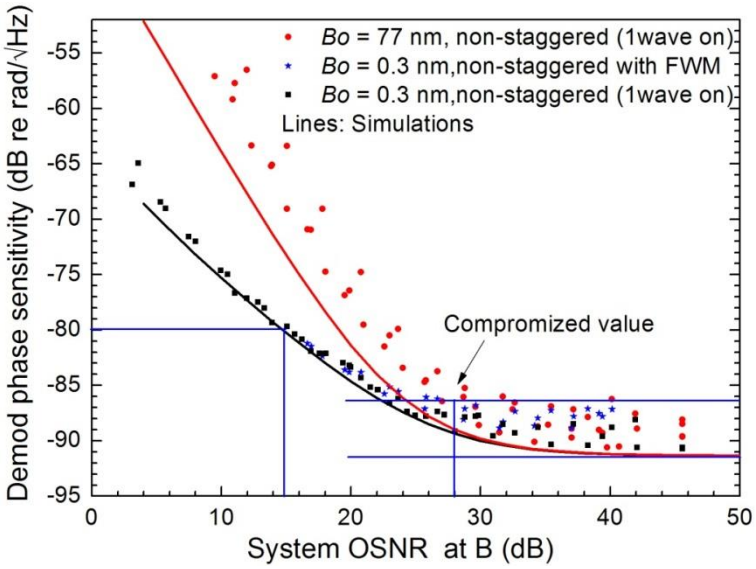

Figure 6.10: Experimental Demod phase sensitivity and theoretical calculation as a function of the measured OSNR (D = −6.6 dB).

The comparison also shows the dependence of the phase noise floor on the OSNR. When the measured system OSNR is larger than 31 to 33 dB (peak OSNR is 37 to 40 dB), the system phase noise floor is dominated by the shot noise and the receiver noise, as good as −90 dB re rad/√Hz , with a variance range of ±1.5 dB, as shown in Figure 6.10. This variance moves the critical OSNR to a compromised value of 26 ~28 dB, with the system OSNR deteriorates more, the ASE noise increases, and the phase noise floor increases linearly from −87 dB re rad/√Hz. The results show that the system OSNR needs to be larger than 15 dB (peak OSNR of 21.5 dB) to achieve a phase noise floor better than −80 dB re rad/√Hz, even without

FWM effects as in a staggered transmitter. The conclusion has a significant impact on the design of a distributed amplified seismic sensor array.

6.3 Conclusions

This chapter experimentally configured a four-wavelength distributed amplified network and characterized its performance in an interferometric sensor system. The four wavelengths amplified network provided us with a network gain >20 dB and a system OSNR >30 dB, providing launched pump powers >70 mW. The gain and OSNR could be further increased by manipulating the launched signal power to the distributed EDFA. The network exhibited similar performances between continuous waves and pulsed waves, showed good agreement with simulations, which confirmed the feasibility of a quick architecture design using VPIphotonics.

Phase noise floor in the system was characterized as a function of the input signal power and the system OSNR, which showed good agreement with predicted results from the phase noise model. Results show that the phase noise increases with the deterioration of the OSNR, when the system OSNR becomes smaller than 26 ~28 dB (peak OSNR of 33 ~35 dB). Comparison also shows that the effects from FWM are less than 2 dB even with a FWM peak of −17 dB, which can be ignored. As discussed in Chapter 4, the phase noise floor varies with the position of the wavelength in the amplifier network, and the advantages of the amplified network are mainly embodied in large scale sensor arrays, so it is necessary to construct sensor systems with more wavelengths, and the optical performance for 16 wavelengths will be investigated in the following chapters.

Chapter 7
16 wavelength sensor network demonstration

Overview: This chapter builds on previous chapters to consider distributed amplifier sensor networks employing 16 wavelengths. Results from a simulation of the network are given followed by laboratory results from a 16 wavelength demonstration of the network. The optical performance from these networks and the phase noise floor for sensor interrogation are characterized. A test phase modulated signal was applied and demodulated from the 16-wavelength laboratory demonstration. Results show that the experimental arrangement can address up to 64×16 sensors with a phase sensitivity unaffected by ASE noise from the distributed amplifier, and can support up to 256×16 with a useful phase sensitivity for many applications of -77 dB re rad/$\sqrt{\text{Hz}}$ at a lower sampling rate.

7.1 16-wavelength (4 active) sensor network demonstration

Previously, I have demonstrated a four-wavelength distributed amplified network and characterized the phase noise floor at each wavelengths. The results have shown that the OSNR and the phase noise performance depend on the position of the channel in the distributed amplified network. From previous analysis, I have shown the distributed amplified network provides channels at the last wavelength (i.e., wavelength of the most distant sensor group located at the end part of the multiplexed array) with the worst OSNR, which leads to a worst phase noise floor. Therefore, it is important to understand the channel performance as a function of the channel position in the network. Here, I investigate the OSNR and the phase noise performance of the last four wavelengths located at the back of a sensor array.

7.1.1 Measurement setup

I built a 16-wavelength emulator to access the performance of the last four wavelengths and it is shown in Figure 7.1 (b). Compared to an actual sensor array with 16 wavelengths, which is shown in Figure 7.1 (a), the four wavelengths of the available fibre lasers were arranged at the back of the network, illustrating the last four wavelengths. In Figure 7.1 (b), the network configuration for the previous 12 wavelengths was replaced by a 12 waves emulator comprised of attenuators and EDF segments (attenuator-EDFs). The first Loss-0 in the distribution bus is equivalent to the accumulated insertion loss of the previous 12 ODMs on the distribution bus.

Each set of EDF-Loss segments along the return bus represents the transmission along four sets of EDF-OAMs, denoting the gain from the amplifier segments and the insertion loss from the OAMs. The settings for the loss and EDFs are shown in the following table. Optical performance of the network output at point B was measured. A lab 'TDM group' with four sensors inside was placed before the network where all wavelengths are present, to simulate loss and signals from all the sensors in the network. The phase noise floor in interrogation of these sensors represents the phase noise we would expect from interrogation of sensors using the last four wavelengths in a full 16-wavelength network.

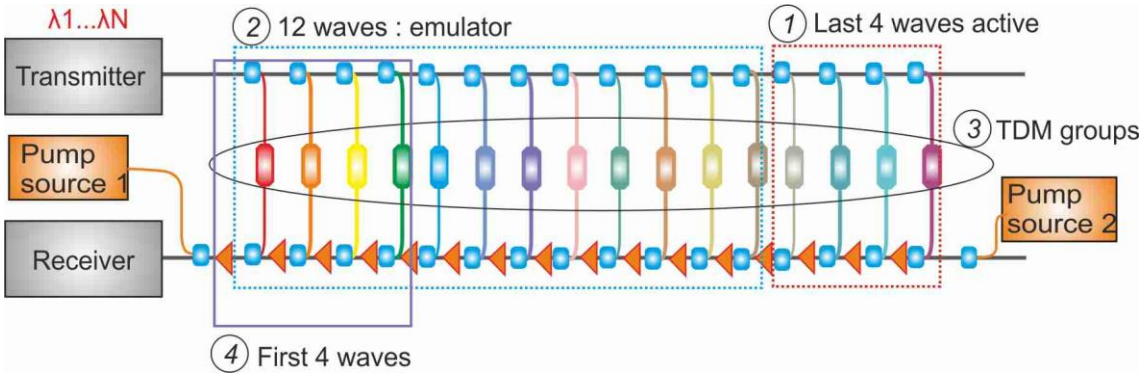

(a)

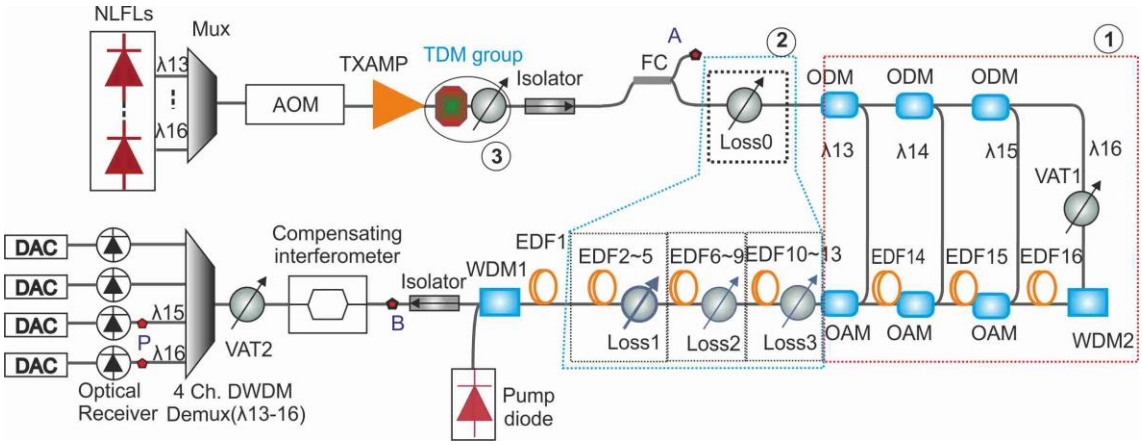

(b)

Figure 7.1: (a) 16-wavelength configuration. (b) Experimental setup of the 16-wavelength emulator, DeMux: Demultiplexer.

Table 7-1: Parameters in the 16-wavelength emulator.

Loss 0	*Loss 1*	*Loss 2*	*Loss 3*	*VAT 1*	*EDF 2 to 5*	*EDF 6 to 9*	*EDF 10 to 13*	*EDF 14/15/16*
3.6 dB	1.2 dB	1.2 dB	1.2 dB	1.9 dB	1.5 m	1.5 m	1.5 m	0.54 m

7.1.2 Results and discussion

The measured system OSNRs (defined in Chapter 6) at the four active wavelengths as a function of the position of the wavelengths are demonstrated in Figure 7.2. The results from the previous four wavelengths network demonstration in Chapter 6 are considered as the first four wavelengths of an actual 16 wavelengths sensor array. Points in different colour indicate the measured OSNRs for different average input signal power, which is the measured average power per wavelength from an OSA at point A. As discussed in the OSNR prediction section 4.5.4, the lights from the TDM groups are approximately continuous wave, thus this represents the power in presence of the sensors. Open circles are from simulations using VPI.

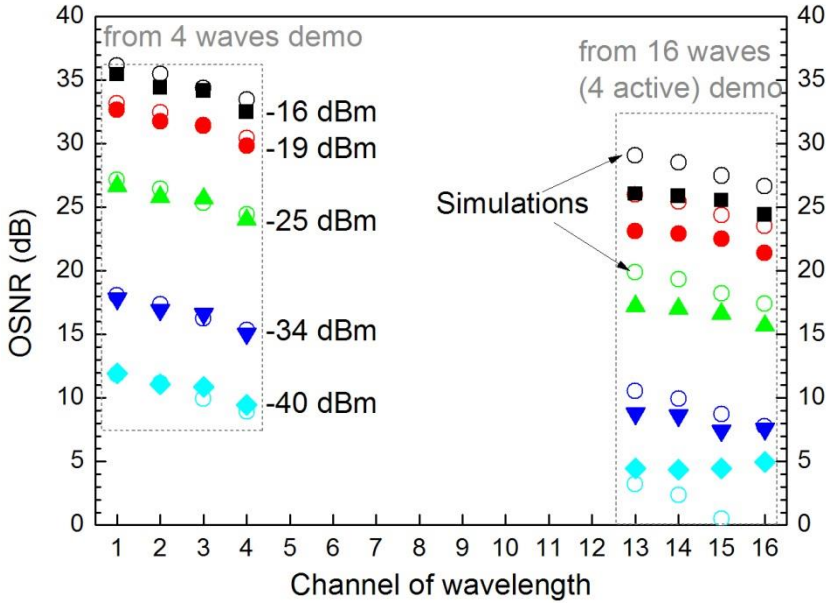

Figure 7.2: System OSNR as a function of the channel number in the 16-wavelength network for different average input signal powers. Values at first four channels are from the previous four wavelengths network demonstration, and last four channels from the 16-wavelength (4 active) network. Pump power at 200 mW.

The OSNR increases with an increase in the input signal power. The difference in the OSNR between the first wavelength and the last wavelength ranges from 7 to 10 dB, and increases with increasing OSNR. The wavelengths at the back experience more ASE power from the front 12 EDF-OAM segments and have lower OSNRs. For the first four wavelengths in a real network with 16 wavelengths, the accumulated ASE from the back amplifier stages will be filtered out, therefore, the previous four-wavelength network demonstration provides an effective emulator for the first four wavelengths in a 16-wavelength system. Simulations for the OSNR using

VPIphotonics are close to experimental results. The differences are less than 1 dB in the first four-wavelength emulator and less than 3 dB in the last four wavelengths emulator.

The measured phase noise floor (average over 300 Hz to 1 kHz) on the last four wavelengths in the emulator was characterized, and is plotted in Figure 7.3, together with the previous results for the first four wavelengths, for different average input signal powers. As predicted, a smaller OSNR leads to a higher phase noise floor. With the same input signal power per channel, the phase noise floor increases with the channel number of the wavelengths.

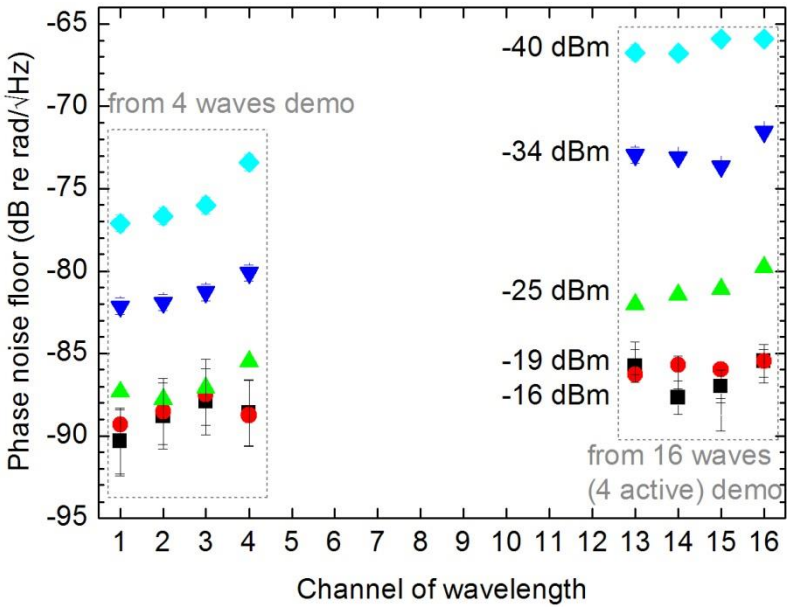

Figure 7.3: Measured phase noise floor as a function of the channel (wavelength) number in a 16-wavelength distributed amplified network for different average input signal power. Pump power at 200 mW.

The best achievable phase noise sensitivity in the distributed amplified network is −90 dB re rad/√Hz at wavelength λ1, which is close to the shot noise limited floor. The entire phase noise floor at all the channels is better than −80 dB re rad/√Hz when the input signal power is larger than −25 dBm. Assuming a launched signal peak optical power of 22 dBm per wavelength (a value comfortably below the onset of most non-linear effects, which is discussed in Section 4.2.2), a TDM group with an insertion loss less than 47 dB would provide such signal power level. The insertion loss of 47 dB is equivalent to 128 sensors in a TDM group.

However, the difference in signal performance between wavelengths is as high as 10 dB, which is bigger than expected. This is because the 16-wavelength emulator has under-estimated the effect of the ASE noise for the channels at the front four wavelengths and over-estimated it for

the back four wavelengths. More seriously, the power contribution from the signals at the missing 12 wavelengths to the distributed amplifier was absent.

7.2 16-wavelength (4 active, 12 idle) network demonstration

Although I have tried to fully model the performance of the 16-wavelength distributed amplified network, using four active wavelengths, there are two deficiencies in the above emulator.

1) The accumulated ASE power from the back amplifier stages on the first four wavelengths were entirely absent, which overestimated the 'band pass filter' effect from the OAMs, and lead to better OSNRs for the first four wavelengths.
2) The gain for both the signal and the ASE were higher in the emulators, because of the absence of the signals at the front twelve wavelengths in the distributed amplifier.

Therefore, it is necessary to build a real 16-wavelength network (15~16 stages of EDF-ODM/OAMs) with 16 laser sources and characterize the system performances. In this network, I have configured the network with 15 stages of EDF-ODM/OAMs. Multiplexed light from 16 laser sources were launched into the network: four are active for phase interrogation, and the other twelve are idle, only for the investigation of the amplification performance.

7.2.1 Measurement setup

7.2.1.1 Experimental arrangement

Although a larger number of wavelengths can be multiplexed, due to cost, practicality and equipment availability, I used 15 sets of EDF-ODM/OAM groups to build a real 16-wavelength network for interferometric sensing at 16 wavelengths, as shown in Figure 7.4 (b). Compared to an actual network with 16 wavelengths, which is shown in Figure 7.4 (a), in our proof-of-principle experimental configuration shown in Figure 7.4 (b), the transmitter consists of four active narrow linewidth fibre lasers for interrogation, and a further idle twelve DFB lasers (from a DWDM telecom source bank) to provide suitable representative signals to assess the optical amplification performance of the array. (The linewidth of the DFB lasers was too broad to allow them to be used for sensor interrogation.) The four narrow linewidth sources were multiplexed, pulsed, frequency-shifted, and amplified, then launched into a "TDM group". The output signal was then combined with the twelve continuous-wave sources and then launched into the 16-wavelength distributed amplified network. The maximum launch power into the sensor array was 22 dBm per wavelength, limited by nonlinear effects.

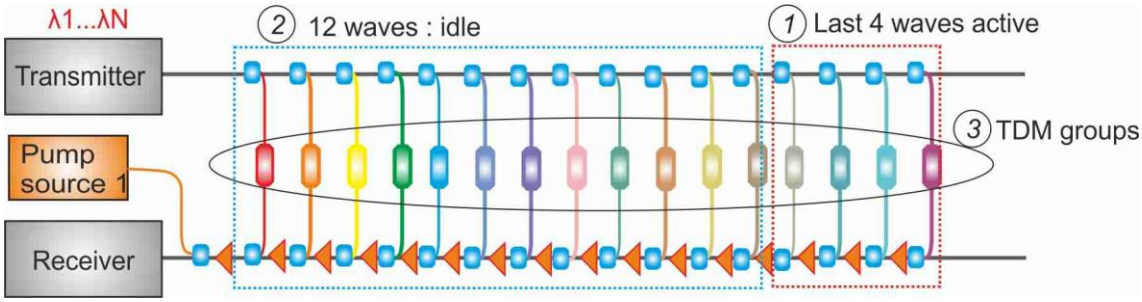

(a)

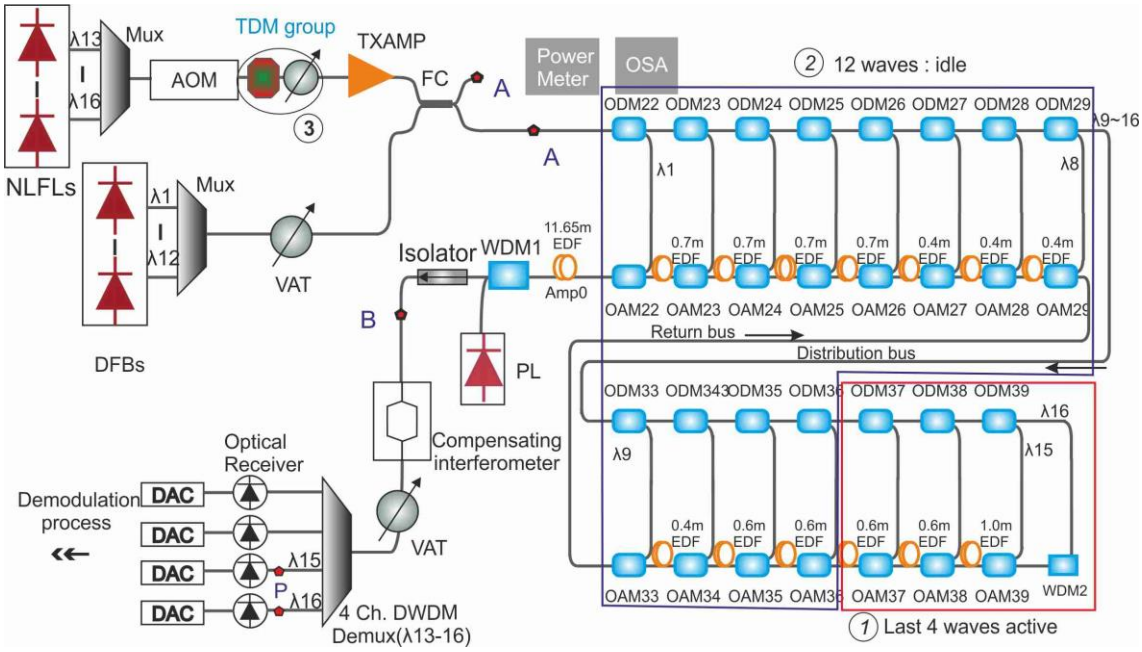

(b)

Figure 7.4: (a) 16-wavelength configuration. (b) Experimental setup of the 16-wavelength (4 active, 12 idle) network.

The experimental arrangement was constructed with only one "TDM group" (described previously) representing all of the sensors in the array. This was located before the array so that each wavelength suffered the loss of this device. This should provide similar optical performance in terms of loss to a fully-loaded system. Later we will show the measured phase noise floor of the sensors in this "TDM group" for characterization of the system performance. The amplified network comprised of 15 pairs of ODM/OAMs along two fibre buses to support the 16 wavelengths. The insertion losses of the ODM/OAMs were measured to determine the lengths of the Er-doped fibre required in each amplifier stage to compensate for their loss. An amplifier segment was located after each ODM/OAM pair. In our experiments all amplifier segments were co-pumped by one 1466 nm pump source coupled into the return bus. The

lengths of amplifier segments used throughout the network were determined by detailed numerical simulations of the system using VPIphotonics, supplemented by the detailed amplifier measurements in Chapter 3 which allowed us to determine the salient physical properties of the erbium doped fibre used.

The return signals from the sensor array were referenced at the compensating interferometer, and attenuated before the demultiplexer to achieve a peak optical power of −27 dBm (D = −6.6 dB) per wavelength at the optical receiver as required to obtain the desired shot noise limited performance. The demultiplexer was used to drop the signal bearing channels. The output of the demultiplexer was then detected and demodulated to extract the phase information.

7.2.1.2 Power budget

The system performance in an amplified array is ultimately limited by the ASE noise from the amplifiers. The injected average signal power into the EDFA segments determines the amplifier performance. The insertion loss (IL) of one sensor was assumed to be 5 dB, increasing by 6 dB for every doubling of the number of sensors in the TDM group, as is consistent with current sensor technology. Assuming the returned optical signal from the TDM group is fully occupied in the time domain by interleaving the pulse returns from different sensors in the group, (i.e., $D = 1/(N + 1)$, and then the returned average optical power equals the pulse peak optical power. When a peak optical power of 22 dBm per wavelength is launched into a fully-loaded system in which a TDM group is included between each ODM/OAM pair, the optical power to Amp0 can be found. In the proof-of-concept experiment, for simplicity, we manually set the number of sensors in each TDM group by adjusting the IL of the VAT in the "TDM group" located before the amplified array, therefore the average signal power per wavelength we monitored at point A equates to the injected power to Amp0 in a practical system.

Table 7-2: power budget per wavelength with 22 dBm peak optical power into the array.

Number of sensors in each TDM group	IL (dB)	Signal power to Amp0 (dBm)	Average signal power at A in the setup (dBm)
1	5	17	17
4	17	5	5
16	29	−7	−7
64	41	−19	−19
128	47	−25	−25
256	53	−31	−31
512	59	−43	−43

7.2.2 Optical performance in the network

7.2.2.1 Amplified optical spectrum

The optical spectra before and after the amplified array were characterized with a launched power at A of −31 dBm, as shown in Figure 7.5. The spectral resolution used to obtain the power spectral density (PSD) is 0.1 nm. Although the wavelengths in our application can be consecutive with a spacing of 100 GHz between each other, I have picked up the wavelengths in two groups with 400 GHz between each group of eight wavelengths, allowing it compatible with obsolete and legacy sensor systems. In such old systems, thin-film optical filters are used to separate the two wavelength groups, thus a wider gap between the two wavelength groups is needed to avoid the overlapping between the filter roll-offs. It can be seen from the spectra that the OSNR for each channel is decreased due to the ASE noise added by the distributed EDFA. It can be seen that the OSNR in figure (a) is larger than in figure (b). The output optical spectrum around the signal wavelengths dipped below the ASE power level between wavelength channels because of the filter effect on the express port of the OAMs along the return bus, as stated previously. Therefore the OSNR at λ1 is superior to the last one (λ16) due to this 'partial rejection effect' from the OAMs.

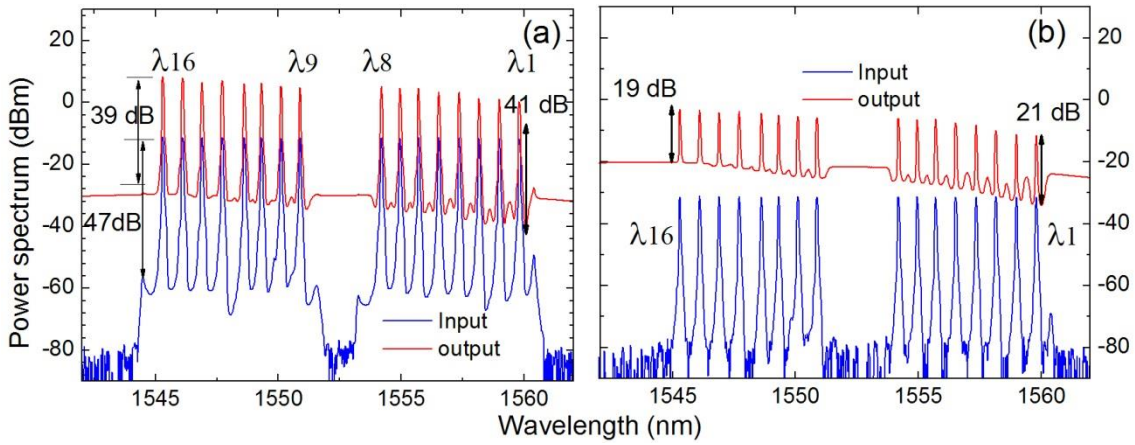

Figure 7.5: Optical power spectrum measured at point A and B in the proof-of-concept experimental setup, with pump power of 200 mW, with the input average signal power per wavelength at point A of (a) −11 dBm and (b) −31 dBm. The OSNR at the last wavelength decreases from 47 dB to (a) 39 dB and (b) 19 dB due to the accumulated ASE.

The 'band pass filter' effect can be further investigated in Figure 7.6. The optical spectrum is measured with an input pump power of 100 mW and an input average signal power of −21 dBm into the amplified network at point A. The output spectrum indicates a 'hollow' shape as deep as 8 dB at λ1. Figure 7.7 demonstrates the simulated results using VPIphotonics with the same

settings. The simulation can predict the 'band pass filter' effect from the OAMs in good agreement with the measured results. The OSNR at the last channel (λ1) is 6 dB worse than at the first channel (λ1). The comparison between the measured and simulated results is shown in Table 7.3:

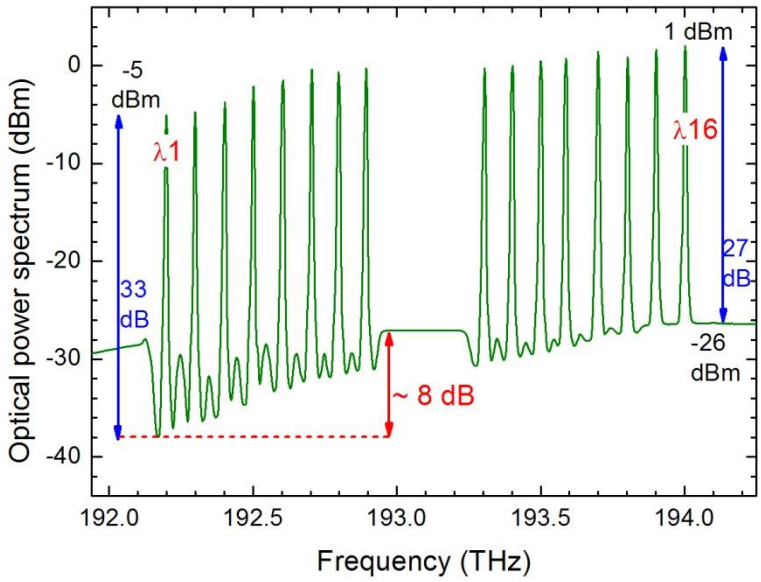

Figure 7.6: Measured optical spectrum from the 16 wavelengths distributed amplified array with 100 mW pump power and −21dBm average signal power per wavelength at A showing the 'band pass filter' effect.

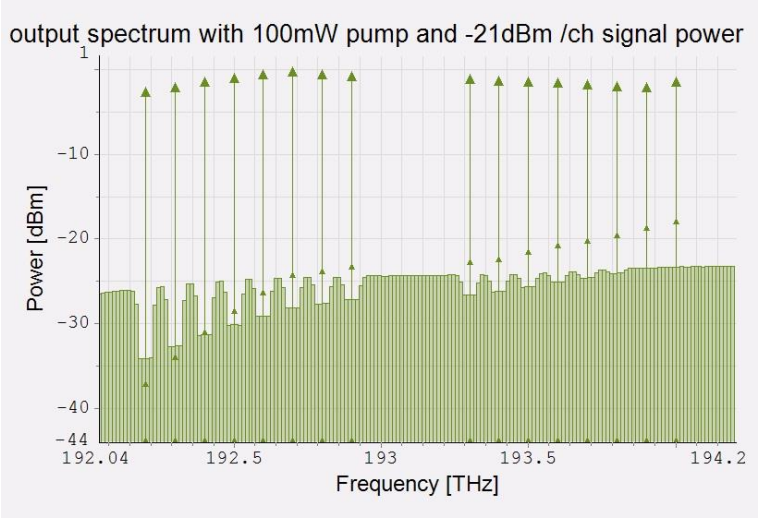

Figure 7.7: Simulated optical spectrum from the 16 wavelengths distributed amplified array with 100 mW pump power and −21dBm equivalent signal power per wavelength showing the 'band pass filter' effect.

Table 7-3: Comparison between the measured and simulated output optical spectrum.

	Signal power at λ1 (dBm)	*Signal power at λ16 (dBm)*	*ASE level (dBm)*	*Concave (dB)*
Measured	−5	1	−26	8
Simulation	−3	−1.5	−25.5	8

7.2.2.2 System OSNR

The system OSNR does not only change with the position of wavelength in the sensor array, but also varies with the input signal power level, even when the amplifiers are fully pumped (>100 mW in this study). I have measured the system OSNR as a function of the average input signal power to the network, as illustrated in Figure 7.8.

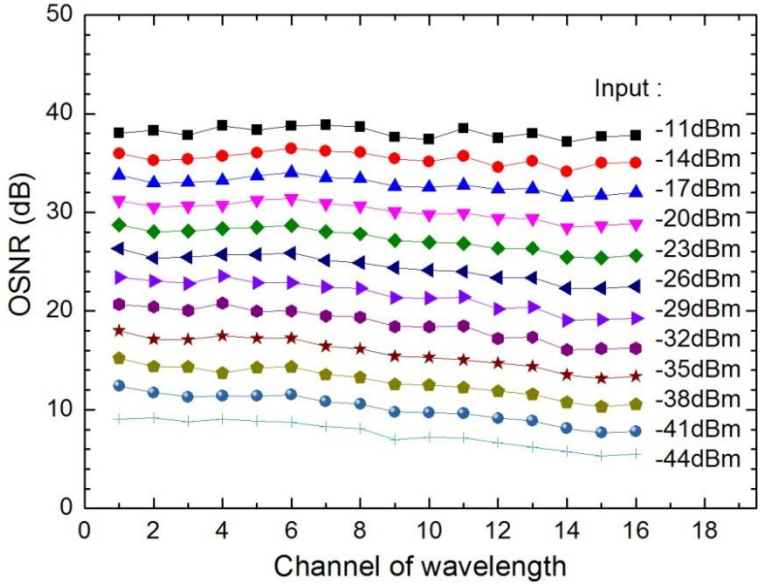

Figure 7.8: Measured OSNR with different average input signal power at point A ranges from −44 dBm to −11 dBm with pump power of 200 mW.

The system OSNR increases linearly with the average input signal power. The OSNR at λ1 is the highest and decreases with the channel number. The difference in OSNR between the first channel and the last channel decreases with the average input signal power as well. This difference ranges from 1 to 5 dB, which is much smaller than the measured value (7 to 10 dB) in the 16-wavelength emulator with four active wavelengths discussed in Section 7.1.

The OSNR at the worst wavelength channel (λ16) limits the system performance. I have investigated the worst OSNR as a function of the input signal power and the equivalent number of sensors in each TDM group in Chapter 4, and the predicted system OSNR from is given by

$$OSNR = \frac{P_{sin} IL_m^{2N-3} IL_{ad}^2 (IL_s / M^2) G_i^{N-1}}{2n_{sp} hvB_O [(G_i - 1)\frac{[1-(IL_m G_i)^{N-1}]}{1-IL_m G_i} + 1]} \tag{7.1}$$

The expression shows that the channel OSNR increases with the input signal power P_{sin} along the return bus. Therefore, I obtained the predicted and measured OSNR for the last channel at point B as a function of the launched power to the array at point A in the proof-of-concept experimental arrangement, as illustrated in Figure 7.9, with measured IL_m = 0.25 dB, G_i = 0.9 dB, and assumed n_{sp} = 1, due to the practical low noise amplifier performance. This figure illustrates the linear relationship between the channel OSNR and the launched signal power level. The predicted and measured OSNR are in good agreement. The values along the top axis show the equivalent number of sensors in each TDM group to achieve those OSNRs providing a launched peak optical power of 22 dBm into a fully-loaded system. It can be seen from the figure that even with 64 sensors per wavelength, the OSNR at the worst channel is still greater than 29 dB.

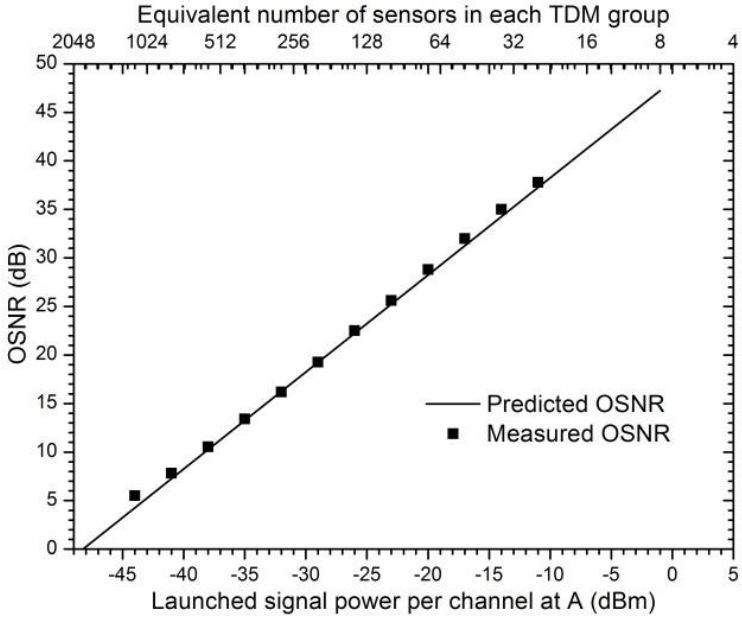

Figure 7.9: Measured and predicted system OSNR as a function of the optical signal power per channel at point A. The values along the top axis show the equivalent number of sensors in each TDM group to achieve those OSNRs providing a launched peak optical power of 22 dBm into a fully-loaded system.

7.2.3 Wavelength channel drop

Channel drop (i.e., failure or vacancy of any channel) is a problem of multiplexed sensor arrays. This may be a practical problem where TDM groups are partially populated on some wavelengths. The consequence of channel drop on the optical performance is investigated experimentally. Figure 7.10 demonstrates the measured output optical power at λ9, when different numbers of wavelengths drop in the 16-wavelength channel network. Different colours are with different numbers of dropped channels. The comparison shows that the channel gain increases when channels drop, because the total input power to the distributed amplifier decreases. However, the gain variance is quite small, as illustrated in Table 7-4, even with four wavelengths drop, the gain variance is less than 1 dB, because the amplifier is working in the small-signal gain region. The measured channel OSNR does not change with the drop of channels, the OSNR is found to be only dependent on the signal power per channel. The maintenance of optical signal performance indicates that the presented distributed amplified network is reasonably resilient to channel drop.

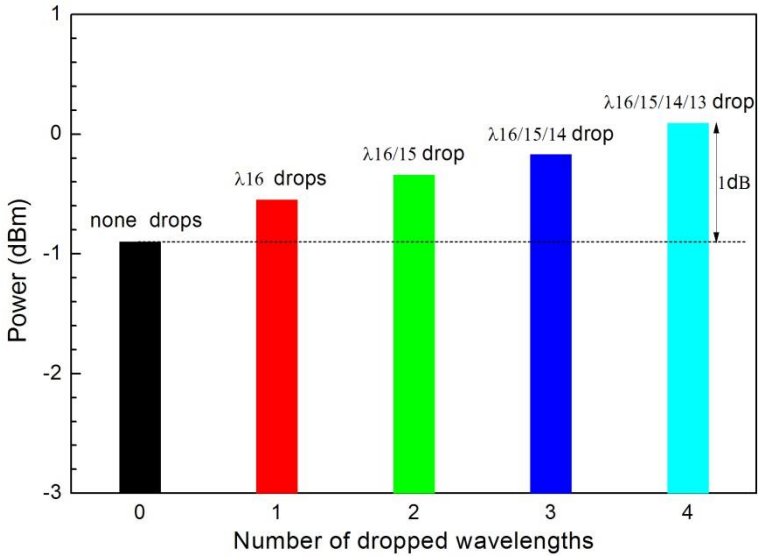

Figure 7.10: Measured output optical power at λ9 with channel drop.

Table 7-4: Changes in gain when channels drop.

Number of drop channels	*1*	*2*	*3*	*4*
Gain increase (dB)	0.2	0.4	0.65	0.8 ~1

7.2.4 Phase noise floor at the last channel

To illustrate the system performance, the phase noise spectrum of one sensor in the TDM group was tested under several average input signal powers. Table 7-5 illustrated the measured phase noise floor of the derivative signal and the OSNR at the last four wavelengths with the average input signal power of −15.1 dBm and −31 dBm. The table shows the system phase noise floor is around −88 dB re rad/√Hz with an average input signal power of −15.1 dBm, and decreases to −77 dB re rad/√Hz with the average signal power reduced by 15 dB. The difference in the phase noise floor between the last four channels is less than 1 dB. This is in agreement with the small differences in the OSNRs between the last four channels in Figure 7.8.

Table 7-5: Measured phase noise floor of the derivative signal and the OSNR in the 16-wavelength system.

Average signal power(dBm)	*Pump power(mW)*	*Wavelength number*	*Phase noise floor (dB re rad/√Hz)*	*OSNR (dB)*
−15.1	100	13	−87.8	35
−15.1	200	13/14/15/16	−86.7/−86.1/−86/−86.2	35 ~36
	200	13 ~16	−86.9 ~−87.5	35
−31	100	13/14/15	−77.6/−76.6/−77	15 ~16

7.2.5 Interrogation of a phase modulation

To demonstrate the signal interrogation ability of the 16-wavelength system, the 'TDM group' in the setup was replaced by a single fibre Michelson interferometer sensor along with a tunable attenuator to simulate a prescribed number of additional "missing sensors". To simulate an applied acoustic signal, one arm of the interferometer is wrapped around a piezoelectric transducer (PZT), allowing the sensor to be phase modulated with an alternating current (AC） supply. A sine signal with a peak-to-peak voltage of 0.4 volts at 1 kHz was applied on the PZT, which provided us with a phase modulation of 0.4 rad to the sensor. The measured phase spectrum at the last wavelength is demonstrated in Figure 7.11.

It is clear to see the applied phase demodulation from the demodulated phase spectra, with an amplitude of −8 dB re rad/√Hz at 1 kHz. The amplitude of the phase modulation signal at the referenced channel is 58 dB lower at 1 kHz, which is discussed in Appendix A. The phase noise floor at the derivative channels was also measured to access the system phase noise floor, with different signal powers measured at point A, as illustrated in Figure 7.12. Spectra in different colours are with different optical powers per wavelength (i.e., equivalent signal power

$P_{se} = P_s - IL_{TDM}$) to the distributed EDFA. The equivalent number of sensors in each TDM group for different input signal powers can be obtained from Table 7-2. And the numbers on different spectra show the equivalent total number of sensors in a fully-loaded array with 16 wavelengths.

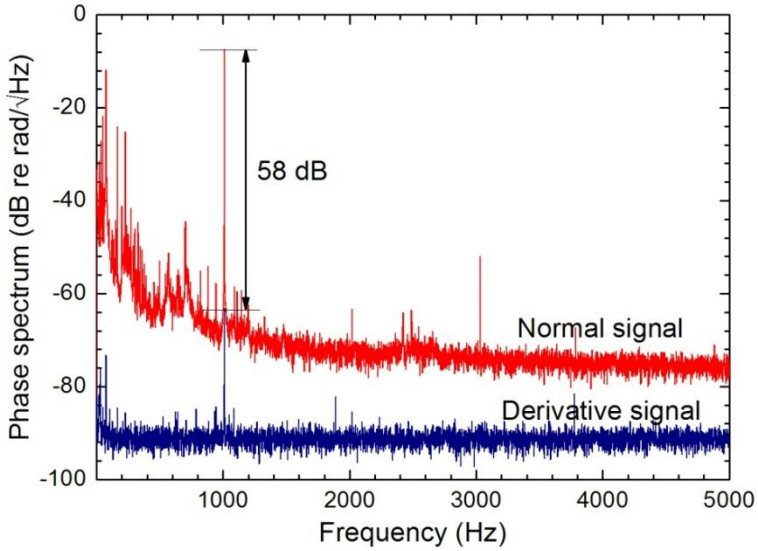

Figure 7.11: Demodulated phase spectrum of the normal and derivative signal, applied with a sine signal modulation of 0.4 rad (−8 dB re rad/√Hz) at 1 kHz.

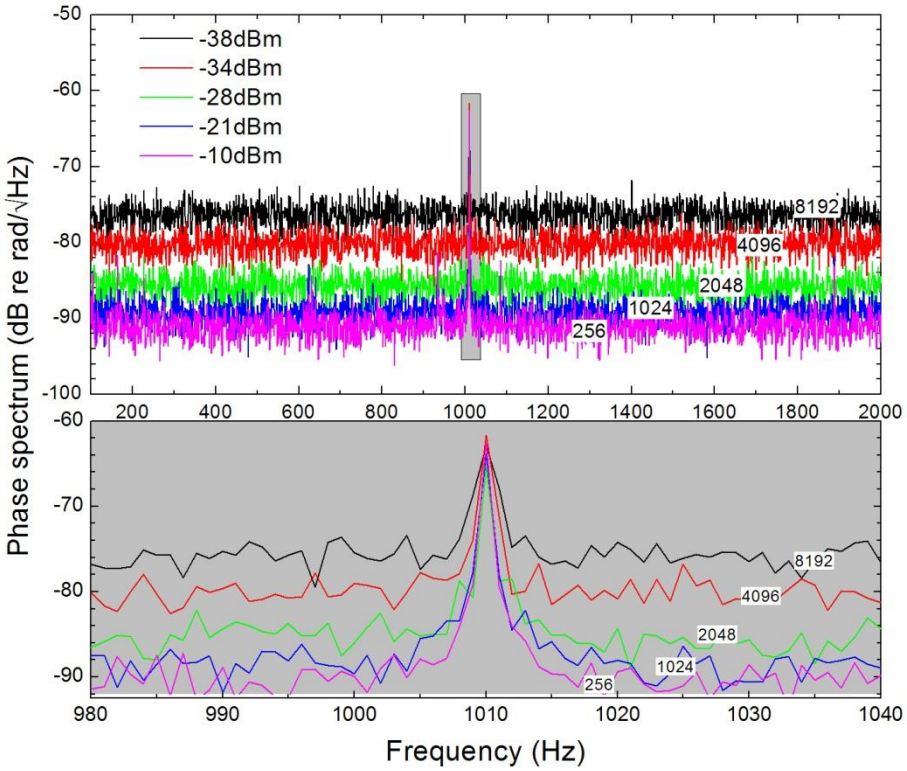

Figure 7.12: System phase spectra with different input signal power. The peaks around 1 kHz corresponds to the phase modulation on the sensor, and were enlarged in the lower figure.

7.3 Discussion and conclusion

This chapter has characterized the optical performance in a 16-wavelength (4 active) system. The performance of the output signal and the system phase noise floor is dependent on the average input signal power per wavelength into the distributed amplifier on the return bus in the network. The performance is in agreement with previous simulations using VPIphotonics and theoretical investigations on the phase sensitivity.

The input signal power into the network of the proof-of-principle experimental configuration with four active wavelength and twelve idle wavelengths can be converted to the number of sensors in each TDM group from Table 7-2, supported by the maximum peak input signal power of 22 dBm into the system in a real system. Table 7-6 summarizes the relationship between the number of sensors and the *Demod phase sensitivity* in the 16-wavelength system.

Table 7-6: Predicted Demod phase sensitivity in dB re rad/√Hz as a function of IL with specified pulse width and sampling rate.

IL (dB)	Equivalent number of sensors per wavelength	Total number of sensors	Measured Demod phase sensitivity	Sensor sensitivity (μrad/√Hz)	Pulse width (ns)	Sampling rate (Hz)	Predicted Demod phase sensitivity
5	1	16	*−92*	0.7		200k	−91
17	4	64	*−90*	0.9	100	200k	−90
29	16	256	*−90*	0.9	25	200k	−90
41	64	1 024	*−88*	***1.1***	25	200k	−88
47	128	2 048	*−85*	1.6	25	100k	−82
53	256	4 096	*−83*	2	25	50k	−77
59	512	8 192	*−76*	4.6	25	25k	−67

The first three columns in the table demonstrate the relationship between the IL of the TDM group and equivalent number of sensors at each wavelength and the total number of sensors. The middle columns in the table illustrate the measured *Demod phase noise sensitivity* (at the derivative signal) as a function of the total number of sensors in a 16-wavelength system, and the converted phase sensitivity (in μrad/√Hz) for each sensor. The phase sensitivity is achieved by removing the aliasing parameter resulting from the TDM interrogation; these values are superior to those predicted in Table 5-7, because of the over-predicted laser frequency noise from the assumed imbalance of one metre. The phase sensitivity remains at the same level when sensor numbers increase from one to 64, with the phase sensitivity better than 1 μrad/√Hz, independent on the ASE noise from the distributed amplifier, similar to the performance of a

passive single-sensor system. They also show that the system can support up to 8 192 sensors with a phase sensitivity less than 5 μrad/√Hz, which is far superior to the reported ~100 μrad/√Hz phase sensitivity in a passive TDM/DWDM array with 384 sensors .

As discussed previously in Chapter 5, bandwidth limitations and added aliased high frequency noise in the TDM architecture ultimately limit the highest level of multiplexing, even with a suitably adjusted sampling rate. The table demonstrates the relationship between the number of sensors and the predicted phase sensitivity with practical sampling rates and pulse-widths in a practical system with existing demodulation technology. Nevertheless, these results show that the configured 16-wavelength network can address up to 64 × 16 sensors with a phase sensitivity independent of ASE noise, and can support up to 256 × 16 with a useful phase sensitivity for many applications of −77 dB re rad/√Hz, even with an adjusted sampling rate. In this proof-of-principle experimental arrangement, the number of wavelengths has been chosen to be 16. This can be further increased by adding more pump sources into the array.

In conclusion, my experimental results show that the proposed distributed amplified network is able to support a total number of 1 024 sensors along one interlink fibre pair, allowing a phase sensitivity of around −88 dB re rad/√Hz, independent on the ASE noise. Further, I show that the current 16-wavelength array could theoretically be expanded to interrogate 4 096 sensors, albeit with a slight compromise in phase sensitivity. The number of interrogation sensors could be further increased by increasing the number of wavelength channels.

Chapter 8

Crosstalk in multiplexed sensor arrays

Overview: So far, we have measured and simulated the optical OSNR and the phase sensitivity in distributed amplified sensor systems with four wavelengths and 16 wavelengths. Another key concern in the application of heavily multiplexed sensor arrays is the channel crosstalk, especially in the time domain, as it leads to measurement error. This chapter investigates how various sources that lead to crosstalk, and experimentally verifies this using TDM groups driven by adjacent wavelengths. It is found that the crosstalk is sensitive to the time spaces between returned pulses, and the measured channel crosstalk is smaller than to −40 dB in the sensor group investigated. In this chapter, I only measured the crosstalk in the non-amplified-networks, and will measure the crosstalk in an amplified network in the following chapter.

8.1 Sources that lead to crosstalk

In practical applications, crosstalk in heavily multiplexed sensor arrays is widely recognized. For example, non-ideal optical pulse generators used for input optical pulse generation and detector with limited bandwidth cause crosstalk among time division multiplexed channels. Limited channel isolation in wavelength multiplexers induces intra channel crosstalk, i.e., light from more than one wavelength returns from each sensor. This intrinsic crosstalk induced noise may exceed other noise sources and set a limit to the system performance.

The intrinsic sources of crosstalk in a multiplexed fibre sensor system are various and complicated, with their effects on the crosstalk indistinguishable, as characterized in Figure 8.1. Crosstalk in a pulsed sensor system results from several sources: (A) non-ideal optical pulse generator, (B) EDFA amplification, (C) Rayleigh back scattering on the leading fibre, (D) multi reflections from connectors and components, (E) limited tap directivity along the leading fibre, (F) leading fibre, and (G) the response property of the receiver. There is also crosstalk from (H) non-ideal wavelength multiplexer in wavelength multiplexed systems.

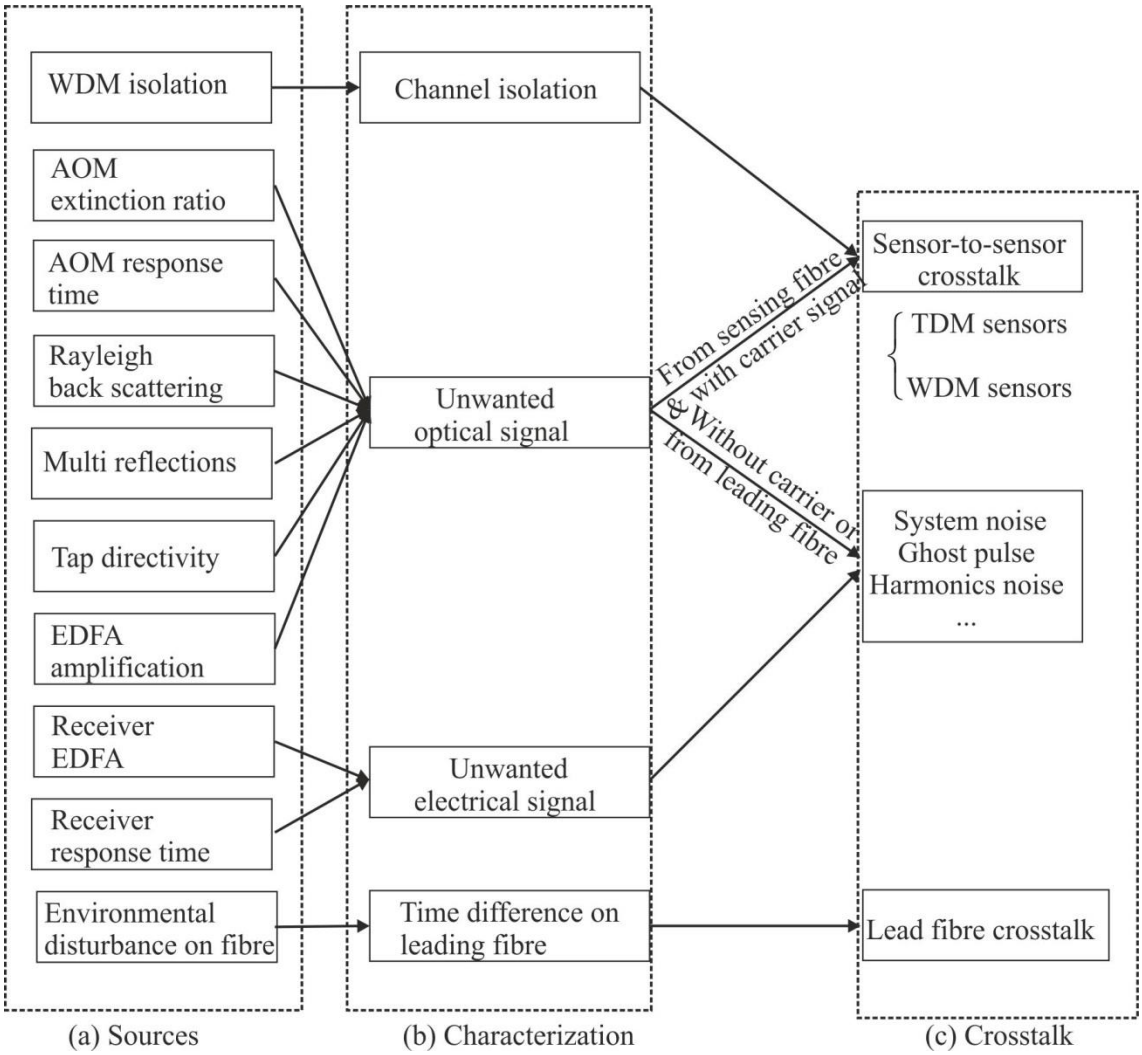

Figure 8.1: Demonstration of crosstalk (sources and effects) in multiplexed fibre sensor systems.

8.1.1 Crosstalk from non-ideal optical pulse generators

The channel crosstalk in a pulsed system is mainly caused by unwanted light pulse power when the optical gate is off, and the most general cause is a non-ideal optical pulse modulator used for input optical pulse generation. A practical optical pulse modulator has a limited extinction ratio (ER), i.e., when the optical pulse modulator is in the 'off' state, there is still a small amount of light passing through the optical pulse modulator, as illustrated in Figure 8.2 (a). The extinction ratio, which is defined as the ratio of the low power level (P_l, when the pulse modulator is off) and the high power level (P_h, when the pulse modulator is on), i.e., $ER = 10\lg(P_h/P_l)$, is of the order of 20 to 35 dB for a single Mach-Zehnder type optical pulse modulator and can reach 60 dB for a cascade pulse modulator consisting of two Mach-Zehnder interferometers [104]. The acousto-optic modulators (AOM) from GOOCH&HOUSEGO are usually used to produce

modulated pulse pairs in fibre interferometric sensor systems, and they have typical extinction ratios of 45 to 50 dB.

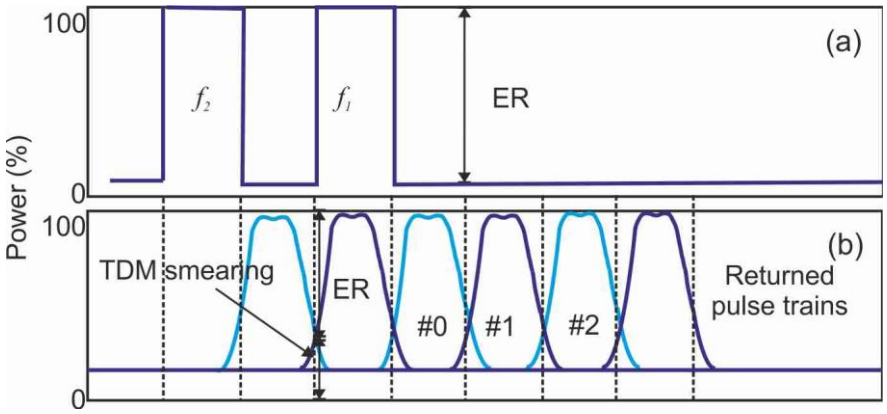

Figure 8.2: Schematic of optical pulses with (a) light still on at the 'off' state and (b) 'smearing effect' between returned interference pulses.

The generated pulses are also characterized with non-ideal rectangular shapes, which are determined by various limited rise/fall time from the control pulse, the RF switch, and the electro-optic modulator. The non-ideal pulse shape also introduces 'tails' to the following 'off' state and can be characterized by a 'smearing effect'. It leads to unwanted light power and smears following pulses (i.e., carried on information from previous sensors, and produce crosstalk between sensors), as illustrated in Figure 8.2 (b). The time smearing from a non-ideal pulse shape leads to crosstalk between sensors. Moreover, optical receivers with limited response time and bandwidth will introduce electrical crosstalk between adjacent pulses as well.

8.1.2 Crosstalk from amplifiers

The placement of optical amplifiers in a sensor system also influences the performance of the optical pulse in two ways. Firstly, the high ASE noise dominates when the optical gate is off, leading to an decreased ER, because the erbium has a relatively long relaxation constant of 8 to 10 ms, the ASE power level from the amplifier does not change immediately when the input signal is turned off for a period, smaller than the full relaxation time of the erbium. Ref [105] investigates that the output ER decreases as the peak optical power of the input pulse decreases, which is illustrated in Figure 8.3. My experimental investigation will show that this does not affect the 100 ns pulses in our applications.

Secondly, the transient gain dynamics of the EDFA induces a power spike, or overshoot at the leading edge of the output signal pulse, which is followed by steady gain conditions [51]. However, the transient effects of the gain saturation and recovery typically occur on a 100 μs to

1 ms time scale. My investigation in the previous Chapter 4 showed that there is no obvious shape changing during the 100 ns pulse duration.

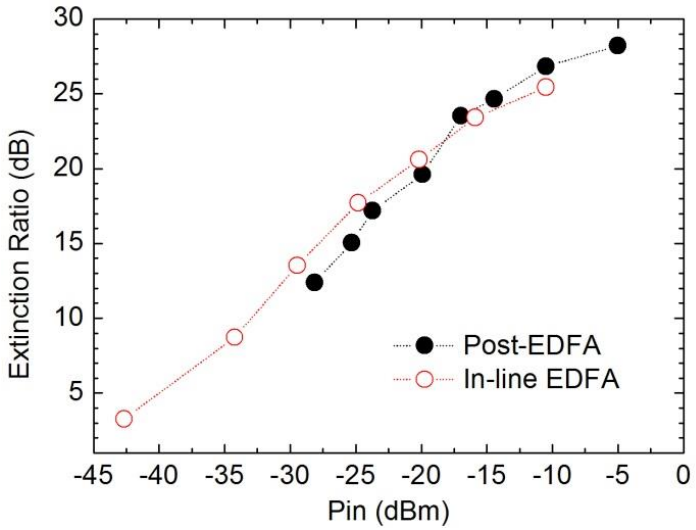

Figure 8.3: ER versus the peak optical power of the input pulse for an EDFA as a post-amplifier and in-line amplifier.

8.1.3 Crosstalk from passive optical components

It is also known that Michelson interferometer based sensor systems have additional crosstalk because of Rayleigh backscattering [106-108]. Rayleigh backscattering from the (high power) transmitted pulses would generate back-reflected light, indistinguishable and interfering with intended reflected modulated pulses returning from the sensor array. More seriously, the Rayleigh back scattering from the leading fibre to each OSU may be 17 dB (or the IL of the TDM groups) higher than other Rayleigh signals, increasing the crosstalk effect.

The reflected signal light from an non-ideal coupler with finite directivity would also interfere with the modulated signal, increase system amplitude noise and phase noise, and induce potential crosstalk to the system [109]. Multiple reflections resulting between partially reflecting components (e.g. connectors, imperfect fibre-to-fibre splices and fibre ends) may build up unwanted Fabry-Perot modes, which would significantly degrade the system performance as well [110]. Any two reflecting components in series would probably form such a Fabry Perot mode. However, isolators before and after these components in dual fibre unidirectional architectures can prevent this. The leading fibre will also induce crosstalk. In practice, a sensor network includes distribution bus and return bus fibres that serve as telemetry links. The telemetry fibres induce phase signals resulting from environmental disturbance.

8.1.4 Crosstalk from wavelength multiplexing

Crosstalk also exists between adjacent wavelength channels induced by the limited optical channel isolation of the wavelength multiplexers employed in WDM systems. Assuming the channel isolation in the demultiplexer employed at the final part of the multiplexed system in order to split off the individual sensor signals to go to detectors is A dB, the other undesired channel optical signal will leak into the desired channel, with an optical suppression of A dB, and both of the two signals will be received by the photo-detector. This corresponds to a crosstalk of −2A dB in the electrical domain.

The performance of the OA/DMs in the new array also influences the crosstalk level. The two main mechanisms that can give rise to crosstalk are known as: (1) inter-channel crosstalk and (2) intra-channel crosstalk. Inter-channel crosstalk refers to the power level of adjacent wavelengths that are coupled into the drop channel of the ODM from the pass channel on the distribution bus, through the TDM groups, and back into the pass channel from the add channel. This results in a small amount of power at all the other wavelengths passing through the TDM group. Inter-channel crosstalk causes unwanted light from adjacent channels to be coupled into each TDM group. However, with a channel isolation of 40 dB, adjacent channels undergo a minimum optical suppression of 80 dB for a ‘drop’ and ‘add’ process, and consequently optical crosstalk by this mechanism is −80 dB. Intra-channel crosstalk from OA/DMs refers to the amount of light at the drop wavelength that passes through the device into the pass channel rather than being coupled into the drop channel. This light will interfere with signals coupled back into the return bus, introducing an intensity noise floor to the system. Because of the double-pass process, the induced crosstalk is small enough to be negligible.

To summarize, all the unwanted low level power generated from the above sources result in crosstalk in two ways: those experiencing sensing fibres (modulated by the carrier signal) induce crosstalk between sensors, and produce unwanted modulation at other channels; others from leading fibre (interference-free signals) deteriorate the system sensitivity as they act as amplitude noise and phase noise, also introduce ghost pulses and produce parasitic harmonics. In the following section I will measure the channel crosstalk on the normal signal in the time domain and wavelength domain, separately. Discussions and conclusions will follow.

8.2 Sensor crosstalk in the TDM system

My previous investigation has revealed that non-ideal optical pulse generators, incorporated EDFAs and non-ideal passive optical components introduce channel crosstalk in the time domain; therefore here I have experimentally characterized the crosstalk level between time division multiplexed channels. The crosstalk investigation in all my experimental are all carried out on normal signals, because the modulation on the derivative signal will be ~60 dB lower.

8.2.1 Crosstalk measurement

I investigated the crosstalk in TDM systems by applying a phase modulation on one of the sensor coils, and measuring the demodulated phase spectrum on adjacent channels; my experimental procedure was as follows. For simplicity and to facilitate future comparison, this experimental investigation does not concern the distributed amplifier.

Optical light from a narrow linewidth fibre laser (NLFL) was pulsed and frequency-shifted and launched into a TDM sensor array. The TDM sensor array was composed of four OSUs, arranged in a tree configuration, each having four single sensors. The TDM group is composed of a total number of 16 sensors, as also shown in Figure 8.5. The fibre delay lengths of 200 m and 10 m between OSUs ensured that all the sensors were grouped in time. The returning signal from the TDM group was amplified again to compensate for the insertion loss of the TDM group, and was then beat at the compensating interferometer and was filtered at a four Channel DWDM Demux before injecting into an optical receiver.

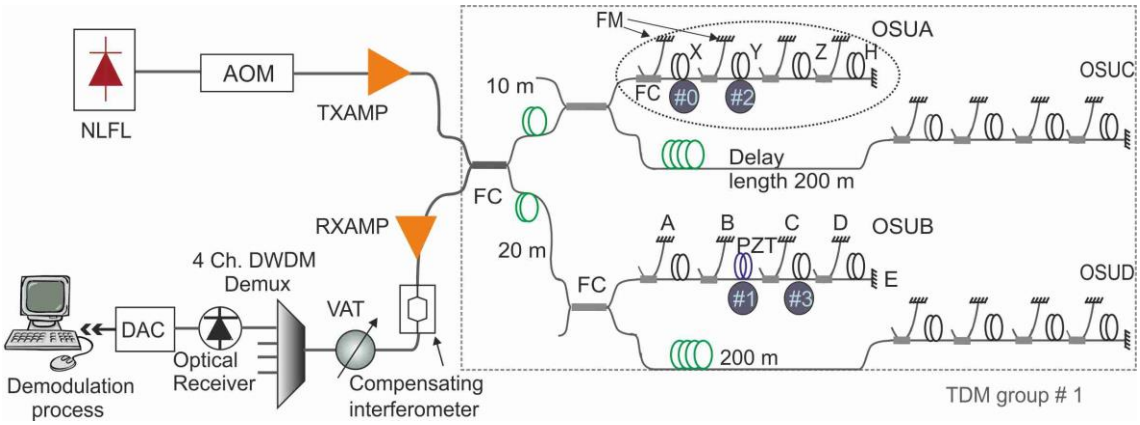

Figure 8.4: Experimental setup to characterize the crosstalk between sensors in the TDM group. The TDM group with 16 sensors was built to characterize the channel crosstalk in the time domain. OSU: optical sensor unit with four sensors. PZT: piezoelectric transducer. FM: Faraday mirror.

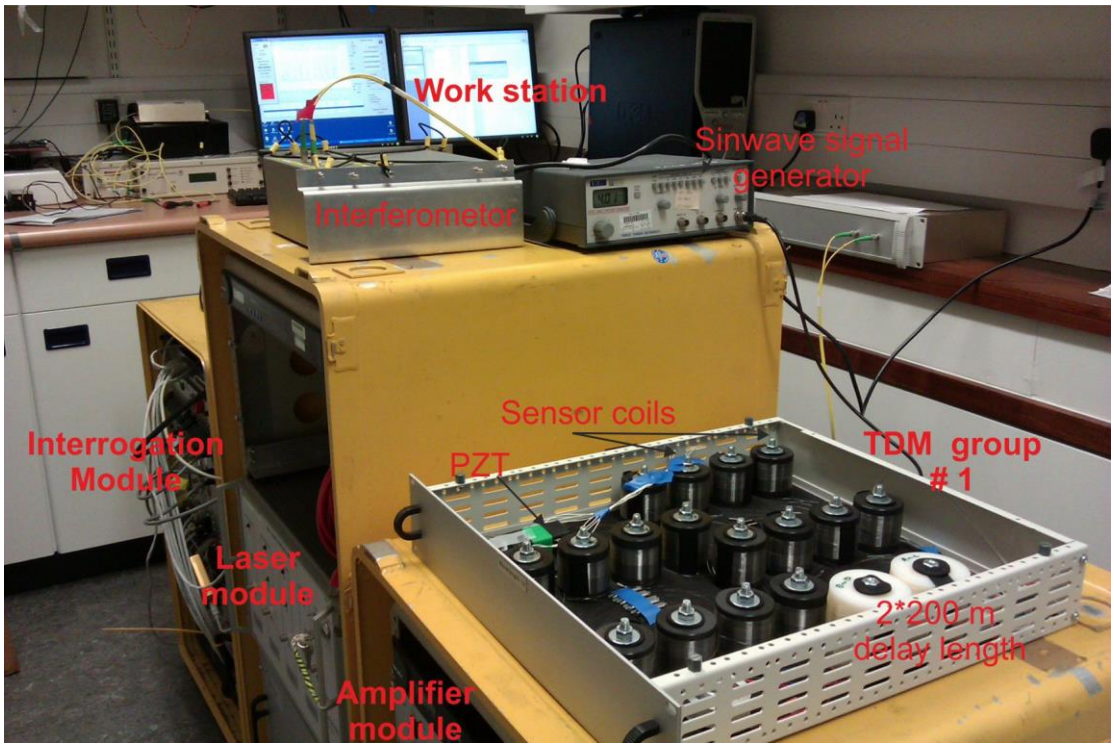

Figure 8.5: TDM sensor array and the interrogation system.

To characterize the crosstalk between these sensors, I wrapped the sensor coil between the mirror B and mirror C of the OSU B around a piezoelectric transducer (PZT). This sensor was defined as sensor # 1, and sensors whose normal channels are located afterwards as sensor # 2, sensor # 3, sensor # 4, and sensor # 5… in sequence. The time diagram of the return pulses from the TDM group is illustrated in Figure 8.6. The sensor before sensor # 1 is named as sensor # 0. A phase modulation at 223 Hz with a Vp-p (peak-to-peak voltage) of 3 volts was applied on sensor # 1, which causes a phase change equivalent to 1 radian (i.e., ~0.35 rad/V). The phase spectrum at sensor # 1 and its adjacent sensors were measured.

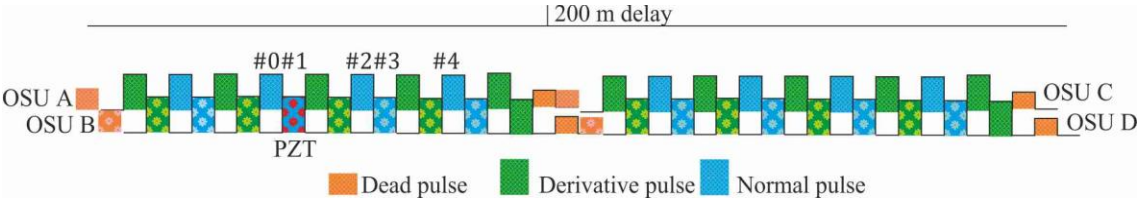

Figure 8.6: Time diagram for the return pulses from TDM group. The pulses from OSUB and OSUD are interleaved with the pulses from OSUA and OSUC, and they are shifted lower to show the interleaving. The PZT phase modulation is applied on the sensor # 1 in OSUB (Refer to Figure A.2).

8.2.2 Results

I first investigated the crosstalk at sensors located exactly before and behind, i.e., sensor # 0 and sensor # 2 when the phase modulation at 223 Hz is applied at sensor # 1. The measured phase spectra are illustrated in Figure 8.7 (a). It can be seen from the figure that a significant peak at 223 Hz was measured at sensor # 1 (in blue), but this peak also appears at sensor # 2 (in red), with the amplitude of −42 dB re rad/√Hz. There are also peaks at harmonics in the phase spectrum of these two sensors. However, no signal was observed at sensor # 0. The results reveal that the channel crosstalk in the TDM group is mainly caused by the 'smearing effect' and happened at sensors located afterwards. Therefore I also future measured the crosstalk in sensors behind sensor # 1, as characterized in Figure 8.7 (b). All the following sensors (# 2, # 3, # 4 and # 5) suffered crosstalk from the sensor # 1, and the crosstalk value ranged from −60 to −42 dB.

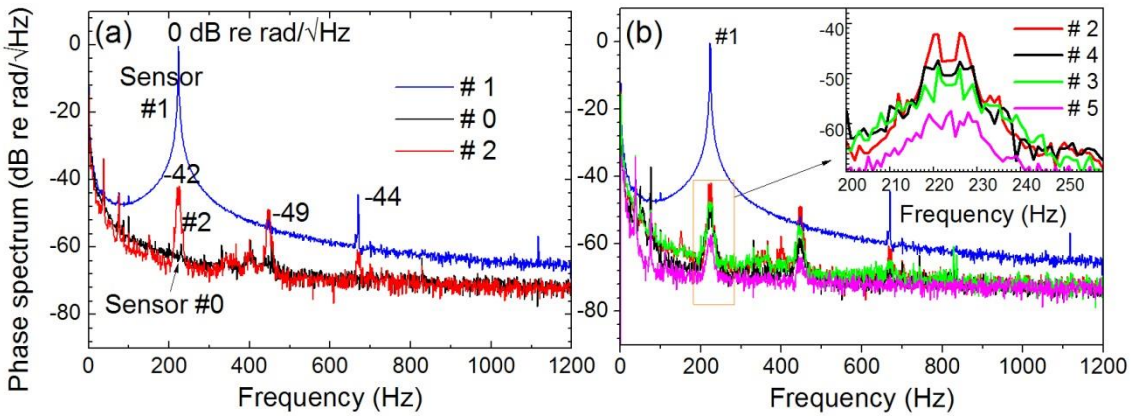

Figure 8.7: Measured phase spectrum at sensor # 1 and (a) adjacent sensors (before: sensor # 0, and behind: sensor # 2). (b) sensors behind (in order: sensor # 2, # 3, # 4 and # 5).

8.2.2.1 Crosstalk to other channels

I have concluded that crosstalk mainly results from the falling edge of imperfect pulse pairs. Therefore, I also investigated the performance of the pulses in the system in a qualitative way. The RF switch and the AOM are specified to provide a good extinction ratio as much as 38 dB, as stated in Table 8-1. However, the extinction ratio read from the captured electrical pulse shape was much smaller than 35 dB, as illustrated in Figure 8.8. it can be seen from Figure 8.8 (b) that the extinction ratio was only measured to be 29 dB when the pulse pair is 'off' for 5 µs. This is because the specified values from the supplier are provided when the pulse is 'off' for several hours, but in a pulsed fibre sensor system, most crosstalk is produced from the falling edge of the pulse pair where a second pair of pulses is returning with a separation of hundreds of

ns, as illustrated in Figure 8.8. The phase information from sensor # 1 carried by the pulse smeared into the following pulses for sensor # 2, # 3, # 4 and etc., therefore, the specified high ER cannot properly be used to predict the crosstalk, the smaller optical suppression in a time of hundreds of nanoseconds' allows crosstalk to later pulses much larger than from the specified ER.

Table 8-1: Specified rise/fall time and ER for the components to produce the pulse pair.

Components	***RF switch***	***AOM***			***Photo-receiver***
Supplier	Mini-circuits	GOOCH&HOUSEGO			NEWFOCUS
Product	ZYSW-2-50DR	80M	110M	200M	1811
Rise/fall time (ns)	6	35	25	10	3
ER (dB)	38 ~ 44	50			

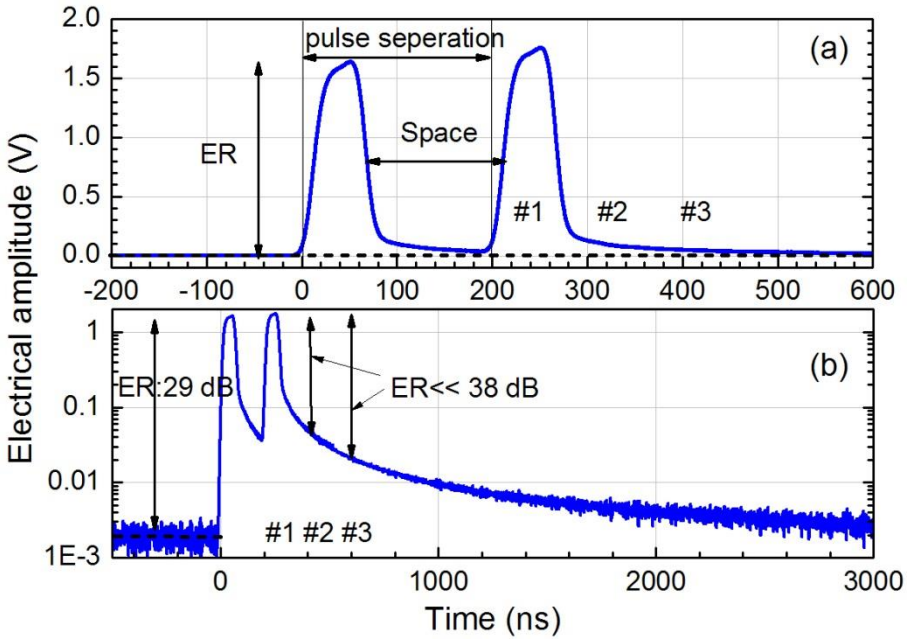

Figure 8.8: Waveform of the pulse pair produced by an AOM with (a) linear scale and (b) logarithmic scale.

8.2.2.2 Crosstalk vs. pulse width

Considering that the sensor-to-sensor crosstalk is mainly from the overlapping between returning pulses, I have reduced the pulse width of the launched pulse pair, to increase the space between the returning consecutive pulses, for crosstalk reduction. In the setup, the separation between return pulses was fixed at 100 ns and the pulse width decreased from 100 ns to 50 ns, producing pulse spaces from zero to 50 ns. Figure 8.9 demonstrates the performance of the interference pulse trains with pulse widths of 50 ns, 70 ns and 100 ns, separately. It can be seen

from Figure 8.9 that the observed optical level between beat pulses increases with an increase in the pulse width, therefore the SNR at each pulse decreases.

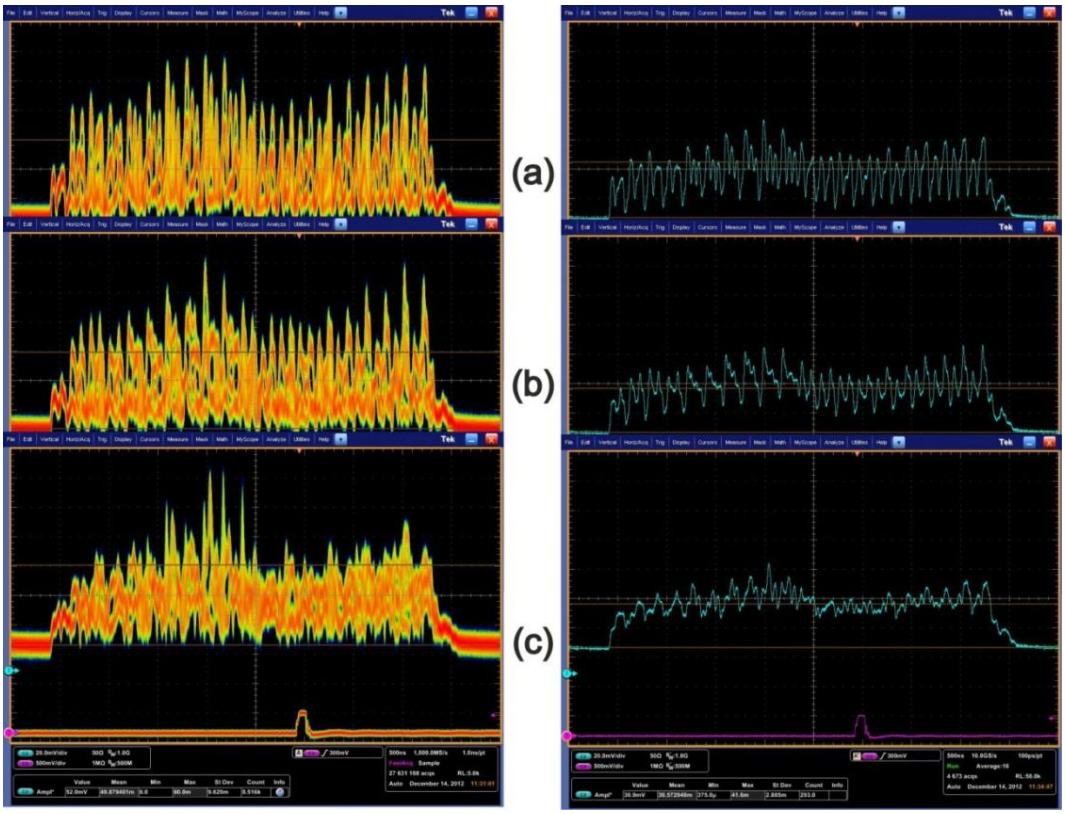

Figure 8.9: Captured pulse trains to the receiver from the TDM group with pulse widths of (a) 50 ns, (b) 70 ns, and (c) 100 ns. Length: 4.3 µs. Left images are the DPS acquisition waveforms, and right ones are the averaged waveforms, from a Tektronix DPO7104 Series Digital Phosphor Oscilloscope.

Figure 8.10 summarizes all the measured crosstalk values at sensors # 2, # 3 and # 4 as a function of the pulse width. It is clear that a larger space (off time between returned pulses from adjacent sensors) produces smaller crosstalk between sensors. The curves in Figure 8.10 indicate that we can achieve a crosstalk greater than −40 dB for pulse widths less than 90 ns (with pulse separation of 100 ns). The 1% (40 dB) crosstalk induced error is the critical acceptance value in sensor arrays. Improved crosstalk of −47 dB was achievable with pulse widths less than 60 ns. The crosstalk is bigger than −40 dB for pulse width of 100 ns, therefore, a fully occupied TDM arrangement, with no space between returned beat pulses, is not recommended in such systems, due to the ‘smearing effect’ induced crosstalk between channels.

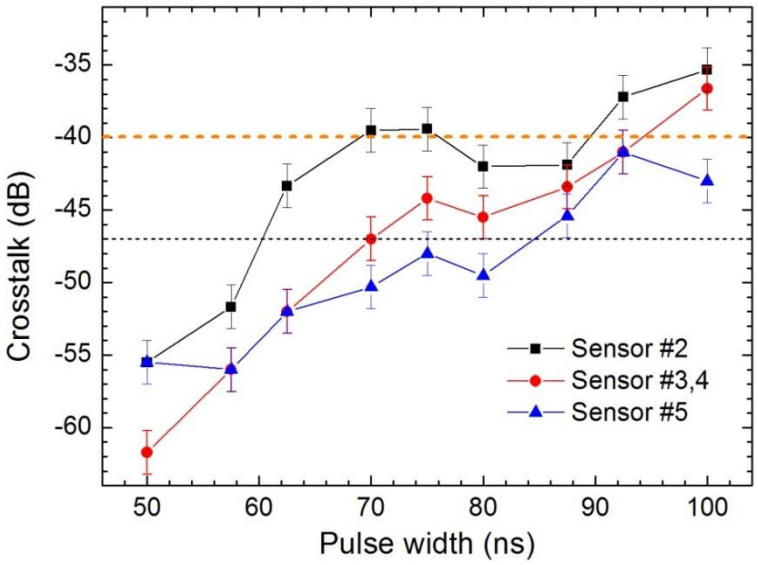

Figure 8.10: Measured crosstalk at sensor # 2, # 3, # 4 and # 5 as a function of the launched pulse width.

8.2.2.3 Crosstalk from EDFA

Amplifiers are commonly employed in current fibre sensor systems. However, the amplification performance of optical pulses, with pulse widths of several hundreds of nanoseconds, are not widely investigated and characterized. My previous simulation has shown that no significant transient response exists in these amplified pulses, thus here I emphasized the change of the extinction ratio after amplification. For an amplifier with the gain ≥ 20 dB, the output extinction ratio can be given by

$$ER_{out} = 10\lg\left(\frac{P_{ASE} + P_h G}{P_{ASE} + P_l G}\right) \tag{8.1}$$

In which P_{ASE} is the constant ASE power during the 'on' and 'off' state, and it increases with a decrease in the input P_h, because, with lower input optical signal, more pump power is lost to ASE. The equation shows a decrease in the extinction ratio after amplification with $GP_l < P_{ASE}$, and also indicates that lower input signal power P_h results in a worse extinction ratio.

I have captured pulse shapes before and after the transmitter amplifier (TXAMP). The launched average optical power is −7 dBm (four wavelengths), and the TXAMP provides a gain of 16 dB. The optical signal was captured with a NEWFOCUS 1811 photoreceiver and captured with a TeKronix digital phosphor oscilloscope 7104 (DC mode with 50 Ω loads). In order to increase the measurement dynamic range, to exactly record the electrical voltage at 'on' and 'off' state, I captured the pulse data with different instrumental resolution settings (i.e., internal amplifier

gain), and then combined them together for an extinction ratio analysis. An optical attenuator was also placed before the photoreceiver to avoid saturation, and to balance the power to the oscilloscope. The data are recorded in Figure 8.11.

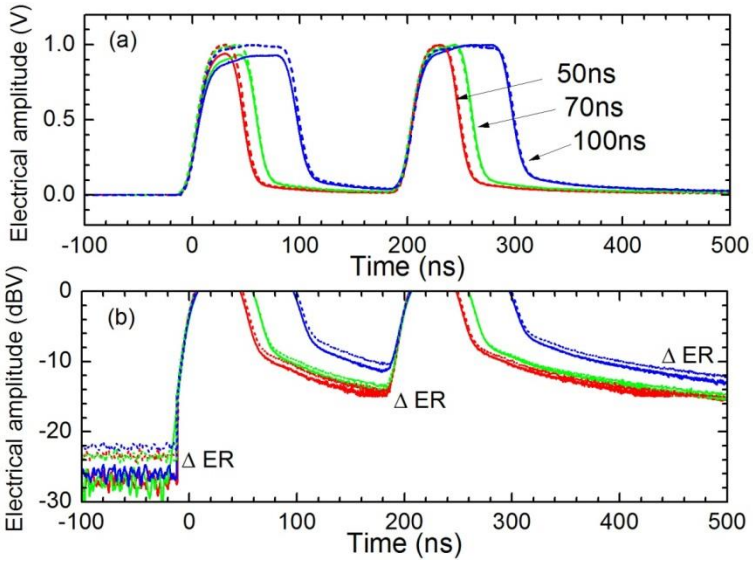

Figure 8.11: Comparison of the measured pulse pair before (line) and after (dotted line) the TXAMP, with pulse width from 50 to 100 ns.

The images in Figure 8.11 show the normalized pulse shapes before (line) and after (dotted line) amplification, with pulse widths of 50 ns, 70 ns and 100 ns in different colours. It is clear that the pulses remain the same shape after the amplification. No transient response and pulse broadening were observed, even with a 50 ns pulse width. However, the amplified low level light at the 'off' state increases more than the high level light at the 'on' state, introducing a worse ER after the amplification. Figure (b) shows the enlarged bottom part of the pulses in a logarithmic scale. It can be seen from the figure that the low level signal experienced a higher gain and ASE power during the 'off' state, introducing a deterioration in the extinction ratio of approximately 4 dB. This is in agreement with previous analysis. Nevertheless, the change in ER from amplification is less than that from the increase in pulse width.

8.2.2.4 Distortion at own harmonics

There were significant signal peaks for the second and third harmonics observed at sensor # 1. This can be explained by the Jacobi-Anger expansion of the phase modulated signal (previously discussed in Chapter 5) by

$$e^{i\phi_0 \cos\omega_m t} = J_0(\phi_0) + 2\sum_{n=-\infty}^{\infty} J_n(\phi_0)\cos\omega_m t \tag{8.2}$$

where $\phi_0 \cos\omega_m t$ is the phase signal of the interest, and $J_n(\phi_0)$ is the *n*-th Bessel function, with its values shown in Figure 8.12. It can be seen from the figure that when $\phi_0 \ll 1, J_0(\phi_0) \approx 1$ and $J_1(\phi_0) \approx \phi_0/2$, the contributions from the 2nd and 3rd harmonics are small enough to be ignored. However, when the amplitude of the phase signal ϕ_0 becomes larger, the contributions to the harmonics increase. Especially when $2.6 < \phi_0 < 6.1$, $J_2(\phi_0) > J_1(\phi_0)$, and when $3.8 < \phi_0 < 6.7$, $J_3(\phi_0) > J_2(\phi_0) > J_1(\phi_0)$.

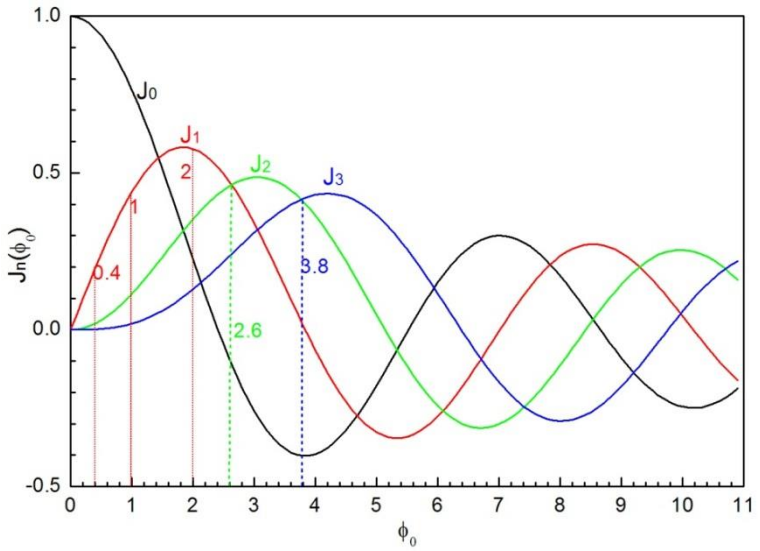

Figure 8.12: Bessel functions for n=0, 1, 2, 3.

In our applications, the amplitude of the applied phase modualtion ϕ_0 ranges from 0.4 rad to 2 rad, resulting in significant 2nd and 3rd harmonics. This would be helpful to explain the existing harmonics. However, it is hard to explain why the 3rd harmonic is larger than the 2nd harmonics, and there are two possible reasons: one can be the intensity noise from the unwanted light power, and the other is from the PZT modulation itself. The intensity noise induced harmonic depends on the phase mismatch between the modulated signal and the unwanted signal, thus it is complicated to verify. The predicted distortion level is found to be sensitive to the phase mismatch and optical field extinction ratio, as discussed in Appendix C.

Here I characterize the phase modulation response in a single PZT. The PZT under test is similar to the one in sensor # 1. It acts as the unique sensor in an sensor array. I have applied a phase modulation at 223 Hz (Vp-p of 2 volts) on the PZT, and the measured phase spectrum is shown in Figure 8.13 (a). The figure indicates that there are some harmonic responses from the piezoelectric ceramic material, showing a −55 dB lower peak at the 2nd harmonic and a larger −46 dB lower peak at the 3rd harmonic.

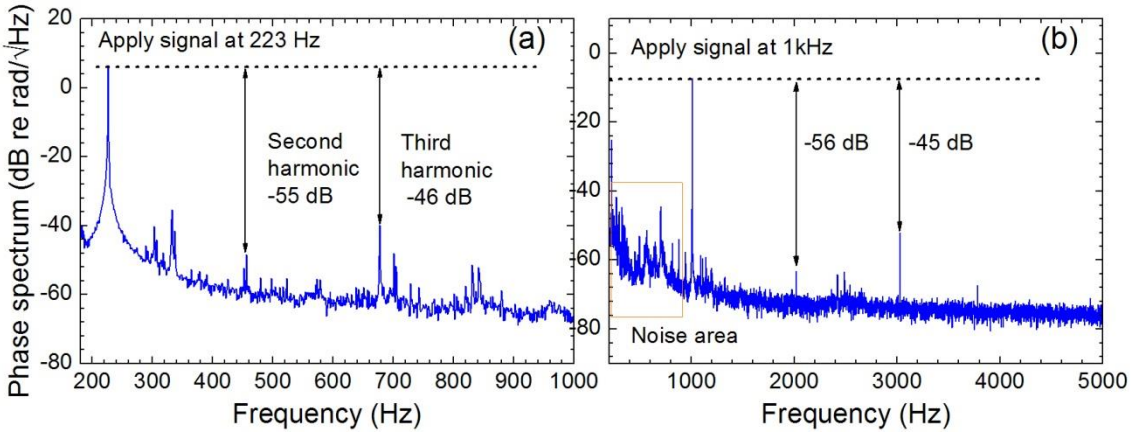

Figure 8.13: Measured phase spectrum at a similar PZT stretcher, with applied phase modulations of (a) 2 rad (6 dB re rad/√Hz) at 223 Hz, and (b) 0.4 rad (−8 dB re rad/√Hz) at 1 kHz.

There are other some random peaks between the harmonics in Figure 8.13 (a). In order to tell whether these random peaks are at PZT's eigen-frequencies, or modulation frequency related, I further characterized the phase spectrum response with a sine phase modulation at 1 kHz, as illustrated in in Figure 8.13 (b). The result reveals that those noise peaks only happen at a low frequency range. No significant peaks between harmonics were observed. The noises below 1 kHz might come from intrinsic resonances in the PZT.

Although characterization of the PZT has shown a similar and larger phase modulation at the 3rd harmonic than at the 2nd harmonic, it is not safe to declare that they are intensity noise independent, therefore I only conclude that these harmonics would come from the Jacobi-Anger expansion, the intensity noise and the PZT's sub-harmonic resonance response together.

8.2.2.5 Conclusion

I have measured and analysed the sensor-to-sensor crosstalk in a TDM group with 16 sensors. With pulse width less than 90 ns and returned pulse separation of 100 ns, the channel crosstalk to adjacent sensor located behind, ranges from −60 dB to –40 dB, and the crosstalk to front sensors is indiscernible. All the measured crosstalk in the current system is less than 1% with pulse width less than 90 ns; this crosstalk level is in our acceptance range.

The crosstalk is mainly due to the smearing effect on the adjacent pulses. With fixed input separation, the crosstalk increases with the pulse width. Crosstalk less than –47 dB can be achieved with pulse separation less than 60 ns in the current sensor system. The employment of an optical amplifier will not induce pulse broadening, and only introduces an extinction ratio of approximately 4 dB in the setup investigated. An applied phase modulation signal with the

amplitude ϕ_0 over 1 rad introduced significant harmonics. Distortion at harmonics observed at the sensor were explained by interference with unwanted signals and PZT' sub-harmonic resonance response. The distortion level is lower than –44 dB.

8.3 Sensor crosstalk in the WDM system

As stated previously, I have found that channel isolation in wavelength multiplexers is an important factor in crosstalk suppression between wavelengths. Assuming that the ratio of the crosstalk channel light intensity to another channel is poor, the other undesired channel optical signal will leak into the desired channel, and both of the two signals will be received by the receiver. However, as the detector cannot distinguish between them, a superimposition of the signals will be created and passed to the digital phase demodulator, consequently the corresponding output will be wrong. For this reason I investigated the sensor-to-sensor crosstalk between two TDM groups, driven by two adjacent wavelengths, by incorporating OA/DMs and WDMs into the sensor system.

8.3.1 Crosstalk measurement

My setup for the crosstalk investigation in the wavelength domain is as follows: light from two fibre laser sources with adjacent wavelength at ITU grid channels of Ch39 and Ch40 were multiplexed at a WDM and then pulsed, frequency shifted and amplified before launching into the sensor array. Returning light from the sensor array was demultiplexed in a second WDM before injecting to the optical receiver. The sensor array was composed of two TDM groups and two OA/DM pairs. At the first ODM, the signal at wavelength Ch39 is coupled into the TDM group # 1 (all sensors driven by Ch39, includes the PZT stretcher of sensor # 1-1), and was then coupled onto the return bus through the OAM. The remaining wavelength at Ch40 continues to the ODM40 and was coupled to the TDM group # 2 under test, then coupled back as well.

Due to the interrogation arrangement, the pulse trains from the two TDM groups will arrive at the receiver simultaneously, introducing channel crosstalk. To investigate the senor-to-sensor crosstalk between TDM groups, I applied a sine phase modulation at 1 kHz with a Vp-p amplitude of 5 volts, equivalent to 1.78 radians on the PZT stretcher in the sensor # 1-1 of the TDM group # 1. The frequency of 1 kHz was chosen to avoid the noise from the PZT eigen-frequencies as investigated previously. The higher amplitude was chosen to increase the dynamic range of the crosstalk measurement, since we have shown previously that the sensor-to-sensor crosstalk should be smaller than −80 dB.

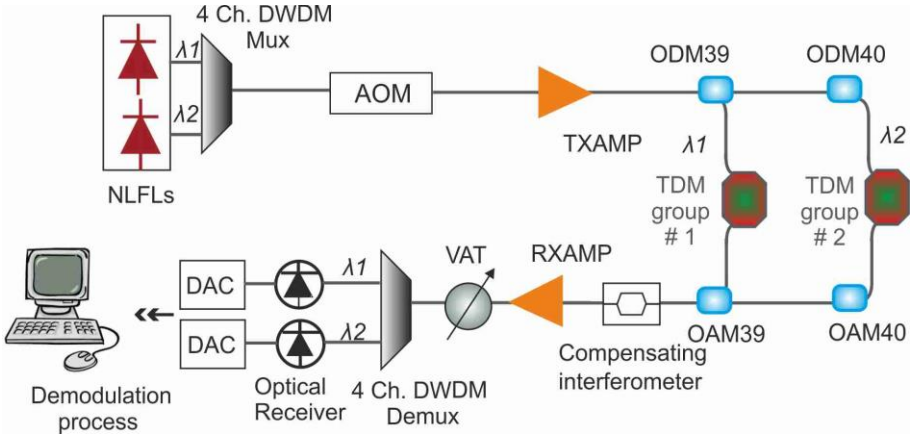

Figure 8.14: Experimental setup to characterize the crosstalk between sensors of which pulses arrive at the receiver simultaneously.

Figure 8.15: Wavelength multiplexed TDM group # 1 and # 2, each with 16 sensors.

8.3.2 Results

I have measured the phase spectrum at sensor # 1-1 with applied sin phase modulation signal, and the sensors in TDM group # 2, some of them were characterized in Figure 8.16. No crosstalk was observed, so it is clear that the crosstalk from the modulated sensor to sensors in TDM group # 2 is smaller than −76 dB. Sensor # 2-1 in the TDM group # 2 shared the same times slots but were driven by different wavelengths, thus providing us with the maximum possible crosstalk. However, the crosstalk value is smaller than −76 dB, thus we can safely conclude that the sensor-to-sensor crosstalk between different TDM groups, driven by adjacent wavelengths, is better than -76 dB.

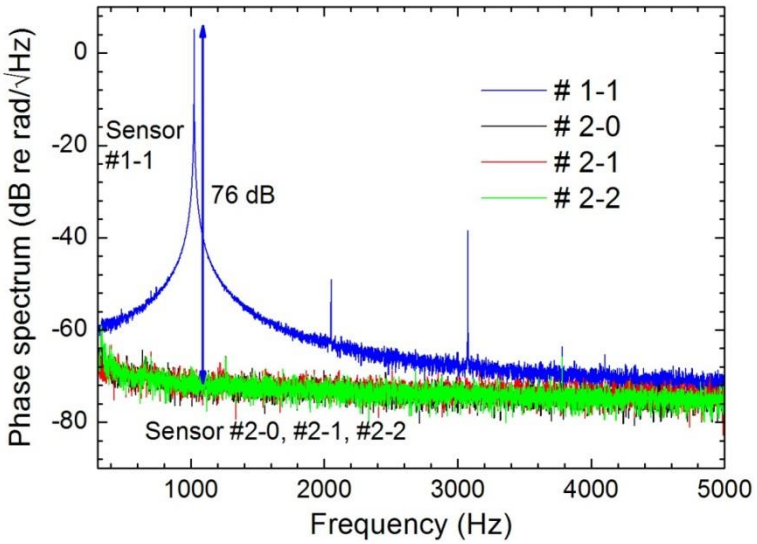

Figure 8.16: Measured phase spectra at sensor # 1-1 of TDM group # 1 (driven by wavelength at Ch39) and sensors in the TDM group # 2 (driven by wavelength at Ch40).

8.3.3 Discussion and conclusions

The crosstalk between sensors driven by different wavelengths is determined by the channel isolation between wavelengths. For simplicity, when there are only two channels with different wavelength λ1 and λ2, and equal optical power. The corresponding two channel outputs of the detectors can be given by

$$\begin{aligned} I_1 &= P_s R[1 + V\cos(\omega_{IF}t + \varphi_1(t))] \\ I_2 &= P_s R[1 + V\cos(\omega_{IF}t + \varphi_2(t))] \end{aligned} \tag{8.3}$$

In which $\varphi_1(t)$ and $\varphi_2(t)$ are the phase shifts induced by two sensors from two adjacent TDM groups (driven by λ1 and λ2). Assuming the crosstalk channel light intensity to another wavelength channel is *m*, then the superposition of signals of I_1 and I_2 at the receiver output of λ1 can be written as

$$\begin{aligned} I &= I_1 + mI_2 \\ &= P_s R[1 + m + V\cos(\omega_{IF}t + \varphi_1(t)) + mV\cos(\omega_{IF}t + \varphi_2(t))] \end{aligned} \tag{8.4}$$

The signal *I* provides the input of the arctan demodulation arithmetic, which is described in earlier chapters. The total demodulated phase, is given by

$$\tan\psi = \frac{\sin\varphi_1(t) + m\sin\varphi_2(t)}{\cos\varphi_1(t) + m\cos\varphi_2(t)} \tag{8.5}$$

The maximum ratio of the sensor crosstalk from λ2 to λ1 is given by

$$C_{WDM} = 20\lg(\frac{m\varphi_2(t)}{\varphi_2(t)}) \tag{8.6}$$

If the channel isolation generated by both the DWDM and OA/DM is $A = -10\log10(m)$, then crosstalk is 2A.

Here the WDM and OA/DMs are characterized. Figure 8.17 (a) shows that the transmission spectrum at three adjacent channels (labelled as Ch1, Ch2 and Ch3) of an 8 channels WDM multiplexer which is similar to the one used in my study. The input signal to the WDM is a wideband ASE source. It can be seen from the figure that although the WDM shows a very small isolation at the overlap areas between each two curves, my input probe signal has a very narrow linewidth of less than 10 kHz, located at the centre at these channels, thus the actual optical suppression in our study is 45 dB, which results in a good sensor-to-sensor crosstalk of −90 dB.

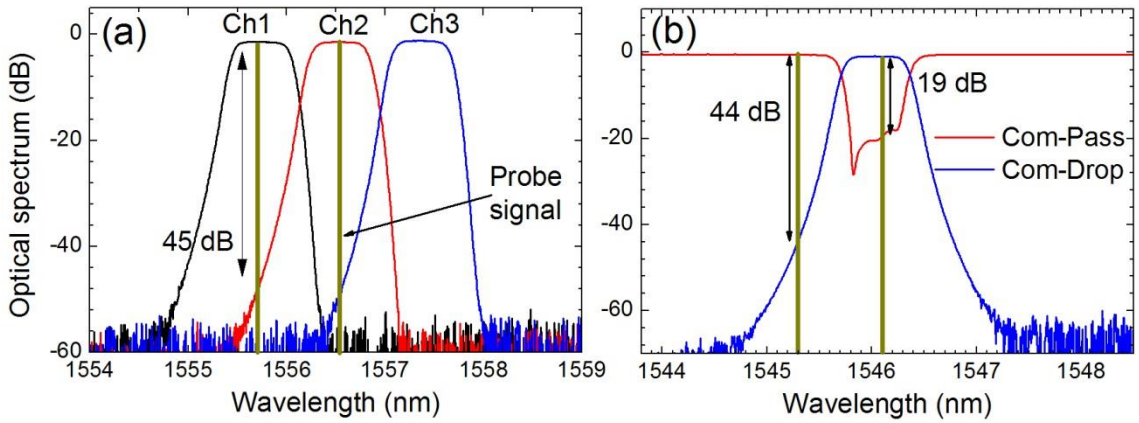

Figure 8.17: Optical transmission spectrum of the (a) 8-Ch WDM and (b) optical add/drop multiplexer at Ch39.

Figure 8.17 (b) shows the transmission spectrum of an ASE source from the common channel to the pass channel (red curve), and drop channel (blue curve), separately. The channel isolation, at the probe wavelength of 1545.3 nm to the drop channel, is 44 dB. This results in a small amount of power at other wavelength (e.g., 1545.3 nm at Ch40) passing through the modulated TDM group (driven by 1546.1 nm at Ch39), resulting in a phase signal modulation at Ch40. This signal will be demodulated as a phase signal applied at the synchronous sensor (# 2-1) driven by Ch40, introducing crosstalk. However, these channels undergo a minimum optical suppression of 88 dB for an 'add' and 'drop' process, and consequently the inter-crosstalk by this mechanism is –160 dB. Another source of crosstalk introduced by OA/DM is the intra channel crosstalk. The 19 dB of isolation at the drop wavelength to the pass channel transmits along the distribution bus and returns when the sensor array is closed at the end. Our array is open at the

far end to eliminate this light. Even if the array is closed, this light will only contribute as an intensity noise floor (and harmonics distortion), in the absence of any crosstalk to other channels.

To conclude, I have tested and discussed the sensor-to-sensor crosstalk between synchronous TDM groups, driven by adjacent wavelengths. Test results and theoretical analysis show that this crosstalk is less than −76 dB, which can be ignored in such systems. The crosstalk is mainly determined by twice the channel isolation value (in dB) of the WDM before the receiver. The effects from the OA/DM pairs are much smaller. However, these values are provided when the system is interrogated by a signal with narrow linewidth and with signal wavelengths located at the centre of the channels in the multiplexers. When these two conditions are not satisfied, the crosstalk will increase.

8.4 Conclusion

This chapter has characterized the crosstalk between sensors. Many sources in a multiplexed sensor system introduce crosstalk. Among these sources, low level light induced by non-ideal optical pulse generators dominates, especially the light smearing at pulse edges. The low level light produces crosstalk between sensors multiplexed in the time domain. With pulse width less than 90 ns and return pulse separation of 100 ns, the crosstalk to adjacent sensors range from −65 dB to −40 dB, and the crosstalk to earlier sensors is indiscernible. With fixed input separation, the crosstalk decreases with the space increment. Crosstalk less than – 47 dB can be achieved with pulse separations of less than 60 ns in the current sensor system. Unwanted low level optical signals also introduce distortion at harmonics. Due to the long coherence length of the fibre laser source, the phase mismatch between the signal and the unwanted signal is almost zero. This introduces a larger distortion at the 3rd harmonic than it does at the 2nd harmonic. However, this distortion is less than −44 dB for both harmonics. The sensor-to-sensor crosstalk between different TDM groups driven by adjacent wavelengths is smaller than −76 dB. The crosstalk is found to be double the value of the channel isolation.

In conclusion, all the measured crosstalk in a network without in-array network is less than 1% (−40 dB) with pulse space larger than 10 ns (100 ns pulse separation); this crosstalk level is in the acceptance range. I will measure and compare the crosstalk in an amplified network in the following Chapter.

Chapter 9

Demonstration of 16 TDM × 16 WDM and 64 TDM × 16 WDM sensor arrays

Overview: This chapter gives details of a laboratory demonstration of the distributed amplified system with real TDM groups. First with 16 simulated sensors in each TDM group (200 kHz sampling rate), then with 48 sensors (50 kHz sampling rate), to allocate more sensors in each period. In this way, the overall performance of the proposed sensor network is characterized in this chapter, showing the performance of the phase sensing. A phase modulation was applied on one of the sensors in the TDM group and successfully monitored with good performances. In this way, 64 (TDM) ×16 (WDM) network was experimentally demonstrated.

9.1 Distributed amplified network 16× 16 sensors

9.1.1 Experimental setup

In previous chapters, I have built up three TDM groups, each with 16 inline Michelson interferometric sensors. Moreover, the channel crosstalk in these TDM groups has been studied. In this chapter I configured these TDM groups into a distributed amplifier sensor array.

I have configured the setup as shown in Figure 9.1, with the lab arrangement shown in Figure 9.2. The setup is similar to the 16-wavelgnth proof-of-principle experimental setup in Chapter 7. Except that this has two fully populated TDM groups, incorporated as two of the 16 wavelength channels for signal interrogation. As previously designed, one of the interferometric sensor coil is wrapped around a PZT stretcher, thus can be phase modulated for interrogation. To access the worst system performance, this TDM group is placed at the last wavelength channel. TDM groups at other wavelength channels are replaced by tunable attenuators, incorporated between each OA/DM pair.

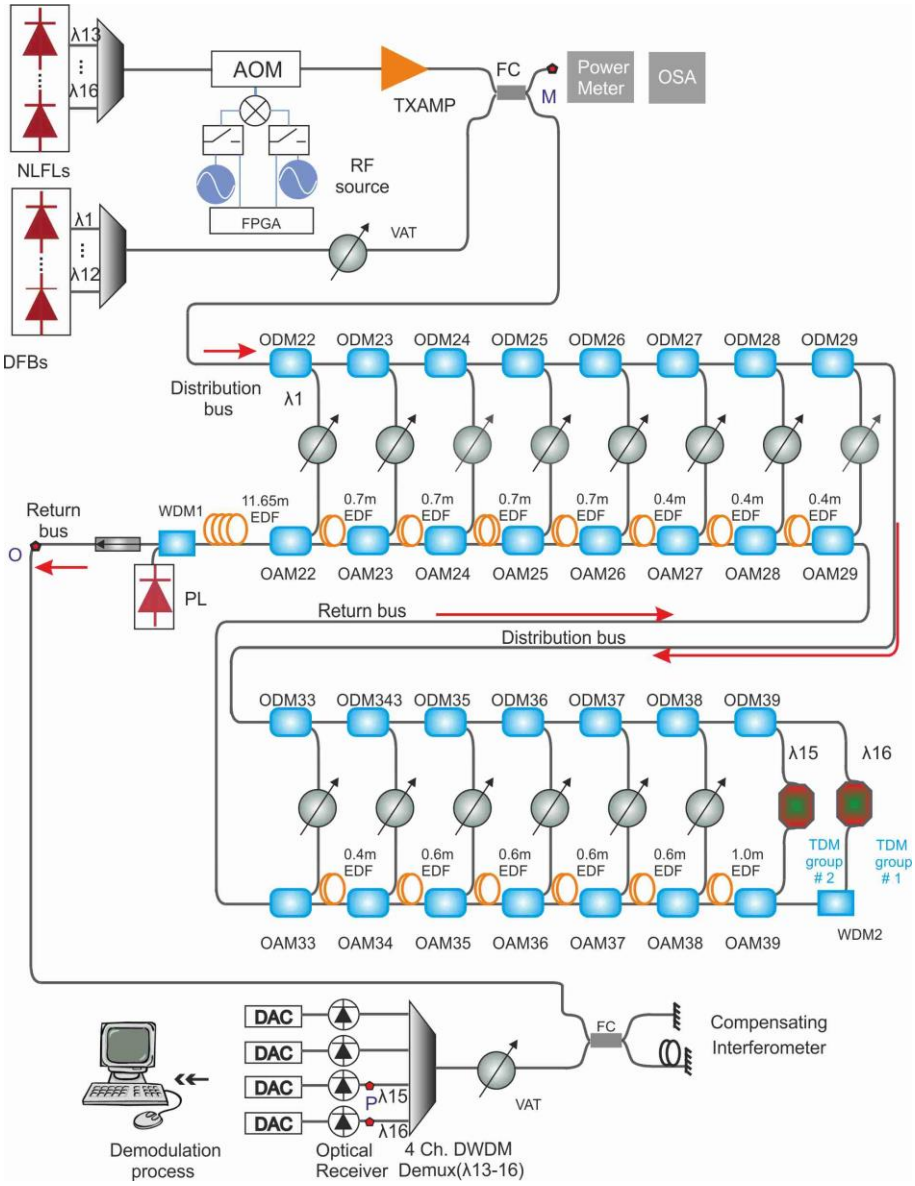

Figure 9.1: Experimental setup for the distributed amplified sensor system with real TDM groups employed. NLFL: narrow linewidth fibre laser source, TXAMP: transmitter optical amplifier, FC: fiber coupler, DWDM Demux: wavelength demultiplexer. DAC: digit analog converter. Pulse repetition: 200 kHz. Pulse separation: 200 ns. Pulse width: 50 ns. Return pulse train: 4.2 μs.

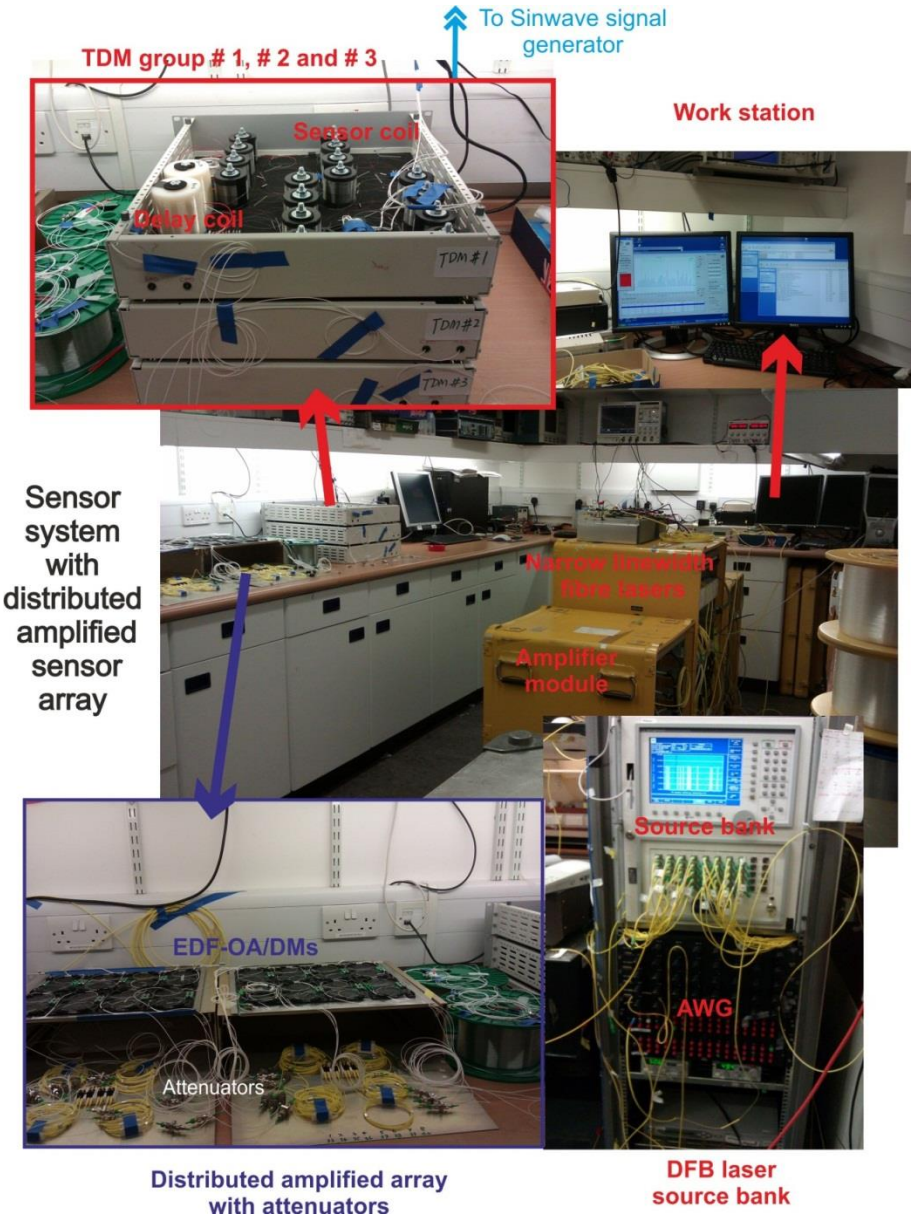

Figure 9.2: Interferometric sensor system with a 16×16 sensors array. AWG: arrayed waveguide gratings.

9.1.2 Experimental results

9.1.2.1 Output spectrum and phase noise floor

The OSNR at the sensor array output indicates effects from the ASE upon the system phase noise floor, and can be utilized to predict the system capability. Therefore, I have measured the output optical spectrum of the distributed amplified network, which is shown in Figure 9.3. The spectrum in the figure shows good signal performance, with system OSNR better than 30 dB for all channels.

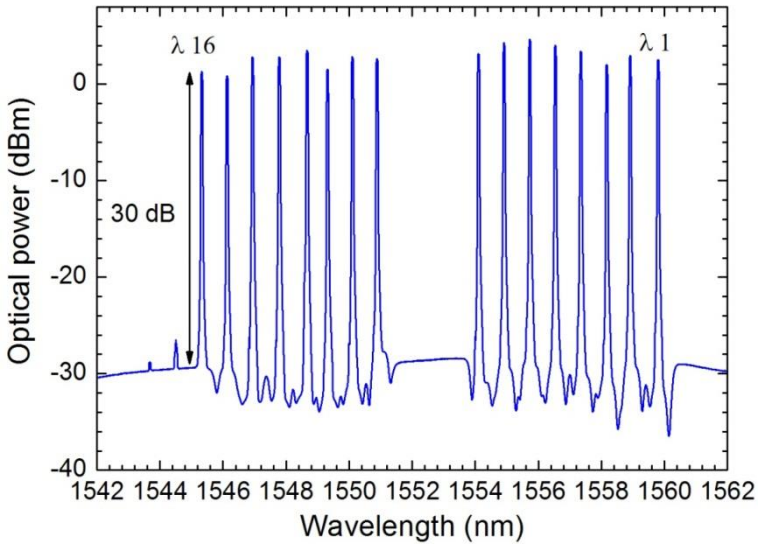

Figure 9.3: Measured output optical spectrum from a real sensor array. Pump power is 63 mW. Input average power at monitoring point M is 3.7 dBm per wavelengths.

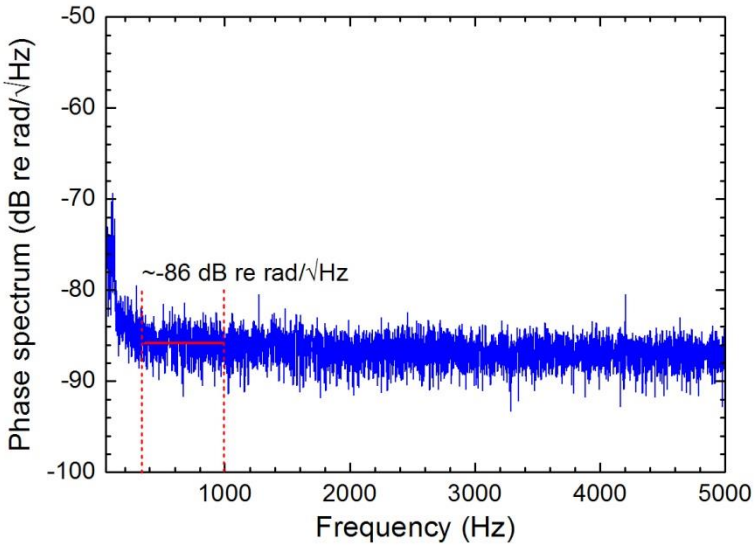

Figure 9.4: Measured phase noise floor of the derivative channel of one sensor in TDM group # 2 (driven by wavelength λ 15) in the sensor array with a distributed EDFA.

The distributed amplified network has demonstrated its capability for expansion, in the absence of performance degradation. Scaling up to 16 × 16 sensors in the network, the system is still equipped with a phase noise floor independence on any effects of ASE accumulated in the distributed amplifier. Figure 9.4 shows the measured phase noise floor at one of the sensors in the TDM group, the system phase noise floor is better than −86 dB re rad/√Hz, with a flat phase spectrum over the frequency range from 300 Hz to 5 kHz.

9.1.2.2 Phase interrogation and crosstalk

A sine signal with a peak to peak voltage of 5 volts at 1 kHz was applied on the PZT stretcher (sensor # 1-1 in TDM group # 1). As characterized previously, this will produce a phase modulation with a peak value of 1.75 rad, which is demodulated from our sensor system, as shown in Figure 9.5. It can be seen from the figure that there is a significant peak value of 4.5 dB re rad/√Hz at 1 kHz in the demodulated phase spectrum, with an excellent SNR of approximately 55 dB. This figure also demonstrated the phase spectrum from its adjacent sensors in the same TDM group, with # 1-0 before it and # 1-2 located after it. Similar to the crosstalk we studied previously, there were harmonics and crosstalk on the sensor behind it. The pulse width is set at 50 ns to reduce the crosstalk effect, thus the crosstalk is smaller than −55 dB, which indicates that the crosstalk can be ignored in such systems with a distributed amplified network (as stated previously, the acceptance is – 40 dB). The measured crosstalk is the same as our previous measured values in sensor networks without the distributed amplifier.

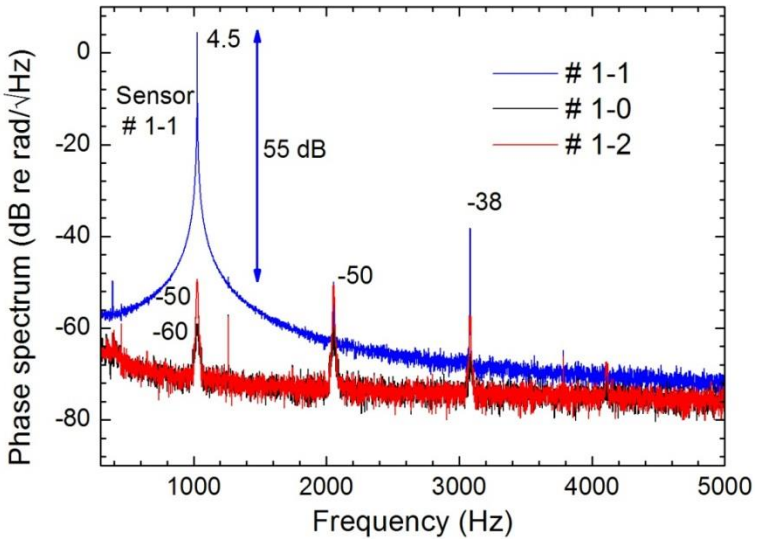

Figure 9.5: Measured phase spectrum at sensor # 1-1 and crosstalk to adjacent sensors in the hybrid multiplexed array with a distributed amplifier.

Because of the implication of amplification in the sensor array, the channel crosstalk between wavelengths would be larger than that in a non-amplified-network. So, I have also investigated the crosstalk between the two TDM groups. Figure 9.6 illustrated the measured phase spectra for the modulated sensor # 1-1 and the synchronous sensors in the other TDM group, in which sensor # 2-1 shares the same time slot with # 1-1, but driven by different wavelengths. As predicted, this is worse than the previous measured values in the network without distributed amplifiers; the crosstalk increases from indistinguishable peaks to −60 dB in the distributed amplified system. However, the crosstalk level is still far away from our range of concern.

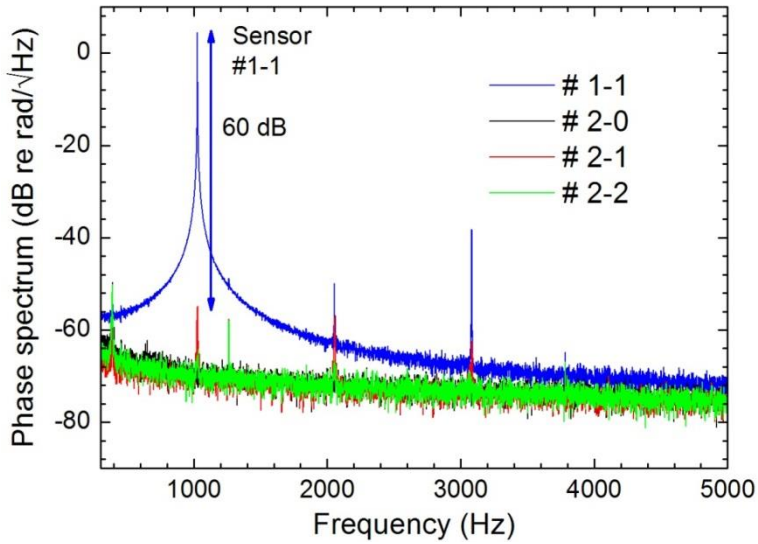

Figure 9.6: Measured phase spectrum at sensor # 1-1 from TDM group # 1 (driven by wavelength λ16) and crosstalk at sensors in the TDM group # 2 (driven by wavelength λ15) in the real sensor array with a distributed EDFA.

9.1.3 Conclusion

The investigation on the optical performance and phase noise floor, together with the phase interrogation from the sensors in the real 16×16 sensor array indicate a good performance of the distributed amplified network. Experimental results illustrate that the system phase noise floor is not affected by the ASE noise at all, and it provides us with a phase sensitivity of −88 dB re rad/√Hz. Compared with previous results from Chapter 8, the incorporation of the distributed amplifier does not change the crosstalk in the time domain, but only introduce some crosstalk in the wavelength domain. However, the crosstalk in the time domain and wavelength domain is low, down to −55 dB and −60 dB, separately, which is far less than our acceptance range of −40 dB.

9.2 Amplified network with 64×16 sensors

9.2.1 Measurement setup

To further demonstrate the scaling up ability of the recommended array architecture, I have time multiplexed the three 16 sensor TDM groups above into a TDM configuration capable of multiplexing 64 sensors, but with $3 \times 16 = 48$ sensors present due to lab limitations. I used couplers and delay coils to combine the contributions from the three 16 sensor TDM groups together, with no sensors connected in place of the 4th 16 sensor TDM group. Figure 9.7 shows

the 64-sensor TDM group with 48 of the 64 sensors present, with a delay time of 5 μs between adjacent sub TDM groups. The insertion loss of the new TDM group is measured to be approximately 42 dB (expected of 41 dB with 64 sensors in the TDM group from Table 7-2) for sensors in TDM group # 1 and # 2.

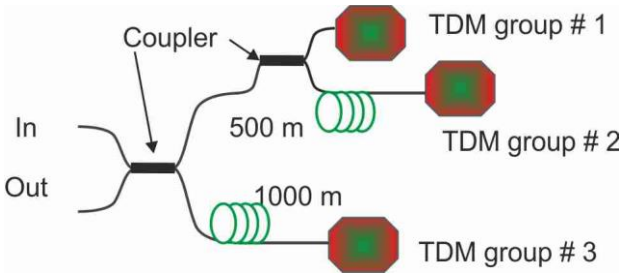

Figure 9.7: New TDM group with 48 sensors inside.

The new-built TDM group was placed at λ2 and λ15 in the network separately, to characterize the system performance. The remaining optical part is similar to the setup shown in Figure 9.1, with the following adjustments to allow for the higher TDM

1) The pulse repetition period (rate) was increased (decreased) from 5 μs (200 kHz) to 20 μs (50 kHz), to leave time for replies from 64 sensors. Accordingly, the carrier frequency was reduced from 50 kHz to 12.5 kHz.
2) The optical signal after the compensating interferometer was launched into a commercial optical receiver (New Focus 1811 Photoreceiver with 125 MHz bandwith) and captured by a digital phosphor oscilloscope (DPO 7104). Therefore the time routing and arctan phase demodulation process is carried out in Matlab, instead of using a digital circuit.

An effective way to reduce the TDM aliased noise components would have been to use the same pulse repetition rate as the 16 sensor TDM group, but to decrease the pulse width for each sensor. However, this would have required the sensor coils in each sensor to be produced with a tighter error margin than the previous timing design, and would have required shorter interrogator response time to make measurements within the narrower pulse. The sensor coil length accuracy was ±1 m, which leads to a time accuracy of ±10 ns in pulse constituent, a value incompatible with the 25 ns pulse duration that would have been required to keep the same overall pulse repetition rate. For these two reasons, the pulse width was kept at 100 ns, and the pulse repetition period reduced to 20 μs, at the expense of increased aliasing noise.

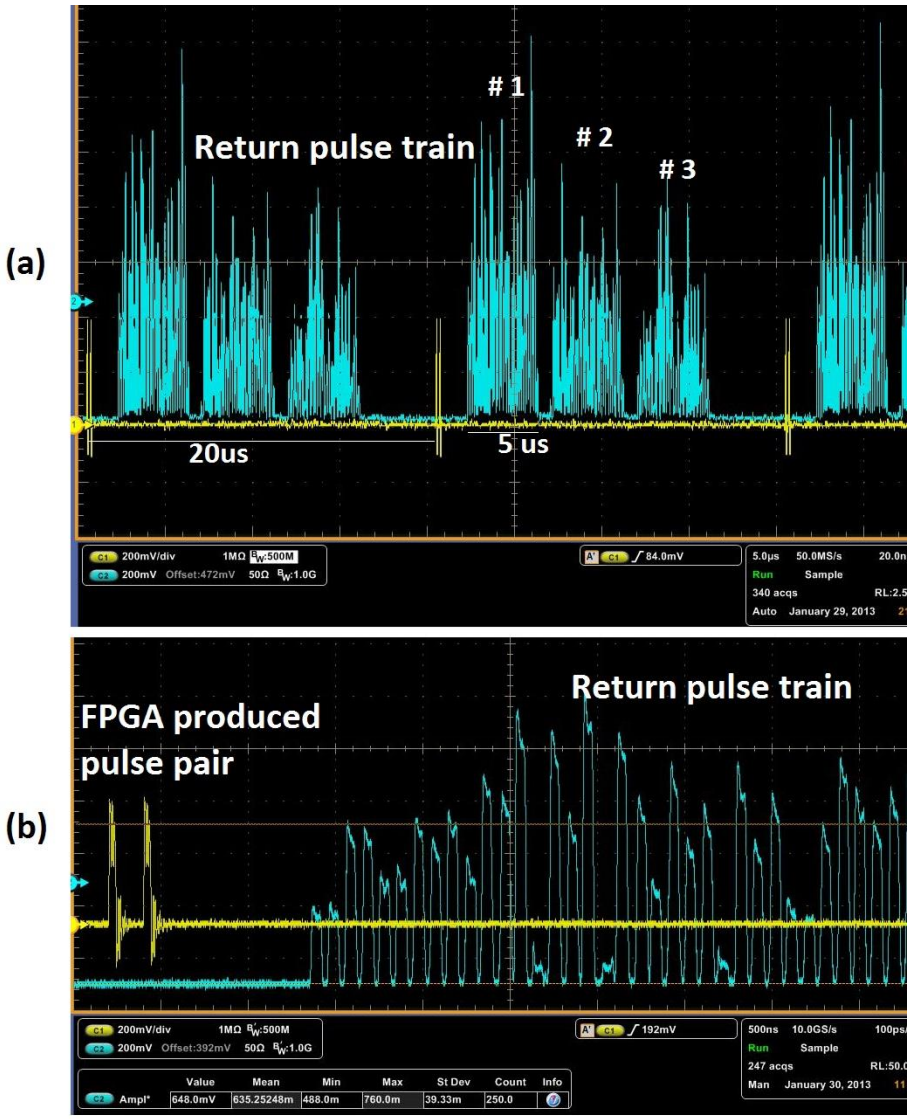

Figure 9.8: Captured pulse trains to the receiver in the system with the new-built TDM group for time duration of (a) 50 μs and (b) enlarged 5 μs. Channel 1 in yellow is the field-programmable gate array (FPGA) produced pulse pair for trigger and channel 2 in blue is the returned pulse trains to the receiver.

Figure 9.8 demonstrates the captured pulse trains. Channel 1 in yellow is the pulse pair produced by field-programmable gate array (FPGA) for generating optical pulses, and channel 2 in blue shows the return pulse train. Figure (a) illustrates 2.5 periods; each period (20 μs) includes three clusters of pulses, donating the pulses from TDM group # 1, # 2, and # 3, consecutively. They are separated by 5 μs. Figure (b) enlarges the beat pulse shape in more detail.

9.2.2 Experimental results

The effect of the accumulated ASE power was monitored by comparing the optical spectrum after the distributed amplified array. Figure 9.9 demonstrates the input and output optical spectrum of the array. In order to make sure of a good input OSNR, the peak signal power to the array is only amplified to 15 dBm (with an input duty cycle D = −23 dB), due to the lack of a good TXAMP. It can be seen from the figure that the average OSNR at the output signal is less than 20 dB at λ16, while it is 14 dB better at λ2. A good SPI optical amplifier can provide us with over 35 dBm peak power per wavelength together with the average OSNR over 34 dB when D = 14 dB for a three wavelengths multiplexed laser source.

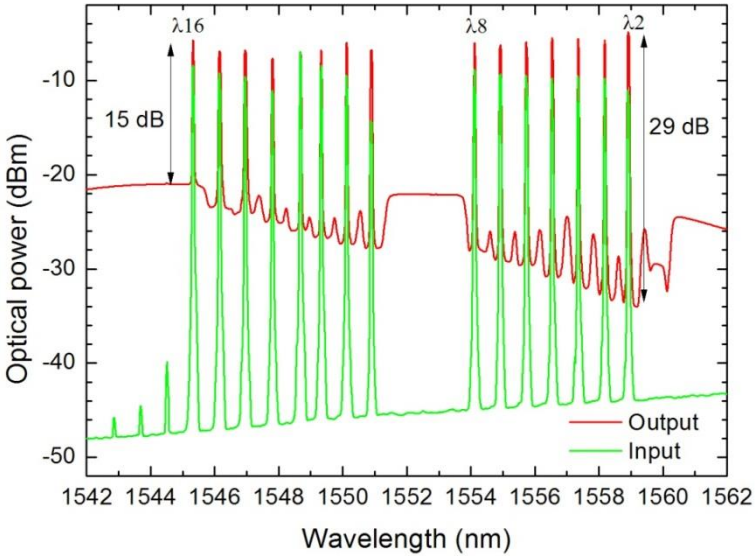

Figure 9.9: Optical spectrum into the amplified array and at the output of the array. Pump power is 126 mW.

A sine phase modulation with a Vp-p amplitude of 1 volts was applied on sensor # 1 of TDM group # 1 at 1093 Hz. The measured system OSNR of 15 dB (peak of ~18 dB) would provide us with a Demod phase sensitivity of −77 dB re rad/√Hz at the derivative channel (See page 143) with an aliasing parameter of 4800, and the output OSNR could have been improved by increasing the input signal power, had more power been available. Figure 9.10 illustrates the demodulated phase spectra at sensor # 1 and its adjacent sensors. The system noise floor is entirely covered under the electrical noise generated at the oscilloscope, due to the limited SNR of only 40 dB over the whole bandwidth for signal capturing on it. However, it is still possible for us to pick the phase information with a SNR of 18 dB from the modulated normal channel of the sensor, which means the system is still capable of interrogating sensors from a 64 × 16

sensor array with the distributed amplified network. No crosstalk was observed in adjacent sensors, but this may be because of the high noise floor achieved.

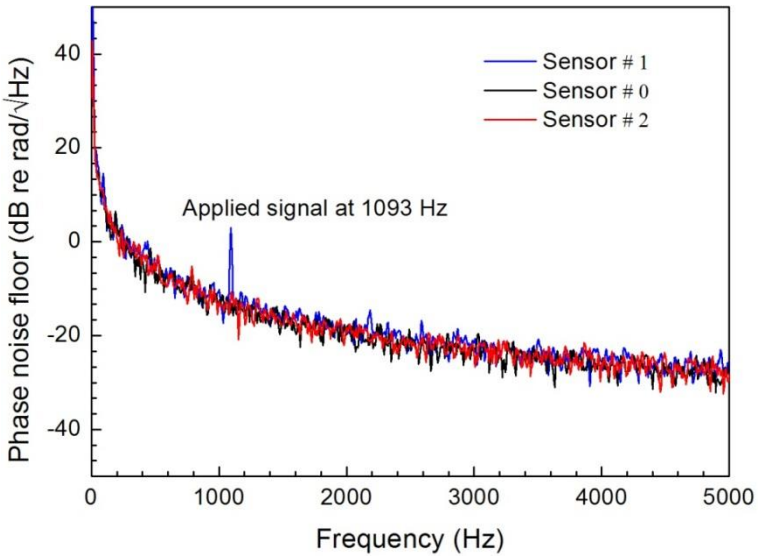

Figure 9.10: Demodulated phase signal at sensor # 1 from the new-built TDM group with 48 sensors inside. # 0 and # 2 are the sensor before and after sensor # 1, respectively.

9.3 Conclusion

We have configured real TDM groups with 16 sensors and 48 sensors, and have employed them to the distributed amplified hybrid multiplexed sensor array, to test the network performance. Experimental results show that the recommended distributed amplified network can support 16×16 sensors without effects from ASE noise and channel crosstalk, and is capable of interrogating phase signal from a 64×16 sensor scale.

Chapter 10
Conclusion and future work

PRM is an emerging market with significant potential. Such systems require several 1000's of sensors to be presented and multiplexed simultaneously to cover a large area of offshore fields. Systems based on the use of fully optical-fibre sensors and telemetry offer significant potential benefits, by eliminating the requirement for costly in-sea electronics and associated power cabling; by increasing reliability through the use of robust, electrically passive optical fibre components; and by providing us with the lowest transmission loss. However, to fully realise these benefits, these approaches typically require significant numbers of individual fibre paths between the sensors and the recording system, which leads to issues with underwater connectivity and the number of fibres in risers and connecting cables. When a small number of optical fibres are used to collect data from many thousands of sensors distributed over the reservoir means that the system is more compact, lighter and should be easier to install.

This study presents a novel distributed amplified hybrid DWDM/TDM array architecture for PRM applications. This architecture employs a distributed EDFA scheme to decrease the distribution loss among multiplexed wavelengths, and employs TDM at each wavelength to increase the total number of sensors that can be supported. It is well suited to the PRM applications, and allows several thousand optical fibre seismic sensors to be multiplexed onto one optical fibre pair.

Summary of conclusion

In this work, I demonstrated a novel high performance fibre-optic sensor array scheme using a distributed EDFA and hybrid TDM/DWDM, for the first time, which provided us with many unique advantages:

- The distributed EDFA compensates for the splitting losses, using commercially available low-doped EDFs and relatively modest pump sources. The pump power is modest enough to be provided by underwater pump diodes, or conveyed to the array from the surface.
- The distributed EDFA does not impair the pulse shape of the optical signal.
- The ASE from the distributed EDFA affects the output OSNR performance, but it is still better than 30 dB, when the equivalent signal power is larger than −20 dBm. The

proposed architecture can support up to 1500 interferometric sensors in a 16-wavelength network, providing all sensors with an excellent SNR superior to 120 dB/√Hz.

- The measured crosstalk in the time domain from this array has similar performance as from an array without a distributed amplifier, and it does not seriously affect the crosstalk in the wavelength domain.
- The number of interrogation sensors could be further increased by increasing the number of wavelength channels. Investigations on the pump power dissipation showed that the array can address up to 32 wavelengths, providing similar performance.

Experimental results showed that this architecture can address up to 64×16 sensors with a Demod phase sensitivity of −90 dB re rad/√Hz, and can support up to 256×16 sensors with a perfectly acceptable Demod phase sensitivity for many applications of −77 dB re rad/√Hz, which is equivalent to the phase change in a fibre displacement length of 2.4×10^{-11} m, even at a lower sampling rate. The relationship is shown in the following table.

Table 10-1: 'Demod phase sensitivity' in terms of the minimum detectable pressure and acceleration.

Demod phase sensitivity (dB re rad/√Hz)	**Displacement[1] (m)**	**Strain[2] (ε)**	**Pressure[3] (dB μPa/√Hz)**	**acceleration[4] (dB g/√Hz)**
−90	5.3×10^{-12}	6.7×10^{-14}	45	−145
−77	2.4×10^{-11}	3×10^{-13}	58	−132

[1] To convert to displacement, multiply the linear interferometer responsivity by $\Delta\phi = 2\pi n_{eff}\Delta L/\lambda$.

[2] To convert to strain, use the return sensing length of 80 m.

[3] This is based on the midrange between possible hydrophone responsivity values of −120 and −150 dB re rad/uPa.

[4] This is based on the typical accelerometer responsivity value of 55 dB re rad/g.

This novel architecture is considered be the best approach to support high sensitivity, high sensor count interferometric sensor arrays (I show viability of up to 4 096 sensors in this work) along only one single fibre pair. This greatly eases the design of cable and risers, and reduces connectivity requirements within the array. As an example, if only 80 channels (Optoplan's Optowave) were multiplexed per optical fibre pair, then 600 optical fibres would be required in

the subsea array for a 6 000 station (24 000 channel) system. In this work, I report multiplexing schemes for optical PRM arrays which allow 1 024 high-performance sensor channels per fibre pair, which in the above example would only require 47 fibres, which is a much more manageable number of fibres. Compared to the current FosarDeep system, which is able to interrogate 256 sensors per fibre pair, this architecture decreases the required number of sensors to a quarter.

In the work, I also have presented an analytical approach to accurately model the phase sensitivity, and provide simple analytical formulae, useful in the design, comparison and optimization of multiplexed amplified interferometric fibre-optic based sensor systems. The approach is widely applicable, but particularly appropriate for fibre-optic sensor systems using amplifiers and TDM, providing us with a parallel comparison with other systems.

To achieve these conclusions, I have modelled the amplification behaviour of a single stage EDFA in Chapter 3, using VPIphotonics. The key properties of the chosen doped fibre have been validated by experimental comparison with simulations, which allows us to predict performance of the proposed architecture work. This provided us with an initial feel for feasibility and defined some general design guidelines. The design rules for the presented array were demonstrated in detail in Chapter 4. The incorporation of EDFAs produce ASE noise and the system OSNR provides us with a direct and measurable approach to monitor the output signal performance from a distributed amplified network. In this Chapter, I also derived the system OSNR as a function of the number of EDF segments and the equivalent signal power. The OSNR is a key characteristic used in our later investigation on the system noise floor. Besides this, the system NF has been used in the literature to characterize the system optical performance, which provides an effectively way for parallel comparison on optical systems. Therefore, I have investigated the NF in our network as a function of the number of sensors and compared it with previous networks, which shows the big advantages of our network.

Then, I have looked into the phase sensitivity in multiplexed interferometric sensors systems in an analytical way in Chapter 5, because it is the ultimate characteristic of a sensor system with various networks. The aim of this study was to investigate performance in sensor systems with amplifiers. Almost all the potential sources of noise in a sensor system were included, and their contribution to the sensor noise floor was investigated. Broadly speaking, performance is limited by direct phase noise sources (e.g. frequency noise in the laser output) and by random noise sources (e.g. ASE), which are converted to phase noise in the demodulation process. Investigations showed that the laser frequency noise due to the tens of meters of patch imbalance dominates. Compensating interferometers and referencing methods are commonly

introduced to reduce this contribution effectively, and improve the phase sensitivity to better than 1 μrad/√Hz (with OSNR of 40 dB), dominated by random noises.

Although the sensitivity of a single sensor is quite good, an unavoidable deterioration from noise aliasing is always the case in real TDM multiplexed sensor systems. Furthermore, the phase sensitivity deteriorates with a decrease in the OSNR, accompanied by a decrease in the equivalent signal power to the distributed amplifier, caused by extra sensors in the TDM group. Therefore, I have introduced the 'Demod phase sensitivity', taking into account the effect from limited electrical bandwidth, limited repetition rate, and covering all the sources of noises with various spectral characteristics. This term provides us with a most effective way to characterize the phase sensitivity in a sensor system utilizing multiplexed technology, and for parallel comparisons between systems.

Furthermore, I have experimentally demonstrated and measured sensor networks with different numbers of wavelengths and sensors, in a step-by-step manner:

1) Four-wavelength sensor network demonstration to investigate the performance of the first four wavelengths in the distributed amplified network.
2) 16-wavelength sensor network (4 stages of EDF-ODM/OAMs, 12 emulators) demonstration, with 4 narrow linewidth fibre laser sources, to investigate the performance of the last (most distance) four wavelength channels in a 16-wavelength sensor array.
3) 16-wavelength sensor network (15 stages of EDF-ODM/OAMs) demonstration, with 4 narrow linewidth fibre laser sources and another 12 DFB lasers.
4) 16-wavelength sensor network (15 stages of EDF-ODM/OAMs) with real TDM groups.
5) Demonstration of 16 TDM × 16 WDM and 64 TDM × 16 WDM sensor arrays.

In Chapter 6, the four-wavelength network provided us with a network gain >20 dB and a system OSNR >30 dB, with a launched pump power over 70 mW, exhibiting good agreement with simulation from VPIphotonics for CW systems. This agreement was also shown in the pump power dissipation. The measured phase noise floor as a function of the system OSNR also showed good agreement with predictions from the phase noise model. In this demonstration, I have also measured FWM effects from four wavelengths with 100 GHz gap between adjacent channels. Experimental comparisons indicate that the noise floor degradation from the FWM effect is less than 2 dB, even with FWM peaks as large as −17 dB, produced in a non-staggered pulse transmitter.

The proposed amplified array benefits a lot from the 'band pass filter' effect from the OAMs on accumulated ASE along the return bus, and therefore, the advantages of our network are mainly manifested in larger scale ($\gg 4$) sensor arrays. Besides this, and the accumulation of the ASE after multi-stages would be the critical factor to limit the size of the network, therefore, I have also configured a network of 16 wavelengths with four active and other twelve stages being replaced by an emulator, as shown in Chapter 7. Measured system performance, including the system OSNR and the phase noise floor at the front and last four wavelength channels were combined together. They all showed good agreement with simulations using VPIphotonics, and with the phase noise prediction from the phase model. However, the performance difference between wavelengths was as large as 10 dB, which was big, due to the fact that the 16-wavelength simulator underestimated the effect from the ASE noise for the front four channels and overestimated it for the back four wavelengths. More importantly, the contribution of the other 12 wavelengths to the distributed amplifier was absent. Therefore, I eventually made a full 16-wavelength network with 15 amplifier stages for demonstration. The network was composed of 15 sets of EDF-OA/DM stages. The results from this proof-of-principle experimental setup are in agreement with predictions. Experimental results confirmed that the arrangement can address up to 64×16 sensors with a phase sensitivity limited only by shot noise and receiver noise, and can support up to 256×16 with a perfectly acceptable phase sensitivity for many applications of -77 dB rad/$\sqrt{\text{Hz}}$, even at a lower sampling rate.

In Chapter 9, I have built fully loaded TDM groups, to make a real $M\times N$ sensor system, and I have made TDM groups with 16 and 64 sensors, interrogated by different demodulation systems. The 16×16 sensor system demonstrated good optical performance and phase noise performance in the absence of any deterioration from the ASE noise. The 16×64 sensor system can effectively demodulate the applied phase modulation.

Besides the network demonstration, I also investigated the crosstalk performance theoretically and experimentally in Chapter 8. I have built three TDM groups for the test, each with 16 sensors inside. The crosstalk between adjacent sensors in one TDM group and between adjacent wavelengths was investigated. The experiments showed undetectable crosstalk between wavelengths, due to the excellent channel isolation in the DWDMs before the receiver. In the TDM group, the crosstalk increases with a decrease in the time space between adjacent pulses in the returned pulse trains. Crosstalk of less than –47 dB can be achieved with a pulse width less than 60 ns in the current sensor system. The crosstalk measurement results from the distributed amplified network from Chapter 9 showed that the distributed EDFA does not affect the crosstalk performance in the time domain.

Outlook

Remote interrogation

All the investigations in this work were done assuming a peak optical power handling of 22 dBm per wavelengths, limited by the MI effects assuming a transmission link length of 50 km. Therefore, the first extension of this study is to investigate the remote interrogation of the distributed amplified network.

Same SNR among different wavelengths

The design objective in chapter 4 was to achieve the same signal powers from each sensor group for different wavelengths, because we were aiming to compensate for the increasing insertion losses at remote wavelengths. However, our investigation has shown that the OAMs along the return bus provide us with different improvements in the OSNR among different wavelengths, so even with the same optical signal power level, the SNR amongst wavelengths is different. Therefore, we can further improve the system design by aiming to balance the SNR among different wavelengths.

Dense wavelength division multiplexing

The next thing to do would be to exploit the dense wavelength division multiplexing. Currently, 25 GHz WDM components are readily available. The trend in telecommunications is for closer and closer spacing, so 12.5 GHz and even some 2.5 GHz spaced components are available. Using this technology, the sensors in the system can be increased by multiple times.

Precise pulse interrogation

In Chapter 5, an increase in the number of sensors in each TDM group is suggested by narrowing the time slot allocated for each sensor, while keeping the repetition rate, to avoid the increase in aliased phase noise components. However, in Chapter 10, sensors are added by decreasing the pulse repetition rate, limited by the existing length error between sensor coils in the TDM groups. This needs to be better controlled when building the next generation of TDM groups. On the transmitter part, pulses with rise/fall time as short as 10 ns would be possible currently.

Amplification performance

The average power from the transmitter decreases with a decrease in the duty cycle, when more sensors are multiplexed in each TDM group. This challenges the transmitter amplifier. Furthermore, there are reports that transient gain saturation (power spikes at the leading edge of

the amplified pulse) and recovery typically occur on a 100 μs to 1 ms time scale [51], but few references exist on the amplification performance with pulse periods in the μs regime.

Various amplification methods

Distributed Raman amplification can be applied in the network as well. The delay length between OSUs provides a ready-made media for Raman amplification. However, the Raman amplification gain in normal SMF28e fibre is quite low, and therefore, I can extend the study only by negotiating with the fibre length and fibre type.

Lowering the cost

For larger multiplexed interferometric sensor systems, multi-channel laser sources with good frequency stability are required, with the increase in the number of wavelengths. These lasers are expensive. The replacement of N single-channel lasers with one proper wide-band (or tunable) laser source, would reduce the total cost of the PRM system by N times.

In conclusion, this study has proposed and fully characterized a novel distributed amplified network which can support more than 1000 sensors along one fibre pair. It greatly eases the design of cable and risers, and reduces connectivity requirements within the array. This significant work on the design and demonstration of a distributed amplified network is well suited to the emerging PRM market. The work has been patented recently [111] and is being transferred from laboratory demonstration to commercial use.

Appendix A Optical operation in the derivative-approach based system

Some applications require very large dynamic range (i.e. >> ~120 dB) at low frequency. These generate signals that induce phase modulations that exceed the bandwidth of the interferometric phase measurement method. To overcome this, a technique is implemented that measures the rate of change of the phase, thus greatly reducing the bandwidth.

This operates by tracking the phase changes between successive optical samples [12]. We developed the TDM group (4C sensor package) based on an inline Michelson configuration, as illustrated in Figure A.1. In the derivative-approach based system, the interferometric sensors are grouped into a cluster of 3 orthogonally mounted accelerometers and a hydrophone known as an OSU. Each sensor is optically separated from its neighbor by a directional coupler with a Faraday mirror attached to one port. The optical power received from each sensor is equalized by tailoring the coupler ratios. This is achieved by carefully selecting unique coupler ratios for each sensor.

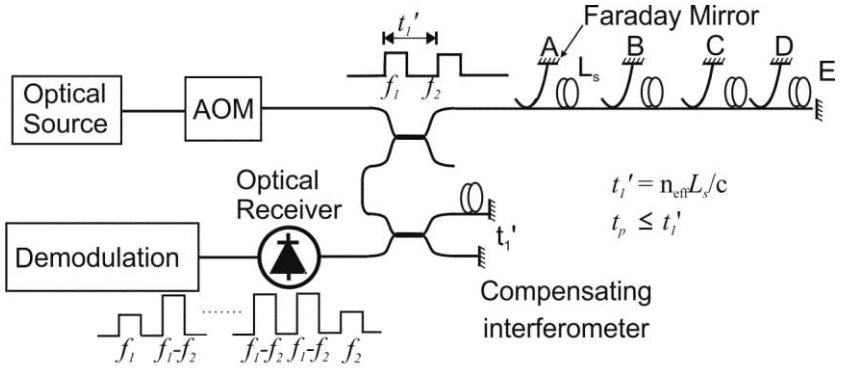

Figure A.1: Optical configuration of derivative-approach based system with one OSU.

The optical pulses are generated from an AOM that operate as both a switch and a frequency shifter. The OSU is interrogated with two optical pulses separated in time by a period $t_1{}' = n_{eff}L_s/c$, which is equal to the single transit time in the sensor fibre with n_{eff}, the fibre effective refractive index, and L_s the sensor fibre length. The optical pulse length t_p is equal to (or slightly less than) the pulse separation. The optical pulse pair reaches the first reflector A in the OSU. The pair is partially reflected from this first reflector, then passes through the first coil and is partially reflected form the second reflector B and so on.

Because the optical pulse separation has been arranged to be equal to the single transit time of light through a sensor coil, the reflection of the first optical pulse from the second reflector B will return after the reflection of the second optical pulse from the first reflector A, and the time separation between these two return pulses is t_1'. Since these two reflections will not overlap in time, an additional optical compensating interferometer is added before the optical receiver. This circuit contains a delay coil which is equal to half a sensor coil in length. This means that the transit time of light through this delay coil is equal to the optical pulse separation (t_1').

The system timing diagram is shown in Figure A.2. The two pulse trains returning from different reflectors in the OSU do not overlap because the pulse separation is only half the return transit time of light through a sensor coil. These two pulse trains have then each gone through the two paths within the compensating interferometer (one path involves going through the delay coil, and the other does not). There are two sets of pulse pair trains at the interferometer output, and because of the function of the delay coil, these sets now overlap with each other, to produce a single pulse with a frequency equal to the frequency difference between the two pulses (the carrier frequency ω_{IF}), as can be seen in Figure A.2 (c) and (d).

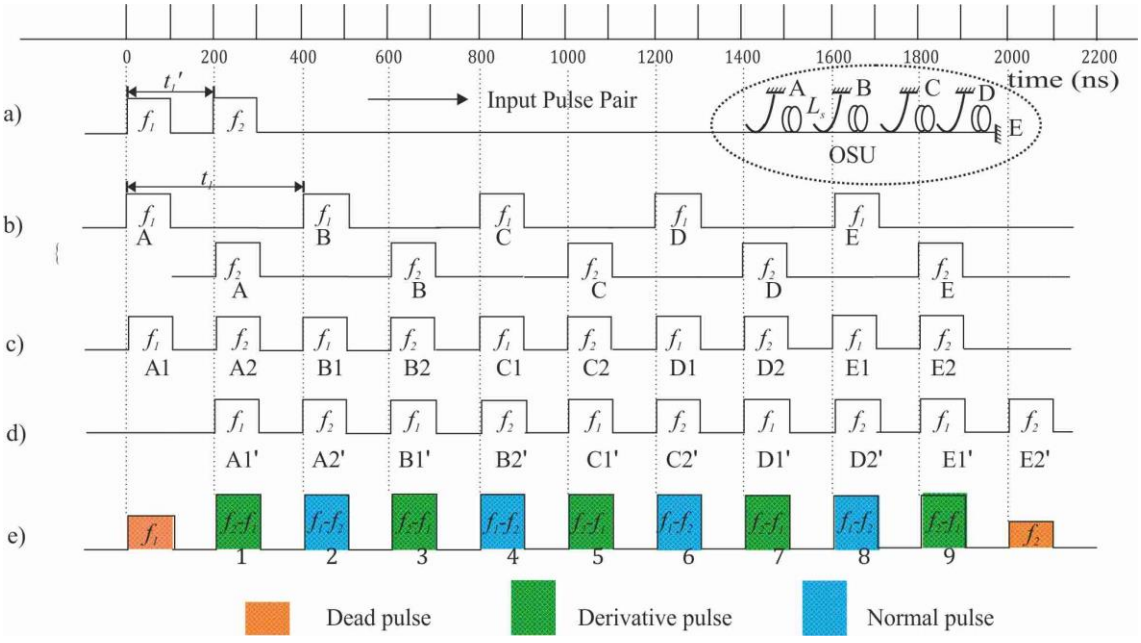

Figure A.2: System time domain diagram for the pulses (a) after the pulse generator, (b) reflected from the OSU, (c) from the compensating interferometer without the delay coil (d) from the compensating interferometer with the delay coil (A1': Delayed first pulse reflected from A, A2': Delayed second pulse reflected from A, and so on), and (e) at the receiver. The output of the four sensors contains a pulse train of four sensor pulses, five derivative pulses, together with two "dead" pulses.

The timing is such that the reflection of the undelayed first pulse from the second reflector arrives back at the receiver at the same time as the reflection of the delayed second pulse from the first reflector. This is the normal sensor pulse. This pulse carries all the phase change from the first sensing fibre imposed as a phase modulation of the carrier frequency (because the first pulse has been through the coil twice and has been exposed to the signal-induced phase change, while the second pulse has not). The phase information from these pulses is the normal signal (from normal channels 2, 4, 6, 8 etc.).

The normal signal can be referenced to a reference sensor which is seismically insensitive, to remove the system noise, therefore it is possible to obtain the normal referenced signal by subtracting signal from the sensor coil D (which is acoustic insensitive in our test) from all the normal signals (from subtracted normal channels $2-8$, $4-8$, $6-8$, etc.).

It can also be seen from the pulse timing diagram that the undelayed reflection of the second pulse from the first reflector overlaps with the delayed reflection of the first pulse from the first reflector. Although these two pulses arrive back at the optical receiver simultaneously, and have been reflected from the same point in the array, they were not reflected at the same time, but at a time interval equal to the pulse separation. They therefore carry a phase modulation which is directly proportional to the change of phase over this time interval. This phase modulation is therefore a representation of the differential of the phase at that point. We call this the derivative pulse.

The derivative pulses contain the derivative of the phase information at the points A, B, C, D and E in the array, and by subtracting the signals from point B from that for point A (channel 3 – channel 1), it is possible to obtain a signal which is a derivative of the signal from the first sensor. The signal from the second sensor is then obtained by subtracting the signal at Point C from that at point B (channel 5 – channel 3), and so on. The phase information demodulated from the subtraction of these derivative pulse pairs is the derivative signal (from subtracted derivative channels $3-1$, $5-3$, $7-5$, etc.).

The derivative signals represent a measure of the rate of change of phase of each sensor. The amplitude of the phase change on each derivative sensor is frequency dependent, but at seismic frequencies (<175Hz) it is much lower than that of the "normal" sensor. At 800 Hz, the phase change on the derivative sensor is 60 dB lower than it is on the normal sensor and it decreases at 6 dB per octave, so that at 100 Hz it is 78 dB lower. The derivative signal can then be used in a number of different ways to reconstruct the normal signal even in overscale situations where the normal signal has exceeded the $\pi/2$ threshold between successive pulses. The derivative signal

offer significant advantages in the seismic seabed industry since it provides a means to overcome or control signal oversizing (i.e. driving the sensor through multiple 2π phase shifts) which occurs frequently during the first break (i.e. the first direct water-borne arrival of the acoustic shots) when the acoustic energy is high.

Subtractions between different points within the system are used to obtain derivative signals, so that system noise components including optical power variations and vibrational pickup along the cable are mitigated. The derivative signals therefore give a much more 'lab friendly' method for measuring and comparing the system noise, because they are essentially insensitive to audio frequency acoustic pickup.

Appendix B Intensity noise in the system from EDFA

The instantaneous photocurrent at the receiver is given by

$$\begin{aligned} i(t) = R\{[E_{s1}\cos(2\pi f_1 t) + E_{s2}\cos(2\pi f_2(t+t_1'))]^2 + 2R[E_{s1}\cos(2\pi f_1 t) + E_{s2}\cos(2\pi f_2(t+t_1'))] \\ \bullet\{\sum_{i=-M}^{M} E_{n1}\cos[2\pi(f_1 + i\delta\upsilon)t + \phi_i] + \sum_{j=-M}^{M} E_{n2}\cos[2\pi(f_2 + j\delta\upsilon)(t+t_1') + \phi_j]\} \\ + R\{\sum_{i=-M}^{M} E_{n1}\cos[2\pi(f_1 + i\delta\upsilon)t + \phi_i] + \sum_{j=-M}^{M} E_{n2}\cos[2\pi(f_2 + j\delta\upsilon)(t+t_1') + \phi_j]\}^2 \end{aligned} \tag{B.1}$$

The first term in the above equation $i_s(t)$, corresponds to the photocurrent from the signal. The second and third term correspond to the signal-ASE beat noise and ASE-ASE beat noise, respectively. We look first at the signal photocurrent, which can be rewritten as

$$\begin{aligned} i_s(t) &= R\{[E_{s1}\cos(2\pi f_1 t)]^2 + [E_{s2}\cos(2\pi f_2(t+t_1'))]^2 \\ &\quad + 2E_{s1}E_{s2}\cos(2\pi f_1 t)\cos(2\pi f_2(t+t_1'))\} \\ &= R\{[E_{s1}\cos(2\pi f_1 t)]^2 + [E_{s2}\cos(2\pi f_2(t+t_1'))]^2 \\ &\quad + E_{s1}E_{s2}\cos(2\pi f_1 t + 2\pi f_2(t+t_1')) + E_{s1}E_{s2}\cos(2\pi f_1 t - 2\pi f_2(t+t_1'))\} \end{aligned} \tag{B.2}$$

The time average of the first and second terms in the above equation, i.e., $I_{s\_d} = R(E_{s1}^2 + E_{s2}^2)/2 = RP_s$ corresponds to the mean signal photocurrent with DC frequency. The third term corresponds to components of twice the optical frequency and has zero time average. The fourth term corresponds to the carrier current oscillating at the intermediate frequency $\omega_{IF} = 2\pi(f_1 - f_2)$ with an amplitude of $RE_{s1}E_{s2}$. Hence, we achieve an expression of the photocurrent of the heterodyne signal without ASE beat noise as

$$I = RP_s(1 + \cos\omega_{IF}t) \tag{B.3}$$

Then looking at the signal-ASE beat noise component, the whole of the ASE terms can be rewritten as

$$\sum_{l=1}^{2}\sum_{k=-M}^{M} E_{nl}\cos[2\pi(f_l + k\delta\upsilon)t + \phi_{l,k}] \tag{B.4}$$

in which $\phi_{2k} = \phi_{1k} + 2\pi k\delta\upsilon t_1'$, and the signal-ASE beat noise term in equation (B.1)can be rewritten as the sum of S1-ASE and S2-ASE

$$\begin{cases} i_{S1-ASE}(t) = 2RE_{s1}\cos(2\pi f_1 t)\sum_{l=1}^{2}\sum_{k=-M}^{M} E_{nl}\cos[2\pi(f_l + k\delta\upsilon)t + \phi_{l,k}] \\ i_{S2-ASE}(t) = 2RE_{s2}\cos[2\pi f_2(t+t_1')]\sum_{l=1}^{2}\sum_{k=-M}^{M} E_{nl}\cos[2\pi(f_l + k\delta\upsilon)t + \phi_{l,k}] \end{cases} \tag{B.5}$$

Let us look at the S1-ASE term first,

$$\begin{aligned} i_{S1-ASE}(t) &= 2RE_{s1}E_{nl}\sum_{l=1}^{2}\sum_{k=-M}^{M}\cos(2\pi f_1 t)\cos[2\pi(f_l + k\delta\upsilon)t + \phi_{l,k}] \\ &= RE_{s1}E_{nl}\sum_{l=1}^{2}\sum_{k=-M}^{M}\{\cos[2\pi(f_1 + f_l + k\delta\upsilon)t + \phi_{l,k}] + \cos[2\pi(f_l + k\delta\upsilon - f_1)t + \phi_{l,k}]\} \end{aligned} \tag{B.6}$$

while the time average of S1-ASE photocurrent $< i_{S1-ASE}(t) >$ is zero, the power defined in equation (B.6) corresponds to a noise variance, and the corresponding electrical power is given by:

$$\begin{aligned} \left\langle i_{S1-ASE}^2(t)\right\rangle &= (RE_{s1}E_{nl})^2 \\ &\times\sum_{l=1}^{2}\sum_{k=-M}^{M}\sum_{m=1}^{2}\sum_{h=-M}^{M}\{\left\langle\cos[2\pi(f_l + k\delta\upsilon + f_1)t + \phi_{l,k}]\cos[2\pi(f_m + h\delta\upsilon + f_1)t + \phi_{m,h}]\right\rangle \\ &+\left\langle\cos[2\pi(f_l + k\delta\upsilon + f_1)t + \phi_{l,k}]\cos[2\pi(f_m + h\delta\upsilon - f_1)t + \phi_{m,h}]\right\rangle \\ &+\left\langle\cos[2\pi(f_l + k\delta\upsilon - f_1)t + \phi_{l,k}]\cos[2\pi(f_m + h\delta\upsilon + f_1)t + \phi_{m,h}]\right\rangle \\ &+\left\langle\cos[2\pi(f_l + k\delta\upsilon - f_1)t + \phi_{l,k}]\cos[2\pi(f_m + h\delta\upsilon - f_1)t + \phi_{m,h}]\right\rangle\} \\ &= (RE_{s1}E_{nl})^2 \\ &\times\sum_{l=1}^{2}\sum_{m=1}^{2}\sum_{k=-M}^{M}\{\left\langle\cos^2[2\pi(f_l + k\delta\upsilon + f_1)t + \phi_{l,k}]\right\rangle + \left\langle\cos^2[2\pi(f_l + k\delta\upsilon - f_1)t + \phi_{l,k}]\right\rangle \\ &+\left\langle\cos[2\pi(f_l + k\delta\upsilon + f_1)t + \phi_{l,k}]\cos[2\pi(f_m + h\delta\upsilon + f_1)t + \phi_{m,k}]\right\rangle \\ &+\left\langle\cos[2\pi(f_l + k\delta\upsilon - f_1)t + \phi_{l,k}]\cos[2\pi(f_m + h\delta\upsilon - f_1)t + \phi_{m,k}]\right\rangle \\ &+2\left\langle\cos[2\pi(f_l + k\delta\upsilon - f_1)t + \phi_{l,k}]\cos[2\pi(f_l + k\delta\upsilon + f_1)t + \phi_{m,k}]\right\rangle\} \end{aligned} \tag{B.7}$$

In the above equation(B.7), the time average of the cross-terms containing products of cosines with random phases $\phi_{l,k} \neq \phi_{m,h}$ vanish, and terms with $\phi_{l,k} = \phi_{m,h}$ still exist. Because ASE1 and ASE2 are two terms from the same source at different times, so the cross terms between them with $\phi_{l,k} = \phi_{m,k}$ also exists. The three remaining terms correspond to components near twice the optical frequencies $f_l + k\delta\upsilon + f_1$, whose power spectra fall outside the electronic bandwidth, and components $f_l + k\delta\upsilon - f_1$ whose uniform power spectrum falls inside the baseband frequency interval. This contribution yields:

$$\begin{aligned}\left\langle i_{S1-ASE}^2(t)\right\rangle &= (RE_{s1}E_{nl})^2\sum_{l=1}^{2}\sum_{k=-M}^{M}\left\langle 2\cos^2[2\pi(f_l+k\delta\upsilon-f_1)t+\phi_{l,k}]\right\rangle \\ &= (RE_{s1}E_{nl})^2\cdot 2\cdot 2M\end{aligned} \tag{B.8}$$

As the mean S-ASE photocurrent is zero, the power defined in equation (B.8) also corresponds to a noise variance. The S-ASE power spectrum is uniform over $[0, B_O/2]$ ([0, M$\delta\upsilon$]) and has a spectral density:

$$\sigma_{S1-ASE}^2(f) = 4(RE_{s1}E_{nl})^2 \tag{B.9}$$

The total S-ASE noise in the electronic detection bandwidth B_e is then:

$$\begin{aligned}\sigma_{S1-ASE}^2 &= 4R^2E_{s1}^2E_{nl}^2B_e \\ \sigma_{S2-ASE}^2 &= 4R^2E_{s2}^2E_{nl}^2B_e\end{aligned} \tag{B.10}$$

The ASE-ASE beat noise term in equation (B.1) can be rewritten as

$$\begin{aligned}i_{ASE-ASE}(t) &= R\{E_{nl}\sum_{l=1}^{2}\sum_{k=-M}^{M}\cos[2\pi(f_l+k\delta\upsilon)t+\phi_{l,k}]\}^2 \\ &= RE_{nl}E_{nm}\sum_{l=1}^{2}\sum_{k=-M}^{M}\sum_{m=1}^{2}\sum_{h=-M}^{M}\cos[2\pi(f_l+k\delta\upsilon)t+\phi_{l,k}]\cos[2\pi(f_m+h\delta\upsilon)t+\phi_{m,h}] \\ &= \frac{1}{2}RE_{nl}E_{nm}\sum_{l=1}^{2}\sum_{k=-M}^{M}\sum_{m=1}^{2}\sum_{h=-M}^{M}\{\cos[2\pi(f_l+k\delta\upsilon+f_m+h\delta\upsilon)t+\phi_{l,k}+\phi_{m,h}] \\ &\quad+\cos[2\pi(f_l+k\delta\upsilon-f_m-h\delta\upsilon)t+\phi_{l,k}-\phi_{m,h}]\}\end{aligned} \tag{B.11}$$

The terms oscillating at twice the optical of frequency in equation (B.11) yield a zero time average photocurrent, while the terms with frequency $f_l + k\delta\upsilon - f_m - h\delta\upsilon$ yield nonzero contributions for $k = h$, corresponding to the mean photocurrent at DC for $l = m$ and ω_{IF} for $l \neq m$:

$$\begin{aligned}I_{ASE\_dc} &= \frac{1}{2}RE_{nl}E_{nm}\sum_{l=1}^{2}\sum_{k=1}^{2M}\cos(0) = 2MRE_{nl}E_{nm} \\ I_{ASE\_IF} &= \frac{1}{2}RE_{nl}E_{nm}\sum_{m=1}^{2}\sum_{l\neq m}^{2}\sum_{k=1}^{2M}\{\cos[2\pi f_{IF}t+\phi_{l,k}-\phi_{m,k}]\} = 2MRE_{nl}E_{nm}\cos(2\pi f_{IF}t+\phi_l-\phi_m)\end{aligned} \tag{B.12}$$

Considering next only the relevant terms in equation (B.11) which oscillate at frequencies $f_l + k\delta\upsilon - f_m - h\delta\upsilon$, the corresponding noise power is given by:

$$\begin{aligned}\left\langle i_{ASE-ASE}^2(t)\right\rangle &= (\frac{1}{2}RE_{nl}E_{nm})^2\left\langle\{\sum_{m=1}^{2}\sum_{h=-M}^{M}\sum_{l=1}^{2}\sum_{k\neq h}^{M}\cos[2\pi(f_l+k\delta\upsilon-f_m-h\delta\upsilon)t+\phi_{l,k}-\phi_{m,h}]\}^2\right\rangle \\ &= 2(\frac{1}{2}RE_{nl}E_{nm})^2\sum_{m=1}^{2}\sum_{h=-M}^{M}\sum_{l=1}^{2}\sum_{k\neq h}^{M}\left\langle\cos^2[2\pi(f_l+k\delta\upsilon-f_m-h\delta\upsilon)t+\phi_{l,k}-\phi_{m,h}]\right\rangle\end{aligned} \tag{B.13}$$

In equation(B.13), we used the property that parts of the cross terms having unrelated random phase noises have zero time average. Recursion verifies that the double sum contains $(2M-1)$ terms at $\delta\upsilon$, $(2M-2)$ terms at $2\ \delta\upsilon$,…, one term at $(2M-1)\delta\upsilon$, and no term at $2M\delta\upsilon$, and also the same number of corresponding terms with negative frequencies and opposite phases. The spectrum density takes value $4\times 2M\times 2\times 2\times(\frac{1}{2}RE_{nl}E_{nm})^2\frac{1}{2}$ near DC, and decrease linearly with frequency to vanish at $\upsilon = B_o$. The ASE-ASE spectrum in $\delta\upsilon = 1Hz$ is thus

$$\sigma^2_{ASE-ASE}(f)=2R^2E^2_{nl}E^2_{nm}B_o(1-f/B_o) \tag{B.14}$$

This expression is given in an interferometer with balanced arms. However, the unbalanced interferometer response acts as a filter to the ASE-ASE and S-ASE beat noise spectrum of ASE noise [112]. When the optical path difference is longer than the coherence length of the ASE noise, no interference pattern in the total photocurrent is obtained. However, the optical field at the interferometer output is composed of two light components from two different paths, one being a delayed version of the other. If the delayed optical path-length different is nL_s, then the light components from the two paths are separated in time by t_1'. When thist'corresponds to half the period of the difference frequency, the two components have opposite signs and will vanish. Therefore, the photocurrent spectrum shows oscillation at $1/t_1'$. The ASE-ASE beat noise from an unbalanced interferometer with delay time of t_1' is given by

$$\sigma^2_{ASE-ASE}(f)=2R^2S^2_{ASE}B_O(1-\frac{f}{B_O})(1+\frac{\cos 2\pi ft_1'}{2}) \tag{B.15}$$

The total ASE-ASE noise power falling into the electrical bandwidth $B_e \ll B_O$ is then approximated by

$$\begin{aligned}\sigma^2_{ASE-ASE} &= 2R^2E^2_{nl}E^2_{nm}B_o\int_0^{B_e}(1-f/B_o)(1+\frac{\cos 2\pi ft_1'}{2})df\\ &\approx 2R^2E^2_{nl}E^2_{nm}B_o(B_e-\frac{B_e}{2B_o})\\ &\approx 2R^2E^2_{nl}E^2_{nm}B_eB_o\end{aligned} \tag{B.16}$$

In the above equations, we have assumed that the ASE noises centred at f_1 have the same noise terms and bandwidth with those centred at f_2. With $E_{s1}=E_{s2}=\sqrt{P_S}$ and $E_{n1}=E_{n2}=\sqrt{S_{ASE}}$, the total noise power falling into the electrical bandwidth B_e can be given by

$$\sigma^2_{S-ASE}=8R^2P_SS_{ASE}B_e \tag{B.17}$$

$$\sigma^2_{ASE-ASE} = 2\aleph R^2 S^2_{ASE} B_e B_o \tag{B.18}$$

The mean signal and ASE noise photocurrent in $\aleph$ polarization states at DC frequency can be expressed by

$$I_{S\_DC} = RP_s \tag{B.19}$$

$$I_{S\_ASE} = R\aleph S_{ASE} B_o \tag{B.20}$$

The amplitude of the photocurrent at the carrier frequency ω_{IF} is

$$I_{S\_IF} = RP_s \tag{B.21}$$

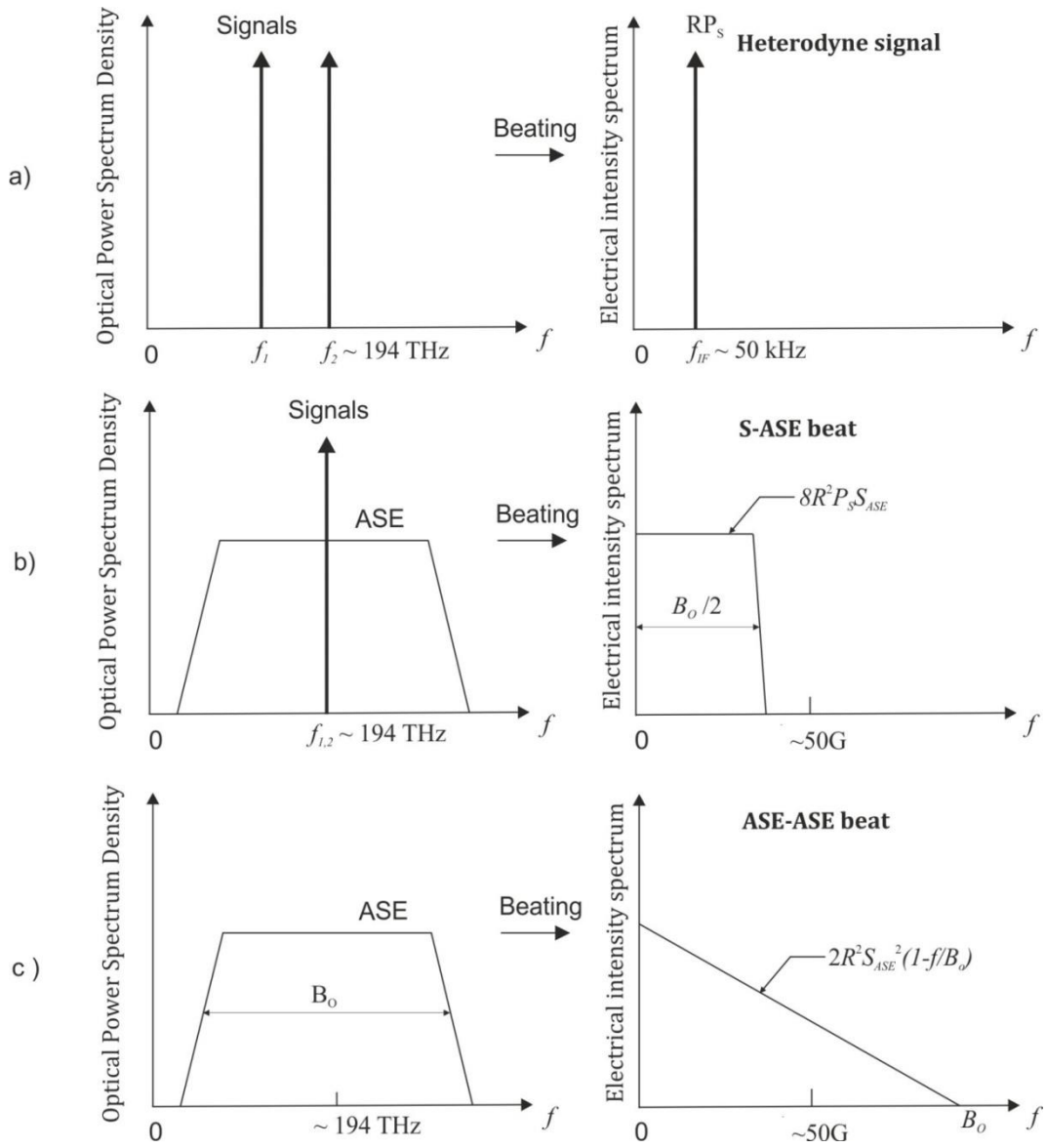

Figure B.1: Distribution of the signal and the intensity noise sources created at the receiver. Lefts are the optical field power spectrum, rights are the intensity spectrum.

Appendix C Distortion at harmonics

The unwanted low light power in the pulse introduces harmonic distortions. The light can be reduced from Rayleigh back scattering, multi reflections, limited tap directivity and EDFA amplification along the return leading fibre, and so on. These low power level lights arrive at the receiver at the same time as the modulated pulse, which can be considered as system intensity noise and will contribute to signal distortion at other harmonics. At the receiver, the electrical field of the wanted high level pulse and low level unwanted signal can be expressed by

$$\begin{aligned} E_1 &= E_h \cos(\omega_1 t + \varphi_i(t)) \\ E_2 &= E_h \cos(\omega_2 t) \\ E_3 &= E_l \cos(\omega_1 t + \varphi_3) \\ E_4 &= E_l \cos(\omega_2 t + \varphi_4) \end{aligned} \tag{C.1}$$

The output intensity of the interference signal is proportional to$(E^* \cdot E)$, so the total intensity at the receiver is

$$\begin{aligned} &I = R(E^* \cdot E) \\ &= R\{2E_h^2 + 2E_l^2 + E_h^2 \cos[\omega_{IF} t + \varphi_i(t)] + E_l^2 \cos(\omega_{IF} t + \varphi_3 - \varphi_4)\} \\ &+ RE_l E_h \{\cos[\omega_{IF} t + \varphi_i(t) - \varphi_4] + \cos[\omega_{IF} t + \varphi_3] + \cos[\varphi_3 - \varphi_i(t)] + \cos(\varphi_4)\} \end{aligned} \tag{C.2}$$

In which φ_3 and φ_4 are the random phases for the low level power light with frequency $\omega_1$and ω_2 respectively. After the arctan demodulation, we get

$$\tan(\psi) = \frac{E_h^2 \sin[\varphi_i(t)] + E_l^2 \sin(\varphi_3 - \varphi_4) + E_l E_h \sin[\varphi_i(t) - \varphi_4] + E_l E_h \sin(\varphi_3)}{E_h^2 \cos[\varphi_i(t)] + E_l^2 \cos(\varphi_3 - \varphi_4) + E_l E_h \cos[\varphi_i(t) - \varphi_4] + E_l E_h \cos(\varphi_3)} \tag{C.3}$$

It is clear that the phase information after demodulation is a function of the random phase noise of the low level light, when φ_3 and φ_4 are in phase with the high level signal light, which is always the case in sensor systems with high coherent laser sources, the demodulated phase information from either of the low level signal pulses is given by

$$\tan(\psi) = \frac{\sin[\varphi_i(t)] + E_l/E_h \sin(\varphi_3)}{\cos[\varphi_i(t)] + E_l/E_h \cos(\varphi_3)} \tag{C.4}$$

It is clear that the induced phase information is proportional to φ_3. In cases when the low power level light are out of phase with the wanted modulated signal fields, saying that $\varphi_3, \varphi_4 = (2n+1)\pi/2$, thus (C.3) is maximized to

$$\tan(\psi) \approx \frac{\sin[\varphi_i(t)] \pm E_l / E_h}{\cos[\varphi_i(t)] + E_l^2 / E_h^2} \tag{C.5}$$

In this situation, system crosstalk is induced in terms of harmonics to the signal. Figure C.1 shows the frequency spectrum of a demodulated signal with $\varphi_i = \cos(2\pi \times 228 \times t)$ and $E_l/E_h = 10^{-1.5}$(i.e., optical ER=30 dB).

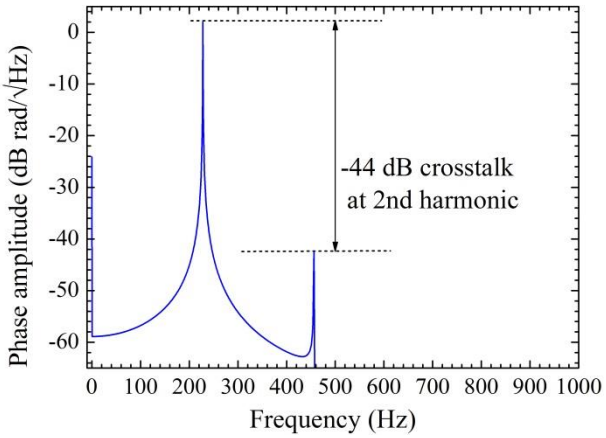

Figure C.1: Illustration of a system crosstalk of −44 dB at the second harmonic from the low level light (in the worst case) with $E_l/E_h = 10^{-1.5}$.

The crosstalk at the 2nd and 3rd harmonics with random phase mismatches between φ_i and φ_3 is summarized in Figure C.2. The distortion level at 2nd harmonics reaches its maximum with phase mismatch at $\varphi_1 - \varphi_3 = (2n+1)\pi/2$, while the distortion at its 3rd harmonics reaches its minimum at these points, except for figure (a) with an extreme optical ER of 10 dB.

The laser sources have long coherence length, therefore the phase mismatch can be approximated to be zero, and we will always observe a larger distortion at the 3rd harmonics than it at the 2nd harmonic.

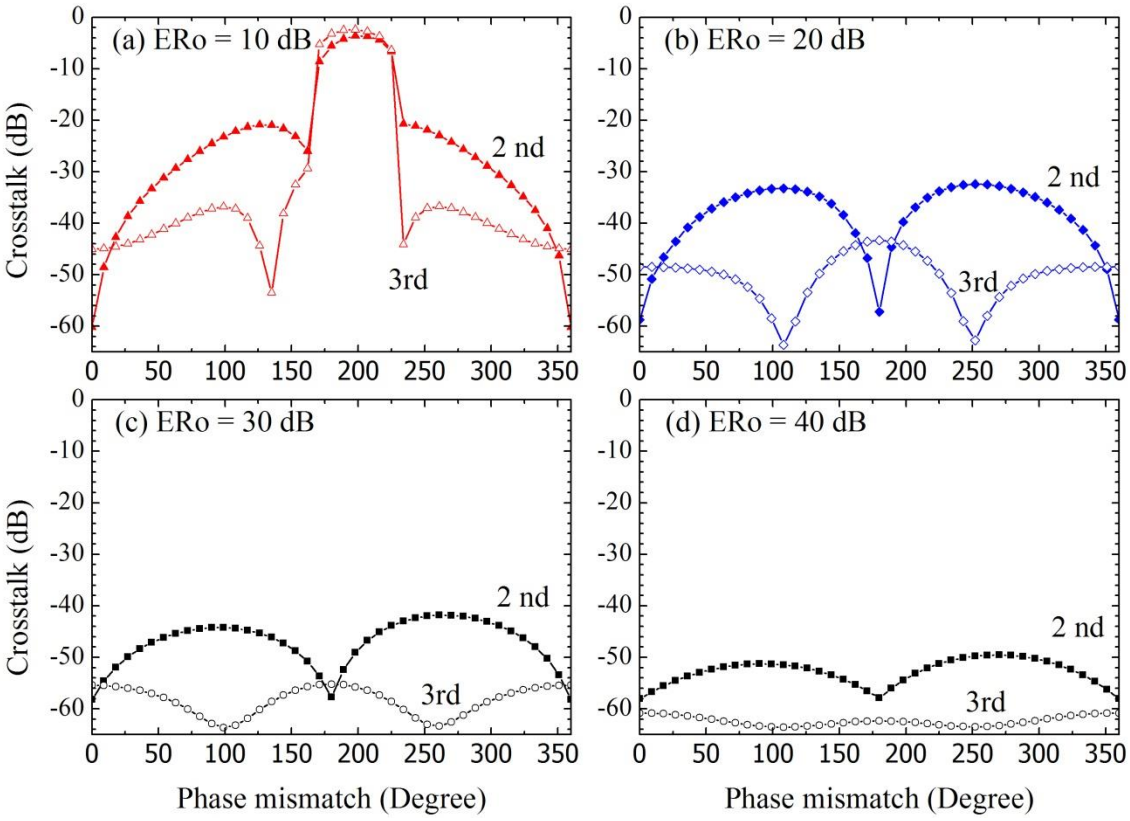

Figure C.2: System crosstalk at the 2nd and 3rd harmonics as a function of phase mismatch.

List of publications

Journal publications

1, Y. Liao, E. Austin, P. J. Nash, S. A. Kingsley, and D. J. Richardson, "Phase Sensitivity Characterization in Fiber-optic Sensor Systems Using Amplifiers and TDM," Journal of Lightwave Technology, vol. 31, pp. 1645-1653, 2013.

2, Y. Liao, E. Austin, P. J. Nash, S. A. Kingsley, and D. J. Richardson, "High performance architecture design for large scale fibre-optic sensor arrays using distributed EDFAs and hybrid TDM/DWDM," *Meas. Sci. Technol.*, 2013.

3, Y. Liao, E. Austin, P. J. Nash, S. A. Kingsley, and D. J. Richardson, "Highly Scalable Amplified Hybrid TDM/DWDM Array Architecture for Interferometric Fiber-Optic Sensor Systems," *Journal of Lightwave Technology*, vol. 31, pp. 882-888, 2013.

Conference publications

4, Y. Liao, E. Austin, P. J. Nash, S. A. Kingsley, and D. J. Richardson, "High performance fibre-optic acoustic sensor array using a distributed EDFA and hybrid TDM/DWDM, scalable to 4096 sensors," *22nd International Conference on Optical Fiber Sensor*, 2012, pp. 84218H-84218H-4.

5, R. Slavik, Y. Liao, E. Austin, P. Petropoulos, and D. J. Richardson, "Full characterization and comparison of phase properties of narrow linewidth lasers operating in the C-band," *21st International Conference on Optical Fiber Sensors,* vol. 7753, 2011.

Patent

6, N. Philip, E. Austin, and Y. Liao, "Optical Sensing System With Amplification," UK Patent, 25088.5GB, 2012.

References

[1] K. K. Clay and A. Dandrige, "Overview of high performance fibre-optic sensing," *Journal of Physics D: Applied Physics*, vol. 37, pp. 197-216, 2004.

[2] J. L. Wagener, C. W. Hodgson, M. J. F. Digonnet, and H. J. Shaw, "Novel fiber sensor arrays using erbium-doped fiber amplifiers," *Journal of Lightwave Technology*, vol. 15, pp. 1681-1688, 1997.

[3] H. Nakstad and J. T. Kringlebotn, "Oil and gas applications: Probing oil fields," *Nature Photonics*, vol. 2, pp. 147-149, 2008.

[4] Ocean bottom seismic - improving cost and reliability [Online].

[5] G. A. Cranch and P. J. Nash, "Large-scale multiplexing of interferometric fiber-optic sensors using TDM and DWDM," *Journal of Lightwave Technology*, vol. 19, pp. 687-699, 2001.

[6] C. W. Hodgson, M. J. Digonnet, and H. J. Shaw, "Large-scale interferometric fiber sensor arrays with multiple optical amplifiers," *Optics Letters*, vol. 22, pp. 1651-3, Nov 1 1997.

[7] C. W. Hodgson, J. L. Wagener, M. J. F. Digonnet, and H. J. Shaw, "Optimization of large-scale fiber sensor arrays incorporating multiple optical amplifiers - Part I: Signal-to-noise ratio," *Journal of Lightwave Technology*, vol. 16, pp. 218-223, 1998.

[8] G. A. Cranch and P. J. Nash, "High multiplexing gain using TDM and WDM in interferometric sensor arrays," *Fiber Optic Sensor Technology and Applications*, vol. 3860, pp. 531-537, 1999.

[9] T. G. Giallorenzi, J. A. Bucaro, A. Dandridge, Jr., G. H. Sigel, J. H. Cole, S. C. Rashleigh, and R. G. Priest, "Optical Fiber Sensor Technology," *IEEE Transactions on Microwave Theory and Techniques*, vol. 30, pp. 472-511, 1982.

[10] J. De Freitas, "Recent developments in seismic seabed oil reservoir monitoring applications using fibre-optic sensing networks," *Measurement Science and Technology*, vol. 22, p. 052001, 2011.

[11] F. El-Hawary, *The ocean engineering handbook*: CRC, 2000.

[12] P. Nash and A. Strudley, "Optimum Optical Architectures for Seismic Reservoir Monitoring," in *Offshore Technology Conference*, 2008.

[13] G. A. Cranch, P. J. Nash, and C. K. Kirkendall, "Large-scale remotely interrogated arrays of fiber-optic interferometric sensors for underwater acoustic applications," *IEEE Sensors Journal*, vol. 3, pp. 19-30, Feb 2003.

[14] K. Yin, M. Zhang, T. Ding, L. Wang, Z. Jing, and Y. Liao, "An investigation of a fiber-optic air-backed mandrel hydrophone," *Optics Communications*, vol. 281, pp. 94-101, 2008.

[15] D. Kersey and A. Dandridge, "Comparative analysis of multiplexing techniques for interferometric fiber sensors," *Proc.SPIE 1120,Fiber Optics'89*, vol. 89, p. 236, 1989.

[16] C. K. Kirkendal, A. D. Kersey, A. Dandridge, M. J. Marrone, and A. R. Davis, "Sensitivity limitations due to aliased high frequency phase noise in high channel-count

TDM interferometric arrays," in *11th International Conference on Optical Fiber Sensors*, 1996, p. Fr14.

[17] P. J. Nash and A. Strudley, "High efficiency TDM/WDM architectures for seismic reservior monitoring," in *20th International Conference on Optical Fiber Sensors*, 2009, pp. T1-T4.

[18] B. J. Vakoc, C. W. Hodgson, M. J. F. Digonnet, G. S. Kino, and H. J. Shaw, "Phase-sensitivity measurement of a 10-sensor array with erbium-doped fiber amplifier telemetry," *Optics Letters*, vol. 23, pp. 1313-1315, 1998.

[19] A. D. Kersey, A. Dandridge, and K. L. Dorsey, "Transmissive serial interferometric fiber sensor array," *Journal of Lightwave Technology*, vol. 7, pp. 846-854, 1989.

[20] A. D. Kersey and A. Dandridge, "Analysis of crosstalk in a multiplexed eight-element interferometric fiber sensor array," in *Optical Communication, 1988. (ECOC 88). Fourteenth European Conference on (Conf. Publ. No.292)*, 1988, pp. 191-194 vol.1.

[21] A. Kersey, K. Dorsey, and A. Dandridge, "Demonstration of an eight-element time-division multiplexed interferometric fibre sensor array," *Electronics Letters*, vol. 24, pp. 689-691, 1988.

[22] A. Kersey and A. Dandridge, "Tapped Serial Interferometric Fiber Sensor Array with Time Division Multiplexing," in *Optical Fiber Sensors*, 1988.

[23] A. Kersey and A. Dandridge, "Multiplexed Mach-Zehnder ladder array with ten sensor elements," *Electronics Letters*, vol. 25, pp. 1298-1299, 1989.

[24] A. D. Kersey, "Demonstration of a hybrid time/wavelength division multiplexed interferometric fibre sensor array," *Electronics Letters*, vol. 27, pp. 554-555, 1991.

[25] K. P. Koo and A. D. Kersey, "Bragg grating-based laser sensors systems with interferometric interrogation and wavelength division multiplexing," *Journal of Lightwave Technology*, vol. 13, pp. 1243-1249, 1995.

[26] T. Berkoff and A. Kersey, "Fiber Bragg grating array sensor system using a bandpass wavelength division multiplexer and interferometric detection," *IEEE Photonics Technology Letters*, vol. 8, pp. 1522-1524, 1996.

[27] K. P. Koo and A. D. Kersey, "Noise and cross talk of a 4-element serial fiber laser sensor array," in *Conference on Optical Fiber Communication. OFC 96.*, 1996, pp. 266-267.

[28] A. D. Kersey, A. Dandridge, A. R. Davis, C. K. Kirdendall, M. J. Marrone, and D. G. Gross, "64-element time-division multiplexed interferometric sensor array with EDFA telemetry," in *Optical Fiber Communications*, 1996, pp. 270-271.

[29] A. Davis, C. Kirkendall, A. Dandridge, and A. Kersey, "64 channel all optical deployable acoustic array," in *Optical Fiber Sensors*, 1997.

[30] P. J. Nash, G. A. Cranch, L. K. Cheng, D. de Bruijn, and I. Crowe, "A 32 element TDM optical hydrophone array," *Proc. SPIE 3483, European Workshop on Optical Fibre Sensors*, vol. 3483, p. 238, 1998.

[31] A. C. Geoffrey and J. N. Phillip, "High multiplexing gain using TDM and WDM in interferometric sensor arrays," in *SPIE Conference on Fiber Optic Sensor Technology and Applications*, 1999, pp. 531-537.

[32] P. J. Nash, J. Latchem, G. Cranch, S. Motley, A. Bautista, C. Kirkendall, A. Dandridge, M. Henshaw, and J. Churchill, "Design, development and construction of fibre-optic

bottom mounted array," in *Optical Fiber Sensors Conference Technical Digest, 2002. OFS 2002, 15th*, 2002, pp. 333-336 vol.1.

[33] G. A. Cranch, C. K. Kirkendall, K. Daley, S. Motley, A. Bautista, J. Salzano, P. J. Nash, J. Latchem, and R. Crickmore, "Large-scale remotely pumped and interrogated fiber-optic interferometric sensor array," *IEEE Photonics Technology Letters*, vol. 15, pp. 1579-1581, 2003.

[34] D. J. Hill, B. Hodder, J. De Freitas, S. D. Thomas, and L. Hickey, "DFB fibre-laser sensor developments," in *Bruges, Belgium-Deadline Past*, 2005, pp. 904-907.

[35] E. Austin, Q. Zhang, S. Alam, M. Zervas, R. Slavik, P. Petropoulos, P. Nash, and D. J. Richardson, "500km remote interrogation of optical sensor arrays," in *21st International Conference on Optical Fiber Sensors*, 2011, pp. 77532M-1.

[36] H. Nakstad and J. T. Kringlebotn, "Realisation of a full-scale fibre optical ocean bottom seismic system," presented at the 19th international conferences on Optical Fibre Sensors, 2008.

[37] J. T. Kringlebotn, "Large Scale Fibre Optic Bragg-Grating Based Ocean Bottom Seismic Cable System for Permanent Reservoir Monitoring," in *Optical Sensors*, 2010, p. SWA1.

[38] C. W. Hodgson, J. L. Wagener, M. J. F. Digonnet, G. S. Kino, and H. J. Shaw, "Large-scale fiber interferometric sensor arrays with multiple optical amplifiers," in *Conference on Optical Fiber Communication. OFC 97.*, 1997, pp. 157-158.

[39] C. W. Hodgson, J. L. Wagener, M. J. F. Digonnet, and H. J. Shaw, "Optimization of large-scale fiber sensor arrays incorporating multiple optical amplifiers. Part II: pump power," *Journal of Lightwave Technology*, vol. 16, pp. 224-231, 1998.

[40] B. J. Vakoc, M. J. F. Digonnet, and G. S. Kino, "Demonstration of a 16-sensor time-division-multiplexed Sagnac-interferometer-based acoustic sensor array with an amplified telemetry and a polarization-based biasing scheme.," *OFS 2002: 15th Optical Fiber Sensors Conference Technical Digest*, pp. 325-328, 2002.

[41] M. Lopez-Amo, L. T. Blair, and P. Urquhart, "Wavelength-Division-Multiplexed Distributed Optical-Fiber Amplifier Bus Network for Data and Sensors," *Optics Letters*, vol. 18, pp. 1159-1161, Jul 15 1993.

[42] S. Diaz, G. Lasheras, M. Lopez-Amo, P. Urquhart, C. Jauregui, and J. M. Lopez-Higuera, "Wavelength-division-multiplexed distributed fiber Raman amplifier bus network for sensors," in *17th International Conference on Optical Fibre Sensors*, Bruges, Belgium, 2005, pp. 242-245.

[43] S. Diaz, G. Lasheras, and M. Lopez-Amo, "WDM bi-directional transmission over 35 km amplified fiber-optic bus network using Raman amplification for optical sensors," *Optics Express*, vol. 13, pp. 9666-9671, 2005.

[44] S. Diaz, B. Cerrolaza, G. Lasheras, and M. Lopez-Amo, "Double Raman Amplified Bus Networks for Wavelength-Division Multiplexing of Fiber-Optic Sensors," *Journal of Lightwave Technology*, vol. 25, pp. 733-739, 2007.

[45] M. Fernandez-Vallejo, S. Diaz, R. A. Perez-Herrera, D. Passaro, S. Selleri, M. A. Quintela, J. M. L. Higuera, and M. Lopez-Amo, "Resilient long-distance sensor system using a multiwavelength Raman laser," in *20th International Conference on Optical Fibre Sensors*, Edinburgh, United Kingdom, 2009, pp. 750320-4.

[46] P. C. Peng, H. Y. Tseng, and S. Chi, "A hybrid star-ring architecture for fiber Bragg grating sensor system," *IEEE Photonics Technology Letters*, vol. 15, pp. 1270-1272, Sep 2003.

[47] Z. Meng, Y. M. Hu, M. Ni, S. D. Xiong, R. H. Zhang, X. L. Li, G. Stewart, F. Z. Dong, and B. Culshaw, "Development of a 32-element fibre optic hydrophone system," *Fiber Optic Sensor Technology and Applications Iii*, vol. 5589, pp. 114-119, 2004.

[48] Y.-G. Han, T. V. A. Tran, S.-H. Kim, and S. B. Lee, "Multiwavelength Raman-fiber-laser-based long-distance remote sensor for simultaneous measurement of strain and temperature," *Optics Letters*, vol. 30, pp. 1282-1284, 2005.

[49] S. Foster, A. Tikhomirov, M. Englund, H. Inglis, G. Edvell, and M. Milnes, "A 16 channel fibre laser sensor array," in *Optical Fibre Technology/Australian Optical Society, 2006. ACOFT/AOS 2006. Australian Conference on*, 2006, pp. 40-42.

[50] S. Goodman, S. Foster, J. Van Velzen, and H. Mendis, "Field demonstration of a DFB fibre laser hydrophone seabed array in Jervis Bay, Australia," in *Proc. SPIE*, 2009, p. 75034L.

[51] E. Desurvire, *Erbium-doped fiber amplifiers: principles and applications*: Wiley, 2004.

[52] M. J. F. Digonnet, B. J. Vakoc, C. W. Hodgson, and G. S. Kino, "Acoustic fiber sensor arrays," *Second European Workshop on Optical Fibre Sensors: Proceedings*, vol. 5502, pp. 39-50, 2004.

[53] S. Diaz, S. Abad, and M. Lopez-Amo, "Fiber-optic sensor active networking with distributed erbium-doped fiber and Raman amplification," *Laser & Photonics Reviews*, vol. 2, pp. 480-497, Dec 2008.

[54] S. Diaz and M. Lopez-Amo, "Comparison of wavelength-division-multiplexed distributed fiber Raman amplifier networks for sensors," *Optics Express*, vol. 14, pp. 1401-1407, 2006.

[55] S. Abad, M. López-Amo, J. M. López-Higuera, D. Benito, A. Unanua, and E. Achaerandio, "Single and double distributed optical amplifier fiber bus networks with wavelength-division multiplexing for photonic sensors," *Optics Letters*, vol. 24, pp. 805-807, 1999.

[56] M. Fernandez Vallejo, R. A. Perez-Herrera, C. Elosua, S. Diaz, P. Urquhart, C. Bariain, and M. Lopez-Amo, "Resilient Amplified Double-Ring Optical Networks to Multiplex Optical Fiber Sensors," *Journal of Lightwave Technology*, vol. 27, pp. 1301-1306, 2009.

[57] R. A. Perez-Herrera, S. Diaz, P. Urquhart, and M. Lopez-Amo, "A resilient Raman amplified double ring network for multiplexing fiber Bragg grating sensors - art. no. 66193E," *Third European Workshop on Optical Fibre Sensors*, vol. 6619, pp. E6193-E6193, 2007.

[58] V. Montoya, M. Lopez-Amo, and S. Abad, "Improved double-fiber-bus with distributed optical amplification for wavelength-division multiplexing of photonic sensors," *IEEE Photonics Technology Letters*, vol. 12, pp. 1270-1272, Sep 2000.

[59] J. Bromage, "Raman amplification for fiber communications systems," *Journal of Lightwave Technology*, vol. 22, pp. 79-93, 2004.

[60] C. K. Kirkendall and J. H. Cole, "Progress in fiber optic acoustic and seismic sensing," *Optical Society of America Technical Digest*, 2006.

[61] A. D. Kersey, M. A. Davis, H. J. Patrick, M. Leblanc, K. P. Koo, C. G. Askins, M. A. Putnam, and E. J. Friebele, "Fiber grating sensors," *Journal of Lightwave Technology,* vol. 15, pp. 1442-1463, 1997.

[62] B. Lee, "Review of the present status of optical fiber sensors," *Optical Fiber Technology,* vol. 9, pp. 57-79, 2003.

[63] S. Knudsen, G. B. Havsgard, A. bERG, and H. Berg, "Permanently installed high resolution Fiber-Optic 3C/4D seismic sensor systems for In-Well Imaging and Monitoring Applications," presented at the Sixth Pacific Northwest Fiber Optic Sensor Workshop, 2003.

[64] J. T. Kringlebotn, H. Nakstad, and M. Eriksrud, "Fibre optic ocean bottom seismic cable system: from innovation to commercial success," in *Society of Photo-Optical Instrumentation Engineers (SPIE) Conference Series*, 2009, p. 270.

[65] M. Eriksrud, "Towards the optical seismic era in reservoir monitoring," *First Break* vol. 28, p. 7, 2010.

[66] O. H. Waagaard, "Method and apparatus for reducing crosstalk interference in an inline Fabry-Perot sensor array," ed: Google Patents, 2006.

[67] O. H. Waagaard and E. Rønnekleiv, "Method and apparatus for providing polarization insensitive signal processing for interferometric sensors," ed: Google Patents, 2006.

[68] E. Rønnekleiv, "Elimination of polarization fading in unbalanced optical measuring interferometers," ed: Google Patents, 2005.

[69] O. H. Waagaard, "Polarization-resolved spatial characterization of birefringent Fiber Bragg Gratings," *Optics Express,* vol. 14, pp. 4221-4236, 2006.

[70] D. S. Russell, "FSR2200901 2 FOSAR Noise Analysis Rev 1 1," 2008.

[71] E. Desurvire, C. R. Giles, and J. R. Simpson, "Gain saturation effects in high-speed, multichannel erbium-doped fiber amplifiers at λ=1.53 μm," *Journal of Lightwave Technology,* vol. 7, pp. 2095-2104, 1989.

[72] E. Desurvire, J. L. Zyskind, and C. R. Giles, "Design Optimization for Efficient Erbium-Doped Fiber Amplifiers," *Journal of Lightwave Technology,* vol. 8, pp. 1730-1741, Nov 1990.

[73] C. R. Giles, "Optical amplifiers: new challenges in lightwave," in *IEEE, Lasers and Electro-Optics Society Annual Meeting, 1993. LEOS '93 Conference Proceedings.* , 1993, pp. 382-383.

[74] C. R. Giles, C. A. Burrus, D. J. DiGiovanni, N. K. Dutta, and G. Raybon, "Characterization of erbium-doped fibers and application to modeling 980-nm and 1480-nm pumped amplifiers," *IEEE Photonics Technology Letters,* vol. 3, pp. 363-365, 1991.

[75] C. R. Giles and E. Desurvire, "Modeling Erbium-Doped Fiber Amplifiers," *Journal of Lightwave Technology,* vol. 9, pp. 271-283, Feb 1991.

[76] J. Wooler. Excited States in Er^{3+} ions [Online].

[77] M. J. Yadlowsky, "Independent control of EDFA gain shape and magnitude using excited-state trapping," *IEEE Photonics Technology Letters,* vol. 11, pp. 539-541, 1999.

[78] P. M. Becker, A. A. Olsson, and J. R. Simpson, *Erbium-doped fiber amplifiers: fundamentals and technology*: Academic press, 1999.

[79] A. Saleh, R. Jopson, J. Evankow, and J. Aspell, "Modeling of gain in erbium-doped fiber amplifiers," *IEEE Photonics Technology Letters,* vol. 2, pp. 714-717, 1990.

[80] S. L. Hansen, K. Dybdal, and C. C. Larsen, "Gain Limit in Erbium-Doped Fiber Amplifiers Due to Internal Rayleigh Backscattering," *IEEE Photonics Technology Letters,* vol. 4, pp. 559-561, Jun 1992.

[81] M. N. Zervas and R. I. Laming, "Rayleigh scattering effect on the gain efficiency and noise of erbium-doped fiber amplifiers," *IEEE Journal of Quantum Electronics,* vol. 31, pp. 468-471, 1995.

[82] A. Hartog and M. Gold, "On the theory of backscattering in single-mode optical fibers," *Journal of Lightwave Technology,* vol. 2, pp. 76-82, 1984.

[83] G. P. Agrawal, *Nonlinear fiber optics,* 4th ed. Amsterdam ; Boston: Elsevier / Academic Press, 2007.

[84] J. Nilsson, P. Blixt, B. Jaskorzynska, and J. Babonas, "Evaluation of Parasitic up-Conversion Mechanisms in Er3+-Doped Silica-Class Fibers by Analysis of Fluorescence at 980 nm," *Journal of Lightwave Technology,* vol. 13, pp. 341-349, Mar 1995.

[85] P. Myslinski, D. Nguyen, and J. Chrostowski, "Effects of concentration on the performance of erbium-doped fiber amplifiers," *Journal of Lightwave Technology,* vol. 15, pp. 112-120, Jan 1997.

[86] VPIphotonics, "Optical Amplifiers: DopedFiber," in *Photonic Modules Reference Mannual*, ed. VPIsystems, Inc., 2011.

[87] M. J. Yadlowsky, "Pump wavelength-dependent spectral-hole burning in EDFA's," *Journal of Lightwave Technology,* vol. 17, pp. 1643-1648, Sep 1999.

[88] J. Nilsson, B. Jaskorzynska, and P. Blixt, "Performance Reduction and Design Modification of Erbium-Doped Fiber Amplifiers Resulting from Pair-Induced Quenching," *IEEE Photonics Technology Letters,* vol. 5, pp. 1427-1429, Dec 1993.

[89] P. J. Nash, G. A. Cranch, and D. J. Hill, "Large-scale multiplexed fiber optic arrays for geophysical applications," in *Proc. SPIE 4202, Industrial Sensing Systems*, 2000, pp. 55-65.

[90] R. I. O. Inc. Low Noise Single-Frequency Planar External Cavity Laser [Online].

[91] S. T. Inc. Low Phase Noise Lasers: Fiber Optic Seismic Sensing Systems & The Missing Link [Online].

[92] R. Smith, "Optical power handling capacity of low loss optical fibers as determined by stimulated Raman and Brillouin scattering," *Applied Optics,* vol. 11, pp. 2489-2494, 1972.

[93] G. P. Agrawal, *Applications of nonlinear fiber optics*. San Diego: Academic Press, 2001.

[94] G. P. Agrawal, "Modulation instability induced by cross-phase modulation," *Physical Review Letters,* vol. 59, pp. 880-883, 1987.

[95] A. R. Chraplyvy, "Limitations on lightwave communications imposed by optical-fiber nonlinearities," *Journal of Lightwave Technology,* vol. 8, pp. 1548-1557, 1990.

[96] T. A. Berkoff and A. D. Kersey, "Signal-processing techniques for absolute displacement strain sensing using a fiber interferometer," *Optics and Lasers in Engineering,* vol. 16, pp. 153-161, 1992.

[97] T. Electronics/LDI. (2003). *http://www.laserdiode.com/images/products/10-4400-0008c-PINFET_Optical_Receiver_Modules.pdf*.

[98] J.P.Gordon and L.F.Mollenauer., "Phase noise in photonic communication systems using linear amplifiers," *Optics Letters*, vol. 15, p. 1351, 1990.

[99] D. Hill and P. Nash, "Fibre-Optic Hydrophone Array for Acoustic Surveillance in the Littoral," presented at the Photonics for Port and Harber and Security, 2005.

[100] Y. Liao, E. Austin, P. J. Nash, S. A. Kingsley, and D. J. Richardson, "Phase Sensitivity Characterization in Fiber-optic Sensor Systems Using Amplifiers and TDM," *Journal of Lightwave Technology*, vol. 31, pp. 1645-1653, 2013.

[101] T. A. Berkoff, A. D. Kersey, and A. Dandridge, "Noise aliasing in interferometric sensors utilizing phase-generated carrier demodulation," *Fiber Optic and Laser Sensors Vii*, vol. 1169, pp. 80-88, 1990.

[102] R. Slavik, Y. Liao, E. Austin, P. Petropoulos, and D. J. Richardson, "Full characterization and comparison of phase properties of narrow linewidth lasers operating in the C-band," *21st International Conference on Optical Fiber Sensors*, vol. 7753, 2011.

[103] R. Bartolo, A. Tventen, C. Kirkendall, P. Juodawlkis, W. Loh, and J. Plant, "Characterization of a Low-phase-noise, High-power (370 mW), External-cavity Semiconductor Laser," DTIC Document2010.

[104] C. C. Chan, W. Jin, H. Ho, and M. Suleyman Demokan, "Performance analysis of a time-division-multiplexed fiber Bragg grating sensor array by use of a tunable laser source," *IEEE Journal of Selected Topics in Quantum Electronics*, vol. 6, pp. 741-749, 2000.

[105] Y. K. Chen, P. C. Law, and S. C. Huang, "Experimental investigation of an optically amplified time-division-multiplexed polarization-insensitive fiber-optic Michelson interferometric sensor system," *Applied Optics*, vol. 37, pp. 6615-6622, 1998.

[106] A. Yurek, A. Dandridge, and A. Kersey, "Coherent backscatter induced excess noise in reflective interferometric fiber sensors," in *Optical Fiber Sensors*, 1988.

[107] C. McGarrity, R. Pechstedt, and D. Jackson, "Studies of Rayleigh interference in fibre illuminated by a long coherence length laser," *Optics Communications*, vol. 104, pp. 259-265, 1994.

[108] M. Marrone, A. Kersey, C. Villarruel, C. Kirkendall, and A. Dandridge, "Elimination of coherent Rayleigh backscatter induced noise in fibre Michelson interferometers," *Electronics Letters*, vol. 28, pp. 1803-1804, 1992.

[109] O. H. Waagaard, E. Rønnekleiv, S. Forbord, and D. Thingbø, "Reduction of crosstalk in inline sensor arrays using inverse scattering," in *19th International Conference on Optical Fibre Sensors*, 2008, pp. 70044Z-70044Z-4.

[110] D. M. Dagenais, K. P. Koo, and F. Bucholtz, "Effects of parasitic Fabry-Perot cavities in fiber-optic interferometric sensors," *Optics Letters*, vol. 18, pp. 388-390, 1993.

[111] N. Philip, E. Austin, and Y. Liao, "Optical Sensing System With Amplification," UK Patent 25088.5GB, 2012.

[112] J. Kang, J. H. Choi, D. Kim, and G. Kweon, "Zero path-length difference interferometry using spontaneous/spontaneous beat noise spectrum," *Optical Engineering for Sensing and Nanotechnology (Icosn 2001)*, vol. 4416, pp. 128-131, 2001.